

UNIVERSITEIT ANTWERPEN
UNIVERSITAIRE INSTELLING ANTWERPEN
Departement Scheikunde

**Mathematical modeling of a
direct current glow discharge in argon**

Proefschrift voorgelegd tot het behalen van de
graad van Doctor in de Wetenschappen
aan de Universitaire Instelling Antwerpen,
te verdedigen door

Annemie BOGAERTS

Promotor: Prof. Dr. R. Gijbels
Antwerpen, 1996

DANKWOORD

Het onderwerp van mijn licentiaatsthesis had me enthousiast (en nieuwsgierig) gemaakt naar welke mechanismen er allemaal achter de (schijnbaar eenvoudige) glimontlading schuilgaan. Daarom besloot ik een doctoraat aan te vatten om het eens “grondiger uit te puzzelen”. Nu, drie jaar later, weet ik inderdaad een heleboel meer. Maar “hoe meer ik weet, des te meer ik beseft dat ik niets weet”, want de “schijnbaar eenvoudige” glimontlading zit complexer in elkaar dan ze doet vermoeden.

Dat deze boeiende zoektocht van mijn doctoraat tot interessante resultaten geleid heeft, heb ik vooral te danken aan een “ervaren gids”, Prof. Gijbels. Door uw gemeente interesse in mijn werk, uw medeleven (bv. als het weer eens niet wilde “convergeren”), en uw vertrouwen (“het zal je deze keer ook wel lukken”), geraakte ik over alle moeilijke hindernissen heen. U bent een “promotor” in de echte betekenis van het woord! Bedankt!

De microbe van het modelleren heb ik van Mark overgekregen. Bedankt voor de leerrijke discussies in het begin, en ook voor de interesse die je daarna bleef tonen voor mijn werk, Mark!

De eerste obstakels op mijn tocht waren de Monte Carlo en fluidum modellen, waar ik als scheikundige niet veel kaas van had gegeten. De eerste Monte Carlo stapjes heeft Laszlo me leren zetten. Bedankt! Het fluidum model voor argon ionen en electronen leek hardnekkiger. Ondanks verwoede hulppogingen van Prof. Malfliet, Prof. Lemmens, en vooral van Bart Van der Linden, die me de eerste kneepjes van het “oplossen van gekoppelde differentiaalvergelijkingen-vak” heeft aangeleerd, bleef het model koppig onstabiel. Niettemin bedankt voor alle hulp! Ook Surendra probeerde via e-mail vanuit New York mee de gekoppelde differentiaalvergelijkingen te “temmen”. *Thanks Surendra, for the numerous interesting e-mail and telephone discussions and for the helpful advice!* Een lichtpuntje in deze donkere tunnel kwam in zicht toen Prof. Gijbels toevallig een bericht zag over de “Escampig”-conferentie in Nederland. Daar leerde ik Wim Goedheer kennen, die werkelijk als een “goede heer” fungeerde en me uiteindelijk hielp deze schijnbaar onoverkomelijke hindernis te overwinnen. Bedankt Wim, aan jou heb ik één van de grootste stappen voorwaarts op mijn onderzoektocht te danken!

Ook andere mensen hebben me onderweg op de juiste sporen gezet, met gegevens over cross secties (*Thanks, Prof. Phelps*), hulp bij computerproblemen (Bedankt, Koen, Walter, Laszlo), enz...

De ontdekkingstocht van mijn doctoraat heeft me ook tot over de landsgrenzen gebracht. Om mijn modellen te verifiëren, waren experimenten nodig die ik in Antwerpen niet kon uitvoeren. Het Erasmus-verblijf van drie maanden aan

het ISAS in Dortmund heeft me meer vertrouwd gemaakt met plasmadiagnostiek en heeft enkele interessante resultaten opgebracht (o.a. dat experimenteel ook niet alles zo eenvoudig te meten is in de glimontlading). Bovendien heeft dit verblijf me zeker ook een aantal levenservaringen rijker gemaakt. Bedankt, Prof. Broekaert, voor die aangeboden kans en voor uw interesse in mijn werk! *Vielen Dank, Norbert, für deine Begeisterung bei den Experimenten! Vielen Dank, Herr Quentmeier und Maria, für eure Hilfe und für die Möglichkeiten um das Gerät drei Monate zu benutzen, obwohl das im Voraus nicht verabredet war! Und Vielen Dank, Norbert, Ingo, Brigitte, Beate, Wolfgang, Dagmar, Karsten und Herr Stuver, für die tolle Arbeitsgruppe und gemütliche Feten!*

Na dit Dortmund-verblijf had ik geleerd dat ik op zoek moest gaan naar meer gerichte experimenten om mijn modellen te testen, bv. laserdiagnostiek om dichtheidsverdelingen te meten. De combinatie van glimontladingen bij Prof. Harrison (“the father of the glow discharges”) en lasers bij Prof. Winefordner maakte van Gainesville, Florida, de uitverkoren plaats. Meten van drie-dimensionele absolute dichtheidsprofielen van gesputterde tantaal atomen en ionen in de glimontlading met behulp van laser atoom absorptie en fluorescentie: het leek een veel te ambitieus project voor zes weken. Maar in dat labo blijkt niets onmogelijk! Dankzij doelgerichte voorbereidingen via e-mail met Ben, en de enthousiaste hulp van iedereen, lukte het ons zelfs om de dichtheidsprofielen van de argon metastabiele atomen er ook nog bij te nemen! *Thanks, Ben (Smith), Jim (Winefordner), Dr. Harrison, Eugene, Rob, Dagmar, Wei, Cindy, and all the others, for the incredible possibilities, the enthusiastic help, the “we can”-mentality, and the nice atmosphere I found in your group!*

Ook op het “thuisfront” heb ik een aangename werksfeer mogen ervaren. Bedankt aan iedereen van het departement scheikunde, en speciaal bedankt aan Lieve, Karlien, Wendy, Ine, Ann, Filip, Stefan, Koen en Wim voor de toffe middaguurtjes!

Op financieel gebied ben ik dank verschuldigd aan het NFWO, voor mijn aspirantenmandaat, voor het onderzoeksverblijf in Florida, en voor de reiskredieten naar congressen.

Tenslotte gaat mijn speciale dank uit naar Wim, mijn ouders en schoonouders. Ook al begrepen jullie niet alles (Wim) en niet veel (ouders en schoonouders) van waar ik mee bezig was, toch waren jullie mijn naaste reisgezellen op mijn zoektocht! Bedankt voor jullie medeleven, jullie interesse en aanmoediging en jullie vertrouwen!

Annemie Bogaerts
Wilrijk, juli 1996.

TABLE OF CONTENTS

Chapter 1:	
The glow discharge: fundamental aspects and analytical applications	1
1.1. Electrical discharges in gases	3
1.2. Processes occurring in the argon glow discharge	5
1.2.1. Collision processes in the plasma	5
1.2.1.1. Elastic collisions	5
1.2.1.2. Ionization and excitation	6
A. Ionization and excitation of argon atoms	6
B. Ionization and excitation of sputtered (analyte) atoms	8
1.2.1.3. Positive ion - electron recombination	11
1.2.1.4. Deexcitation	13
1.2.2. Processes occurring at the walls	13
1.2.2.1. Secondary electron emission	13
1.2.2.2. Sputtering	16
1.3. Regions in the glow discharge	21
1.3.1. The cathode dark space	21
1.3.2. The negative glow	23
1.3.3. The Faraday dark space	24
1.3.4. The positive column	24
1.3.5. The anode zone	25
1.3.6. Influence of discharge parameters on the various regions	26
1.4. The glow discharge in analytical chemistry	28
1.4.1. Glow discharge source configurations	28
1.4.2. Glow discharge electrical operation modes	30
1.4.3. Analytical applications of the glow discharge	31
1.4.3.1. Glow discharge mass spectrometry	32
1.4.3.2. Glow discharge atomic emission spectrometry	36
1.4.3.3. Glow discharge atomic absorption and fluorescence spectrometry	38
1.4.3.4. Glow discharges in a broader perspective	39
1.5. References	43

Chapter 2:	
Mathematical modeling of a direct current glow discharge in argon	59
2.1. Introduction and aim of the work	61
2.2. Description of the models	64
2.2.1. Monte Carlo model for the fast electrons	64
2.2.2. Fluid model for the argon ions and slow electrons	69
2.2.3. Monte Carlo model for the argon ions and fast argon atoms in the cathode dark space (CDS)	70
2.2.4. Fluid model for the argon metastable atoms	75
2.2.5. Monte Carlo model for the thermalization of the sputtered copper	77
atoms	81
2.2.6. Fluid model for the sputtered copper atoms and ions	83
2.2.7. Monte Carlo model for the copper ions in the cathode dark space	84
2.2.8. Combination of the models	89
2.3. Results of the models	91
2.3.1. Discharge conditions	109
2.3.2. Densities of the plasma species	113
2.3.3. Electric field and potential distributions	124
2.3.4. Energy distributions and mean energies of the species	136
2.3.5. Collision processes of the plasma species	142
2.3.6. Crater profiles and etching rates at the cathode	
2.3.7. Remarks on the input parameters and conclusion	145
	146
2.4. Comparison with one-dimensional models	146
2.4.1. Discharge conditions	149
2.4.2. Densities of the plasma species	150
2.4.3. Electric field and potential distributions	150
2.4.4. Energies of the plasma species	153
2.4.5. Collision processes of the plasma species	154
2.4.6. Crater profiles and etching rates at the cathode	
2.4.7. Conclusion	
	155
2.5. Explanation of relative sensitivity factors in GDMS by means of the modeling work	155
2.5.1. Introduction	158
2.5.2. The empirical model by Vieth and Huneke	160

2.5.3. The explicit approach based on the modeling results	165
2.5.4. Results	
2.5.5. Conclusion	167
2.6. References	
Summary and conclusion / Samenvatting en besluit	173
Mathematical modeling of a direct current glow discharge in argon	175
Wiskundige simulaties van een gelijkstroom-glimontlading in argon	180
Appendix	187
Publications	189
Contributions at conferences	191
Scientific visits	195
Scientific prizes	195

CHAPTER 1

**The glow discharge: fundamental aspects
and analytical applications**

1.1. ELECTRICAL DISCHARGES IN GASES [1,2]

A gas in its normal state is almost a perfect isolator. However, when a sufficiently high voltage is applied between two electrodes, placed in a low pressure gaseous environment, atoms and molecules of the gas will break down electrically, giving rise to electron-ion pairs. This permits current to flow through the gas medium, making the gas to become a conductor. This phenomenon is called an "electrical discharge". Electrical discharges are subdivided according to their current-voltage characteristics. Figure 1.1 [1] shows the subdivision into the most common types of electrical discharges as a function of their current-voltage behavior.

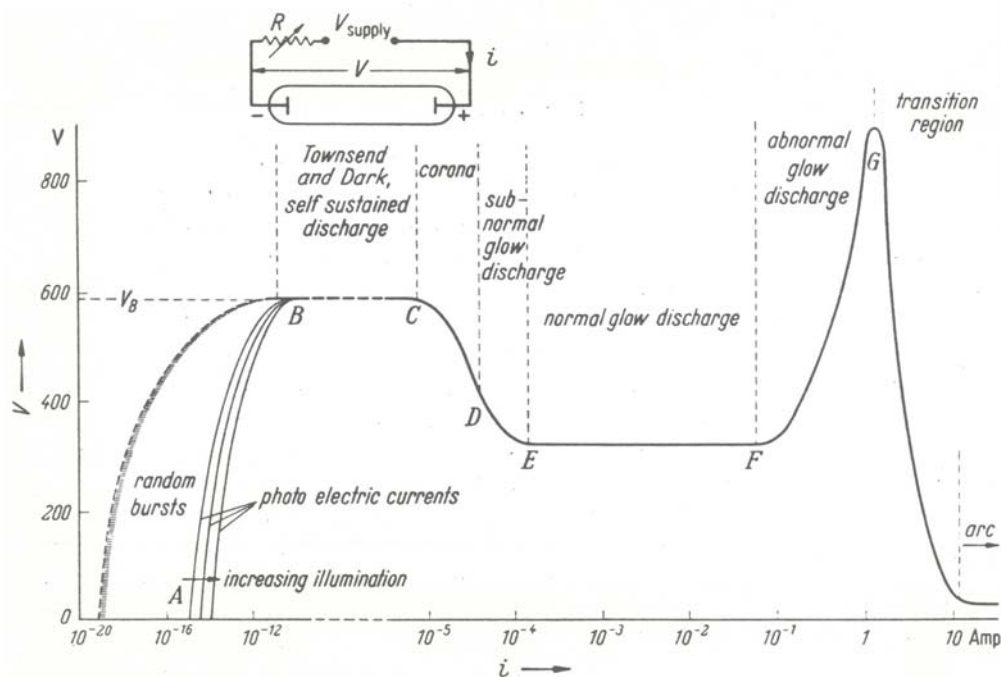


Figure 1.1: Current-voltage characteristics of various types of electrical discharges [1].

If a very low voltage is applied across the electrodes, extremely small currents (ca. 10^{-18} A) are observed, occurring in random bursts. Such currents are due to electron multiplication in the gas by ionizational collisions. The original electrons arise from ionization by cosmic rays. If the cathode would be illuminated by ultra violet (uv) light, a somewhat higher steady current, of about 10^{-12} or 10^{-13} A would be observed. Indeed, the photoelectric current gives rise to more original electrons, resulting in more electron multiplication and hence in a higher current. The higher current is however reverted to the random bursts by removal of the uv light. This

phenomenon is characteristic for a "non-selfsustained discharge", which is presented in region AB.

If the potential V is further increased, the current rises rapidly and does not change anymore by removal of the external uv light. Indeed, each electron leaving the cathode and moving towards the anode produces ions and excited atoms by ionization and excitation collisions. These ions, and the photons created from the excited atoms, can strike the cathode and release new electrons. If at least one electron is created at the cathode for each electron moving from cathode to anode, the process repeats itself and a "selfsustaining discharge", also called "Townsend or dark discharge", has been formed (region BC). The lowest voltage at which this occurs, is called the "Breakdown voltage, V_B ". The currents flowing in this kind of discharge are so small (i.e. 10^{-12} - 10^{-6} A) that the emitted light is extremely low, which explains the name of "dark discharge". Also the space charges are negligible, so that the electric field is only determined by the potential and the geometry and is uniform across the discharge.

If the current is allowed to increase further to about 10^{-4} A, the discharge becomes "visible" with light and dark regions between cathode and anode. Moreover, the potential across the electrodes drops, until it reaches a constant value (region CDE). From now on, space charges start playing a role in the discharge, distorting the uniform field. The potential drop shows that the discharge conditions are now more favorable, making ionization easier and reducing losses of ions and electrons, so that a lower potential is sufficient to sustain the discharge. A "glow discharge" has now been established (region DEFG).

The glow discharge itself can still be subdivided in three types of discharges. When the glow discharge develops from the Townsend discharge and the potential drops with increasing current, the glow discharge is in the "subnormal" regime (region DE). If the current is increased further from 10^{-4} to 0.1 A, the voltage remains constant and the glow discharge is in the "normal" mode (region EF). The discharge covers only a part of the cathode. If the current increases, the covered area rises proportionally, so that the current density remains constant. The potential remains therefore also constant, since it depends on the current density and not on the current itself. When the whole cathode is covered, the potential will start rising with increasing current. The glow discharge is now in the "abnormal" mode (region FG). This is the region in which glow discharges for analytical purposes usually operate.

If the current still increases, the potential rises to a maximum and falls then off to very low values. The ion current towards the cathode is now so large that the cathode is being heated. Thermoelectric emission starts playing a major role and the mechanism of the glow discharge has become insignificant. This kind of discharge is called the "arc discharge" (region GH).

1.2. PROCESSES OCCURRING IN THE ARGON GLOW DISCHARGE [1-7]

The glow discharge is a complex kind of gas plasma, existing of a variety of plasma species, i.e. electrons, atoms, ions, excited species, different clusters, photons, etc. The plasma species can in principle all collide with each other, giving rise to a large number of plasma processes. Since the glow discharges employed for analytical purposes mostly use argon as discharge gas, and because our modeling work is concentrated on an argon glow discharge, only those processes occurring in an argon glow discharge will be described here. In addition to the most important collision processes in the plasma, an overview will be given of the different processes occurring at the walls of the glow discharge cell.

1.2.1. Collision processes in the plasma

In principle, all kinds of plasma species present in the plasma can collide with each other. The number of possible plasma processes is tremendous and probably not all processes are known in the literature. It is hence not feasible to give a systematic and comprehensive overview of all the possible processes. We will therefore restrict ourselves to the ones most relevant for analytical glow discharges, i.e. ionization (and recombination) and excitation (and deexcitation), and to the plasma species playing a role in these processes, i.e. electrons, argon atoms, singly charged positive argon ions, metastable argon atoms, and atoms and ions of the cathode material. Collision processes involving multiply charged particles and clusters will not be considered here, since these species are not included in our modeling work and our knowledge about their relevant processes is too limited to give a complete overview.

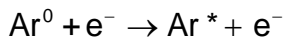
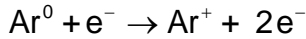
1.2.1.1. Elastic collisions

Since this type of collision is widely occurring in the discharge, it will be briefly described here. Elastic collisions do not result in internal changes of the energy of the collision partners; their effect is only to redistribute the kinetic energy of the particles. This redistribution is considerable for species with comparable masses (e.g. two atoms), but is negligible for particles with very different masses (e.g. atom + electron).

1.2.1.2. Ionization and excitation

A. Ionization and excitation of argon atoms

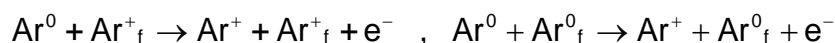
* Electron impact ionization and excitation



Electron impact ionization is one of the most important and best-known processes in the glow discharge. It is the essential process in a self-sustaining plasma, since the electrons formed in this way can again give rise to ionization, leading to electron multiplication. It can occur by the collision of electrons with argon atoms in the ground state (**direct electron impact ionization**) and also with argon atoms in the metastable level at 11.55 eV or 11.72 eV (**two-step electron impact ionization**). The minimum electron energy required for the first process is 15.76 eV (i.e. the ionization potential of argon), whereas the second process can already occur at electron energies above 4 eV. Nevertheless, the first process is much more important in the glow discharge due to the much higher argon ground state atom density compared to the argon metastable atom density (see Chapter 2, Section 2.3.2). The cross sections of both processes increase with the electron energy, reach a maximum of about 3×10^{-16} and 8×10^{-16} cm² at about 80 and 10 eV, respectively, whereafter they decrease again, because the residence time of the electron around the argon atom becomes too short for efficient ionization [8, 9] (see Chapter 2, figure 2.2).

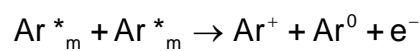
The mechanism of **electron impact excitation** is the same as for ionization, but less energy is transferred to the atom, so that no electron can be ejected, it can only jump to a higher energy level within the atom. The total cross section of electron impact excitation as a function of the electron energy shows the same behavior as for electron impact ionization. The minimum energy required is 11.55 eV (i.e. the energy of the lowest excited level). A maximum of about 1.6×10^{-16} cm² is reached at about 20 eV [10] (see Chapter 2, figure 2.2). Cross section data for excitation from the argon ground state to individual excited energy levels of argon are presented in refs. [10, 11].

* Fast argon ion and argon atom impact ionization and excitation



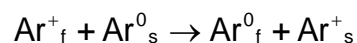
In analogy to electron impact ionization and excitation, argon ions and atoms can also cause the ionization and excitation of argon atoms if their energy is sufficiently high. The cross sections of these processes behave in a similar manner as the ones for electron impact ionization and excitation, i.e. rising with increasing impact energy, until a maximum is reached, and falling off at high energies. However, the cross section curves are shifted towards higher energies, due to the larger masses of atoms and ions. Indeed, the process becomes only important at ion and atom energies of more than 100 eV and the maximum is reached above 1000 eV. The cross section values at the maximum are comparable to the ones for electron impact excitation and ionization [12] (see Chapter 2, figure 2.4). In the glow discharge, highly energetic argon ions and atoms are only found close to the cathode, where they have gained much energy from the electric field in front of the cathode. Therefore, argon ion and atom impact ionization and excitation are only significant close to the cathode, and the importance of these processes in the glow discharge increases with increasing discharge voltages. At voltages of about 1 kV which are commonly used in analytical glow discharges, these processes are clearly not negligible (see Chapter 2, Section 2.3.5).

* Argon metastable atom collisions leading to the ionization of one of the atoms



When two argon metastable atoms collide with each other, they have together sufficient energy (2 times 11.55 eV) to knock off one electron and to bring about the ionization of one of the atoms. The rate constant of this process is about $6.4 \times 10^{-10} \text{ cm}^3 \text{ s}^{-1}$ [13]. The process is however of minor importance in the glow discharge, compared to electron impact ionization (see Chapter 2, Section 2.3.5).

* Symmetric charge transfer



When a fast argon ion collides with a slow argon atom, an electron can be transferred from the atom to the ion without changes in kinetic energy of the two colliding particles. In this way a fast argon atom and a slow argon ion are formed. It is hence not a real ionization process since there is no increase in the number of ions; only a fast argon ion has disappeared and a new slow argon ion has been created. However, the process is included in this overview since it is of major importance in the glow discharge. Indeed, this process is responsible for the creation of a large flux of fast argon atoms bombarding the cathode, which leads to

sputtering (see further). The cross section of this process is at the order of $5 \times 10^{-15} \text{ cm}^2$ at energies of a few eV and decreases slightly towards higher energies [14] (see Chapter 2, figure 2.4).

* Thermal ionization/excitaton and photoionization/photoexcitation

In principle, the argon atoms can be ionized or excited due to any suitable energy input. Therefore thermal and photoionization and -excitation are also included in this overview. Thermal ionization/excitation occurs due to the energy received by impact with argon gas atoms or with the atoms of the walls. Since the glow discharge can be considered as a "cold" plasma (i.e. the gas temperature is about 300 K or slightly higher), the thermal processes can be considered negligible [3]. Photoionization and excitation however, can be of importance [3]. The cross section of photoionization shows a maximum of about $3.7 \times 10^{-17} \text{ cm}^2$ (i.e. about 7 times lower than the maximum in the electron impact ionization cross section) at the threshold photon energy (i.e. 15.8 eV, corresponding to about 800 Å) and decreases very rapidly towards higher energies. The cross section of photoexcitation is comparable to the one of photoionization [3].

B. Ionization and excitation of sputtered (analyte) atoms

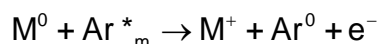
In principle, the same processes that cause the ionization and excitation of argon atoms, apply also to the ionization and excitation of analyte atoms. However, very little is known of the above mentioned processes concerning the analyte atoms.

Only electron impact ionization data are available from the literature [15]. In addition to the above mentioned processes, two other collision types seem to be of special importance for the ionization and excitation of analyte atoms.

* Electron impact ionization and excitation

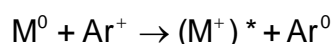
The mechanisms are the same as for the corresponding processes of argon atoms. The cross section of electron impact ionization as a function of the electron energy is of comparable shape and magnitude for all elements [15]. Therefore, this process can be considered as rather unselective. The electron impact ionization cross section for copper is presented in figure 2.2 (see Chapter 2). We expect a similar curve for the cross sections of electron impact excitation of the analyte atoms, but are not aware of data in the literature.

* Penning ionization



If an argon metastable atom collides with an analyte atom, the energy of the metastable level (i.e. 11.55 eV) can be used to ionize the analyte atom if the ionization potential of the latter is lower than the metastable energy. Since most of the atoms of the periodic table have an ionization potential lower than this value, Penning ionization is also more or less an unselective process. Cross sections of this process are rather difficult to find in the literature for all elements. However some empirical formulae are available, expressing a relation between the cross section and the mass and radius or polarizability of the colliding particles [16, 17]. Generally, the Penning ionization cross sections between argon metastable atoms and analyte atoms are in the order of $5 \times 10^{-15} \text{ cm}^2$ [16, 18]. This process is suggested to be dominant in low pressure discharges [19-22]. In analogy to Penning ionization, the corresponding Penning excitation process is mentioned in ref. [23], i.e. the creation of excited analyte atoms by collision with argon metastable atoms, but we are not further aware of relevant data.

* Asymmetric charge transfer



The collision between an analyte atom and an argon ion can lead to the transfer of an electron from the atom to the ion, if the energy difference between the argon ion ground state or metastable level and the energy levels of the resulting analyte ion is sufficiently small; the efficiency of this process generally decreases with growing energy difference between the levels. Asymmetric charge transfer is therefore a more or less selective process, unlike Penning ionization which occurs unselectively for all elements having an ionization potential below the argon metastable energy level, independently of the relative position of the levels.

A wide range of cross section data of asymmetric charge transfer is available in the literature (for an overview, see [24]). However, most data apply to the high or very high energy range (several tens of eV to MeV), and are hence not of interest for the glow discharge where the ions are characterized by thermal energies (especially in the NG which constitutes the major part of the discharge and also the most important region for ionization). A number of cross section data can also be found in the literature for thermal energies (see [24]), but they mainly concern reactions of rare

gases and molecular gases and do not deal with reactions between rare gas ions and metal atoms, which are of interest in the glow discharge.

Cross sectional data of asymmetric charge transfer between rare gas ions and metals are much more difficult to find in the literature. A number of papers have described the asymmetric charge transfer process in a qualitative manner or have shown evidence for the occurrence of such processes in glow discharges (e.g. refs. [25-39]). Quantitative cross section data, mostly obtained experimentally, are available in the literature, in connection with metal-vapour ion (hollow cathode) lasers, for specific combinations of reactants, for example He⁺-Cd [40-42], He⁺-Zn [43], He⁺-Hg [44-50], He⁺-Cs [51], He⁺-Rb [52], Ne⁺-Zn [53], Ar⁺-Cu [54] and Xe⁺-Ca,Sr [55]. Ref. [55] presents cross-sectional data for the different combinations of reactions between He⁺, Xe⁺ or Cs⁺ ions with Fe, Mo, Al, Ti, Ta and C atoms, at energies ranging from 1 to 5000 eV. To our knowledge, asymmetric charge transfer cross section data between Ar⁺ ions and various transition element metals (Fe, Ta, Mo, ...) at thermal energies are unfortunately rarely available in the literature. It is also dangerous to deduce the cross sections from data between other elements. Indeed, the process of asymmetric charge transfer seems to be fairly complicated; for example, it is not always true that the smallest energy difference between energy levels yields the highest cross section [26, 43, 44].

Because of the virtual non-availability of the cross section data, the relative importance of this process in the glow discharge is still a controversial subject. Steers and coworkers have clearly demonstrated the occurrence of asymmetric charge transfer between Ar⁺ and Cu [33,34], for Ne⁺-Cu and Ne⁺-Al [35], for Ar⁺-Fe [36] and between Ar⁺ and Ti [37]. Recently, also Wagatsuma and Hirokawa [39] showed evidence for the occurrence of this process for Ar⁺-Fe and Ne⁺-Fe in a Grimm-type glow discharge. The process has also been shown to be important in hollow cathode discharges between Ne⁺ and Cu [32, 57, 58], Ar⁺, Ne⁺ and Fe [38], Ar⁺ and Ti [30], He⁺ and Cu [27] and between Ar⁺ and Cu [54]. In the early investigations of Coburn and Kay [59], Penning ionization was considered to be the most important ionization process and charge transfer was neglected. These workers considered only charge transfer in which the ground state of the analyte ions is formed; since ΔE is then far too large, they ruled out that possibility. However, as was demonstrated by Steers and coworkers [33-37], the resulting analyte ion can also be formed in an excited state so that ΔE becomes much smaller. Levy et al. [20] found, on the other hand, that charge transfer between Ar⁺ and Cu is unimportant in low-pressure, low-current discharges. Indeed, the Cu ion possesses only one energy level which has only a good overlap with the argon ions in the metastable state (see Chapter 2, Section 2.5) and it is highly possible that the argon ions in the metastable state have low densities in a low-pressure discharge.

However, a large number of elements do possess ionic energy levels that have a good overlap with the argon ion ground state level, but these elements were not investigated in ref. [20] so that the conclusions of this paper cannot be generalized. In refs. [41, 43], cross section data are available for He⁺/Cd and He⁺/Zn, resp.; in these cases, a good energy overlap is found and moreover the Penning ionization and asymmetric charge transfer cross sections are measured to be of comparable magnitude. From our calculated argon ion number density data (see Chapter 2, Section 2.3.2), we expect that asymmetric charge transfer can have a non-negligible role for specific elements, also in low pressure glow discharges (see Chapter 2, Section 2.3.5).

1.2.1.3. Positive ion - electron recombination

Electron-ion recombination is the reverse process of ionization, i.e. an electron coalesces with a positive ion to form a neutral atom. From the conservation laws of momentum and energy follows that a simple two-body coalescence is not allowed [3]. However, some alternative recombination processes can occur. To our knowledge, the recombination processes apply to both argon and analyte ions, and they will therefore be discussed simultaneously (A⁺ is an arbitrary ion).

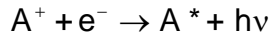
** Three-body recombination*



A third body takes part in the collision process, taking away the excess energy and allowing to satisfy the conservation laws. The third body B can be every particle present in the plasma, or it can be the cell wall. If the third body is a heavy particle, the electron can lose only a small fraction (i.e. $2m_e/M_B$) of its energy to the third body. Therefore, this reaction is very slow [5, 6]. Massey and Burhop [60] estimated that the coefficient of this three-body recombination process is about $10^{-11} \times p \text{ cm}^3 \text{ s}^{-1}$, where p is the gas pressure in Torr. Therefore, for a gas pressure of about 1 Torr, and for electron and argon ion densities of the order of 10^{11} cm^{-3} (see Chapter 2, Section 2.3.2), the rate of this recombination process is of the order of $10^{11} \text{ cm}^{-3} \text{ s}^{-1}$. When comparing this with typical ionization rates of the order of $10^{16} \text{ cm}^{-3} \text{ s}^{-1}$ (see Chapter 2, Section 2.3.5), it can be concluded that this kind of recombination is insignificant in our glow discharge. However, when the third body is an electron, the three-body recombination process is clearly more efficient, since the electrons can better take away the excess energy. Rate constants for this process are reported in the order of $10^{-24} \text{ cm}^6 \text{ s}^{-1}$ [61, 62]. For electron and argon ion

densities at the order of 10^{11} cm^{-3} , the rate of this recombination is about $10^9 \text{ cm}^{-3} \text{ s}^{-1}$. Hence, this process is also negligible compared to ionization in our glow discharge.

* Radiative recombination



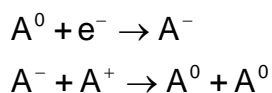
The excess energy is carried away by a photon. The rate constant of this process is about $10^{-11} \text{ cm}^3 \text{ s}^{-1}$ in the case of argon [63], yielding a recombination rate of about $10^{11} \text{ cm}^{-3} \text{ s}^{-1}$ at typical electron and argon ion densities, which is again negligible compared to the ionization rate.

* Dissociative recombination



When the ion is molecular, a two-body recombination process is possible since the collision product can dissociate and the recombination energy is converted into kinetic and potential energy of the dissociation products. When AB^+ is equal to Ar_2^+ , the rate constant is in the range of 10^{-7} - $10^{-6} \text{ cm}^3 \text{ s}^{-1}$ [63]. The process is hence clearly more efficient than radiative recombination. Nevertheless, this process will not be of major importance in the glow discharge since Ar_2^+ ions are not considered to be dominant species in the glow discharge.

* Two stage recombination



The electron attaches to a neutral atom to form a negative ion. The negative ion collides with a positive ion, an electron is transferred, and two neutral atoms are formed. The probability of forming a negative ion (step 1) depends on the electronegativity of the atom. For argon, the probability is very low, so that this kind of recombination is also negligible.

In general, it can be concluded that electron-ion recombination is only significant at high electron and ion densities and will be of minor importance in our practical low pressure argon glow discharges. In principle, the neutralization of the charge on a positive ion may also be accomplished by a negative ion. However, negative ions

are rather improbable in argon glow discharges, so that this process can also be considered negligible.

1.2.1.4. Deexcitation

Whereas recombination is the inverse of ionization, deexcitation is the inverse of excitation. Indeed, except from the metastable levels, the excited levels of the atoms are only short-living, and the electron configuration soon returns to the ground state in one or several transitions. Each transition is accompanied by the emission of a photon with specific energy. If such a photon has an energy between 1.7 and 3.0 eV (corresponding to 720 nm and 410 nm, respectively), it is detected by our eyes. Hence, the deexcitation processes produce a glow and are therefore responsible for the characteristic name of the “glow” discharge.

1.2.2. Processes occurring at the walls

When a particle collides at the walls of the glow discharge, different phenomena may occur, depending on the kind of particle. An electron may be reflected, absorbed or cause the emission of secondary electrons. An ion or atom may be reflected (possibly in another form), implanted (probably with structural rearrangements), cause secondary electron emission or eject one of the wall atoms (called sputtering). The latter two processes are of special importance for the glow discharge, and will therefore be discussed in more detail. Secondary electron emission can occur at all walls, whereas sputtering is more or less restricted to the cathode, since high particle bombarding energies are required for this process.

1.2.2.1. Secondary electron emission

When a particle strikes a surface, an electron can be emitted. This process is especially important to maintain the glow discharge, i.e. new electrons can be supplied to compensate for the electron losses at the walls. Secondary electron emission can be caused by the bombardment of electrons, ions, neutrals and photons. The number of electrons emitted per incident particle is called the secondary electron emission coefficient. It depends on the kind of bombarding particles and their energy, and on the kind of wall material.

* By electron bombardment

This process is only important at the anode walls, and is negligible at the cathode since the strong electric field in front of it prevents the electrons from bombarding the cathode. When electrons strike a surface, three types of electrons are emitted (see figure 1.2 [64]), i.e. (i) the elastically reflected primaries, with energies equal to the energy of the incident electron, (ii) inelastically reflected primaries, with energies lower than the incident electron energy, and (iii) true secondary electrons, with energies of a few eV. The latter group is often the major one. The secondary electron emission coefficient by electron bombardment, δ , is in the order of 1, but depends on the electron energy and the kind of surface material. It typically shows a maximum at electron energies of about 600-800 eV [3, 65].

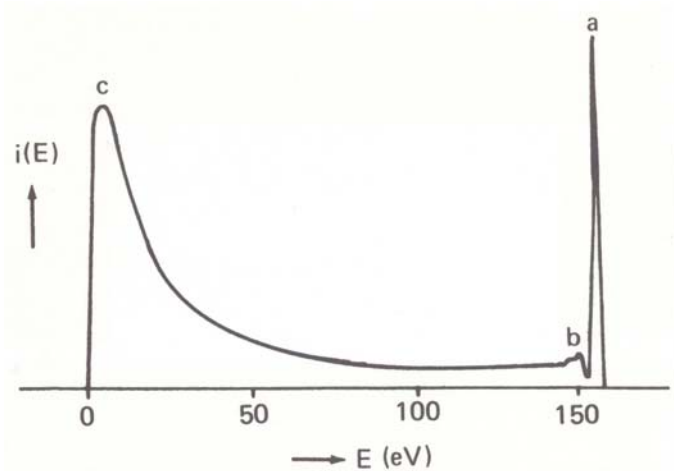


Figure 1.2: Energy distribution of secondary electrons emitted by silver; (a) elastically reflected primaries, (b) inelastically reflected primaries, (c) "true" secondary electrons [64].

* By positive ion and atom bombardment

This process can occur at both cathode and anode walls. The secondary electron emission coefficient, γ , is nearly independent of the ion or atom kinetic energy at energies below 500-1000 eV. It is typically in the order of 0.1 for positive argon ions and nearly zero for neutral ground state argon atoms. At higher energies, γ starts to increase with the ion or atom kinetic energy (see figure 1.3 [66]). This suggests that secondary electron emission results from a constant potential energy component (ca. 0.1 for the argon ions and almost zero for the argon atoms), and a kinetic energy component (equal for both) which only plays a role at energies beyond 500-1000 eV. The mechanism of "potential energy ejection" is explained by Auger neutralization [5]. The potential energy component of the ions is of the order of the ionization potential, which seems highly sufficient for secondary electron emission. Neutral ground state atoms do not possess such a potential energy component which explains that γ is negligible at energies below 500-1000 eV. However, metastable atoms do possess a potential energy (i.e. the energy of the excited metastable level),

hence they will give rise to a higher secondary electron emission coefficient. However, rather little quantitative information is available. For helium (2^3S) metastables, a secondary electron emission coefficient of 0.29 on a gold surface was reported by Stebbings [67]. Hasted extended this work and observed values in the order of 0.1-0.25 for surfaces of molybdenum, tungsten and platinum [68]. Oechsner

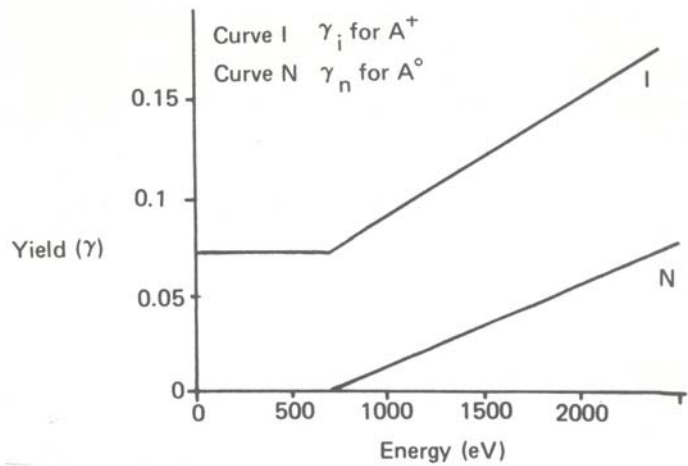


Figure 1.3: Secondary electron emission coefficient as a function of energy for argon ion and atom bombardment of molybdenum [66].

measured secondary electron emission coefficients for 1.05 keV Ar^+ ions on 11 different polycrystalline surfaces [69]. He proposed a theoretical formula which showed good agreement with the experimentally obtained values:

$$\gamma = \frac{0.2}{\varepsilon_F} (0.8 E_i - 2 \Phi)$$

where ε_F is the Fermi energy measured from the bottom of the valence band, E_i is the effective potential energy of the incoming ion, and Φ is the work function of the metal. If this formula is applicable to other species than Ar^+ ions too, the secondary electron emission coefficient of argon metastable atoms ($E_i = 11.55$ eV) on metal surfaces could be calculated and typical values of about 0.005-0.05 would be obtained.

It should be noticed that the value of the secondary electron emission coefficient by ion and atom bombardment is largely dependent on the surface conditions (crystal phase, contaminations). Moreover, the values characteristic for pure metals can differ significantly from the ones of alloys or nonconducting materials [3].

** By photon bombardment*

The ejection of electrons due to photon bombardment is called photoemission. The photoelectric yield γ_p for most pure metals is only 10^{-4} - 10^{-3} electrons per photon in the visible and near uv wavelength range, since the photons are usually more efficiently reflected. It increases however towards shorter wavelengths (i.e. of the

order of 0.1 at 100 nm [3]). The effects of photoelectric emission in glow discharges are however not well understood.

* Field emission

At extremely high electric fields (ca. 10^7 V/cm), electrons can be emitted by the mere action of the electric field. However, since such high electric fields do not occur in practical glow discharges, this effect can be considered negligible.

1.2.2.2. Sputtering

When energetic particles (i.e. gas ions, gas atoms and also ions of the cathode material) bombard the cathode surface, they can penetrate into the surface and set up a series of collisions between atoms of the cathode material, until they have lost their energy. In this three-dimensional collision cascade, which lasts for a very short period of time only (ca. 10^{-12} sec. [70]), atoms lying at the surface can obtain some energy larger than their surface binding energy so that they can escape from the surface. This is called sputtering. It is believed that the majority of the sputtered particles are neutral atoms. Ions can also be sputtered, but positive ions will immediately return back to the cathode, by the strong electric field in front of it. The energy of the sputtered atoms is in the order of 5-15 eV [71].

The collision cascade does not always lead to sputtering. Most of the time, it just heads off into the interior of the cathode material. The energy of the bombarding particles is then entirely dissipated to lattice vibrations, i.e. heating of the cathode. The sputtering process is hence rather inefficient: only about 1% of the incident energy reappears as the energy of the sputtered particles [1, 3].

The most important quantities with respect to sputtering are the sputtering yield, the sputtering rate and the escape and sampling depths. These quantities will be explained in somewhat more detail.

1) Sputtering yield

The sputtering yield, Y , is defined as the number of sputtered atoms per incident particle. Analytical expressions or estimates for sputtering yield data have been developed by many authors from theories [72, 73], empirical relations [74, 75] and computer simulations [76] of sputtering processes. Sigmund has developed a comprehensive theory describing the effects of different ion-target combinations and energies, based on the assumption that sputtering is closely related to other ion-bombardment phenomena, and solving the linearized Boltzmann equation [72]. The

calculation consists of 4 different steps: (i) the determination of the amount of energy deposited by energetic particles near the surface, (ii) the conversion of this energy into a number of low energy recoil atoms, (iii) the determination of the number of these atoms that can reach the surface, and (iv) the selection of those atoms that have sufficient energy to overcome the surface binding forces. However, systematic derivations from the original Sigmund formula have been pointed out for some cases, such as light-ion and low-energy sputtering [77]. A few modifications to this original formula have been proposed [73], but some discrepancies still remained. On the other hand, also a number of empirical formulae have been developed [74, 75, 77]. In the formulae proposed by Matsunami et al. [75, 77] the discrepancies of the Sigmund formula have been solved, and these formulae can hence be applied to all ion-target combinations [78]. In our modeling calculations, we use the so-called second Matsunami formula for normal incidence [77, 78]:

$$Y(E) = 0.42 \frac{\alpha Q K \sigma_n(\varepsilon)}{U_s [1 + 0.35 U_s \sigma_e(\varepsilon)]} \left[1 - \sqrt{\frac{E_{th}}{E}} \right]^{2.8}$$

where:

- * $Y(E)$ is the sputtering yield for incident ions (and atoms) of energy E ;
- * U_s is the sublimation energy of the cathode material (in eV);
- * Q is an empirical parameter, dependent on the cathode material;
- * $\sigma_n(\varepsilon)$ and $\sigma_e(\varepsilon)$ are Lindhard's elastic and inelastic reduced stopping cross sections:

$$\sigma_e(\varepsilon) = 0.079 \frac{(M_1 + M_2)^{3/2}}{M_1^{3/2} M_2^{1/2}} \frac{Z_1^{2/3} Z_2^{1/2}}{(Z_1^{2/3} + Z_2^{2/3})^{3/4}} \sqrt{\varepsilon}$$

$$\sigma_n(\varepsilon) = \frac{3.441 \sqrt{\varepsilon} \ln(\varepsilon + 2.718)}{1 + 6.355 \sqrt{\varepsilon} + \varepsilon (-1.708 + 6.882 \sqrt{\varepsilon})}$$

- * ε is the reduced energy:

$$\varepsilon = \frac{0.03255}{Z_1 Z_2 (Z_1^{2/3} + Z_2^{2/3})^{1/2}} \frac{M_2}{M_1 + M_2} E$$

where Z_1 and Z_2 are the atomic numbers of the bombarding and sputtered particles, resp., and M_1 and M_2 are their mass numbers.

- * K is the conversion factor from $\sigma_n(\varepsilon)$ to $S_n(E)$ (reduced energy to energy in eV):

$$K = \frac{S_n(E)}{\sigma_n(\varepsilon)} = 8.478 \frac{Z_1 Z_2}{\left(Z_1^{2/3} + Z_2^{2/3}\right)^{1/2}} \frac{M_1}{M_1 + M_2}$$

* α is an empirical parameter, function of M_1/M_2 :

$$\alpha = 0.08 + 0.164 \left(\frac{M_2}{M_1}\right)^{0.4} + 0.0145 \left(\frac{M_2}{M_1}\right)^{1.29}$$

* E_{th} is an empirical parameter, function of M_1/M_2 and U_s . It represents the minimum energy required for sputtering:

$$E_{th} = U_s \left[1.9 + 3.8 \left(\frac{M_1}{M_2}\right) + 0.134 \left(\frac{M_2}{M_1}\right)^{1.24} \right]$$

This empirical formula is in principle valid for all combinations of bombarding ions/atoms and cathode materials [78].

From this formula it can be concluded that the sputtering yield is a complex function of the incident energy and the masses and atomic numbers of the bombarding particles and surface target. The influence of the different factors determining the sputtering yield will be briefly discussed.

* The kind of discharge gas: Inert gases are mainly used, since they provide high sputtering yields, and they will not undergo chemical reactions with the cathode material.

* The masses of the incident particles: In general, the sputtering yield increases less than linearly with the masses of the bombarding particles. H_2^+ forms an exception, i.e. it gives unusually high sputtering yields due to chemical reactions with the cathode material which result in low redeposition. From the Matsunami formula (see above) it can also be concluded that the sputtering yield does not reach a maximum as the masses of bombarding particles and surface target are close to each other (see examples in ref. [78]), which has sometimes been suggested from simplified sputtering yield expressions [3].

* The energy of the incident particles: A threshold energy of the incident particles is required to give sputtering. Indeed, the atoms at the cathode surface must obtain sufficient energy to overcome their surface binding energy. A good measure of the surface binding energy is the heat of sublimation. It is suggested that the minimum

energy for sputtering must be about four times the heat of sublimation of the cathode material [79]. Above this minimum energy, the sputtering yield increases with the energy of the bombarding particles. It reaches a broad maximum at energies in the order of several keV, where after it decreases again, as ion implantation becomes important [3].

* The angle of the incident particles: Oechsner has found that for rare gas ions bombarding a polycrystalline copper target with energies of 0.5-2 keV, the sputtering yield reaches a maximum at incident angles of about $60-80^\circ$ relative to the surface normal [80]. Indeed, at low incident angles, the sputtering yield increases with rising angle due to the increased probability of the collisional cascade to propagate back to the cathode surface and hence to result in sputtering. At incident angles higher than $60-80^\circ$ the sputtering yield decreases, since the incoming particles are more likely to reflect off the surface without any penetration or momentum transfer, so that sputtering becomes unlikely.

* The kind of cathode material: In general, the sputtering yield increases with the atomic number of the cathode material, within each row of the periodic table (see figure 1.4 [81]). Copper, silver and gold have the highest sputtering yield among transition metals. This trend is explained in the following manner [5]: It is stated that if the penetration depth in the surface increases, a larger fraction of the energy is expended in collisions that do not lead to sputtering. The increase in sputtering yield is associated with the filling of the electron shells, especially the d shells. As the shells fill, the target looks more opaque, and the incident particles are not able to penetrate very deeply and give hence rise to more sputtering.

However, it should be noticed that the sputtering yields of the different elements seldom differ more than a factor of ten among each other, as opposed by the rates of evaporation which differ by several orders of magnitude [81]. Owing to these rather uniform sputtering yields, the glow discharge is relatively free from matrix effects.

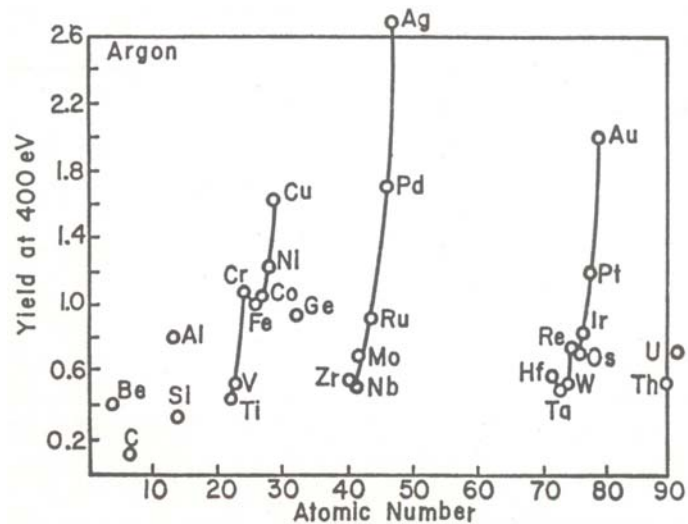


Figure 1.4: Sputtering yields of various transition elements for 400 eV Ar^+ ion bombardment [81].

* The cathode surface: Besides the kind of cathode material, also the cathode surface has influence on the sputtering yield, i.e. the sputtering yield decreases by surface contaminations, or by the formation of oxide layers or adsorbed gas layers on the cathode surface. Moreover, the sputtering can result in the formation of a regular pattern of submicroscopic cones on the surface. These are due to some components in the cathode material with a lower sputtering yield. These components can migrate over the cathode surface and form small clusters, thereby protecting the underlying material from sputtering. This effect also results in lowering of the sputtering yield.

* The cathode temperature: In typical glow discharge conditions the sputtering yields decrease slightly with increasing temperature, since the more loosely bound atoms on the surface tend to be annealed to positions of stronger binding [81].

2) The sputtering rate

The sputtering rate is defined as the amount of cathode material sputtered per unit time, and can be expressed in weight or in depth per unit time. Typical values of the sputtering rate are 3-600 Å/min (which corresponds to about 1-200 monolayers per min.), depending on discharge conditions [81].

3) The penetration depth and sampling depth

The **penetration depth** gives information about the depth at which incident particles can penetrate into the surface. As mentioned before, a higher penetration depth generally results in a lower sputtering yield. The penetration depth for 1 keV Ar⁺ ions is roughly 10 Å in copper [23]. The **sampling or escape depth** defines the depth from which one can obtain analytical information of the cathode. It depends on the characteristics of the collision cascade, which are determined by the energy of the bombarding particles, and the atomic numbers and masses of the bombarding and cathode atoms. In general, it is less than one fourth of the penetration depth [81].

1.3. REGIONS IN THE GLOW DISCHARGE [1]

The glow discharge can be subdivided into various regions between cathode and anode, differing in light intensity, potential and electric field distribution, space charge, and current density (see figure 1.5 [3]). The actual position and the occurrence of the various regions depend on the discharge parameters, like pressure, voltage, current, kind of gas and distance between cathode and anode. In this section, a short description of the different regions will be given, and the influence of the parameters will be explained. The description is made for large discharge cells, where all regions are present.

It has to be mentioned that the glow discharge used for analytical purposes is in general relatively small and does not contain all the regions.

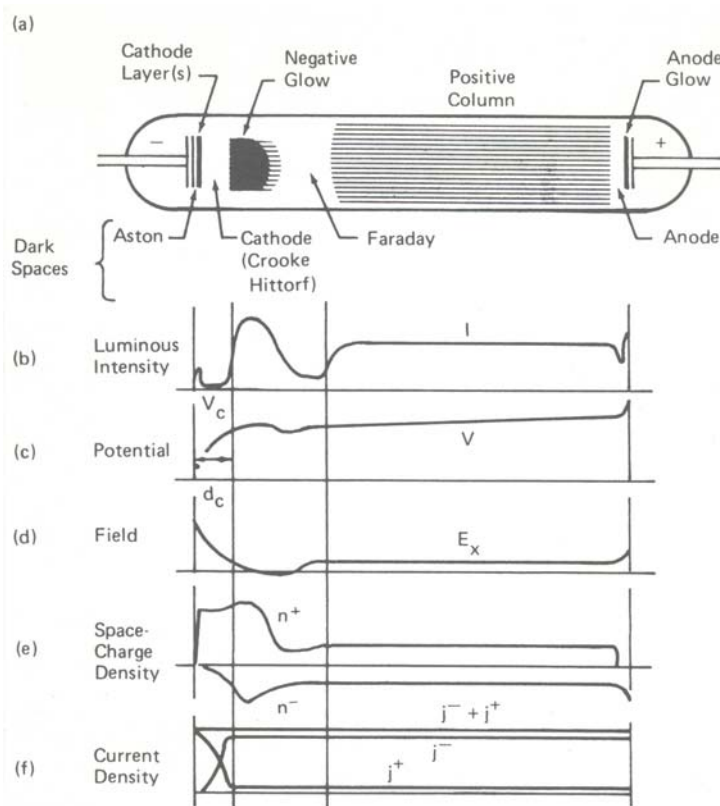


Figure 1.5: Schematic representation of the subdivision of the glow discharge into different regions (a), differing in luminous intensity (b), potential distribution (c), electric field (d), space charge density (e) and current density (f) [3].

1.3.1. The cathode dark space

The cathode dark space (CDS) is the thin, dark layer in front of the cathode, also called “Crookes or Hittorf dark space”. Strictly speaking, it is not completely dark but appears so to the eye in comparison with the other luminous parts of the discharge. It includes actually a number of dark and bright layers. The **electrical current** in this region is mainly carried by the gas (argon) ions.

The cathode dark space is the **most important part** of the discharge. It is the essential zone to sustain the discharge. Electrons leave the cathode and are accelerated by the electric field in front of the cathode. When they have acquired

sufficient energy, they can cause ionization collisions, thereby creating new electrons (electron multiplication) and also ions. The ions are accelerated towards the cathode. Upon bombardment on the cathode, they can release new electrons which can again produce ionization collisions. In this way, the continuity of the processes is ensured, and the glow discharge is self-sustaining.

The cathode dark space is characterized by a **large potential difference**. Almost the entire potential difference between anode and cathode falls off in the cathode dark space, therefore, it is also called cathode fall, V_c . The large potential difference over a small distance gives rise to a **high electric field** in the cathode dark space. The electric field is extremely negative at the cathode, and goes more or less linearly to virtually zero at the end of the cathode dark space.

Due to the high cathode fall, the electrons will be accelerated to high velocities and they will not play a significant role in determining the space charge. The ions will not reach such high velocities due to their much higher masses (lower mobilities) and therefore, they will determine the space charge. Hence, the cathode dark space is characterized by a **highly positive space charge**. The latter is in turn responsible for the characteristic potential and electric field distributions via Poisson equation.

The **optical characteristics** of the cathode dark space are determined by the occurrence of excitation processes of the plasma species (electrons, ions, fast atoms). If the species possess the amount of energy for efficient excitation (ca. 20 eV for electrons, higher than 100 eV for the ions and atoms), they will cause excitation collisions, and the subsequent deexcitations are responsible for the emission of light. The electrons leave the cathode with energies of a few eV. This is too low for excitation, resulting in a thin dark layer at the cathode (the Aston dark space). They attain however rapidly the energy suitable for excitation, giving rise to a small bright layer (the first cathode layer). These two layers can be distinguished very sharply, since the electrons still have beam characteristics close to the cathode, i.e. all electrons have nearly the same energy, and reach hence at the same place the maximum probability for excitation. After the excitation collisions in the first cathode layer, the electrons have lost their energy and they possess, again, not enough energy for excitation, hence a dark layer arises. When the electrons have once more received sufficient energy for excitation, the second cathode layer is formed. Since some electrons have undergone collisions whereas others have not, and since secondary electrons are created in ionization collisions, the electron beam is not monoenergetic anymore. Therefore, the second cathode layer is rather vague, and a third cathode layer is probably not visible anymore. On their further trajectory away from the cathode, the electrons gain much energy from the electric field and their energy becomes too high for efficient excitation (see Chapter 2, figure 2.2 for the excitation cross section as a function of the electron energy). Therefore, the remaining part of the cathode dark space is rather dark. Beside the electrons, the gas (argon) ions and fast atoms can also give rise to excitation. The latter processes

occur only at sufficiently high ion and atom energies (100 - 1000 eV and more), and are therefore only significant at high discharge voltages and sufficiently close to the cathode. These processes give rise to a bright layer at the cathode, **the cathode glow**. Moreover, if the cathode is covered with a thin metallic or oxide layer of an alkali or alkaline earth (MgO, Na₂O, Li₂O), another kind of bright layer is present at the cathode, **the cathode light**. This arises from the strongest spectral lines of these elements when they are sputtered away from the cathode.

The **energy distribution** of electrons and ions in the cathode dark space depends on the pressure and voltage in the cell. At low pressure and high voltage, the collision frequency of electrons and ions is rather low, and they will therefore be more or less monoenergetic, with energies approaching the total discharge voltage. At higher pressure, there will be more collisions, and the energy will be spread out, giving rise to a certain energy distribution. The energy distribution of the various charged plasma species is clearly not Maxwellian, since the particles gain more energy from the electric field than they lose by collisions. Therefore, it is stated that the cathode dark space is far from hydrodynamic equilibrium.

1.3.2. The negative glow

The negative glow (NG) is the bright, large region adjacent to the cathode dark space. It is more or less **equipotential** and **field-free**. The electrons are hence not accelerated anymore but are slowed down by collisions. Therefore, they will play a role, together with the argon ions, in determining the space charge. Positive and negative space charges are more or less equal to each other, resulting in **charge neutrality**. The **electrical current** is predominantly carried by the electrons.

The **optical characteristics** of the negative glow are explained by the fact that the electrons do not gain energy anymore but lose their energy in various collisions. Since the number of electrons in this region is much higher (due to electron multiplication), and since they possess more suitable energies for excitation, the number of excitation collisions is much higher. Therefore, the negative glow is characterized by a bright light, the color of which depends on the discharge gas [1]. In the case of an argon discharge, the negative glow possesses a dark blue color [1]. When the electrons travel through the negative glow, they lose their energy. At the end, they have too low energies for excitation, resulting in a much lower light intensity. The maximum light intensity is therefore observed in the beginning and center of the negative glow.

The **energy distribution** of electrons in the negative glow is more spread out towards lower energies. When the negative glow is sufficiently long, the electrons will be more or less thermalized (Maxwellian distribution) at the end of this region. However, in the negative glow of an analytical discharge, electrons with energies

ranging from thermalized to the total discharge voltage (primary electrons) can still be present (see Chapter 2, Section 2.3.4).

1.3.3. The Faraday dark space

The Faraday dark space is usually not present in analytical discharges. It is a dark and **nearly equipotential** region. Due to the large electron multiplication in the negative glow, a small excess of electrons is found at the end of the negative glow. This **net negative space charge** leads to a **small negative electric field** in the Faraday dark space, which draws the electrons out of the negative glow into the Faraday dark space. The **electrical current** in this region is therefore carried by the electrons.

Concerning the **optical characteristics**, the Faraday dark space can be considered as a repetition of the Aston dark space: the electrons leave the negative glow with too low energies for excitation. Therefore, the Faraday dark space is rather dark. However, in rare gas discharges, the Faraday dark space is sometimes characterized by a halo of light. This phenomenon is stated to be owing to the light emission of metastable atoms in collisions with ground state atoms.

1.3.4. The positive column

The positive column is again a rather luminous region, but not as bright as the negative glow. It is only present in the discharge at sufficiently large cathode-anode distances, which is mostly not the case in analytical discharges. This region is also **nearly equipotential**. It is characterized by **charge neutrality** and a **small negative constant electric field**. The **current** is carried by electrons which are accelerated by the electric field.

The **optical characteristics** of the positive column can be explained as follows. The electrons will again gain energy by the electric field. The interface between Faraday dark space and positive column is defined as the position where the electrons have enough energy for excitation and ionization. Therefore the positive column is a bright zone. The interface between Faraday dark space and positive column is however rather vague, since the electrons are not monoenergetic but can have widely different energies, reaching the optimum energy for excitation at different positions. The color of the positive column is also characteristic for the discharge gas, but differs from the color in the negative glow and is less intense. The positive column of an argon discharge is characterized by a dark red color [1].

The positive column can have a uniform outlook or can be filled with **striations**, i.e. bright and dark layers which can be stationary or moving. The

occurrence of striations is explained in the same way as the cathode layers in the cathode dark space, i.e. the electrons gain energy from the electric field, cause excitation (bright layer), lose thereby energy so that they cannot give rise to excitation anymore (dark layer), gain once more energy, etc.

The formation of the positive column with the increase of cathode-anode distance, is explained in the following way. The electrical current in the Faraday dark space is carried by electrons which leave the negative glow and travel towards the anode. When the distance between cathode and anode increases, some of these electrons are lost due to diffusion towards the walls. To compensate for this loss and to produce sufficient electrons that ensure the electrical current towards the anode, the positive column is formed and the small negative electric field of it directs the electrons towards the anode.

It is stated that the positive column approaches the characteristics of a plasma in hydrodynamic thermal equilibrium, since the **energy distribution** of the electrons in this region is more or less Maxwellian.

1.3.5. The anode zone

The characteristics of this region differ according to whether the anode is in contact with the positive column, the Faraday dark space or the negative glow.

When the anode is in touch with the positive column, a negative electric field and a potential increase are required in front of the anode, to attract electrons and to guarantee the electrical current to the anode (see above). When the distance between cathode and anode decreases, the positive column disappears and the anode will be in direct contact with the Faraday dark space. Since the latter region is characterized by an excess of electrons, a potential increase is not required to ensure the electrical current to the anode. Hence, the anode is equipotential with the bulk plasma and there is no electric field in front of the anode.

With further decrease of the distance between cathode and anode, also the Faraday dark space disappears, and only cathode dark space and negative glow remain. The anode is then in contact with the negative glow. This situation is usually encountered in analytical glow discharges. In this case, the plasma carries the most positive potential, and the anode zone is characterized by a negative potential fall, that repels the electrons and attracts the positive ions. The situation is hence comparable to the cathode fall in the cathode dark space, but both the anode potential fall and the length of the anode zone are much smaller than in the cathode dark space.

An illustration of the potential distribution in an analytical glow discharge (cathode dark space, negative glow and anode zone) is given in figure 1.6.

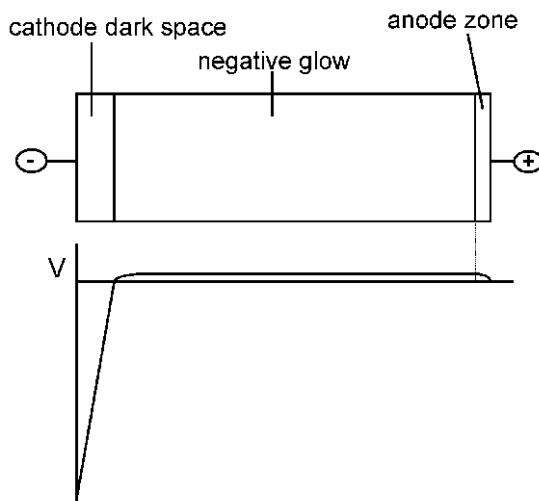


Figure 1.6: Schematic representation of the three regions occurring in an analytical glow discharge, and the corresponding potential distribution.

1.3.6. Influence of discharge parameters on the various regions

The occurrence of the various regions depends on the pressure, the distance between the electrodes, the potential, the electrical current, the kind of discharge gas and the kind of cathode material.

1) Pressure: As the pressure increases, the cathode dark space, negative glow and Faraday dark space are compressed towards the cathode, whereas the positive column takes up the major part of the discharge volume. Moreover, cathode dark space, negative glow and Faraday dark space cannot be so well distinguished from each other anymore. A decrease in pressure has the opposite effect, i.e. the positive column, and later also the Faraday dark space and negative glow will disappear in the anode. The latter is now in direct contact with the cathode dark space, and a so-called “obstructed discharge” is formed. By still lowering the pressure, the discharge will extinguish, since the cathode dark space is the essential zone to sustain the discharge.

2) Cathode-anode distance: The effect is similar to the pressure effect. When the distance increases, the positive column spreads out towards the remaining volume, and with decreasing distance, the positive column and later also the Faraday dark space and negative glow will disappear in the anode.

3) Voltage: When the voltage increases, the cathode dark space becomes shorter. Indeed, the cathode dark space is needed to sustain the discharge. At higher voltages, the discharge will be more easily self-sustained since more ionization occurs, so that a smaller cathode dark space will be sufficient. Moreover, the negative glow will become longer at higher voltages. Indeed, the length of the negative glow is determined by the range of the electrons before they are thermalized. At higher voltages, the electrons enter the negative glow with higher energies and they will need a longer distance before being thermalized.

4) Current: The current has actually no influence on the length of the various regions, but it affects the light intensity, i.e. at higher currents, the amount of excitation increases, yielding more intense light emission.

5) Discharge gas: The discharge gas determines the color of the negative glow and positive column (see before). Moreover, it has an effect on the length of the cathode dark space, i.e. the cathode dark space is shorter when the discharge gas can be more easily ionized.

6) Cathode material: It influences the length of the cathode dark space. If the cathode material easily emits secondary electrons, the discharge can be more easily sustained and a shorter cathode dark space will be sufficient.

In practice, the discharge conditions and the cathode-anode distance in analytical glow discharge cells are such that only the cathode dark space, negative glow and a small anode zone are present (see figure 1.6, above).

1.4. THE GLOW DISCHARGE IN ANALYTICAL CHEMISTRY

1.4.1. Glow discharge source configurations [81-85]

In its simplest form, the glow discharge is created by two electrodes inserted in an (inert) gas. The two electrodes can be mounted in five different geometries (see figure 1.7).

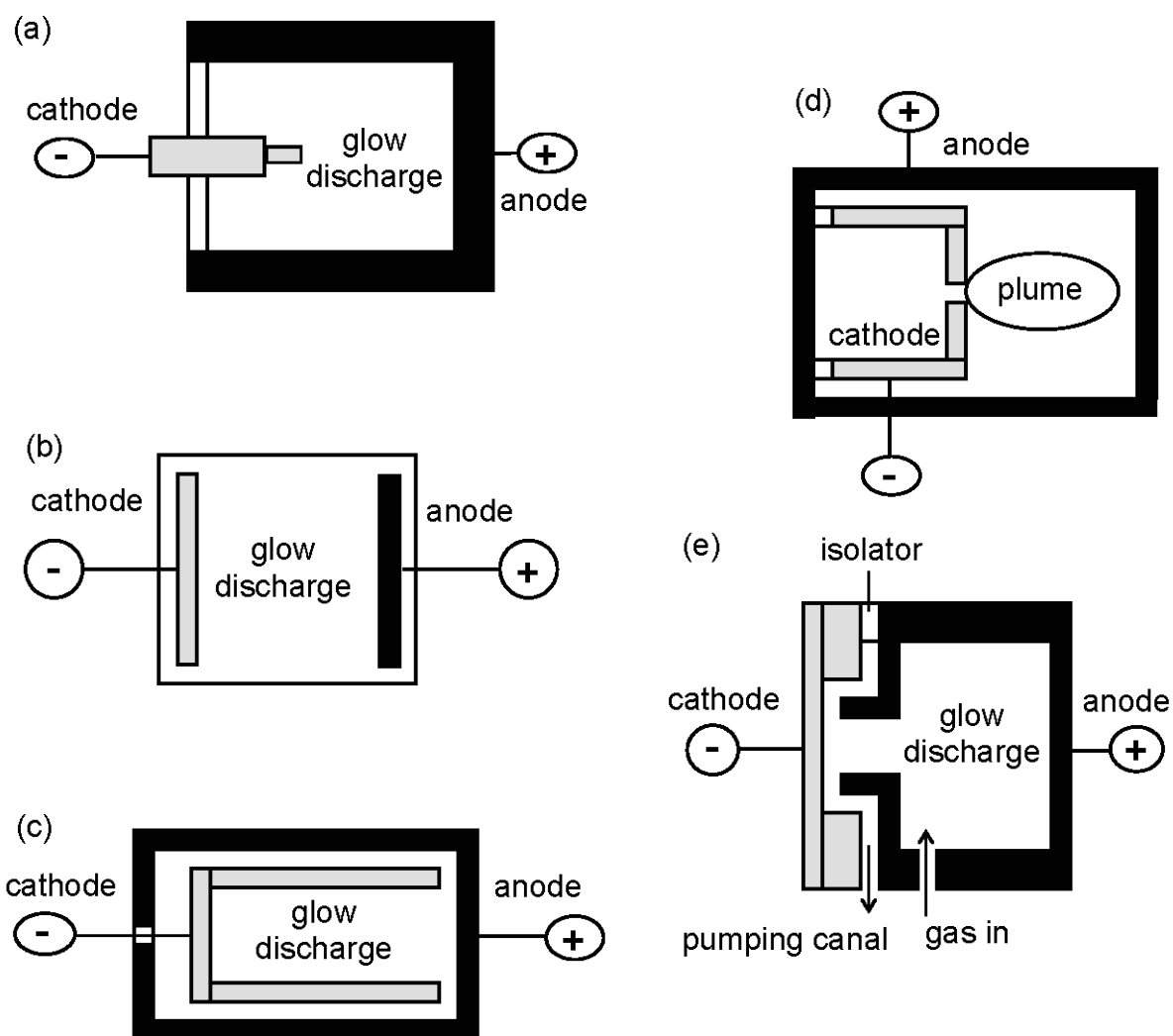


Figure 1.7: Different glow discharge source configurations; (a) the coaxial cathode, (b) the planar diode, (c) the hollow cathode lamp, (d) the hollow cathode plume, (e) the Grimm type glow discharge.

The **coaxial cathode** (figure 1.7a) is the most widely used source configuration in GDMS applications. Samples can be made in pin-form (with a few millimeters exposed to the discharge) or in disk-form (partly shielded so that only the top part is exposed to the discharge). The sample acts as cathode whereas the anode is formed by the cell body itself.

The **planar diode** (figure 1.7b) is the simplest analytical source. It is used for analyzing samples in disk form. The cathode (sample) and anode are in parallel configuration and are placed inside a tube. This type of source was used by Coburn et al. for etching and deposition purposes both in dc [86] and rf mode [59].

In the **hollow cathode lamp** (figure 1.7c) the cathode forms a cavity rather than a pin or disk. This geometry was first described by Paschen in 1916 [87] and was adapted by Schüller and Gollnow for analytical measurements in 1935 [88]. It can be considered as three planar cathodes placed so close to each other that their negative glow regions coalesce into a single negative glow. This results in increased sputtering and ionization/excitation, yielding a much better analytical sensitivity. A disadvantage of this source is the extensive machining required to make hollow cathodes from metal samples. Because most of the sputtering occurs at the cathode base, studies have been performed using a disk sample as the base of the cathode. Hollow cathode devices are particularly used as sources for atomic emission spectrometry. Moreover, the high radiation intensity emitted by this source, makes it attractive as primary source for atomic absorption or fluorescence spectrometry.

In the **hollow cathode plume** (figure 1.7d) the sample is mounted in the base of the hollow cathode, in which also an orifice is made. A highly energetic flamelike plume, where excitation and ionization processes occur, is ejected through this hole. Due to the high atom population, this geometry is also characterized by a high sensitivity. The source was developed by Marcus and Harrison [89-92]. The physical processes of this source are not fully understood but the plume is believed to arise from pressure and field effects due to the special construction of the cathode orifice.

The **Grimm configuration** (figure 1.7e) is extensively used in GD-AES. It was first introduced in 1968 by Grimm [93] and forms the basic design for all commercial emission instruments. The cell body (anode) approaches the cathode very closely (at a distance smaller than the length of the cathode dark space), so that the discharge is constricted to a well defined part of the sample surface. It is therefore called an "obstructed discharge". Moreover, an additional pumping canal close to the cathode reduces the pressure near the cathode, thereby minimizing redeposition. The Grimm configuration can however only be used for flat samples. This type of source is particularly useful for in-depth analysis, since the flat sample is ablated layer by layer.

1.4.2. Glow discharge electrical operation modes [81,82]

The simplest and cheapest operation mode is the **direct current (dc)** mode. Voltages are typically in the order of 500 - 1500 V, yielding electrical currents ranging from a few to several hundreds of mA, depending on the pressure in the cell and the discharge configuration. This type of discharge mode is the oldest one and the most widely used in glow discharge applications. However, it has the serious drawback of not being able to analyze non-conducting samples directly. Indeed, since in a glow discharge the sample to be analyzed acts as the cathode, which is sputter-bombarded by positive ions, it must be conducting. If not, the surface would be charged up, preventing the positive ions from further bombarding. Due to this drawback of the dc mode, attention is being drawn during the latest decade to the **radio frequency (rf)** operation mode.

The **radio frequency** mode is indeed able to analyze non-conductors directly, since the positive charge accumulated during one half-cycle will be neutralized by negative charge accumulation during the next half-cycle, so that no charging up occurs. Operation with rf-power of a glow discharge using a non-conducting sample yields a negative dc bias voltage on the sample surface. Indeed, during the half-cycles in which the non-conducting electrode is positive, surface charging will occur much faster than in the half-cycles in which the electrode is negative, due to the much higher mobility of the electrons compared to the positive ions. This self-bias phenomenon permits to establish a time averaged cathode and anode in the glow discharge, so that sputter-bombardment of positive ions on the cathode is still possible. Since the electrons try to follow the rf electric field, they oscillate between the two electrodes and spend more time in the plasma before they are lost, which results in a higher ionization efficiency. This leads to the second advantage of rf discharges, i.e. they can be operated at much lower pressures for the same current than dc discharges, which is interesting for reducing redeposition and spectral interferences. The rf-powered GD source was initially introduced by Wehner and coworkers as sputtering cells [94]. The capability of rf powered GDMS for direct analysis of nonconductors was demonstrated in the 1970s by Coburn and Kay [95] and by Donohue and Harrison [96]. However, it took until the late 1980s before rf GDMS was revisited [97]. Since then, extensive work has been done in this field [98-129]. Rf discharges have been combined with optical emission spectrometers [110,129], quadrupole mass spectrometers [97,99,108,127], a Fourier transform mass spectrometer [102], an ion trap mass spectrometer [103], a time-of-flight system [115] and two sector-based mass spectrometers [109,121,125], but up to now there is no commercial rf-GDMS instrument and only one commercial rf-GD-AES instrument (JY 5000 RF, Jobin Yvon) available.

The third mode of operation of a glow discharge is the **pulsed mode**, which can be employed in combination with a conventional dc or with an rf glow discharge. Voltage and current are applied only during short periods of time (generally msec range). Hence, compared to a normal dc discharge, higher peak voltages and peak currents can be obtained for the same average power. Therefore, more highly-energetic gas ions can be produced, yielding more sputtering, a higher concentration of analyte atoms in the plasma and hence better analytical sensitivity [130-142]. In addition to the better sensitivity, the pulsed mode has a second advantage for mass spectrometry, i.e. the analytically important ions and the interfering ions are formed during a different time in the pulse. By coupling this “time-resolved” production of ions to a time-resolved detection, spectral interferences in the mass spectrum can be reduced [133,136]. Moreover, the construction of a pulsed dual discharge system allows for simultaneous analyses with two electrodes, rendering the possibility of in situ calibration of an unknown sample against a reference standard [137]. Gated detection of atomic emission from a pulsed rf glow discharge was also reported to improve the analytical sensitivity and to reduce spectral interferences [131,132,139]. Also in glow discharge atomic absorption and fluorescence spectrometry, background-free analytical measurements during the discharge-off portion of the cycle have been reported [134,138]. Recently, Harrison and coworkers introduced the microsecond pulsed glow discharge as source for atomic emission, absorption, fluorescence and mass spectrometry [142]. Due to the still higher peak currents and voltages which can be obtained during the short pulses, this source has still a better analytical sensitivity.

1.4.3. Analytical applications of the glow discharge

In glow discharges used for analytical purposes, the cathode of the discharge consists of the material to be analyzed. Due to the bombardment of the cathode by plasma species, atoms of the cathode material are sputtered away from the cathode and enter the glow discharge plasma, where they are subject to a wide range of collisions (especially ionization and excitation). Due to these sputtering and collision processes, the plasma is filled with atoms, ions and photons, representative for the material to be analyzed. This makes the glow discharge useful as source for a variety of analytical techniques (see figure 1.8). Analytical applications of the different glow discharge techniques will be discussed here in somewhat more detail.

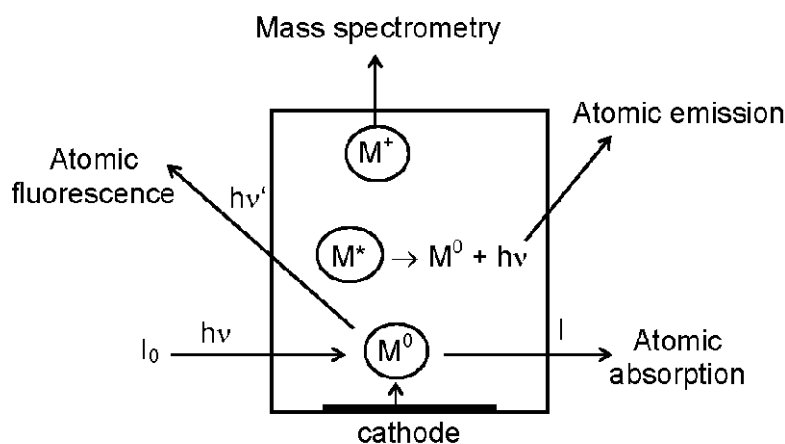


Figure 1.8: The glow discharge as a versatile analytical tool.

1.4.3.1. Glow discharge mass spectrometry (GDMS) [81-85,143-147]

GDMS is based on the measurement of the ions formed by ionization of the sputtered atoms. The glow discharge has been known as an ion source in mass spectrometry for more than 60 years. Gas discharges were indeed already used in the 1920s and 1930s as ion source in the first mass spectrographs of Aston, Thompson and Bainbridge [148,149]. However, the early popularity was followed by a decline into relative obscurity during the next 30 years, due to the development of the simple electron impact ion source. There was indeed more interest at that time for the analysis of organic samples with relatively high vapor pressure; hence simple ionization in the gas phase by an electron beam was largely sufficient. When the interest also shifted to the analysis of inorganic materials with lower vapor pressure, there was again need for other sources, with sufficient energy for atomization and ionization. Since spark and arc discharges were already widely used as excitation sources for atomic emission spectrometry, it was obvious that these sources would also be applied for mass spectrometry. These sources exhibit a high sensitivity, large applicability and only few spectral interferences, but they do not yield a stable ion population. This led to the reexamination of the glow discharge as stable, low energy ion source.

The glow discharge was first brought back to the attention of mass spectroscopists as ion source for the analysis of solids (both in dc and rf mode) by Coburn et. al [59,86,150]. Harrison and coworkers [151-153] developed the hollow cathode source for both bulk solids and solution residue analysis. The analytical capabilities of the latter source have also been investigated by Evans et al. [154,155]. In 1978, Bruhn reported the development of a quadrupole based dc

GDMS system dedicated to elemental analysis [156]. Hecq and coworkers used a conventional glow discharge to investigate reactive sputtering processes and ionization phenomena [157,158]. Marcus, King and Harrison studied the capabilities of a hollow cathode plume [89]. A Grimm-type glow discharge was developed as an ion source for a quadrupole mass analyzer by Jakubowski and coworkers [159]. In the last decade, various ion source modifications and applications have demonstrated the versatility and analytical potential of GDMS.

To date, all common mass analyzers have been explored for use in GDMS. The first commercially available GDMS instruments used a double-focusing mass analysis system, permitting the acquisition of high-resolution spectra with high sensitivity [160]. Modern GDMS began however with quadrupole-based mass analyzer systems, which were employed for fundamental and development research of GDMS [156,159,161-164], and this research resulted finally in the commercial availability of a quadrupole GDMS system [165]. Promising results have also been obtained from the coupling of a glow discharge to ion trap mass spectrometric systems [99,166,167], double [99] and triple [168-169] quadrupole instruments, time-of-flight mass spectrometers [115,170], and Fourier transform mass spectrometers [102,170-174]. The commercial GDMS systems available at present employ however only double-focusing and quadrupole based mass spectrometers. Typical working conditions for GDMS are 1-5 mA, 800-1500 V, 0.2-2 torr [146]. Detection limits of GDMS are in the ppb region.

GDMS permits the analysis of a broad range of sample types. The most important applications are found in the bulk analysis of metals, but semiconductors, nonconductors, thin films, solutions and gaseous samples can in principle be analyzed as well.

a. Bulk metal analysis: Bulk metals are the most interesting sample types for GDMS. Due to the low detection limits for almost all elements of the periodic table, it is of particular interest for analyzing high-purity metals, like aluminium, gallium, titanium, copper, platinum, etc [160,165,175-187]. Also metallic alloys can be easily analyzed by GDMS [162,163,175,186-202]. Isotope ratio measurements on metals can also be carried out with GDMS, as is described in ref. [203,204]. A common problem in GDMS are the spectral interferences by various types of cluster ions. Recently, a paper has been published, reporting the suppression of cluster interferences by sampling from a reversed hollow cathode ion source. It was found that the analyte ions are characterized by a peak at high energy, whereas argon ions and cluster ions possess a peak at low energy. By sampling only high energy ions, the argon ion and cluster ion interferences can be suppressed [205]. Another recent paper makes use of these clusters for quantification [206]. Indeed, argides, dimers and doubly charged analyte ions are sometimes less disturbed by interferences and can

therefore better be employed for quantification than singly charged analyte ions [206].

To obtain quantitative results in GDMS, a variety of approaches has been proposed [147]. The easiest approach is the ion beam ratio method. The assumption is made that the ratio of the ion current for any one isotope with respect to the total ion current (except the signal arising from the discharge gas ions) is representative for the concentration of that isotope in the sample. Since the ion signal for the matrix is generally large compared to the individual trace species, especially for a high purity metal or semiconductor, the matrix ion current is in good approximation equal to the total ion current and the matrix atoms can be assumed to have a concentration of 100 %. Since this method cannot correct for the variation in analytical sensitivity among different elements, it provides only semi-quantitative results, i.e. accuracies of a factor of 2-3. Real quantitative results require that differences in elemental sensitivities be characterized using standards similar to the material under study. This characterization generates relative sensitivity factors (RSF) that can be employed to correct the measured ion beam ratios. Since RSFs vary only slightly between matrices of the same general composition, exact matrix matching is not required to yield quantitative results with accuracies of 15-20 % [191]. The RSF method of quantification is the most widely employed in GDMS. Generally, the RSFs of different elements in GDMS lie within one order of magnitude, which makes GDMS a technique with rather uniform sensitivity for most elements. Experimental RSFs have been reported for different kinds of matrices [163,175,180,186-191,197,200,201,207-212]. Furthermore, some empirical models based on fitting parameters have been developed to predict RSFs [191,196,197,213,214]. In ref. [197] it was found that the theoretically calculated RSF values correlated better with the experimental ones when 1 % H₂ was added to the argon discharge gas.

b. Semiconductors: Since impurities even at extremely low concentration levels can seriously alter the semiconductor properties, their concentrations have to be known very accurately. Although they are nonmetallic in much of their chemical activity, the semiconductors exhibit certain allotropic forms that conduct electricity to a certain degree. Therefore, in certain forms, they can serve directly as cathodic samples in GDMS. A few applications have been reported in the literature [180,215].

c. Nonconductors: Since the sample in the glow discharge acts as the cathode bombarded by positive ions, the concept seems to restrict the applications of GDMS to the analysis of electrically conducting materials, because non-conductive materials would be charged up. This problem can be overcome by using rf discharges, like mentioned before [95,96,99,101-103,109,112,113,121,123]. In a dc discharge, nonconductors can however also be analyzed when applying certain modifications. Two methods are reported in the literature. The first exists in mixing the

nonconducting sample as a powder with a conductive binder (Cu, Ag, Ga) and pressing it into an electrode. This method was first described for GD-AES [216] using copper and graphite as host matrices, in a range of sample-to-host ratios. The method is generally well-established, as can be seen from the large number of papers in the literature [107,120,175,217-225]. However, in addition to the increase in sample preparation time compared to direct analysis of conducting solids, the mixing with the conductive matrix can introduce contaminations. Other problems arise from the trapping of water vapor and atmospheric gases in the sample during the compaction process. Also the time to reach steady state conditions with a composite cathode can be prohibitively long. The second approach is the use of a metallic secondary cathode diaphragm in front of the flat nonconducting sample surface [226,227]. Due to the redeposition of a part of the sputtered metal atoms from the secondary cathode, a very thin conductive layer is formed on the nonconductive material. The sampling depth is large enough (ca. 5 Å) to allow atomization of the nonconducting sample as well. This method has recently been applied to the analysis of atmospheric particulate matter (aerosols) [228].

d. Thin film analysis and depth profiling: The concept of sputtering in a glow discharge implies that the sample is being eroded "layer after layer". It is therefore possible to perform trace analysis of successive layers as a function of depth (i.e. depth-profiling). Although depth-profiling is more typically done in glow discharge atomic emission spectrometry (see below), some applications of GDMS can be found in the literature too [212,229-233]. Since transient signals have to be monitored (intensity as a function of time), quadrupole based mass spectrometers are preferable due to their fast scanning capability. Nevertheless, also double focusing instruments can be employed, as was demonstrated for the in-depth analysis of cylindrical samples [211].

e. Solutions: Although GDMS is a typical solid analysis technique, some attempts have been made to analyze solutions as well [151-153,234-240]. Analyzing solutions can be performed in a number of ways: (i) by evaporation of a solution sample onto the surface of a conducting electrode, (ii) by electrodepositing certain metals of the solution onto the cathode, (iii) by electrothermal vaporization (i.e. placing microliter aliquots of solution sample on a filament that serves as cathode, dry the sample to a residue film by passing currents through the filament, ash away organic constituents, and finally atomize the residue in the glow discharge), and (iv) by mixing a solution aliquot with powdered matrix material, following by drying the mixture. Recently, Sikharulidze has proposed a method for direct analysis of aqueous solutions by GDMS [241]: the solution enters the vacuum of a glow discharge cell through a capillary and the water vapor itself is used as the discharge gas. This would be a low energy and cheap alternative (no noble gas) to ICP-MS.

f. Gaseous samples: Since stable glow discharge plasmas can also be obtained with molecular gases (nitrogen, oxygen, air, water vapor,...), the glow discharge can also be used for gas analysis. McLuckey et al. designed a glow discharge ion source that used ambient air as discharge gas, to analyze trace impurities present in the sampled air [166,242]. A recent application is the detection of trace quantities of vapor explosives in the field by glow discharge ion trap mass spectrometry [167].

g. Other applications: Although GDMS is a typical technique for the analysis of inorganic samples, some attempts have been made to analyze organic samples as well. For the analysis of organic samples by GDMS, three categories can be distinguished, according to the sample introduction scheme of the organic sample, i.e. (i) as liquid or gas chromatographic effluents [243-247], (ii) as deposits on the cathode surface [248,249] and (iii) directly as discharge gas components [166,167, 242]. Some examples of organic samples that have recently been analyzed by GDMS, include the examination of polymers [117], the identification of impurities in petroleum [239], and the analysis of lead in waste oil samples [240]. In addition to the analysis of organic samples, another “exotic” application of GDMS has been reported in the literature, describing the analysis of materials of nuclear origin with the VG 9000 mass spectrometer placed in a glove-box [250].

1.4.3.2. Glow discharge atomic emission spectrometry (GD-AES) [251-254]

GD-AES is based on the measurement of the spontaneous light emission of excited sputtered atoms in the plasma. Although the first glow discharges were employed as ion source for mass spectrometry in the 1920s-1930s, this application lost interest during the next 30 years. The optical emission literature however shows sustained use of the glow discharge, which had been developed both as line source and as direct analysis emission source [255-258]. The hollow cathode mode, first described by Paschen [87] was of particular interest. However, for routine analysis of compacted metal samples, the breakthrough of GD-AES first occurred at the end of the 1960s with the work of Grimm [93] who introduced the restricted glow discharge, called after his inventor. Since then, the number of applications of GD-AES have been growing very rapidly.

The two sources that are now still extensively used in GD-AES are the hollow cathode lamp and the Grimm type source (for their description, see above). Dispersive spectrometers with a diffraction grating are most frequently used for GD-AES. For sequential multielement determinations, monochromators in the Ebert or Czerny-Turner mountings are utilized, whereas simultaneous multielement analyses are performed with polychromators in the Paschen-Runge setup [251]. However, also multiplex spectrometers, such as Hadamard transformation spectrometers [259]

and especially Fourier transform interferometers [260,261] are useful in combination with glow discharges [251]. The radiation detection is mostly accomplished by photomultipliers. Glow discharges for AES operate at higher currents than for GDMS, i.e. 600 - 1000 V, 25 - 100 mA, 1-5 torr for the Grimm source, and 200 – 500 V, 10 - 100 mA, 0.1 - 1 torr for the hollow cathode lamp [146]. Detection limits are in the order of 0.1 - 10 ppm [146].

The analytical applications of GD-AES are similar to the GDMS applications. Multielement analyses of bulk samples for major, minor and trace elements have been described for most industrially important matrices, like steel and other metal alloys [124,262-266]. Moreover, the analysis of semiconductors by GD-AES has been recently reported [267]. Also nonconductors can be analyzed with GD-AES, either by mixing with a conducting powder [90,92,131,268-276] or by using an rf glow discharge [98,100,106,112]. Some reports have been made on the analysis of solution samples [258,275,277-283] and gas samples [284].

Finally, GD-AES is particularly widely applied in depth-profiling analyses. A large number of applications have been reported [285-302], among them also some analyses performed with an rf powered glow discharge [118,119,297]. Most results are presented as relative intensity versus sputtering time, and it is not straightforward to convert this into concentration of elements as a function of depth, since the sputtering rate and the glow discharge conditions change during in-depth profiling of layers of varying chemical composition. Several empirically based quantification schemes have been developed in the literature to deal with this problem [288,294,295,298-302].

1.4.3.3. Glow discharge atomic absorption and fluorescence spectrometry (GD-AAS and GD-AFS) [83,303]

In GD-AAS a light beam with well-defined wavelength is sent through the plasma, and the intensity loss after passage through the sputtered atom population is measured. GD-AFS is based on the excitation of the sputtered atoms by an external radiation source and the measurement of the subsequently emitted radiation. Both techniques are less used in glow discharge applications than GDMS and GD-AES, but they are receiving wider notice in the literature as their advantages come to be appreciated. Compared to GD-AES, for example, these methods have higher spectral resolution and fewer spectral interferences.

The use of a glow discharge as atomic absorption cell was first introduced by Russell and Walsh in 1959 [304] for the direct analysis of metals. Their observation that also atomic fluorescence was occurring in the cell eventually led to the use of GD-AFS as well [305]. During the 1960s and 1970s, several types of sputtering cells (i.e. hollow cathode cells and cells with flat electrodes) have been investigated for

use in GD-AAS and GD-AFS [305-310]. In 1987, Bernhard [311] reported that gas jets striking the sputtering surface significantly increase the sampling rate and hence the absorption signal. A commercial atomic absorption cell, based on this principle and called "Atomsource" [311] (Analyte Corp., Medford, OR), was made available and has further stimulated the applications of gas-jet-enhanced sputtering. In addition to dc sources, also an rf powered glow discharge device was recently introduced as atomization source for AAS [111,114,128].

As primary radiant sources for GD-AAS, modulated or pulsed hollow cathode lamps are commonly used. Tunable lasers are employed in special cases. Modulated Grimm-type cells are applied for multielement simultaneous GD-AAS because of the ease of changing the cathode to select the elements of interest [312]. Hollow cathode lamps or tunable lasers are utilized as primary radiation sources for GD-AFS. Due to their high irradiances and narrow spectral bandwidths, the lasers yield detection limits that are many decades lower than those commonly obtained with GD-AAS and GD-AFS [134,313,314]. Even single atom detection has been reported [313]. Typical discharge conditions for GD-AAS and GD-AFS are 4 - 10 torr, 60 - 200 mA, 300 - 800 V [146].

The applications of both GD-AAS and GD-AFS include the bulk analysis of metals [315] and of a wide variety of alloys [305,306,310,314,316-322], the analysis of powders [316,323], nonconductors [324-328] and dried solutions [308,309,314, 317,329-334].

1.4.3.4. Glow discharges in a broader perspective

Beside the four analytical applications described above, which make use of the glow discharge in its simple form as spectroscopic source, the glow discharge can also be employed in a hybrid construction, in combination with lasers, graphite furnaces, other discharges or magnetic fields. A short overview of these application fields will be given here. Moreover, some more exotic forms of glow discharges will be reported. Finally, it should be noticed that the glow discharge is extensively used for etching and deposition purposes, and also as a new class of lasers. The latter application fields will also briefly be discussed.

a. Laser-based methods: [335]

The development of cost-effective laser systems has generated a variety of laser techniques that can be coupled to a glow discharge. The atomization and the ionization/excitation steps occur independently from each other in the glow discharge. A laser can be employed to enhance either of these two steps.

First, the laser can be utilized to ablate material from the sample cathode, enhancing the atomization step [336]. The laser can also ablate material from a

secondary sample (not the cathode) into the glow discharge [336,337]. In the latter case, the sample must not be conductive, expanding the analytical applications of glow discharges to the analysis of nonconductors without the need to apply rf power. Beside the enhanced atomization, the possibility of performing spatially resolved measurements is an additional advantage of this method.

Second, the laser can also be used to enhance the excitation/ionization processes in the discharge. The usefulness of this laser enhancement has been demonstrated in a variety of application areas, such as atomic fluorescence (see above), optogalvanic effect spectroscopy [338-341] (i.e. the laser results in alterations in the ionization rate of the discharge, which are electrically detected by the resulting changes in voltage or current), laser enhanced ionization [340] (i.e. directly measuring the electrons released when the ionization in the discharge is enhanced due to laser photons) and resonance ionization mass spectrometry [336] (i.e. the laser is used for selectively ionization enhancement of sputtered species in the discharge, increasing both the sensitivity and selectivity in GDMS).

b. Furnace atomization nonthermal excitation spectrometry (FANES) [342]

In analogy to the laser ablation glow discharge technique, FANES makes also use of an external atomization source (i.e. thermal vaporization from a graphite furnace) whereas the created atoms are excited and/or ionized in the glow discharge plasma. The concept of FANES was first proposed by Falk [343] who used a low-pressure dc glow discharge with the furnace playing the role of cathode (i.e. hollow cathode; HC-FANES). Another type of FANES system is based on a dc glow discharge in which the furnace comprises the anode (i.e. hollow anode; HA-FANES) [344]. The third type makes use of an rf glow discharge, and is described by Blades et al. [345,346] and by Sturgeon and coworkers [347-351]. The latter sources also have a hollow anode geometry but operate in helium at atmospheric pressure. These three types of sources are markedly different from classical glow discharge sources, i.e. (i) sample volatilization is accomplished thermally and the rate of volatilization can be three orders of magnitude higher than typical sputtering rates, (ii) all three FANES discharges involve "hot" electrodes, with temperatures ranging from 800 K to 2800 K, and (iii) the HA-FANES and rf-FANES operate at much higher pressures than conventional glow discharges, which results in a longer residence time for the analyte atoms in the plasma.

c. Glow discharges enhanced by cross-excitation

In conventional glow discharges, the majority of the sputtered material is present as ground state atoms. To increase the number densities of excited atoms and hence the emission line intensities and the sensitivity in GD-AES applications, a laser can be applied, as explained above, but also an auxiliary discharge can be employed. This is called cross-excitation or boosted discharges. Several methods

of cross-excitation have been investigated, i.e. the application of (i) a secondary dc discharge [352-358], (ii) an rf discharge [359,360] and (iii) a microwave discharge [275,360-365].

d. Magnetron discharges:

Another method to improve the performance of a conventional glow discharge, is based on magnetic enhancement. One simple device among magnetically enhanced glow discharges is the magnetron glow discharge. In this device, permanent magnets are used to form a magnetic field of a few hundred Gauss in the plasma. Electrons in the plasma are forced to move in closed-loop trajectories parallel to the cathode surface. Hence, the electron path length is increased and the ionization of the discharge gas is significantly enhanced. Therefore, the magnetron discharge can operate at much lower pressures than conventional discharges. Lower pressure operation provides higher ion and electron kinetic energies, leading to higher atomization and excitation/ionization efficiencies, and hence a better analytical sensitivity. However, while the sputtering in a conventional discharge is rather uniform, it is more or less confined to a ring in the magnetron. The characterization of magnetron discharges, both in dc and rf mode, and the applications in combination with mass spectrometry and atomic emission spectrometry, are discussed in refs. [116,366-384].

e. Gas assisted sputtering glow discharges:

Another way to increase the analytical sensitivity of a glow discharge is to use a gas-jet discharge. Due to the gas jet impinging on the sample surface, the sputter-ablation is improved by both reduced redeposition and increased sample transport. This results in a higher sputtered atom population in the plasma and hence better analytical sensitivity. The gas-jet glow discharge was first developed by Bernhard in GD-AAS and has led to a commercially available GD-AAS source (see above). This type of glow discharge has also been reported for other applications in AAS, AES and MS [385-397].

f. Elemental composition mapping of solid surfaces by glow discharges:

A conventional glow discharge cannot be used for elemental mapping, since the whole cathode is ablated at the same time, and an average signal output is obtained. However, in a paper by Winchester and coworkers, description is made of an instrument which sustains a number of glow discharges simultaneously [398]. Each discharge exhibits atomic emission lines, characteristic of the sample surface beneath it. In this way, rapid macro-scale (i.e. up to many tens of square cm's) elemental composition mapping of solid surfaces can be performed, with a spatial resolution of about 1 mm.

g. A glow discharge using a solution as cathode:

An exotic type of glow discharge, in which an electrolyte solution is used as cathode, and the anode is placed at a distance of a few mm from this solution, has been reported in the literature, as forming the basis of glow discharge electrolyse [399]. Recently, such an arrangement has also been adapted as sputtering source in analytical chemistry [400]. A stable glow discharge was produced in atmospheric pressure air, using water as a cathode. By sputtering of the water cathode, the composition of water solutions could be analyzed by GD-AES.

h. Glow discharges in etching and deposition applications:

Although only glow discharge applications in analytical chemistry have been described up to now, it should be noticed that the glow discharge is also extensively used in the microelectronics industry, for etching and deposition purposes, and for surface modification.

Due to the sputter-bombardment of plasma species onto the cathode (called the target), material of the cathode is removed. This process is called **sputter etching** or **physical etching**, and can be carried out in order to clean the target or to make it thinner, or to generate selectively topographic patterns on the surface. The ejected material from the cathode (predominantly atoms) can also be used further, in a second application of sputtering. After ejection, the atoms can move through the plasma until they strike and condense on the surface in the plasma, called the substrate. By repeating this process over and over, a coating of several atomic or molecular layers of target material can be built up on the substrate. The resulting coating is generally less than 1 μm thick. This process is called **sputter deposition** or **physical deposition** and is currently the main application of sputtering in the microelectronics industry [3].

In contrast to physical (sputter) etching and deposition, glow discharges are also frequently used in **chemical (plasma) etching and deposition** applications. In this case, reactive gases are employed instead of noble gases. **Chemical etching** relies on the chemical combination of the solid surface to be etched, with an active gaseous species produced in the discharge. Development has evolved primarily in and around the semiconductor industry and hence on related materials. Probably the most common applications of plasma etching are the etching of silicon and silicon oxides in a discharge of CF_4 to form volatile SiF_4 . In **chemical deposition**, more commonly named **plasma enhanced-chemical vapour deposition (PE-CVD)**, a molecular gas is ionized, excited and/or dissociated in the plasma as a result of electron bombardment. The radicals, atoms, ions and excited species created hereby, diffuse towards the substrate where they are deposited. Typical examples are the deposition of amorphous hydrogenated carbon layers (a-C:H) from a CH_4 plasma and the deposition of amorphous hydrogenated silicon layers (a-Si:H) from a SiH_4 plasma.

i. Glow discharges used as a new class of lasers [401]

Glow discharges in the hollow cathode configuration represent a new class of metal ion lasers. The upper laser levels are excited via asymmetric charge transfer collisions between buffer gas ions and metal atoms. The lasers provide discrete wavelengths in the 220 - 2000 nm spectral region. The most attractive feature of hollow cathode metal ion lasers is that they provide hundreds of milliwatts of continuous wave (CW) radiation in the ultra violet (UV) ($\lambda \leq 320$ nm) region. Some potential applications of these devices include pumping CW UV dye lasers, dimers or crystals in the 300 - 400 nm region, generation of CW tunable radiation in the 200 nm region, and photolithography.

1.5. REFERENCES

1. G. Francis, in S. Flügge, *Handbuch der Physik*, vol. 22, Springer-Verlag, Berlin (1956).
2. M. J. Druyvensteyn and F. M. Penning, *Rev. Mod. Phys.* **12**, 87 (1940).
3. B. Chapman, *Glow Discharge Processes*, Wiley, New York (1980).
4. J. B. Hasted, *Physics of Atomic Collisions*, Butterworths, London (1972).
5. E. W. McDaniel, *Collision Phenomena in Ionized Gases*, Wiley, New York (1964).
6. E. W. McDaniel, J. B. A. Mitchell and M. E. Rudd, *Atomic Collisions: Heavy Particle Projectiles*, Wiley, New York (1993).
7. F. Llewellyn-Jones, *Ionization and Breakdown in Gases*, Science Paperbacks, London (1966).
8. R. J. Carman, *J. Phys. D* **22**, 55 (1989).
9. H. A. Hyman, *Phys. Rev. A* **20**, 855 (1979).
10. E. Eggarter, *J. Chem. Phys.* **62**, 833 (1975).
11. L. R. Peterson, J. E. Allen, Jr., *J. Chem. Phys.* **56**, 6068 (1972).
12. A. V. Phelps, *J. Chem. Phys. Ref. Data* **20**, 557 (1991).
13. C. M. Ferreira and A. Ricard, *J. Appl. Phys.* **54**, 2261 (1983).
14. A. V. Phelps, *J. Appl. Phys.* **76**, 747 (1994).
15. L. Vriens, *Phys. Lett.* **8**, 260 (1964).
16. L. A. Riseberg, W. F. Parks, L. D. Scheerer, *Phys. Rev. A* **8**, 1962 (1973).
17. M. Bourène and J. Le Calve, *J. Chem. Phys.* **58**, 1452 (1973).
18. S. Inaba, T. Goto, S. Hattori, *J. Phys. Soc. Jpn* **52**, 1164 (1983).
19. R. L. Smith, D. Serxner, K. R. Hess, *Anal. Chem.* **61**, 1103 (1989).
20. M. K. Levy, D. Serxner, A. D. Angstadt, R. L. Smith and K. R. Hess, *Spectrochim. Acta* **46B**, 253 (1991).
21. E. W. Eckstein, J. W. Coburn and E. Kay, *Int. J. Mass. Spectrom. Ion Phys.* **17**, 129 (1975).
22. W. Vieth and J. C. Huneke, *Spectrochim. Acta* **45B**, 941 (1990).
23. D. Fang and R. K. Marcus, in *Glow Discharge Spectroscopies*, R. K. Marcus (ed.), Plenum Press, New York (1993), Chapter 2.
24. A. Bogaerts and R. Gijbels, *J. Anal. Atom. Spectrom.*, in press: Sept. 1996.
25. C. F. Melius, *J. Phys. B*, **7**, 1692 (1974).
26. J. M. Green and C. E. Webb, *J. Phys. B*, **7**, 1698 (1974).
27. L. Csillag, M. Janossy, K. Rozsa and T. Salamon, *Phys. Lett.*, **50A**, 13 (1974).
28. S. Johansson and U. Litzen, *J. Phys. B*, **11**, L703 (1978).
29. I. M. Littlewood, J. A. Piper and C. E. Webb, *J. Phys. B*, **12**, 1399 (1979).

30. K. Danzmann and M. Kock, *J. Phys. B*, **14**, 2989 (1981).
31. J. L. Barrett, M. G. Mlynczak and J. J. Leventhal, *J. Chem. Phys.*, **75**, 2705 (1981).
32. P. B. Farnsworth and J. P. Walters, *Spectrochim. Acta*, **37B**, 773 (1982).
33. E. B. M. Steers and R. J. Fielding, *J. Anal. Atom. Spectrom.*, **2**, 239 (1987).
34. E. B. M. Steers and F. Leis, *J. Anal. Atom. Spectrom.*, **4**, 199 (1989).
35. E. B. M. Steers and F. Leis, *Spectrochim. Acta*, **46B**, 527 (1991).
36. E. B. M. Steers and A. P. Thorne, *J. Anal. Atom. Spectrom.*, **8**, 309 (1993).
37. E. B. M. Steers, A. P. Thorne and Z. Weiss, *12th European Sectional Conference on the Atomic and Molecular Physics of Ionized Gases, Europhysics Conference Abstracts*, **18E**, 65 (1994).
38. R. S. Hudson, L. L. Skrumeda and W. J. Whaling, *J. Quant. Spectrosc. Radiat. Transfer*, **38**, 1 (1987).
39. K. Wagatsuma and K. Hirokawa, *Spectrochim. Acta*, **51B**, 349 (1996).
40. V. A. Kartazaev and Y. A. Tolmachev, *Opt. Spectrosc.*, **45**, 620 (1979).
41. P. Baltayan, J. C. Pebay-Peyroula and N. Sadeghi, *J. Phys. B* **18**, 3618 (1985).
42. O. P. Bochkova, I. A. Ivakin, A. V. Kuligin, V. N. Ostrovskii and Y. A. Tomachev, *Opt. Spectrosc.*, **70**, 9 (1991).
43. P. Baltayan, J. C. Pebay-Peyroula and N. Sadeghi, *J. Phys. B* **19**, 2695 (1986).
44. A. R. Turner-Smith, J. M. Green and C. E. Webb, *J. Phys. B*, **6**, 114 (1973).
45. R. Johnsen and M. A. Biondi, *J. Chem. Phys.*, **73**, 5045 (1980).
46. V. N. Ostrovskii, *Sov. Phys. JETP*, **57**, 766 (1983).
47. A. K. Belyaev, *J. Phys. B*, **26**, 3877 (1993).
48. R. Johnsen, M. T. Leu and M. A. Biondi, *Phys. Rev. A*, **8**, 1808 (1973).
49. M. S. Aleksandrov, O. P. Bochkova, V. S. Ivanov, A. V. Kuligin, Y. A. Piotrovskii and Y. A. Tolmachev, *Opt. Spectrosc.*, **69**, 311 (1991).
50. Y. A. Piotrovskii, Y. A. Tolmachev and S. V. Kasyanenko, *Opt. Spectrosc.*, **52**, 452 (1982).
51. H. A. Schuessler, C. H. Holder, Jr. and O. Chun-Sing, *Phys. Rev. A*, **28**, 1817 (1983).
52. D. Fogel and Y. A. Tolmachev, *Opt. Spectrosc.* **49**, 450 (1980).
53. V. A. Kartazaev, Y. A. Piotrovskii and Y. A.; Tolmachev, *Opt. Spectrosc.*, **44**, 362 (1978).
54. S. C. Rae and R. C. Tobin, *J. Appl. Phys.* **64**, 1418 (1988).
55. K. B. Butterfield, D. C. Gerstenberger, T. Shay, W. L. Little and G. J. Collins, *J. Appl. Phys.*, **49**, 3088 (1978).
56. J. A. Rutherford and D. A. Vroom, *J. Chem. Phys.*, **74**, 434 (1981).

57. E. M. van Veldhuizen and F. J. de Hoog, *J. Phys. D*, **17**, 953 (1984).
58. B. E. Warner, K. B. Persson and G. J. Collins, *J. Appl. Phys.*, **50**, 5694 (1979).
59. J. W. Coburn and E. Kay *Appl. Phys. Lett.*, **18**, 435 (1971).
60. H. S. W. Massey and E. H. S. Burhop, *Electronic and Ionic Impact Phenomena*, Oxford University Press, Oxford (1952).
61. R. van de Sanden, *Ph.D. Dissertation*, Technical University Eindhoven (1991).
62. V. S. Vorob'ev, *Plasma Sources Sci. Technol.* **4**, 163 (1995).
63. M. A. Biondi, *Phys. Rev.* **129**, 1181 (1963).
64. E. Rudberg, *Phys. Rev.* **4**, 764 (1934).
65. L. Reimer, *Scanning Electron Microscopy*, Springer-Verlag, Berlin (1985).
66. D. B. Medved, P. Mahadevan and J. K. Layton, *Phys. Rev.* **129**, 2086 (1963).
67. R. F. Stebbings, *Proc. Roy. Soc. (London)* **A241**, 270 (1957).
68. J. B. Hasted and P. Mahadevan, *Proc. Roy. Soc. (London)* **A249**, 42 (1959).
69. H. Oechsner, *Phys. Rev. B* **17**, 1052 (1978).
70. A. Benninghoven, *Surf. Sci.* **53**, 596 (1975).
71. R. V. Stuart and G. K. Wehner, *J. Appl. Phys.* **35**, 1819 (1964).
72. P. Sigmund, *Phys. Rev.* **184**, 383 (1969).
73. M. W. Weissmann and P. Sigmund, *Radiat. Eff.* **19**, 7 (1973).
74. J. Bohdanský, J. Roth and H. L. Bay, *J. Appl. Phys.* **51**, 2861 (1980).
75. N. Matsunami, Y. Yamamura, Y. Itikawa, N. Itoh, Y. Kazumata, S. Miyagawa, K. Morita and R. Shimizu, *Radiat. Eff. Lett.* **50**, 39 (1980).
76. M. T. Robinson and I. M. Torrens, *Phys. Rev.* **B9**, 5008 (1974).
77. Y. Yamamura, N. Matsunami and N. Itoh, *Radiat. Eff.* **71**, 65 (1983).
78. N. Matsunami, Y. Yamamura, Y. Itikawa, N. Itoh, Y. Kazumata, S. Miyagawa, K. Morita, R. Shimizu and H. Tawara, *Atom. Data and Nucl. Data Tables* **31**, 1 (1984).
79. G. K. Wehner and G. S. Anderson, in *Handbook of Thin Film Technology*, L. I. Maissel and R. Glang (eds.), McGraw-Hill, New York (1970), Chapter 3.
80. H. A. Oechsner, *Physics (N.Y.)* **261**, 37 (1973).
81. W. W. Harrison and B. L. Bentz, *Prog. Analyt. Spectrosc.* **11**, 53 (1988).
82. W. W. Harrison, in *Inorganic Mass Spectrometry*, F. Adams, R. Gijbels and R. Van Grieken (eds.), Wiley, New York (1988), Chapter 3.
83. K. R. Hess and R. K. Marcus, *Spectroscopy* **2**, (1987).
84. W. W. Harrison, K. R. Hess, R. K. Marcus and F. L. King, *Anal. Chem.* **58**, 341A (1986).
85. F. L. King and W. W. Harrison, *Mass Spectrom. Rev.* **9**, 285 (1990).
86. J. W. Coburn, *Rev. Sci. Instrum.* **41**, 1219 (1970).
87. F. Paschen, *Ann. Phys.* **50**, 901 (1916).
88. H. Schüler and H. Gollnow, *Z. Phys.* **93**, 611 (1935).

89. R. K. Marcus and W. W. Harrison, *Spectrochim. Acta* **40B**, 933 (1985).
90. R. K. Marcus and W. W. Harrison, *Anal. Chem.* **58**, 797 (1986).
91. R. K. Marcus, F. L. King and W. W. Harrison, *Anal. Chem.* **58**, 972 (1986).
92. R. K. Marcus and W. W. Harrison, *Anal. Chem.* **59**, 2369 (1987).
93. W. Grimm, *Spectrochim. Acta* **23B**, 443 (1968).
94. G. S. Anderson, N. W. Mayer and G. K. Wehner, *J. Appl. Phys.* **33**, 2991 (1962).
95. J. W. Coburn and E. Kay, *Appl. Phys. Lett.* **19**, 350 (1971).
96. D. L. Donohue and W. W. Harrison, *Anal. Chem.* **47**, 1528 (1975).
97. D. C. Duckworth and R. K. Marcus, *Anal. Chem.* **61**, 1879 (1989).
98. M. R. Winchester and R. K. Marcus, *J. Anal. Atom. Spectrom.* **5**, 575 (1990).
99. D. C. Duckworth and R. K. Marcus, *Appl. Spectrosc.* **44**, 649 (1990).
100. M. R. Winchester, C. Lazik and R. K. Marcus, *Spectrochim. Acta* **46B**, 483 (1991).
101. D. C. Duckworth and R. K. Marcus, *J. Anal. Atom. Spectrom.* **7**, 711 (1992).
102. R. K. Marcus, P. R. Cable, D. C. Duckworth, M. V. Buchanan, J. M. Pochkowski and R. R. Weller, *Appl. Spectrosc.* **46**, 1327 (1992).
103. S. A. McLuckey, G. L. Glish, D. C. Duckworth and R. K. Marcus, *Anal. Chem.* **64**, 1606 (1992).
104. C. M. Lazik and R. K. Marcus, *Spectrochim. Acta* **47B**, 1309 (1992).
105. C. M. Lazik and R. K. Marcus, *Spectrochim. Acta* **48B**, 863 (1993).
106. C. M. Lazik and R. K. Marcus, *Spectrochim. Acta* **48B**, 1673 (1993).
107. S. K. Ohorodnik, S. De Gendt, S. L. Tong and W. W. Harrison, *J. Anal. Atom. Spectrom.* **8**, 859 (1993).
108. C. R. Shick, Jr., A. Raith and R. K. Marcus, *J. Anal. Atom. Spectrom.* **8**, 1043 (1993).
109. D. C. Duckworth, D. L. Donohue, D. J. Smith, T. A. Lewis and R. K. Marcus, *Anal. Chem.* **65**, 2478 (1993).
110. T. R. Harville and R. K. Marcus, *Anal. Chem.* **65**, 3636 (1993).
111. G. Absalan, C. L. Chakrabarti, J. C. Hutton, M. H. Back, C. Lazik and R. K. Marcus, *J. Anal. Atom. Spectrom.* **9**, 45 (1994).
112. R. K. Marcus, *J. Anal. Atom. Spectrom.* **9**, 1029 (1994).
113. C. R. Shick, Jr., A. Raith and R. K. Marcus, *J. Anal. Atom. Spectrom.* **9**, 1045 (1994).
114. M. Parker and R. K. Marcus, *Appl. Spectrosc.* **48**, 623 (1994).
115. D. P. Myers, M. J. Heintz, P. P. Mahoney, G. Li, G. M. Hieftje, *Appl. Spectrosc.* **48**, 1337 (1994).
116. M. J. Heintz, P. J. Galley and G. M. Hieftje, *Spectrochim. Acta* **49B**, 745 (1994).

117. R. K. Marcus, T. R. Harville, Y. Mei, C. R. Shick, Jr., *Anal. Chem.* **66**, 902A (1994).
118. N. Bordel-Garcia, R. Pereiro-Garcia, M. Fernandez-Garcia, A. Sanz-Medel, T. R. Harville and R. K. Marcus, *J. Anal. Atom. Spectrom.* **10**, 671 (1995).
119. F. Präbeler, V. Hoffmann, J. Schumann and K. Wetzig, *J. Anal. Atom. Spectrom.* **10**, 677 (1995).
120. S. De Gendt, R. Van Grieken, W. Hang and W. W. Harrison, *J. Anal. Atom. Spectrom.* **10**, 689 (1995).
121. A. I. Saprykin, J. S. Becker, H.-J. Dietze, *J. Anal. Atom. Spectrom.* **10**, 897 (1995).
122. M. Parker and R. K. Marcus, *Spectrochim. Acta* **50B**, 617 (1995).
123. S. De Gendt, R. Van Grieken, S. K. Ohorodnik and W. W. Harrison, *Anal. Chem.* **67**, 1026 (1995).
124. T. R. Harville and R. K. Marcus, *Anal. Chem.* **67**, 1271 (1995).
125. A. I. Saprykin, F.-G. Melchers, J. S. Becker and H.-J. Dietze, *Fres. J. Anal. Chem.* **353**, 570 (1995).
126. M. J. Heintz and G. M. Hieftje, *Spectrochim. Acta* **50B**, 1125 (1995).
127. C. R. Shick, Jr. and R. K. Marcus, *Appl. Spectrosc.* **50**, 454 (1996).
128. M. Parker and R. K. Marcus, *Appl. Spectrosc.* **50**, 366 (1996).
129. V. Hoffmann, H.-J. Uhlemann, F. Präbeler, K. Wetzig and D. Birus, *Fres. J. Anal. Chem.*, in press: July-August (1996).
130. J. A. Strauss, N. P. Ferreira and H. G. C. Human, *Spectrochim. Acta* **37B**, 947 (1982).
131. K. Wagatsuma and K. Hirokawa, *Anal. Chem.* **56**, 2732 (1984).
132. K. Wagatsuma and K. Hirokawa, *Spectrochim. Acta* **43B**, 831 (1988).
133. J. A. Klingler, P. J. Savickas and W. W. Harrison, *J. Am. Soc. Mass Spectrom.* **1**, 138 (1990).
134. M. Glick, B. W. Smith and J. D. Winefordner, *Anal. Chem.* **62**, 157 (1990).
135. C. L. Chakrabarti, K. L. Headrick, J. C. Hutton, Z. Bicheng, P. C. Bertels and M. H. Back, *Anal. Chem.* **62**, 574 (1990).
136. J. A. Klingler, C. M. Barshick and W. W. Harrison, *Anal. Chem.* **63**, 2571 (1991).
137. J. A. Klingler and W. W. Harrison, *Anal. Chem.* **63**, 2982 (1991).
138. M. R. Winchester, S. M. Hayes and R. K. Marcus, *Spectrochim. Acta* **46B**, 615 (1991).
139. M. R. Winchester and R. K. Marcus, *Anal. Chem.* **64**, 2067 (1992).
140. C. Pan and F. L. King, *Anal. Chem.* **65**, 3187 (1993).
141. X. Cai and J. C. Williams, *Appl. Spectrosc.* **49**, 891 (1995).
142. W. Hang, W. O. Walden and W. W. Harrison, *Anal. Chem.* **68**, 1148 (1996).

143. F. L. King and W. W. Harrison, in *Glow Discharge Spectroscopies*, R. K. Marcus (ed.), Plenum Press, New York (1993), Chapter 5.
144. D. Colodner, V. Salters and D. C. Duckworth, *Anal. Chem.* **66**, 1079A (1994).
145. Y. Mei and R. K. Marcus, *Trends in Anal. Chem.* **12**, 86 (1993).
146. W. W. Harrison, C. M. Barshick, J. A. Klingler, P. H. Ratliff and Y. Mei, *Anal. Chem.* **62**, 943A (1990).
147. F. L. King, J. Teng and R. E. Steiner, *J. Mass Spectrom.* **30**, 1061 (1995).
148. F. W. Aston, *Mass Spectra and Isotopes*, 2nd ed., Longmans, Green and Co, New York (1942).
149. K. T. Bainbridge and E. B. Jordon, *Phys. Rev.* **50**, 282 (1936).
150. J. W. Coburn and E. Kay, *J. Appl. Phys.* **43**, 4965 (1972).
151. W. W. Harrison and C. W. Magee, *Anal. Chem.* **46**, 461 (1974).
152. E. H. Daughtrey, Jr. and W. W. Harrison, *Anal. Chem.* **47**, 1024 (1975).
153. D. L. Donohue and W. W. Harrison, *Anal. Chem.* **47**, 1528 (1975).
154. B. N. Colby and C. A. Evans, Jr., *Anal. Chem.* **46**, 1236 (1974).
155. J. R. Wallace, D. F. Natusch, B. N. Colby and C. A. Evans, Jr., *Anal. Chem.* **48**, 118 (1976).
156. C. G. Bruhn, B. L. Bentz and W. W. Harrison, *Anal. Chem.* **50**, 373 (1978).
157. M. Hecq, A. Hecq and M. Liemans, *J. Appl. Phys.* **49**, 6176 (1978).
158. M. Hecq and A. Hecq, *J. Appl. Phys.* **56**, 672 (1984).
159. N. Jakubowski, D. Stüwer and G. Tölg, *Int. J. Mass Spectrom. Ion Proc.* **71**, 183 (1986).
160. J. E. Cattle, E. F. Hall, C. J. Shaw and P. J. Turner, *Int. J. Mass Spectrom. Ion Proc.* **46**, 11 (1983).
161. B. L. Bentz, C. G. Bruhn and W. W. Harrison, *Int. J. Mass. Spectrom. Ion Proc.* **28**, 409 (1978).
162. C. G. Bruhn, B. L. Bentz and W. W. Harrison, *Anal. Chem.* **51**, 673 (1979).
163. N. Jakubowski, D. Stüwer and W. Vieth, *Anal. Chem.* **59**, 1825 (1987).
164. N. Jakubowski, D. Stüwer and W. Vieth, *Fres. Z. Anal. Chem.* **331**, 145 (1988).
165. R. C. Hutton and A. Raith, *J. Anal. Atom. Spectrom.* **7**, 623 (1992).
166. D. C. Duckworth, C. M. Barshick, D. H. Smith and S. A. McLuckey, *Anal. Chem.* **66**, 92 (1994).
167. S. A. McLuckey, D. E. Goeringer, K. G. Asano, G. Vaidyanathan and J. L. Stephenson, Jr., *Rapid. Comm. Mass Spectrom.* **10**, 287 (1996).
168. F. L. King, A. L. McCormack and W. W. Harrison, *J. Anal. Atom. Spectrom.* **3**, 883 (1988).
169. F. L. King and W. W. Harrison, *Int. J. Mass. Spectrom. Ion Proc.* **89**, 171 (1989).

170. K. L. Busch, *J. Mass Spectrom.* **30**, 233 (1995).
171. C. M. Barshick and J. R. Eyler, *J. Am. Soc. Mass Spectrom.* **3**, 122 (1992).
172. C. H. Watson, J. Wronka, F. H. Laukien, C. M. Barshick and J. R. Eyler, *Spectrochim. Acta* **48B**, 1445 (1993).
173. C. M. Barshick and J. R. Eyler, *J. Am. Soc. Mass Spectrom.* **4**, 387 (1993).
174. C. H. Watson, C. M. Barshick, J. Wronka, F. H. Laukien and J. R. Eyler, *Anal. Chem.* **68**, 573 (1996).
175. K. Robinson and E. F. H. Hall, *J. Metals* **39**, 14 (1987).
176. G. Kudermann and K. Blaufuss, *Mikrochim. Acta* **I**, 269 (1987).
177. G. Kudermann, *Fres. Z. Anal. Chem.* **331**, 697 (1988).
178. H. Saisho, M. Tanaka and K. Nakamura, *J. Res. Nat. Bur. Standards* **93**, 398 (1988).
179. L. F. Vassamillet, *J. Anal. Atom. Spectrom.* **4**, 451 (1989).
180. A. P. Mykytiuk, P. Semeniuk and S. Berman, *Spectrochim. Acta Rev.* **13**, 1 (1990).
181. P. Wilhartitz, H. M. Ortner, R. Krismer and H. Krabichler, *Mikrochim. Acta* **II**, 259 (1990).
182. D. Fang and P. Seegopaul, *J. Anal. Atom. Spectrom.* **7**, 959 (1992).
183. W. Vieth and J. C. Huneke, *Anal. Chem.* **64**, 2958 (1992).
184. M. van Straaten, K. Swenters, R. Gijbels, J. Verlinden and E. Adriaenssens, *J. Anal. Atom. Spectrom.* **9**, 1389 (1994).
185. A. Held, P. Taylor, C. Ingelbrecht, P. De Bievre, J. A. C. Broekaert, M. van Straaten and R. Gijbels, *J. Anal. Atom. Spectrom.* **10**, 849 (1995).
186. M. Saito, *Spectrochim. Acta* **50B**, 171 (1995).
187. M. Saito, *Fres. J. Anal. Chem.* **351**, 148 (1995).
188. N. E. Sanderson, E. Hall, J. Clark, P. Charlabous and D. Hall, *Mikrochim. Acta* **I**, 275 (1987).
189. P. K. Chu, J. C. Huneke and R. J. Blattner, *J. Vac. Sci. Technol.* **A5**, 295 (1987).
190. K. B. Lee, D. W. Moon and K. W. Lee, *Bull. Korean Chem. Soc.* **10**, 524 (1989).
191. W. Vieth and J. C. Huneke, *Spectrochim. Acta* **46B**, 137 (1991).
192. D. J. Hall and P. K. Robinson, *Amer. Lab.*, August, p. 74 (1987).
193. J. Ihaio, J. Zhu and D. M. Lubman, *Anal. Chem.* **64**, 142 (1992).
194. A. Raith, W. Vieth, J. C. Huneke and R. C. Hutton, *J. Anal. Atom. Spectrosc.* **7**, 943 (1992).
195. S. Itoh, F. Hirose and R. Hasegawa, *Spectrochim. Acta* **47B**, 1241 (1992).
196. R. W. Smithwick III, *J. Am. Soc. Mass Spectrom.* **3**, 79 (1992).
197. R. W. Smithwick III, D. W. Lynch, J. C. Franklin, *J. Am. Soc. Mass Spectrom.* **4**, 278 (1993).

198. X. Feng and G. Horlick, *J. Anal. Atom. Spectrom.* **9**, 823 (1994).
199. T. Takahashi and T. Shimamura, *Anal. Chem.* **66**, 3274 (1994).
200. C. Venzago and M. Weigert, *Fres. J. Anal. Chem.* **350**, 303 (1994).
201. T. Tanaka, T. Kubota and H. Kawaguchi, *Anal. Sciences* **10**, 895 (1994).
202. N. Jakubowski, I. Feldmann and D. Stüwer, *Spectrochim. Acta* **50B**, 639 (1995).
203. D. L. Donohue and M. Petek, *Anal. Chem.* **63**, 740 (1991).
204. L. R. Riciputi, D. C. Duckworth, C. M. Barshick and D. H. Smith, *Int. J. Mass Spectrom. Ion Proc.* **146/147**, 55 (1995).
205. R.-C. Deng and P. Williams, *Anal. Chem.* **66**, 1890 (1994).
206. K. L. Goodner, J. R. Eyler, C. M. Barshick and D. H. Smith, *Int. J. Mass Spectrom. Ion Proc.* **146/147**, 65 (1995).
207. P. M. Charalambous, *Steel Research* **58**, 192 (1987).
208. W. W. Harrison, *J. Anal. Atom. Spectrom.* **3**, 867 (1988).
209. J. C. Huneke, *J. Res. Natl. Bur. Stand. (US)* **92**, 392 (1988).
210. W. S. Taylor and J. K. Dulak, *Spectroscopy* **4**, 41 (1989).
211. M. van Straaten, *Ph. D. Dissertation*, University of Antwerp (1993).
212. Ch. Jonkers, *Ph. D. Dissertation*, University of Antwerp (1995).
213. G. I. Ramendik, B. M. Manzon, D. A. Tyurin, N. E. Benyaev and A. A. Komleva, *Talanta* **34**, 61 (1987).
214. G. I. Ramendik, D. A. Tyurin, Yu. I. Babikov, *Anal. Chem.* **62**, 2501 (1990).
215. D. M. P. Milton, R. C. Hutton and G. A. Ronan, *Fres. J. Anal. Chem.* **343**, 773 (1992).
216. M. Dogan, K. Laqua and H. Massman, *Spectrochim. Acta* **27B**, 65 (1972).
217. T. J. Loving and W. W. Harrison, *Anal. Chem.* **55**, 1526 (1983).
218. S. L. Tong and W. W. Harrison, *Spectrochim. Acta* **48B**, 1237 (1993).
219. D. C. Duckworth, C. M. Barshick and D. H. Smith, *J. Anal. Atom. Spectrom.* **8**, 875 (1993).
220. J. C. Woo, N. Jakubowski and D. Stuewer, *J. Anal. Atom. Spectrom.* **8**, 881 (1993).
221. Y. Mei and W. W. Harrison, *Anal. Chem.* **65**, 3337 (1993).
222. D. C. Duckworth, C. M. Barshick, D. A. Bostick and D. H. Smith, *Appl. Spectrosc.* **47**, 243 (1993).
223. M. Battagliarin, E. Sentimenti and R. Scattolin, *Spectrochim. Acta* **50B**, 13 (1995).
224. S. De Gendt, W. Schelles, R. Van Grieken and V. Müller, *J. Anal. Atom. Spectrom.* **10**, 681 (1995).
225. J. Teng, C. M. Barshick, D. C. Duckworth, S. J. Morton, D. H. Smith and F. L. King, *Appl. Spectrosc.* **49**, 1361 (1995).

226. D. M. P. Milton and R. C. Hutton, *Spectrochim. Acta* **48B**, 39 (1993).
227. W. Schelles, S. De Gendt, V. Müller and R. Van Grieken, *Appl. Spectrosc.* **49**, 939 (1995).
228. W. Schelles, K. Maes, S. De Gendt and R. Van Grieken, *Anal. Chem.* **68**, 1136 (1996).
229. M. Hecq, A. Hecq and M. Fontignies, *Anal. Chim. Acta* **155**, 191 (1983).
230. D. J. Hall and N. E. Sanderson, *Surf. Interface Anal.* **11**, 40 (1988).
231. N. Jakubowski and D. Stüwer, *J. Anal. Atom. Spectrom.* **7**, 951 (1992).
232. A. Raith, R. C. Hutton and J. C. Huneke, *J. Anal. Atom. Spectrom.* **8**, 867 (1993).
233. U. Behn, F. A. Gerbig and H. Albrecht, *Fres. J. Anal. Chem.* **349**, 209 (1994).
234. W. A. Mattson, B. L. Bentz and W. W. Harrison, *Anal. Chem.* **48**, 489 (1976).
235. G. O. Foss, H. J. Svec and R. J. Conzemius, *Anal. Chim. Acta* **147**, 151 (1983).
236. N. Jakubowski, D. Stüwer and G. Tölg, *Spectrochim. Acta* **46B**, 155 (1991).
237. I. Evetts, D. Milton and R. Mason, *Biol. Mass Spectrom.* **20**, 153 (1991).
238. C. M. Barshick, D. C. Duckworth and D. H. Smith, *J. Am. Soc. Mass Spectrom.* **4**, 47 (1993).
239. C. M. Barshick, D. H. Smith, J. H. Hackney, B. A. Cole, J. A. Cole and J. W. Wade, *Anal. Chem.* **66**, 730 (1994).
240. C. M. Barshick, D. H. Smith, J. W. Wadae and C. K. Bayne, *J. Anal. Atom. Spectrom.* **9**, 83 (1994).
241. G. G. Sikharudlidze, Poster presented at the "1996 Winter Conference on Plasma Spectrochemistry, Fort Lauderdale, FL (1996).
242. S. A. McLuckey, G. L. Glish, K. G. Asano and B. G. Grant, *Anal. Chem.* **60**, 2220 (1988).
243. J. R. Chapman and J. A. E. Pratt, *J. Chromatogr.* **394**, 231 (1987).
244. G. A. Mills, V. Walker, M. R. Clench and V. C. Parr, *Biomed. and Env. Mass Spec.* **16**, 259 (1988).
245. I. Sofer, J. Zhu, H. S. Lee, W. Antos and D. M. Lubman, *Appl. Spectrosc.* **44**, 1391 (1990).
246. J. Zhao, J. Zhu and D. M. Lubman, *Anal. Chem.* **64**, 1426 (1992).
247. D. Carazatto and M. J. Bertrand, *J. Am. Soc. Mass Spectrom.* **5**, 305 (1994).
248. R. Mason and D. Milton, *Int. J. Mass Spectrom. Ion Proc.* **52**, 65 (1983).
249. R. Mason and D. Milton, *Int. J. Mass Spectrom. Ion Proc.* **91**, 209 (1989).
250. M. Betti, G. Rasmussen, T. Hiernaut, L. Koch, D. M. P. Milton and R. C. Hutton, *J. Anal. Atom. Spectrom.* **9**, 385 (1994).
251. J. A. C. Broekaert, in *Glow Discharge Spectroscopies*, R. K. Marcus (ed.), Plenum Press, New York (1993), Chapter 4.

-
252. H. Hocquaux, in *Glow Discharge Spectroscopies*, R. K. Marcus (ed.), Plenum Press, New York (1993), Chapter 8.
 253. J. A. C. Broekaert, *J. Anal. Atom. Spectrom.* **2**, 537 (1987).
 254. J. A. C. Broekaert, *Appl. Spectrosc.* **49**, 12A (1995).
 255. F. T. Burks, *Spectrochim. Acta* **5**, 322 (1952).
 256. I. A. Berezin, *Zavod. Lab.* **27**, 859 (1961).
 257. G. A. Pevtsov, V. Z. Krasilshchik and A. F. Yabovlera, *J. Anal. Chem. USSR* **23**, 1569 (1968).
 258. W. W. Harrison and N. J. Prakash, *Anal. Chim. Acta* **49**, 151 (1970).
 259. P. J. Treado and M. D. Morris, *Anal. Chem.* **61**, 723A (1989).
 260. L. M. Faires, *Anal. Chem.* **58**, 1023A (1986).
 261. J. A. C. Broekaert, K. R. Brushwyler, C. A. Monnig and G. M. Hieftje, *Spectrochim. Acta* **45B**, 769 (1990).
 262. H. W. Rademacher and M. C. de Swardt, *Spectrochim. Acta* **30B**, 353 (1975).
 263. R. A. Kruger, L. R. P. Butler, C. J. Liebenberg and R. G. Böhmer, *Analyst (London)* **102**, 949 (1977).
 264. M. Dogan, *Spectrochim. Acta* **36B**, 103 (1981).
 265. T. Yamada, J. Kashima and K. Naganuma, *Anal. Chim. Acta* **124**, 275 (1981).
 266. K. Wagatsuma and K. Hirokawa, *Anal. Chem.* **56**, 908 (1984).
 267. I. M. Dharmadasa, M. Yves, J. S. Brooks, G. H. France and S. J. Brown, *Semicond. Sci. Technol.* **10**, 369 (1995).
 268. S. El Alfy, K. Laqua and H. Maßmann, *Fres. J. Anal. Chem.* **263**, 1 (1973).
 269. S. Caroli, A. Alimonti and K. Zimmer, *Spectrochim. Acta* **38B**, 625 (1983).
 270. G. S. Lomdahl and J. V. Sullivan, *Spectrochim. Acta* **39B**, 1395 (1984).
 271. A. B. M. ElNady, K. Zimmer and G. Zaray, *Spectrochim. Acta* **40B**, 999 (1985).
 272. H. Mai and H. Scholze, *Spectrochim. Acta* **41B**, 797 (1986).
 273. I. B. Brenner, K. Laqua and M. Dvorachek, *J. Anal. Atom. Spectrom.* **2**, 623 (1987).
 274. G. Ehrlich, U. Stahlberg, V. Hoffmann and H. Scholze, *Spectrochim. Acta* **46B**, 115 (1991).
 275. S. Caroli, O. Senofonte, M. G. Del Monte Tamba, M. Cilia, I. B. Brenner and M. Dvorochek, *Spectrochim. Acta* **48B**, 877 (1993).
 276. F. Flórian, W. Fischer and H. Nickel, *J. Anal. Atom. Spectrom.* **9**, 257 (1994).
 277. P. A. Büger and W. Fink, *Fres. Z. Anal. Chem.* **244**, 314 (1969).
 278. J. A. C. Broekaert, *Spectrochim. Acta* **35B**, 225 (1980).
 279. J. M. Brackett and T. J. Vickers, *Spectrochim. Acta* **38B**, 979 (1983).
 280. S. Caroli, O. Senofonte, P. Delle Femmine, *Analyst* **108**, 196 (1983).
 281. F. Chen and J. C. Williams, *Anal. Chem.* **62**, 489 (1990).
-

282. C. M. Strange and R. K. Marcus, *Spectrochim. Acta* **46B**, 517 (1991).
283. K. R. Hess, C. M. Barshick, D. C. Duckworth and D. H. Smith, *Appl. Spectrosc.* **48**, 1307 (1994).
284. R. Pereiro, T. K. Starn and G. M. Hieftje, *Appl. Spectrosc.* **49**, 616 (1995).
285. M. Ancey, R. Berneron and P. Parnière, *R. C. Met. Phys.* **582** (1971).
286. R. Berneron, *Spectrochim. Acta* **33B**, 665 (1978).
287. R. Berneron and J. C. Charbonnier, *Surf. Interface Anal.* **3**, 134 (1981).
288. A. Bengtson, *Spectrochim. Acta* **40B**, 631 (1985).
289. K. Wagatsuma and K. Hirokawa, *Anal. Chem.* **58**, 1112 (1986).
290. A. Bengtson and M. Lundholm, *J. Anal. Atom. Spectrom.* **3**, 879 (1988).
291. Z. Weiss, *Surf. Interf. Anal.* **17**, 641 (1991).
292. Z. Weiss, *Spectrochim. Acta* **47B**, 859 (1992).
293. O. Dessenne, A. Quentmeier and H. Bubert, *Fres. J. Anal. Chem.* **346**, 340 (1993).
294. R. Payling and D. G. Jones, *Surf. Interface Anal.* **20**, 787 (1993).
295. R. Payling, D. G. Jones and S. A. Gower, *Surf. Interface Anal.* **20**, 959 (1993).
296. A. Quentmeier, *J. Anal. Atom. Spectrom.* **9**, 355 (1994).
297. D. G. Jones, R. Payling, S. A. Gower and E. M. Boge, *J. Anal. Atom. Spectrom.* **9**, 369 (1994).
298. A. Bengtson, *Spectrochim. Acta* **49B**, 411 (1994).
299. S. Oswald, V. Hoffmann and G. Ehrlich, *Spectrochim. Acta* **49B**, 1123 (1994).
300. Z. Weiss, *J. Anal. Atom. Spectrom.* **10**, 891 (1995).
301. R. Payling, D. G. Jones and S. A. Gower, *Surf. Interface Anal.* **23**, 1 (1995).
302. R. Payling, *Surf. Interface Anal.* **23**, 12 (1995).
303. E. H. Piepmeier, in *Glow Discharge Spectroscopies*, R. K. Marcus (ed.), Plenum Press, New York (1993), Chapter 3.
304. B. J. Russell and A. Walsh, *Spectrochim. Acta* **15**, 883 (1959).
305. D. S. Gough, P. Hannaford and A. Walsh, *Spectrochim. Acta* **28B**, 197 (1973).
306. B. M. Gatehouse and A. Walsh, *Spectrochim. Acta* **16**, 602 (1960).
307. J. A. Goleb, *Anal. Chem.* **35**, 1978 (1963).
308. A. Goleb and J. K. Brody, *Anal. Chim. Acta* **28**, 457 (1963).
309. B. W. Gandrud and R. K. Skogerboe, *Appl. Spectrosc.* **25**, 243 (1971).
310. D. S. Gough, *Anal. Chem.* **48**, 1926 (1976).
311. A. E. Bernhard, *Spectroscopy* **2**, 24 (1987).
312. K. Ohls, J. Flock and H. Loepp, *Fresenius Z. Anal. Chem.* **332**, 456 (1988).
313. B. W. Smith, J. B. Womack, N. Omenetto and J. D. Winefordner, *Appl. Spectrosc.* **43**, 873 (1989).

314. B. W. Smith, N. Omenetto and J. D. Winefordner, *Spectrochim. Acta* **39B**, 1389 (1984).
315. W. O. Walden, W. W. Harrison, B. W. Smith and J. D. Winefordner, *J. Anal. Atom. Spectrom.* **9**, 1039 (1994).
316. D. C. McDonald, *Anal. Chem.* **49**, 1336 (1977).
317. K. Ohls, *Fresenius Z. Anal. Chem.* **327**, 111 (1987).
318. A. E. Bernhard and H. L. Kahn, *Am. Lab.* **20**, 126 (1988).
319. D. S. Gough and R. J. Meldrum, *Anal. Chem.* **52**, 642 (1980).
320. H. Bubert, *Spectrochim. Acta* **39B**, 1377 (1984).
321. B. M. Patel and J. D. Winefordner, *Appl. Spectrosc.* **40**, 667 (1986).
322. S. A. Dashin, Y. A. Karpov, O. A. Kushlyansky, I. A. Mayorov and M. A. Bolshov, *Spectrochim. Acta* **46B**, 467 (1991).
323. M. R. Winchester, S. M. Hayes and R. K. Marcus, *Spectrochim. Acta* **46B**, 615 (1991).
324. A. I. Drobyshev and Y. I. Turkin, *Spectrochim. Acta* **36B**, 1153 (1981).
325. M. R. Winchester, S. M. Hayes and R. K. Marcus, *Spectrochim. Acta* **46B**, 615 (1991).
326. M. R. Winchester and R. K. Marcus, *Appl. Spectrosc.* **42**, 941 (1988).
327. S. J. O'Gram, J. R. Dean, W. R. Tomlinson and J. Marshall, *Anal. Chim. Acta* **294**, 95 (1994).
328. S. A. Dashin, I. A. Mayorov and M. A. Bolshov, *Spectrochim. Acta* **48B**, 531 (1993).
329. K. C. Ng, A. H. Ali and J. D. Winefordner, *Spectrochim. Acta* **46B**, 309 (1991).
330. C. A. Morgan, C. L. Davis, B. W. Smith and J. D. Winefordner, *Appl. Spectrosc.* **48**, 261 (1994).
331. J. B. Womack, E. M. Gessler and J. D. Winefordner, *Spectrochim. Acta* **46B**, 301 (1991).
332. C. L. Davis, B. W. Smith, M. A. Bolshov and J. D. Winefordner, *Appl. Spectrosc.* **49**, 907 (1995).
333. B. M. Patel and J. D. Winefordner, *Spectrochim. Acta* **41B**, 469 (1986).
334. C. L. Davis, B. W. Smith and J. D. Winefordner, *Microchem. Journal* **52**, 383 (1995).
335. K. R. Hess, in *Glow Discharge Spectroscopies*, R. K. Marcus (ed.), Plenum Press, New York (1993), Chapter 10.
336. K. R. Hess and W. W. Harrison, in *Lasers and Mass Spectrometry*, D. M. Lubman (ed.), Oxford University Press, London, 1990, p. 205.
337. Y. Iida, *Spectrochim. Acta* **45B**, 427 (1990).
338. C. M. Barshick, R. W. Shaw, J. P. Young and J. M. Ramsey, *Anal. Chem.* **66**, 4154 (1994).

339. Z. Zhu and E. H. Piepmeier, *Spectrochim. Acta* **49B**, 1775 (1994).
340. C. M. Barshick, R. W. Shaw, J. P. Young and J. M. Ramsey, *Anal. Chem.* **67**, 3814 (1995).
341. R. W. Shaw, C. M. Barshick, L. W. Jennings, J. P. Young and J. M. Ramsey, *Rapid Comm. Mass Spectrom.* **10**, 316 (1996).
342. J. M. Harnly, D. L. Styris and P. G. Rigby, in *Glow Discharge Spectroscopies*, R. K. Marcus (ed.), Plenum Press, New York (1993), Chapter 9.
343. H. Falk, *Spectrochim. Acta* **32B**, 437 (1977).
344. P. G. Riby, J. M. Harnley, D. L. Styris and N. E. Ballou, *Spectrochim. Acta* **46B**, 203 (1991).
345. D. C. Liang and M. W. Blades, *Spectrochim. Acta* **44B**, 1059 (1989).
346. D. L. Smith, D. C. Liang, D. Steel and M. W. Blades, *Spectrochim. Acta* **45B**, 493 (1990).
347. R. E. Sturgeon, S. N. Willie, V. Luong, S. Berman and J. G. Dunn, *J. Anal. Atom. Spectrom.* **4**, 669 (1989).
348. R. E. Sturgeon, S. N. Willie, V. T. Luong and S. S. Berman, *J. Anal. Atom. Spectrom.* **5**, 635 (1990).
349. R. E. Sturgeon, S. N. Willie, V. T. Luong and S. S. Berman, *Anal. Chem.* **62**, 2370 (1990).
350. R. E. Sturgeon, S. N. Willie, V. T. Luong and S. S. Berman, *J. Anal. Atom. Spectrom.* **6**, 19 (1991).
351. R. E. Sturgeon, S. N. Willie, V. T. Luong and S. S. Berman, *Spectrochim. Acta* **46B**, 1021 (1991).
352. R. M. Lowe, *Spectrochim. Acta* **31B**, 257 (1976).
353. D. S. Gough and J. V. Sullivan, *Analyst (London)* **103**, 887 (1978).
354. J. V. Sullivan and J. C. Van Loon, *Anal. Chim. Acta* **102**, 25 (1978).
355. J. V. Sullivan, *Anal. Chim. Acta* **105**, 213 (1979).
356. D. C. McDonald, *Spectrochim. Acta* **37B**, 747 (1982).
357. G. S. Lomdahl, R. McPherson and J. V. Sullivan, *Anal. Chim. Acta* **148**, 171 (1983).
358. G. S. Lomdahl and J. V. Sullivan, *Spectrochim. Acta* **39B**, 1395 (1984).
359. P. E. Walters and H. G. C. Human, *Spectrochim. Acta* **36B**, 585 (1981).
360. N. P. Ferreira, J. A. Straus and H. G. C. Human, *Spectrochim. Acta* **38B**, 899 (1983).
361. S. Caroli, A. Alimonti and F. Petrucci, *Anal. Chim. Acta* **136**, 269 (1982).
362. S. Caroli, O. Senofonte, N. Violante and L. Di Simone, *Appl. Spectrosc.* **41**, 579 (1987).
363. F. Leis, J. A. C. Broekaert and K. Laqua, *Spectrochim. Acta* **42B**, 1169 (1987).

-
364. F. Leis, J. A. C. Broekaert and E. B. M. Steers, *Spectrochim. Acta* **46B**, 243 (1991).
365. F. Leis and E. B. M. Steers, *Spectrochim. Acta* **49B**, 289 (1994).
366. R. A. Kruger, R. M. Bombelka and K. Laqua, *Spectrochim. Acta* **35B**, 581 (1980).
367. R. A. Kruger, R. M. Bombelka and K. Laqua, *Spectrochim. Acta* **35B**, 589 (1980).
368. J. B. Ko, *Spectrochim. Acta* **39B**, 1405 (1984).
369. S. Caroli, O. Senofonte, N. Violante and R. Astrologo, *J. Anal. Atom. Spectrom.* **3**, 887 (1988).
370. S. Tanguay and R. Sacks, *Appl. Spectrosc.* **42**, 576 (1988).
371. R. Simonneau and R. Sacks, *Appl. Spectrosc.* **43**, 141 (1989).
372. L. McCaig, N. Sesi and R. Sacks, *Appl. Spectrosc.* **44**, 1176 (1990).
373. S. Brewer, T. Holbrook, Z. Shi, K. Trivedi and R. Sacks, *Appl. Spectrosc.* **45**, 1327 (1991).
374. K. Trivedi, S. Brewer, L. McCaig, N. Sesi and R. Sacks, *Spectrochim. Acta* **46B**, 229 (1991).
375. L. McCaig, Z. Shi, T. H. Woodrum, S. Brewer and R. Sacks, *Appl. Spectrosc.* **46**, 1762 (1992).
376. Z. Shi, T. H. Woodrum, K. Dehghan, S. Brewer and R. Sacks, *Appl. Spectrosc.* **46**, 46 of/en 49 of/en 749 (1992).
377. T. Mehdi, P. B. Legrand, J.-P. Dauchot, M. Wautelet and M. Hecq, *Spectrochim. Acta* **48B**, 1023 (1993).
378. M. J. Heintz, K. Mifflin, J. A. C. Broekaert and G. M. Hieftje, *Appl. Spectrosc.* **49**, 241 (1995).
379. C. Molle, S. Springael, M. Wautelet, J.-P. Dauchot and M. Hecq, *Appl. Spectrosc.* **49**, 872 (1995).
380. M. J. Heintz, D. P. Myers, P. P. Mahoney, G. Li and G. M. Hieftje, *Appl. Spectrosc.* **49**, 945 (1995).
381. Z. Shi, S. Brewer and R. Sacks, *Appl. Spectrosc.* **49**, 1232 (1995).
382. C. Molle, M. Wautelet, J. P. Dauchot and M. Hecq, *J. Anal. Atom. Spectrom.* **10**, 1039 (1995).
383. M. J. Heintz and G. M. Hieftje, *Spectrochim. Acta* **50B**, 1109 (1995).
384. A. I. Saprykin, J. S. Becker and H.-J. Dietze, *Fres. J. Anal. Chem.*, in press (1996).
385. H. J. Kim and E. H. Piepmeier, *Anal. Chem.* **60**, 2040 (1988).
386. P. R. Banks and M. W. Blades, *Spectrochim. Acta* **44B**, 1117 (1989).
387. P. R. Banks and M. W. Blades, *Spectrochim. Acta* **46B**, 501 (1991).
388. P. R. Banks and M. W. Blades, *Spectrochim. Acta* **47B**, 1203 (1992).
-

389. P. R. Banks and M. W. Blades, *Spectrochim. Acta* **47B**, 1287 (1992).
390. P. R. Banks and M. W. Blades, *Spectrochim. Acta* **47B**, 1435 (1992).
391. H. J. Kim, E. H. Piepmeier, G. L. Beck, G. G. Brumbaugh and O. T. Farmer, III, *Anal. Chem.* **62**, 639 (1990).
392. C. L. Chakrabarti, K. L. Headrik, J. C. Hutton, P. C. Bertels and M. H. Back, *Spectrochim. Acta* **46B**, 183 (1991).
393. J. C. Hutton, C. L. Chakrabarti, P. C. Bertels and M. H. Back, *Spectrochim. Acta* **46B**, 193 (1991).
394. J. C. Hutton and C. L. Chakrabarti, *Spectrochim. Acta* **46B**, 1287 (1991).
395. J. A. C. Broekaert, T. Bricker, K. R. Brushwyler and G. M. Hieftje, *Spectrochim. Acta* **47B**, 131 (1992).
396. H. J. Kim, Y. S. Park, J. H. Cho, G. H. Lee, K. H. Cho, K. B. Lee and H. S. Kim, *J. Anal. Atom. Spectrom.* **10**, 335 (1995).
397. G. H. Lee, H. R. Song, E. H. Kim, S. Kang, M. C. Park, D. S. Kim, H. Kim and H. J. Kim, *Bull. Korean Chem. Soc.* **16**, 699 (1995).
398. M. R. Winchester and M. L. Salit, *Spectrochim. Acta* **50B**, 1045 (1995).
399. Y. Kanzaki, N. Nishimura and O. Matsumoto, *J. Electroanal. Chem. Interfacial Electrochem.* **167**, 297 (1984).
400. T. Cserfalvi, P. Mezei and P. Apai, *J. Phys. D* **26**, 2184 (1993).
401. D. C. Gerstenberger, R. Solanki and G. J. Collins, *IEEE Journal. of Quant. Electron.* **16**, 820 (1980).

CHAPTER 2

**Mathematical modeling of a
direct current glow discharge in argon**

2.1. INTRODUCTION AND AIM OF THE WORK

In spite of the extensive use of glow discharges in a wide range of application fields, the underlying physics of the discharges is not yet fully understood. An important step towards a better understanding is the accurate description of the glow discharge. One way to reach this goal is by mathematical modeling. Detailed modeling of analytical glow discharges has not been carried out before. However, glow discharges used for plasma etching and deposition, which operate at lower voltages (i.e. a few hundred volts), have been studied more thoroughly in the plasma physics literature. The processes occurring in both kinds of glow discharges are mostly quite similar, so that the basics of the models to describe analytical glow discharges can be deduced from existing models in the plasma physics literature. However, analytical chemists are especially interested in the behavior of the sputtered species, whereas plasma physicists focus more on the electrical characteristics of the glow discharge. Moreover, since both glow discharges operate at different discharge conditions, it can be expected that other plasma processes come into play in both cases.

Three basic groups of models have been reported in the plasma physics literature to describe glow discharges. In a **fluid model** [1-11] the plasma species are considered as a continuum in equilibrium with the electric field; they are described by the continuity equations and by the flux equations of diffusion and of migration in the electric field (the latter only for charged particles). This kind of modeling is only an approximation, especially for the electrons, which are not in equilibrium with the electric field (i.e. they gain more energy from the electric field than they lose by collisions). The second approach is a **kinetic (Boltzmann) model** [12-14], which copes with the non-equilibrium situation of the various plasma species by describing them with the Boltzmann transport equation. The third way is via **Monte Carlo simulations** [15-26]. The species are simulated one after the other. Their trajectory is described by Newton's laws and their collision processes are treated with random numbers. By following in this statistical way a large number of particles, the glow discharge can be simulated. This model is the most accurate one, because it deals with the particles on the lowest microscopical level. However, in order to reach satisfactory statistics, a large number of particles have to be followed, and this can lead to a long calculation time for slow-moving particles. Hence, each model has its advantages and disadvantages. Therefore, it is desirable to use a combination of different models to describe the various species in the glow discharge. Species that are not in equilibrium with the electric field, like the fast electrons, must be treated with a Monte Carlo model, whereas species that are more or less in equilibrium with the electric field can be described with a fluid model.

In this work, a combined mathematical model of the analytical glow discharge is presented, consisting of various submodels for the different plasma species. The species that are assumed to be present in the plasma, include argon atoms at rest, singly charged positive argon ions, fast argon atoms, argon metastable atoms, fast and slow electrons, and atoms and ions of the cathode material. Table 2.1 summarizes the different models used to describe these species. The models are all coupled to each other by the interaction processes between the plasma species. The combined models are solved iteratively until final convergence is reached, in order to obtain an overall picture of the glow discharge.

Table 2.1: Overview of the different models used in this work to describe the plasma species.

Plasma species	Model
Fast electrons	Monte Carlo (entire discharge)
Slow electrons	Fluid (entire discharge)
Ar ⁺ ions	Fluid (entire discharge)
Ar ⁺ ions	Monte Carlo (CDS)
Ar _f ⁰ atoms	Monte Carlo (CDS)
Ar _m [*] metastable atoms	Fluid (entire discharge)
M ⁰ atoms (thermalization)	Monte Carlo (entire discharge)
M ⁰ atoms + M ⁺ ions (diffusion, ionization)	Fluid (entire discharge)
M ⁺ ions	Monte Carlo (CDS)

Since plasma physicists are particularly interested in the electrical characteristics of the glow discharge as such, a substantial number of models can be found in the plasma physics literature, describing the behavior of electrons and gas (e.g. argon) ions, with fluid approaches [1-11], Boltzmann models [12-14] or Monte Carlo simulations [15-26], or with a combination of these models (Monte Carlo or Boltzmann approaches for the fast electrons, and fluid models for the slow electrons and gas ions, i.e. so-called “hybrid” models [27-35] or particle-in-cell approaches [36-41]). Some models are also reported describing the fast argon atoms [13, 42-47] or the argon (or other gas) metastable atoms [48-53] in the glow discharge. Modeling of the behavior of sputtered cathode atoms and ions, which is of analytical importance, is however less frequently encountered in the literature. The thermalization process of the sputtered atoms has been described only with a simplified analytical model [54-56], but not yet with a Monte Carlo simulation. Sputtered atom density profiles have been calculated with a simple diffusion equation [54-60]. However, only a few papers, describing glow discharges used as metal-vapor hollow cathode lasers, also treat the ions of the cathode material, in a

fluid model [61-63]. To our knowledge, a Monte Carlo simulation of the behavior of these ions has not yet been carried out before.

The models we have developed are partly based on the ones found in the plasma physics literature. However, they had to be modified, when applied to glow discharges used for analytical purposes: other processes come into play and interest goes to other species and other processes in the plasma. Moreover, the modeling work is completely carried out in three dimensions. Finally, to our knowledge, it is the first time that all the models for the different plasma species were combined into a comprehensive modeling network, to obtain an overall picture of the glow discharge.

The models are applied to the discharge geometry of a standard cell of the VG9000 glow discharge mass spectrometer (VG Elemental, Fisons) for analyzing flat samples [64] (see figure 2.1). It is however assumed that the glow discharge is in a closed configuration, without argon gas inlet and without exit slit to the mass spectrometer. This means that there is no gas flow and that the argon gas is more or less at rest, uniformly distributed throughout the cell. The discharge gas (argon) is assumed to be without impurities. The cell walls are made of tantalum and the cathode exists of pure copper. Since the glow discharge cell is cylindrically symmetrical, the three-dimensional geometry can be reduced to two dimensions for the fluid models. The explicit treatment of the particles in the Monte Carlo models is however carried out in three dimensions.

In the following, a description is given of the submodels and of the way they are combined. The results of the models are presented and compared with available literature data and with experimental observations. Moreover, the results of the three-dimensional models are compared with results of one-dimensional models. Finally, the modeling work is used to explain variations in RSFs in GDMS.

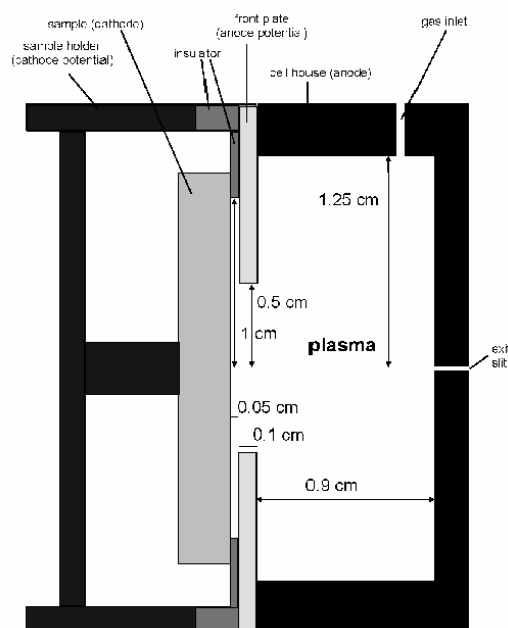


Figure 2.1: Schematic representation of the glow discharge cell to which the models are applied.

2.2. DESCRIPTION OF THE MODELS

2.2.1. Monte Carlo model for the fast electrons

The electrons start at the cathode created by ion induced secondary electron emission. The flux of electrons starting at the cathode is determined from the argon ion flux in the argon ion-slow electron fluid model (see below). Secondary electron emission at the cathode is assumed to be only due to ion bombardment, since atom bombardment causes very little secondary electron emission in the energy range considered here [65]. The electrons emitted by the cathode are characterized by an energy distribution between 0 and 6 eV with a maximum of 4 eV [65]. The electron energy distribution is approximated here by a single value of 4 eV. This choice is justified because it has no influence on the final results, the reason being the rapid acceleration of the electrons in the cathode dark space (CDS). The initial axial position is zero, and the initial radial position is determined from the radial distribution of the argon ion flux bombarding the cathode. The angular distribution is assumed to be isotropic in the forward direction [16].

The electrons are followed one after the other throughout the whole three-dimensional discharge. During successive time steps (Δt), the trajectory is calculated by Newton's laws:

$$z = z_0 + v_{z_0} \Delta t + \frac{qE_{ax}}{2m} (\Delta t)^2$$

$$x = x_0 + v_{x_0} \Delta t + \frac{qE_{rad} \cos(\alpha)}{2m} (\Delta t)^2$$

$$y = y_0 + v_{y_0} \Delta t + \frac{qE_{rad} \sin(\alpha)}{2m} (\Delta t)^2$$

$$v_z = v_{z_0} + \frac{qE_{ax}}{m} \Delta t$$

$$v_x = v_{x_0} + \frac{qE_{rad} \cos(\alpha)}{m} \Delta t$$

$$v_y = v_{y_0} + \frac{qE_{rad} \sin(\alpha)}{m} \Delta t$$

where z_0 , x_0 , y_0 and z , x , y are the position coordinates before and after Δt , v_{z_0} , v_{x_0} , v_{y_0} and v_z , v_x , v_y are the velocities before and after Δt , E_{ax} and E_{rad} are the axial and radial electric field (obtained from the argon ion-slow electron fluid model, see below), α is the azimuthal angle of the radial position (i.e. the angle of the radial position coordinates with respect to the x-axis), and q and m are the electron charge

and mass, respectively. The probability of collision during that time step is calculated by:

$$\text{Prob}_{\text{coll}} = 1 - \exp(-\Delta s \Sigma(n\sigma_{\text{coll}}(E)))$$

where Δs is the distance travelled during Δt ; n and $\sigma_{\text{coll}}(E)$ are the densities of the target particles and the cross sections of the different collision types of the electron with energy E . This equation is only valid when Δs is small enough so that the densities of the target particles and the electron energy (and hence $\sigma_{\text{coll}}(E)$) can be regarded constant over this distance.

A random number between 0 and 1 is generated with a subroutine program, described in ref. [66], and compared with the calculated probability of collision. If the probability is lower than the random number, no collision occurs and the electron is followed during the next time step. If the probability is higher, a collision takes place. Collision processes incorporated in the model, are total electron impact excitation from the argon atom ground state and from the argon metastable level, electron impact ionization of argon (from the ground state and from the metastable level) and of sputtered copper atoms, and elastic collisions with argon ground state atoms. Electron impact excitation of sputtered copper atoms is not incorporated, since the cross section of this process could not be found in the literature. Elastic collisions with other plasma species can be neglected, since the argon ground state atom densities are much higher than the densities of other plasma species. The cross sections of all these processes as a function of the electron energy are obtained from refs. [14, 67-73] and are represented in figure 2.2.

To determine which collision takes place, the fractional probabilities of all the collisions are computed:

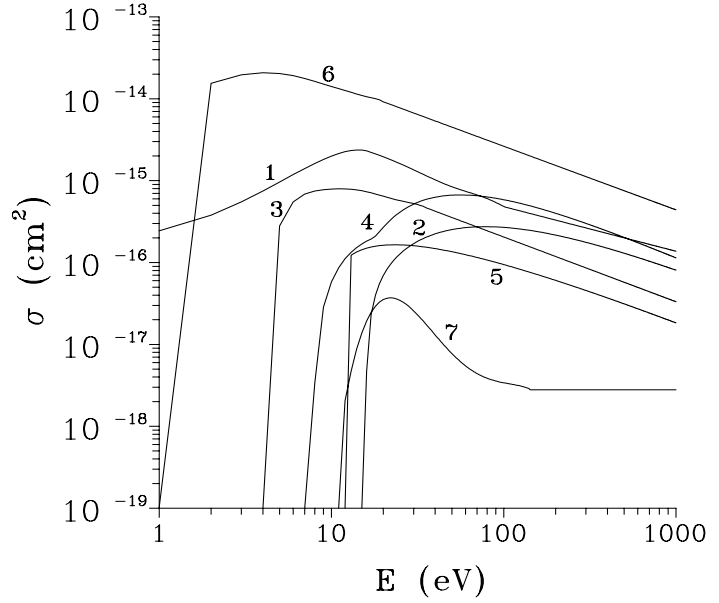
$$[n\sigma]_{\text{tot}} = n_{\text{Ar}}\sigma_{\text{exc,Ar}} + n_{\text{Ar}}\sigma_{\text{ion,Ar}} + n_{\text{Ar,met}}\sigma_{\text{exc,met}} + n_{\text{Ar,met}}\sigma_{\text{ion,met}} + n_{\text{Cu}}\sigma_{\text{ion,Cu}} + n_{\text{Ar}}\sigma_{\text{ela,Ar}}$$

$$P_{\text{exc,Ar}} = \frac{n_{\text{Ar}}\sigma_{\text{exc,Ar}}}{[n\sigma]_{\text{tot}}}, P_{\text{ion,Ar}} = \frac{n_{\text{Ar}}\sigma_{\text{ion,Ar}}}{[n\sigma]_{\text{tot}}}, P_{\text{exc,met}} = \frac{n_{\text{Ar,met}}\sigma_{\text{exc,met}}}{[n\sigma]_{\text{tot}}}, P_{\text{ion,met}} = \frac{n_{\text{Ar,met}}\sigma_{\text{ion,met}}}{[n\sigma]_{\text{tot}}},$$

$$P_{\text{ion,Cu}} = \frac{n_{\text{Cu}}\sigma_{\text{ion,Cu}}}{[n\sigma]_{\text{tot}}}, P_{\text{ela,Ar}} = \frac{n_{\text{Ar}}\sigma_{\text{ela,Ar}}}{[n\sigma]_{\text{tot}}}$$

The sum of the fractional probabilities is equal to unity, and the interval [0,1] is divided into segments with lengths corresponding to these fractional probabilities. A new random number between 0 and 1 is generated, and the interval into which this random number falls, determines the type of collision that occurs.

Figure 2.2: Cross sections of the electron collision processes incorporated in the model, as a function of the electron energy; (1) elastic collisions [67, 68]; (2) electron impact ionization of argon ground state atoms [14]; (3) electron impact ionization of the argon metastable levels [71]; (4) electron impact ionization of copper ground state atoms [73]; (5) total electron impact excitation of argon ground state atoms [69]; (6) total electron impact excitation from the argon metastable levels [72]; (7) electron impact excitation of the argon ground state level to the metastable levels [70].



The new energy and direction after the collision depend on the type of collision:

(i) **Excitation:** The new energy E is given by [16]:

$$E = E_0 - E_{\text{exc}}$$

where E_{exc} is the excitation threshold energy (i.e. taken as 12 eV for excitation from the argon ground state, and 1.8 eV for excitation from the argon metastable level), and E_0 is the electron energy before collision.

(ii) **Ionization:** The total energy before collision is divided between the primary (original) electron and the secondary electron created in the ionization collision, using a random number (RN). The energy of the **primary electron** (E_{prim}) after the collision is defined by [16]:

$$\text{RN} = \frac{\int_0^{E_{\text{prim}}} \sigma_{\text{ion,diff}}(E_0, \varepsilon) d\varepsilon}{\sigma_{\text{ion}}(E_0)}$$

where $\sigma_{\text{ion,diff}}(E_0, \varepsilon)$ and $\sigma_{\text{ion}}(E_0)$ are the differential ionization cross section to create a primary electron with energy ε and the total ionization cross section, respectively, E_0 is the energy before collision and ε is the energy of the primary electron after collision. The differential ionization cross section for ionization of ground state argon atoms is also adopted from ref. [14].

For the ionization of metastable argon atoms and of copper atoms, no differential ionization cross section could be found, and the energy of the primary electron is therefore computed by [15]:

$$E_{\text{prim}} = (E - E_{\text{ion}}) \text{RN}$$

The energy of the secondary electrons after the collision is in all cases given by [16]:

$$E_{\text{sec}} = E_0 - E_{\text{ion}} - E_{\text{prim}}$$

where E_{ion} is the ionization threshold energy (i.e. 15.76 eV for ionization from argon ground state atoms, 4.8 eV for ionization from argon metastable levels, and 7.7 eV for ionization of copper atoms), and the other symbols have been explained before.

(iii) Elastic collision: The kinetic energy of an electron which has undergone an elastic collision with an argon atom is calculated by [74]:

$$E = E_0 \left[1 - 2 \frac{m_e}{m_{\text{Ar}}} (1 - \cos \chi) \right]$$

which is deduced from the hard-sphere model. χ is the scattering angle of the electron after collision (see below).

The new direction after each kind of collision is determined by anisotropic scattering [27]. The scattering angle χ and the azimuthal angle of scattering ψ are defined by two random numbers [27]:

$$\text{RN} = \frac{2\pi}{\sigma(E_0)} \int_0^\chi \sigma(E_0, \chi') \sin \chi' d\chi'$$

$$\psi = 2\pi \text{RN}$$

where $\sigma(E_0)$ is the total cross section of a particular collision and $\sigma(E_0, \chi)$ is the angular differential cross section, adopted from ref. [27]. Substituting the analytical expression of $\sigma(E_0, \chi)/\sigma(E_0)$ [27] into the integral, and solving it analytically, yields:

$$\chi = 2 \arcsin \sqrt{\frac{\exp[\text{RN} \ln(1 + E_0)] - 1}{E_0}}$$

The new three-dimensional direction after collision (defined by the axial and azimuthal angles θ and ϕ) can now be calculated from the axial and azimuthal

angles of scattering, χ and ψ , and from the axial and azimuthal angles before collision, θ_0 and ϕ_0 , by transformation of the coordinate frame of reference (see figure 2.3):

$$\begin{pmatrix} \sin(\theta) \cos(\varphi) \\ \sin(\theta) \sin(\varphi) \\ \cos(\theta) \end{pmatrix} = \begin{pmatrix} \cos(\theta_0) \cos(\varphi_0) & -\sin(\varphi_0) & \sin(\theta_0) \cos(\varphi_0) \\ \cos(\theta_0) \sin(\varphi_0) & \cos(\varphi_0) & \sin(\theta_0) \sin(\varphi_0) \\ -\sin(\theta_0) & 0 & \cos(\theta_0) \end{pmatrix} \times \begin{pmatrix} \sin(\chi) \cos(\psi) \\ \sin(\chi) \sin(\psi) \\ \cos(\chi) \end{pmatrix}$$

When the new energy and three-dimensional direction after collision are calculated, the electron trajectory during the next time step is again calculated by Newton's laws, etc. This procedure is repeated until the electrons collide at the walls or until they reach energies lower than the lowest threshold of inelastic collisions (i.e. 1.8 eV; excitation from the argon metastable level). Indeed, when the electrons in the negative glow (NG) have energies lower than this threshold, they are transferred to the slow electron group (described in the argon ion-slow electron fluid model, see below), because they cannot produce inelastic collisions anymore and are therefore no longer important as "fast electrons". Their only role is to carry electrical current and to provide negative charge density. In the CDS, such a transfer is not included, since slow electrons do not remain slow due to rapid acceleration and are therefore not assumed to be created.

When the electrons collide at the walls of the cell (made of tantalum), they can be absorbed, reflected or cause secondary electron emission. The secondary electron emission coefficient for tantalum, δ , as a function of the electron energy, is taken from ref. [75] and is rather high (maximum 1.3 at 600 eV), which means that electrons cause easily the emission of a secondary electron. When δ is higher than 1, at least one secondary electron is emitted. The calculated value of δ (if $\delta < 1$) or of $\delta-1$ (if $\delta > 1$) is compared with a random number (RN) between 0 and 1. If δ (or $\delta-1$) $<$ RN, no secondary electron emission takes place and the electron is

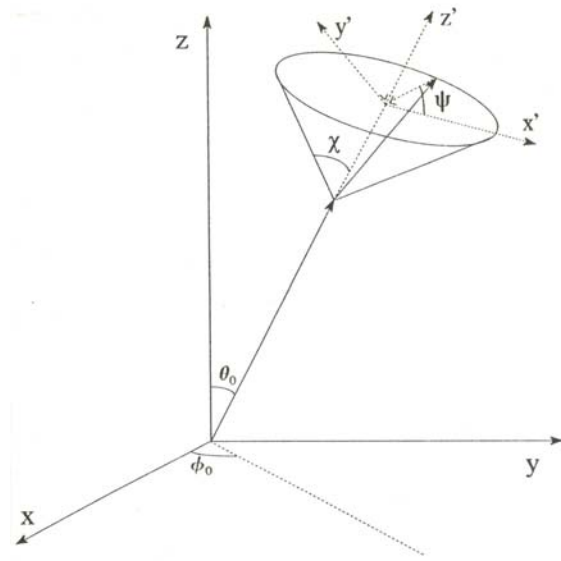


Figure 2.3: Definition of the two frames of reference and the different angles in the three-dimensional system: xyz : laboratory frame of reference; $x'y'z'$: particle scattering frame of reference; θ_0 and ϕ_0 : axial and azimuthal angles of the particle before scattering; χ and ψ : scattering angle and azimuthal angle of scattering.

When the electrons collide at the walls of the cell (made of tantalum), they can be absorbed, reflected or cause secondary electron emission. The secondary electron emission coefficient for tantalum, δ , as a function of the electron energy, is taken from ref. [75] and is rather high (maximum 1.3 at 600 eV), which means that electrons cause easily the emission of a secondary electron. When δ is higher than 1, at least one secondary electron is emitted. The calculated value of δ (if $\delta < 1$) or of $\delta-1$ (if $\delta > 1$) is compared with a random number (RN) between 0 and 1. If δ (or $\delta-1$) $<$ RN, no secondary electron emission takes place and the electron is

simply absorbed by the walls. If δ (or $\delta-1$) $>$ RN, secondary electron emission has taken place. It is assumed that about 10% of the electrons are emitted as primary electrons (i.e. they are just reflected with no change in energy and in a direction symmetrical to the normal of the wall), whereas the remaining 90% are emitted as secondary electrons, with energies of 4 eV and in a direction randomly chosen with respect to the normal of the wall [76].

When the electron has disappeared (by transfer to the slow electron group or by absorption at the cell walls), the secondary electrons created from this “primary” electron (by ionization collisions or by secondary electron emission at the cell walls) are treated in the same way. Moreover, besides the primary electrons starting at the cathode, and the secondary electrons created by electron impact ionization, new electrons are also formed in the CDS by fast argon ion and atom impact ionization (see below), and their trajectory and collision processes are also calculated by this Monte Carlo model. A large number of electrons (e.g. 10^4 - 10^5) have to be followed in this way, to reach statistically valid results.

2.2.2. Fluid model for the argon ions and slow electrons

The electrons which are transferred to the slow electron group are treated together with the argon ions in a fluid model. The motion of the argon ions and slow electrons is assumed to be collisionally dominated and described by diffusion and by migration in the electric field. The relevant equations are the continuity equations of argon ions and electrons, the flux equations based on diffusion and migration for the argon ions and slow electrons, and the Poisson equation to obtain a self-consistent electric field distribution:

$$\frac{\partial n_{Ar^+}(z,r)}{\partial t} + \nabla \cdot \overline{j_{Ar^+}}(z,r) = R_{Ar^+}(z,r)$$

$$\frac{\partial n_{e,slow}(z,r)}{\partial t} + \nabla \cdot \overline{j_{e,slow}}(z,r) = R_{e,slow}(z,r)$$

$$\overline{j_{Ar^+}}(z,r) = -\mu_{Ar^+} n_{Ar^+}(z,r) \nabla V(z,r) - D_{Ar^+} \nabla n_{Ar^+}(z,r)$$

$$\overline{j_{e,slow}}(z,r) = \mu_{e,slow} n_{e,slow}(z,r) \nabla V(z,r) - D_{e,slow} \nabla n_{e,slow}(z,r)$$

$$\nabla^2 V(z,r) + \frac{e}{\epsilon_0} (n_{Ar^+}(z,r) - n_{e,slow}(z,r) - n_{e,fast}(z,r)) = 0$$

where n_{Ar^+} and $n_{e,slow}$ are the argon ion and slow electron densities, $\overline{j_{Ar^+}}$ and $\overline{j_{e,slow}}$ are the corresponding fluxes, V is the electrical potential, $n_{e,fast}$ is the fast electron

density which is taken from the fast electron Monte Carlo model (see above), and R_{Ar^+} and $R_{e,slow}$ are the creation rates of argon ions and slow electrons, which result also from the Monte Carlo model. Finally, D_{Ar^+} , $D_{e,slow}$, μ_{Ar^+} and $\mu_{e,slow}$ are the argon ion and slow electron diffusion coefficients and mobilities, respectively. Their numerical values are assumed to be [27]: $D_{Ar^+} = 100 \text{ cm}^2\text{s}^{-1}$, $D_{e,slow} = 2 \times 10^5 \text{ cm}^2 \text{ s}^{-1}$, $\mu_{e,slow} = 2 \times 10^5 \text{ cm}^2 \text{ s}^{-1} \text{ V}^{-1}$, at 1 Torr and 298 K. μ_{Ar^+} is given by the Frost formula [77]:

$$\mu_{Ar^+} = \frac{\mu_{i,0}}{\sqrt{1 + a|E/n|}}$$

where a is $7.36 \times 10^{14} \text{ cm}^{-2} \text{ V}^{-1}$, $\mu_{i,0}$ is $1420 \text{ cm}^2 \text{ s}^{-1} \text{ V}^{-1}$ at 1 Torr and 298 K, E is the electric field and n is the argon gas atom density.

The five equations can be reduced to three equations by inserting the third and fourth equations in the first and second ones, respectively. Boundary conditions of these equations are taken as: $V = -V_c$ at the cathode wall (where V_c is the applied discharge voltage) and $V = 0$ at the other cell walls (= anode); $n_e = 0$ at all walls; $\nabla n_i = 0$ at all walls [2]. Due to the severe nonlinearity and strong coupling of the equations, solving this model is a difficult numerical problem. The method we used was developed by Goedheer and coworkers [1, 2]. It is a fully implicit method, based on the Scharfetter-Gummel exponential scheme for the transport equations [1-4, 78, 79]. The advantage of this scheme is its ability to switch between situations where either the migration component or the diffusion component of the particle flux is dominant (i.e. high and low electric field, CDS and NG, respectively). The basic idea is that the particle flux is assumed constant between mesh points, instead of the densities. Even with this method, the time step has to be small enough (typical 10^{-10} - 10^{-9} s) to avoid instabilities. More details about the solution method can be found in refs. [1, 2, 80].

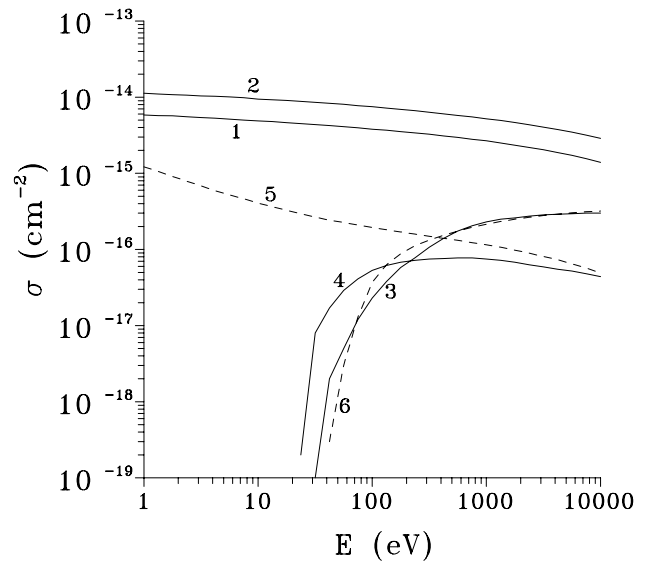
2.2.3. Monte Carlo model for the argon ions and fast argon atoms in the cathode dark space (CDS)

Since the argon ions are not completely in equilibrium with the strong electric field present in the CDS, they are described in this region with a Monte Carlo model, together with the fast argon atoms which are created from the argon ions by symmetric charge transfer and elastic collisions (see below). This Monte Carlo simulation can be carried out independently from the fast electron Monte Carlo model. Indeed, electron-ion collisions are not taken into account due to the relatively low density of both species, compared to the argon gas atom density, and hence the

motion of ions and electrons can be assumed to be independent from each other [29].

The flux of argon ions starting at the interface between CDS and NG is obtained from the above argon ion-slow electron fluid model. The argon ions can however also start within the CDS, when they are created by electron impact ionization. The flux of these ions is determined from the fast electron Monte Carlo model (i.e. by the electron impact ionization rates). Moreover, the argon ions can also be formed in the CDS by fast argon ion and atom impact ionization, calculated in this model (see below). All the argon ions are followed, one after the other, throughout the entire CDS. Their trajectory is also calculated by Newton's laws (see above) and the occurrence of a collision and the kind of collision are also determined by random numbers, similar to the electron Monte Carlo model. Collision processes taken into account are symmetric charge transfer, elastic collisions and ion impact ionization and excitation. The cross sections of these processes as a function of the argon ion energy are adapted from refs. [81, 82] and are presented in figure 2.4 (solid lines).

Figure 2.4: Cross sections of the argon ion and fast argon atom collision processes incorporated in the model, as a function of the ion and atom energy. Solid lines: argon ion collisions: (1) symmetric charge transfer [81]; (2) elastic collisions [81]; (3) fast argon ion impact ionization of argon ground state atoms [82]; (4) fast argon ion impact excitation of the argon ground state to the metastable levels [82]. Dashed lines: fast argon atom collisions: (5) elastic collisions [81]; (6) fast argon atom impact ionization of argon ground state atoms, and fast argon atom impact excitation of the argon ground state to the metastable levels [82].



It should be mentioned that argon ion impact excitation (and also argon atom excitation, see below) are not so well described in the literature. The cross sections that we have found correspond only to excitation to the argon metastable levels. Moreover, it was stated [83] that these cross sections are subject to large uncertainties and that they must be considered as upper limits. These cross section values have actually no effect on the argon ion (and atom) behavior. However, they are quite significant for the calculation of the argon metastable atom density (see below). Assuming that the mechanisms of electron impact excitation and argon ion and atom impact excitation to the metastable level are similar, it is expected that

their cross sections are also of equal magnitude. Therefore, we have lowered the cross sections of argon ion and atom impact excitation to the metastable level by a factor of 2, so that the maxima are more or less equal to the maximum in the cross section of electron impact excitation to the metastable level.

The new energy and direction after collision depend upon the type of collision:

(i) Symmetric charge transfer: When a fast argon ion collides with a slow argon atom, an electron is transferred from the atom to the ion without any change in kinetic energy of the species, and hence a fast argon atom and a slow argon ion arise. The fast argon atom takes the energy and direction of the ion before collision and the new argon ion starts at rest, so its energy after collision is 0 eV and its new direction is taken parallel to the electric field.

(ii) Elastic collision: Since data for the differential angular cross section are not generally available in the literature, the angular distribution can be approximated as isotropic in center-of-mass [83]:

$$\frac{\sigma(E_0, \chi)}{\sigma(E_0)} = \frac{1}{4\pi}$$

The same formula as for the electrons, based on a random number, can be used to find the scattering angle in the center-of-mass, χ_{COM} :

$$\text{RN} = \frac{2\pi}{\sigma(E_0)} \int_0^{\chi_{\text{COM}}} \sigma(E_0, \chi') \sin \chi' d\chi'$$

Substituting the value of $\sigma(E_0, \chi)/\sigma(E_0)$ into the integral, and solving it analytically, yields:

$$\chi_{\text{COM}} = \arccos(1 - 2 \text{RN})$$

Conversion of χ_{COM} to the scattering angles of the ion and atom after collision in the laboratory frame of reference, $\chi_{\text{lab,ion}}$ and $\chi_{\text{lab,atom}}$, is carried out in the following way [74]:

$$\tan(\chi_{\text{lab,ion}}) = \frac{\sin(\chi_{\text{COM}})}{\frac{m_{\text{ion}}}{m_{\text{atom}}} + \cos(\chi_{\text{COM}})} \Rightarrow \chi_{\text{lab,ion}} = \frac{\chi_{\text{COM}}}{2}$$

$$\chi_{\text{lab,atom}} = \frac{1}{2}(\pi - \chi_{\text{COM}})$$

The azimuthal angles of scattering of ion and atom are both defined by random numbers: $\psi_{\text{ion}} = 2\pi\text{RN}$, $\psi_{\text{atom}} = 2\pi\text{RN}$.

The new three-dimensional direction after collision for both the ion and the atom (i.e. the new axial and azimuthal angles θ and φ) can now be defined from the axial and azimuthal angles of scattering, χ and ψ , and from the axial and azimuthal angles before collision, θ_0 and φ_0 , in the same way as for the electrons (see figure 2.3):

$$\begin{pmatrix} \sin(\theta) \cos(\varphi) \\ \sin(\theta) \sin(\varphi) \\ \cos(\theta) \end{pmatrix} = \begin{pmatrix} \cos(\theta_0) \cos(\varphi_0) & -\sin(\varphi_0) & \sin(\theta_0) \cos(\varphi_0) \\ \cos(\theta_0) \sin(\varphi_0) & \cos(\varphi_0) & \sin(\theta_0) \sin(\varphi_0) \\ -\sin(\theta_0) & 0 & \cos(\theta_0) \end{pmatrix} \times \begin{pmatrix} \sin(\chi) \cos(\psi) \\ \sin(\chi) \sin(\psi) \\ \cos(\chi) \end{pmatrix}$$

The new energy of the ion after collision, E_{ion} can be found by [74]:

$$E_{\text{ion}} = E_0 \left[1 - \frac{4\mu^2}{m_{\text{ion}} m_{\text{atom}}} \cos^2(\chi_{\text{lab,atom}}) \right] = E_0 \left[1 - \cos^2(\chi_{\text{lab,atom}}) \right]$$

where E_0 is the energy of the ion before collision and μ is the reduced mass of the collision partners. The energy of the atom after collision, E_{atom} , is defined by the law of conservation of energy:

$$E_{\text{atom}} = E_0 - E_{\text{ion}}$$

(iii) Ion impact ionization: It is assumed that the energy before collision is equally divided between the primary (original) ion and the ion created in the ionization collision. Since this process is much less important than charge transfer in determining the energy, the assumption is not at all critical since it has no noticeable effect on the energy of the ions. The angular distribution is approximated by delta functions in the forward direction, i.e. no scattering so that the three-dimensional direction remains unchanged [83]. After this ionization collision, not only the original ion is followed, but also the argon ion that has been created in the collision.

(iv) Ion impact excitation: The energy after collision is given by: $E = E_0 - E_{exc}$, where E_{exc} is the excitation threshold. The three-dimensional direction remains also the same as before the collision [83].

After the collision, the argon ion is followed during the next time step, and so on, until it collides at the walls where it will be neutralized and hence disappears from the plasma.

In the symmetric charge transfer and elastic collisions of the argon ions, fast argon atoms are created. The determination of the energy and three-dimensional direction of these argon atoms is discussed above. The argon atoms are also followed throughout the CDS. Their trajectory is also defined by Newton's laws (given above), but since they are neutral, they do not feel the influence of an electric field. The occurrence of a collision and the kind of collision are determined in a similar way as for the electrons (see above). Collision processes incorporated for the fast argon atoms, are elastic collisions, atom impact ionization and excitation. The cross sections as a function of the atom energy are adapted from refs. [81, 82] and are illustrated in figure 2.4 (dashed lines). The new energy and three-dimensional direction after the collisions are defined in the same way as for the argon ions (see above). Then the argon atoms are followed during the next time step, etc.

When the atoms collide at the walls of the cell, they can be implanted or reflected. It is assumed that 90% is implanted whereas the remaining part is reflected. When they are implanted, they disappear from the plasma. When they are reflected, their new three-dimensional direction is assumed symmetrical to the old direction with respect to the normal of the wall. Their new energies are calculated as for a collision between two elastic impenetrable spheres [74]:

$$E = E_0 \left[1 - \frac{2m_{atom}m_{wall}}{(m_{atom} + m_{wall})^2} \right]$$

The assumptions about the probability of reflection and implantation and about the new energy and direction after reflection are not critical, since they were found to have no influence on the results. The argon atoms are followed on their way until they are implanted in the walls or until they reach energies lower than a certain threshold (taken as 1 eV). Indeed, it takes a long time to simulate atoms with lower energies in a Monte Carlo model, and since they are not important anymore as fast atoms (they cannot produce cathode sputtering or ionization and excitation anymore), they are put in the large "slow" argon atom group, where they are considered at rest.

2.2.4. Fluid model for the argon metastable atoms

Argon atoms possess two metastable levels, lying closely to each other, i.e. the $(3p^54s) \ ^3P_2$ level and the $(3p^54s) \ ^3P_0$ level, at 11.55 and 11.72 eV above the ground state, respectively. The 3P_0 level is stated to be populated by a fraction of only 10-20 % of the 3P_2 level [84, 85]. Since for our purpose, only the total metastable density is important, the two metastable levels were combined in one collective level lying at 11.55 eV. Two other levels are situated close to the metastable levels, which can decay to the ground state by emission of radiation, i.e. the $(3p^54s) \ ^3P_1$ level and the $(3p^54s) \ ^1P_1$ level, at 11.62 and 11.83 eV above the ground state, respectively.

Since the argon metastable atoms are neutral and since they are considered thermalized, they can be treated with a fluid model. The model exists of a balance equation taking into account all the different production and loss processes that could be found in the literature. The production processes include (i) fast electron, (ii) fast argon ion and (iii) fast argon atom impact excitation from ground state argon atoms, and (iv) radiative recombination between Ar^+ ions and slow electrons. Dissociative recombination between Ar_2^+ and electrons is neglected, since Ar_2^+ ions are not assumed to be present in the plasma.

The loss processes comprise (i) fast electron impact ionization from the metastable level, (ii) fast electron impact excitation from the metastable level to higher energy levels, (iii) transfer to the nearby 3P_1 and 1P_1 levels by collision with thermalized electrons, which is called electron quenching, (iv) metastable-metastable collisions resulting in the ionization of one of the metastable atoms, (v) Penning ionization of sputtered cathode (copper) atoms, (vi) two-body collisions with ground state argon atoms (i.e. collisional transfer from the metastable levels to the nearby 3P_1 and 1P_1 levels, and collision induced emission), and (vii) three-body collisions with ground state argon atoms, resulting in the formation of Ar_2^* . An additional loss process is diffusion to the walls, followed by deexcitation at the walls. It is assumed that the gas is pure argon, so that destruction of argon metastable atoms due to reactions with impurity gas molecules (quenching) is neglected. These production and loss processes result in the balance equation:

$$\frac{\partial n_{Ar,met}(z,r)}{\partial t} - D_{Ar,met} \frac{1}{r} \frac{\partial}{\partial r} \left(r \frac{\partial n_{Ar,met}(z,r)}{\partial r} \right) - D_{Ar,met} \frac{\partial^2 n_{Ar,met}(z,r)}{\partial z^2} = R_{prod}(z,r) - R_{loss}(z,r)$$

The first term on the left-hand side is the time-dependent variation, which becomes zero at steady state. The second and third term relate to diffusion in the radial and axial directions, respectively. The diffusion coefficient, $D_{Ar,met}$, is taken to be

54 cm² s⁻¹ at 1 Torr [86]. The first term on the right-hand side includes the production processes whereas the second term comprises all the loss processes:

$$\begin{aligned}
 R_{\text{prod}}(z,r) &= R_{\text{e,exc}}(z,r) + R_{\text{i,exc}}(z,r) + R_{\text{a,exc}}(z,r) + k_{\text{recom}} n_{\text{e,slow}}(z,r) n_{\text{Ar}^+}(z,r) \\
 R_{\text{loss}}(z,r) &= R_{\text{ion,met}}(z,r) + R_{\text{exc,met}}(z,r) + k_{\text{quen}} n_{\text{e,slow}}(z,r) n_{\text{Ar,met}}(z,r) + 2k_{\text{met}} [n_{\text{Ar,met}}(z,r)]^2 \\
 &+ k_{\text{PI}} n_{\text{Cu}}(z,r) n_{\text{Ar,met}}(z,r) + k_{2\text{B}} n_{\text{Ar}}(z,r) n_{\text{Ar,met}}(z,r) + k_{3\text{B}} [n_{\text{Ar}}(z,r)]^2 n_{\text{Ar,met}}(z,r)
 \end{aligned}$$

$R_{\text{e,exc}}(z,r)$ is the electron impact excitation rate to the metastable level, which is calculated in the fast electron Monte Carlo model. The cross section of this process is taken from ref. [70] (see also figure 2.2). $R_{\text{i,exc}}(z,r)$ and $R_{\text{a,exc}}(z,r)$ are the argon ion and atom impact excitation rates, respectively, calculated in the argon ion and atom Monte Carlo simulation, with the relevant cross sections adopted from ref. [82] and presented in figure 2.4 (see above). k_{recom} is the rate constant of argon ion-electron radiative recombination, which is taken to be 10^{-11} cm³ s⁻¹ [87].

$R_{\text{ion,met}}(z,r)$ and $R_{\text{exc,met}}(z,r)$ are the electron impact ionization and excitation rates from the metastable level, respectively, calculated in the electron Monte Carlo model (see above) with the cross sections [71, 72] presented in figure 2.2. k_{quen} is the rate constant of electron quenching to the nearby ³P₁ and ¹P₁ levels, which is taken to be 2×10^{-7} cm³ s⁻¹ [53]. k_{met} represents the rate constant of metastable-metastable collisions, which is assumed to have a value of 6.4×10^{-10} cm³ s⁻¹ [48, 88]. The term describing the loss by metastable - metastable collisions contains a factor 2. Indeed, two metastable argon atoms are lost in one such collision process. k_{PI} is the rate constant of Penning ionization of the sputtered copper atoms. Reliable values for the cross sections of this process between argon metastable atoms and metals are very difficult to find. We used an empirical formula [89] which we fitted to some experimentally obtained cross sections [89, 90] in order to arrive at approximate values for other elements. The Penning ionization cross section of copper at thermal energies was in this way computed to be 4.9×10^{-15} cm² which corresponds to a k_{PI} of 2.36×10^{-10} cm³ s⁻¹. $k_{2\text{B}}$ and $k_{3\text{B}}$ are the rate constants of two-body and three-body collisions with argon ground state atoms, respectively. Their numerical values are taken from ref. [84], i.e. $k_{2\text{B}} = 2.3 \times 10^{-15}$ cm³ s⁻¹ and $k_{3\text{B}} = 1.4 \times 10^{-32}$ cm⁶ s⁻¹. $n_{\text{Ar,met}}$, $n_{\text{e,slow}}$, n_{Ar^+} , n_{Cu} and n_{Ar} represent the densities of argon metastable atoms, slow electrons, argon ions, sputtered copper atoms and argon ground atoms, resp.

The loss due to diffusion and subsequent deexcitation at the walls is determined by the boundary conditions, i.e. $n_{\text{Ar,met}} = 0$ at the walls. The balance equation (differential equation) is discretized to a finite difference equation and solved with the Thomas algorithm [91]. The time step used is typically 10^{-6} s.

2.2.5. Monte Carlo model for the thermalization of the sputtered copper atoms

The atoms of the cathode material (copper) are sputtered away from the cathode due to the bombardment by plasma species (i.e. argon ions, fast argon atoms and also copper ions, see below). They enter the plasma and lose their initial energies of a few eV almost immediately by elastic collisions with the argon gas particles, where after they diffuse further into the plasma or back towards the cathode. Since the thermalization is much faster than the diffusion, it can be assumed already finished when diffusion starts [55]. Both processes can therefore be separated in time when modeling the behavior of the sputtered atoms, i.e. the simulation of the thermalization process results in a thermalization profile, which is used afterwards as the starting distribution in the description of the diffusion process (see below).

The thermalization process of the sputtered copper atoms is simulated with a Monte Carlo model. The sputtered atoms leave the cathode with an energy and angular distribution given by [55]:

$$\Psi(E, \theta) = \frac{2UE \cos \theta}{(E + U)^3 \pi}$$

where U is the surface binding energy of the cathode material, mostly taken equal to the sublimation energy (i.e. 3.49 eV for copper [92]), and θ is the axial angle. Using two random numbers (RN) between 0 and 1, the specific angle and energy of a sputtered atom starting at the cathode are calculated from the above equation as:

$$RN_1 = \int_0^\infty dE' \int_0^\theta 2\pi \sin(\theta') \Psi(E, \theta') d\theta'$$

$$RN_2 = \int_0^E dE' \int_0^{\pi/2} 2\pi \sin(\theta') \Psi(E, \theta') d\theta'$$

which results in:

$$\theta = \frac{1}{2} \arccos(1 - 2RN_1)$$

$$E^2(RN_2 - 1) + E(2URN_2) + U^2 RN_2 = 0$$

where the positive root gives E .

The azimuthal angle, φ , is also determined by a random number between 0 and 1:

$$\varphi = 2\pi RN$$

The initial axial (z) coordinate is zero, the initial radial coordinates (x and y) are determined from the radial distribution of the fluxes of the bombarding particles. The trajectory of the sputtered atoms is calculated with Newton's laws, similar as in the electron Monte Carlo model, but since the sputtered copper atoms are neutral, they do not experience the force of the electric field.

Thermalization is caused by energy losses due to collisions. Only elastic collisions with the argon gas atoms are incorporated, because this process has the highest cross section and the density of the argon gas atoms is much higher than that of any other species in the plasma. The cross section of elastic collisions between atoms depends on the interaction potential assumed between these atoms. The screened Coulomb potential presents a realistic view of atomic interactions [93]. It is based on a simple Coulomb repulsion between the atoms at very small distances of separation, combined with a screening function to simulate the interaction between the atomic electrons, which makes itself felt at large separations:

$$V(r) = \frac{Z_1 Z_2 e^2}{r} g(r)$$

where Z_1 and Z_2 are the atomic numbers of the interacting atoms, r is the distance of separation and $g(r)$ is the screening function. The screened Coulomb potential used in this model is the Molier potential, with a screening function given by [93]:

$$g(r) = 0.35 e^{-0.3 \frac{r}{a_s}} + 0.55 e^{-1.2 \frac{r}{a_s}} + 0.1 e^{-6 \frac{r}{a_s}}$$

where a_s is the screening radius $(0.468 / (\sqrt{Z_1} + \sqrt{Z_2})^{0.668})$, in Å). Based on the interaction potential, Lindhard et al. derived the following differential cross section [94, 95]:

$$d\sigma = \pi a_s^2 \frac{dt}{2t^{3/2}} f(t)$$

where

$$t = \left(\frac{m_2 E}{(m_1 + m_2) Z_1 Z_2 e^2} \frac{a_s}{\gamma E} \right)^2$$

and E is the initial energy, T is the recoil energy, $0 \leq T \leq \gamma E$ (maximum recoil energy), $\gamma = 4m_1m_2/(m_1+m_2)^2$, m_1 and m_2 are the masses of the scattered particle and the recoiling particle, respectively, and Z_1 , Z_2 and a_s are explained above. $f(t)$ depends on the interaction potential. For a screened Coulomb potential:

$$f(t) = 1.309 t^{1/6} \left[1 + \left(2.618 t^{2/3} \right)^{2/3} \right]^{-3/2}$$

The total elastic cross section as a function of the sputtered particle's energy is determined by integrating Lindhard's differential cross section $d\sigma$ over all possible energy losses dT :

$$\sigma_{\text{ela}}(E) = \int_0^{\gamma E} d\sigma$$

Because the differential cross section $d\sigma$ for a screened Coulomb potential is rather complicated, its integration is facilitated by using the differential cross section for a power-law potential with varying the power 'n' as a function of the energy to approximate the screened Coulomb potential [96] (and see below):

$$\sigma_{\text{ela}}(E) = nC \gamma^{-1/n} E^{-2/n}$$

where

$$C = \frac{\pi}{2} \lambda_n a_s^2 \left(\frac{m_1}{m_2} \right)^{1/n} \left(\frac{2Z_1Z_2 e^2}{a_s} \right)^{2/n}$$

$$\gamma = \frac{4m_1m_2}{(m_1+m_2)^2}$$

$$n = 1 + 4 \exp(-1.9 \varepsilon^{0.1})$$

$$\varepsilon = \frac{m_2 E}{m_1 + m_2} \frac{a_s}{Z_1 Z_2 e^2}$$

and λ_0 is a constant depending on n .

Based on this elastic cross section, the probability of collision during a time step Δt is calculated and compared to a random number, in order to determine whether a collision takes place, in a manner similar to the electron Monte Carlo model. If a collision takes place, the new energy and three-dimensional direction have to be determined. Sielanko [96] has derived an analytical expression for the scattering angle in the center-of-mass frame of reference, χ_{COM} , using Lindhard's differential cross section for a power-law potential approximating the Molier potential

by choosing the parameters n and K_n as a function of the energy and the impact parameter:

$$\sin^2\left(\frac{\chi_{\text{COM}}}{2}\right) = \left(1 + \frac{p^2 \varepsilon^{2/n}}{(K_n^2 \beta_n^2)^{1/n}}\right)^{-n}$$

The complete description of this formula is found in ref. [96]. The impact parameter is calculated from the cross section using a random number between 0 and 1 [18]. The conversion of the scattering angle into the laboratory frame of reference, χ_{lab} , is achieved by [74]:

$$\tan(\chi_{\text{lab}}) = \frac{\sin(\chi_{\text{COM}})}{m_1/m_2 + \cos(\chi_{\text{COM}})}$$

where m_1 and m_2 are the masses of the sputtered and gas atoms, respectively. The azimuthal angle of scattering is determined by a random number:

$$\psi = 2\pi \cdot \text{RN}$$

The new energy E depends on the scattering angle and is given by [96]:

$$E = E_0 \left[1 - \sin^2\left(\frac{\chi_{\text{COM}}}{2}\right)\right]$$

where E_0 is the energy before collision.

The new direction in the three-dimensional space, determined by θ and φ , is obtained from θ_0 and φ_0 before collision and from the scattering angles χ and ψ , by transformation of the coordinate frame of reference, similar to the electron Monte Carlo model (see above). After the new energy and direction are determined, the atom is followed during the next time step, and the procedure is repeated.

When the atoms collide at the walls of the cell, they can be adsorbed or reflected. Little is known about reflection or sticking coefficients for atoms with low energies. We used a sticking coefficient of 0.5 since this yielded the best agreement between calculated and experimental sputtered atom density profiles (see below). In the case of adsorption, the atom disappears from the plasma. In the case of reflection, the atom is assumed to be reflected back without any change in kinetic energy and in a direction symmetrical with respect to the normal to the walls, as if pure elastic reflection has taken place. This assumption has no influence on the

results, because only a small part of the atoms has a chance to reach the walls before thermalization.

The atoms are followed until they are adsorbed at the walls or until they are thermalized (i.e. when their energies have become lower than 0.03 eV). By following in this way a large number of sputtered atoms, the thermalization profile can be obtained.

2.2.6. Fluid model for the sputtered copper atoms and ions

When the copper atoms have been thermalized, their further transport is diffusion dominated, i.e. starting from the initial distribution of thermalized particles (thermalization profile) they can diffuse further into the plasma or back towards the cathode. The sputtered copper atoms can also be ionized in the plasma, leading to the formation of copper ions. The three most important ionization mechanisms include Penning ionization by argon metastable atoms, asymmetric charge transfer by argon ions, and electron impact ionization. The transport of the copper ions created in this way is controlled by diffusion and by migration in the electric field. The loss of copper ions could be caused by electron-ion recombination. However, as is demonstrated in Chapter 1, this process can be considered negligible and is therefore omitted in the present model. The above described behavior of copper atoms and ions is expressed in the following equations:

$$\frac{\partial n_{\text{Cu}}(\mathbf{z}, r)}{\partial t} + \nabla \cdot \overline{\mathbf{j}}_{\text{Cu}}(\mathbf{z}, r) = R_{\text{prod,Cu}}(\mathbf{z}, r) - R_{\text{loss,Cu}}(\mathbf{z}, r)$$

$$\frac{\partial n_{\text{Cu}^+}(\mathbf{z}, r)}{\partial t} + \nabla \cdot \overline{\mathbf{j}}_{\text{Cu}^+}(\mathbf{z}, r) = R_{\text{prod,Cu}^+}(\mathbf{z}, r)$$

$$\overline{\mathbf{j}}_{\text{Cu}}(\mathbf{z}, r) = -D_{\text{Cu}} \nabla n_{\text{Cu}}(\mathbf{z}, r)$$

$$\overline{\mathbf{j}}_{\text{Cu}^+}(\mathbf{z}, r) = -D_{\text{Cu}^+} \nabla n_{\text{Cu}^+}(\mathbf{z}, r) - \mu_{\text{Cu}^+} n_{\text{Cu}^+}(\mathbf{z}, r) \nabla V(\mathbf{z}, r)$$

$$R_{\text{prod,Cu}}(\mathbf{z}, r) = J_0 F_T(\mathbf{z}, r)$$

$$R_{\text{loss,Cu}}(\mathbf{z}, r) = R_{\text{prod,Cu}^+}(\mathbf{z}, r) = n_{\text{Cu}}(\mathbf{z}, r) \left[R_{\text{e,ion}}(\mathbf{z}, r) + k_{\text{PI}} n_{\text{Ar,met}}(\mathbf{z}, r) + k_{\text{CT}} n_{\text{Ar}^+}(\mathbf{z}, r) \right]$$

The first and second equations present the continuity equations of copper atoms and ions, respectively. n_{Cu} and n_{Cu^+} are the densities of copper atoms and ions, and $\overline{\mathbf{j}}_{\text{Cu}}$ and $\overline{\mathbf{j}}_{\text{Cu}^+}$ are the respective fluxes (governed by diffusion for the atoms (third equation) and diffusion and migration controlled for the ions (fourth equation)). The diffusion coefficient of the copper atoms in argon (D_{Cu}) is calculated with a

formula of the rigid-sphere model for a mixture of two chemical species [97]. Since it can be assumed in a first approximation that diffusion is not determined by the charge of a particle, the diffusion coefficient of the copper ions (D_{Cu^+}) is taken to be equal to that of the copper atoms, i.e. $D_{Cu} = D_{Cu^+} = 144.6 \text{ cm}^2 \text{ s}^{-1}$ at 1 Torr argon and 298 K. The mobility of the copper ions (μ_{Cu^+}) is adopted from ref. [98] where a graph of the mobility as a function of the ion mass in argon, neon and helium was presented. It was taken to be $1837.4 \text{ cm}^2 \text{ s}^{-1} \text{ V}^{-1}$ at 1 Torr argon. $V(z,r)$ presents the potential distribution throughout the discharge, calculated in the argon ion-slow electron fluid model (see above).

The production rate of the copper atoms ($R_{\text{prod,Cu}}$; fifth equation) is given by the sputtered flux from the cathode (J_0) multiplied by the thermalization profile ($F_T(z,r)$). $F_T(z,r)$ is computed in the Monte Carlo model of the thermalization process (see above). J_0 is calculated from an empirical formula of the sputtering yield, adopted from ref. [92] (see also Chapter 1, Section 1.2.2.2), and the flux energy distributions of the particles bombarding the cathode (i.e. the argon ions and fast atoms, and also the copper ions (see below)):

$$J_0 = - \int_E \left\{ Y_{\text{Ar-Cu}}(E) [f_{\text{Ar}^+}(0,E) + f_{\text{Ar}}(0,E)] + Y_{\text{Cu-Cu}}(E) f_{\text{Cu}^+}(0,E) \right\} dE$$

where $Y_{\text{Ar-Cu}}(E)$ and $Y_{\text{Cu-Cu}}(E)$ present the sputter yields of bombarding argon particles and copper particles on a copper cathode, respectively, as a function of the bombarding particle energies [92]. $f_{\text{Ar}^+}(0,E)$, $f_{\text{Ar}}(0,E)$ and $f_{\text{Cu}^+}(0,E)$ are the flux energy distributions of argon ions, argon atoms and copper ions at the cathode, respectively. The (-)-sign indicates that the flux of sputtered copper atoms is in the opposite direction of the fluxes of the bombarding particles.

The loss rate of the copper atoms ($R_{\text{loss,Cu}}$) is equal to the production rate of copper ions ($R_{\text{prod,Cu}^+}$) and expresses the ionization of copper atoms by electron impact ionization, Penning ionization and asymmetric charge transfer (sixth equation). $R_{\text{e,ion}}$ is the electron impact ionization rate, calculated in the electron Monte Carlo model (see above) with the cross section of ref. [73] (see figure 2.2). $n_{\text{Ar,met}}$ and n_{Ar^+} are the densities of argon metastable atoms and argon ions, respectively. k_{PI} and k_{CT} are the rate coefficients of Penning ionization and asymmetric charge transfer, respectively. k_{PI} was taken equal to $2.36 \times 10^{-10} \text{ cm}^3 \text{ s}^{-1}$ (see above). Cross sections or rate constant values for asymmetric charge transfer between argon ions and transition metal atoms are very difficult to find in the literature (see also Chapter 1, Section 1.2.1.2). However, we found a value of k_{CT} between argon ions and copper atoms equal to $2 \times 10^{-10} \text{ cm}^3 \text{ s}^{-1}$ in ref. [63]. Since this rate constant was not directly measured, but was deduced from a fitting procedure in a mathematical model, it can be subject to large uncertainties. However, the fact that k_{CT} is in the same order of magnitude as k_{PI} is like expected when the ion

possesses suitable energy levels for asymmetric charge transfer [99, 100]. Therefore, and since we could not find more accurate data, we used this value in our model.

The continuity equations for the copper atoms and ions (first and second equations) are coupled to each other through $R_{\text{loss,Cu}} = R_{\text{prod,Cu}^+}$. The boundary conditions for this system are determined by the sticking coefficients of copper atoms and ions. For the copper ions, both the boundary conditions $n_{\text{Cu}^+} = 0$ (i.e. sticking coefficient $A_{\text{Cu}^+} = 1$) and $\nabla n_{\text{Cu}^+} = 0$ (i.e. sticking coefficient $A_{\text{Cu}^+} = 0$) at all walls resulted in exactly the same density profiles, which indicates that the boundary conditions have actually no influence for Cu^+ . This was also observed by van Veldhuizen et al. [61].

For the copper atoms, however, varying the boundary conditions between $n_{\text{Cu}} = 0$ (i.e. $A_{\text{Cu}} = 1$) and $\nabla n_{\text{Cu}} = 0$ (i.e. $A_{\text{Cu}} = 0$) yielded clearly different results for the atom density. We have measured three-dimensional density profiles of sputtered tantalum atoms in a six-way cross glow discharge with laser induced fluorescence [101]. These measured density profiles showed best agreement with the modeling calculations if a sticking coefficient of 0.5 was assumed. Therefore, we adopt this value of 0.5 also in the present model.

The coupled differential equations are discretized to finite difference equations [91] and the resulting bi-tridiagonal system is solved with the extended Thomas algorithm, described in the appendix of ref. [91]. A typical time step of 10^{-6} s was used.

2.2.7. Monte Carlo model for the copper ions in the cathode dark space

The copper ions are not in equilibrium with the strong electric field in the CDS. Therefore, they are not only treated with the above described fluid model, but also explicitly with a Monte Carlo model in the CDS. Input data for this model are the flux of copper ions entering the CDS from the NG, and the flux of copper ions created in the CDS. Both data are taken from the above described fluid model. Hence, the copper ions start their trajectory at the interface between CDS and NG, or at specific positions within the CDS, in the exact proportion determined by the fluid model. They are followed one after the other during successive time steps. Their trajectory is described by Newton's laws, similar to the electron Monte Carlo model (see above).

The only collision processes that are incorporated are elastic collisions with argon gas atoms. The numerical value of the cross section of this process is taken to be 10^{-16} cm², independent of the energy. This order of magnitude was deduced

from cross section curves found in ref [102]. Other values were also tested, and it was found that the results did not vary much so that the choice of this cross section value is not so critical. We took this value since the energy distribution of copper ions at the cathode calculated with this cross section, especially the peak height at maximum energy, showed good agreement with experimentally measured energy distributions of copper ions at the cathode [103] (see further). Other possible collisions of the copper ions are estimated to be negligible: asymmetric charge transfer with argon atoms would have a considerably lower cross section, and collisions with other plasma particles (copper atoms, argon ions, argon metastable atoms, electrons,...) are unimportant due to the much lower densities of these species compared to the argon atom density.

The occurrence of an elastic collision during a time step Δt is determined by a random number, similar to the electron Monte Carlo model. The new energy and direction after the elastic collision are determined with the same procedure as explained in the Monte Carlo model for the argon ions and fast atoms (see above), with the only difference being that the masses of the two colliding particles are not equal to each other. In these elastic collisions, fast argon atoms can be formed, which are also treated in a Monte Carlo model, exactly in the same way as in Section 2.2.3 (see above). The copper ions are followed until they collide at the walls, where they will be neutralized and disappear from the plasma.

2.2.8. Combination of the models

The different models are coupled to each other by the interaction processes between the different plasma species. The models are therefore solved together by an iterative procedure, in order to obtain an overall picture of the glow discharge. The flow chart of the coupling is presented in figure 2.5.

The procedure starts with the argon ion-slow electron fluid model, described in Section 2.2.2, assuming arbitrary argon ion and slow electron creation rates (R_{Ar^+} and $R_{e,slow}$). Results of this model are, among others, (i) the axial and radial electric field distributions throughout the discharge (E_{ax} and E_{rad}), (ii) the interface between CDS and NG for all radial positions ($d_c(r)$, defined as the position where the calculated potential goes through zero), (iii) the argon ion flux entering the CDS ($j_{Ar^+,d_c}(r)$), and (iv) the argon ion flux bombarding the cathode ($j_{Ar^+,0}(r)$), both as a function of the radial position.

This information is used in the Monte Carlo models. From the argon ion flux bombarding the cathode, the electron flux starting at the cathode as a function of the radial position is obtained: $j_{e,0}(r) = -\gamma j_{Ar^+,0}(r)$, where γ is the ion induced secondary electron emission coefficient (taken as 0.083 for argon bombardment on a copper

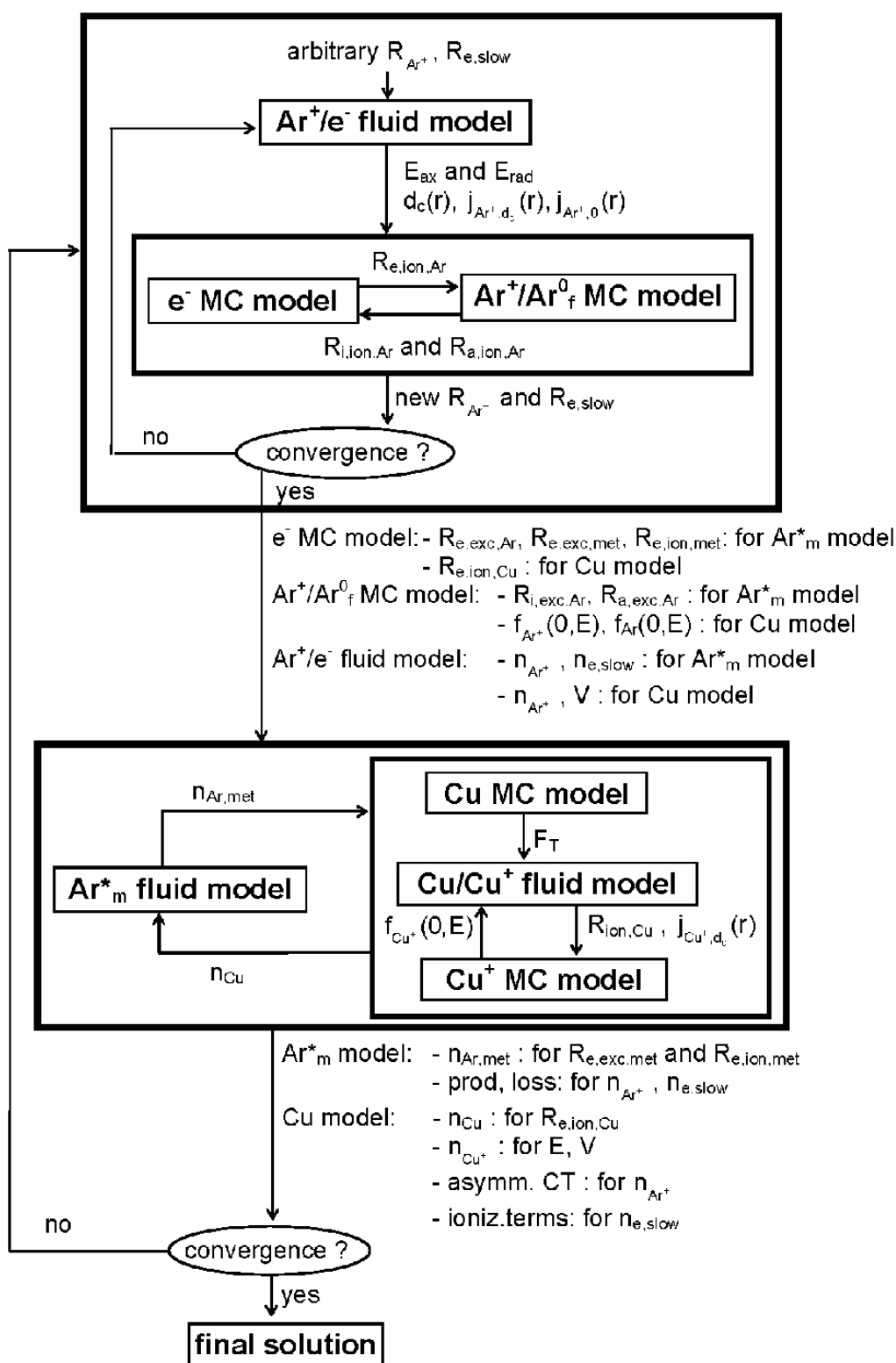


Figure 2.5: Flow chart of the combined models.

cathode [104]). The fast electron Monte Carlo model is calculated, as described in Section 2.2.1. This model yields, among others, the ionization rate of argon atoms (i.e. the creation rate of argon ions) by electron impact, as a function of axial and radial positions ($R_{e,ion,Ar}$).

This is used in the argon ion and fast atom Monte Carlo model (Section 2.2.3) as the number of argon ions created in the CDS. The argon ion flux starting at the interface between CDS and NG as a function of radial position is obtained from the argon ion-slow electron fluid model ($j_{Ar^+,dc}(r)$, see above). Outputs of the argon ion and fast atom Monte Carlo model are, among others, the argon ion and atom impact ionization rates (i.e. the creation rates of electrons, $R_{i,ion,Ar}$ and $R_{a,ion,Ar}$).

Next, the fast electron Monte Carlo model is calculated again, incorporating these electrons formed by argon ion and atom impact ionization. With the new creation rate of argon ions (i.e. by electron impact ionization) the argon ion and fast atom Monte Carlo model is again calculated. This is repeated until convergence is reached (i.e. when the argon ion flux bombarding the cathode, calculated in the argon ion and fast atom Monte Carlo model, does not change anymore). This is generally achieved after two or three iterations.

The creation rate of the slow electrons ($R_{e,slow}$), resulting from the electron Monte Carlo model, and the argon ion creation rates ($R_{Ar^+} = R_{e,ion,Ar} + R_{i,ion,Ar} + R_{a,ion,Ar}$), calculated in the electron and argon ion and fast atom Monte Carlo models, are used as inputs in the argon ion-slow electron fluid model. This yields new axial and radial electric field distributions, a new interface between CDS and NG, and new argon ion fluxes entering the CDS and bombarding the cathode. This information is again put into the Monte Carlo models. The whole procedure is repeated until final convergence is reached (i.e. generally after 5-10 iterations).

Results of the electron, argon ion and fast atom Monte Carlo models, and of the argon ion-slow electron fluid model, which are of importance from the argon metastable atom fluid model and for the three copper models, are the following.

The electron Monte Carlo model yields the electron impact excitation rate to the argon metastable level ($R_{e,exc,Ar}$) and the electron impact excitation and ionization rates from the argon metastable level ($R_{e,exc,met}$ and $R_{e,ion,met}$), which are used as production and loss terms, respectively, in the argon metastable atom fluid model. It also gives the electron impact ionization rate of copper atoms ($R_{e,ion,Cu}$) which is used as loss term for the copper atoms and production term for the copper ions in the copper atom and ion fluid model.

The argon ion and fast atom Monte Carlo model calculates the argon ion and atom impact excitation rates to the argon metastable level ($R_{i,exc,Ar}$ and $R_{a,exc,Ar}$) which are production terms in the argon metastable atom fluid model. They also give the argon ion and atom flux energy distributions at the cathode ($f_{Ar^+}(0,E)$ and $f_{Ar}(0,E)$) which are needed to calculate the flux of sputtered copper atoms in the copper ion and atom fluid model.

Finally, the argon ion-slow electron fluid model yields the argon ion and slow electron densities (n_{Ar^+} and $n_{e,slow}$) which are exploited in some production and loss terms of the argon metastable atom fluid model (i.e. electron - argon ion recombination and electron quenching). Moreover, the argon ion density and the potential distribution (V) resulting from the argon ion-slow electron fluid model are made use of in the copper atom and ion fluid model for the asymmetric charge transfer ionization and for the migration component of the copper ion transport, respectively.

With these input values, the argon metastable atom fluid model and the copper models are solved. The argon metastable atom model (Section 2.2.4) yields the argon metastable atom density ($n_{Ar,met}$) which is required for the Penning ionization rate of the copper atoms in the copper atom and ion fluid model. Then, the copper models are calculated. The Monte Carlo model of the copper atom thermalization process (Section 2.2.5) yields the thermalization profile (F_T), which is the input in the copper atom and ion fluid model (Section 2.2.6). Results of the copper atom and ion fluid model are, among others, the flux of copper atoms entering the CDS ($j_{Cu^+,dc}(r)$) and the number of copper ions created in the CDS ($R_{ion,Cu}$), which are both needed in the copper ion Monte Carlo model (Section 2.2.7). One of the results of the copper ion Monte Carlo model is the flux energy distribution of the copper ions bombarding the cathode ($f_{Cu^+}(0,E)$). This allows calculating the updated flux of copper atoms sputtered from the cathode, used in the copper atom and ion fluid model. The copper atom Monte Carlo model, copper atom and ion fluid model and copper ion Monte Carlo model are solved iteratively until convergence is reached (typically after 2-3 iterations). Then, the resulting copper atom density (n_{Cu}) is put into the argon metastable atom fluid model for the Penning ionization loss term. The argon metastable atom fluid model and the three copper models are solved iteratively until convergence, which is reached after typically 2 iterations.

Results of the argon metastable atom fluid model and the three copper models, which can in principle influence the results in the electron, argon ion and fast atom Monte Carlo models and in the argon ion-slow electron fluid model, are the following.

The argon metastable atom fluid model yields the argon metastable atom density, which is used to recalculate the electron impact excitation and ionization rates from the metastable level in the electron Monte Carlo model. Moreover, some of the production and loss terms can influence the argon ion and slow electron densities in the argon ion-slow electron fluid model, although this effect is almost negligible.

The copper atom and ion fluid model yields the copper atom density which determines the new electron impact ionization rate of copper atoms in the electron Monte Carlo model. The copper ion density can influence the electric field and potential distributions in the argon ion-slow electron fluid model. The asymmetric

charge transfer ionization term can affect the argon ion density in the argon ion-slow electron fluid model, and the three ionization terms of copper can influence the slow electron density in the argon ion-slow electron fluid model.

These data are again put into the electron, argon ion and fast atom Monte Carlo models and in the argon ion-slow electron fluid model, and the entire model is solved until final convergence is reached. The effects of the argon metastable atom fluid model and of the copper models are however negligible at the discharge conditions investigated in this work, so that final convergence is actually reached already after one iteration.

The program source codes are written in Fortran. The calculations are performed on a Sun Sparcserver 20 workstation. The Monte Carlo models typically take each about ten minutes in simulating about 10.000 particles. The solution of the coupled equations in the argon ion-slow electron fluid model requires at least three hours. The calculations in the argon metastable atom fluid model and in the copper atom-copper ion fluid model take each about one minute. The whole iteration procedure until final convergence continues therefore several days.

2.3. RESULTS OF THE MODELS

2.3.1. Discharge conditions

A. Calculations

The models have been applied to the standard glow discharge cell of the VG9000 mass spectrometer for analyzing flat samples (see figure 2.1). Pure argon is used as discharge gas and the cathode is assumed to be made of pure copper.

Results will be presented for the typical discharge conditions of 75 Pa and 1000 V. When voltage and pressure are given, the electrical current can be calculated in the model, assuming a certain gas temperature. The choice of the gas temperature is not straightforward, because it cannot be measured in the glow discharge cell of the VG9000 mass spectrometer. Generally, the gas is assumed to be at room temperature. In the literature, however, gas temperatures are reported at the order of 900-1400 K in a Grimm-type glow discharge. The latter operates, however, at much higher currents (i.e. 40-80 mA), so that higher temperatures are expected than in the VG9000 glow discharge. Moreover, the VG9000 glow discharge cell is cooled with liquid nitrogen, which further complicates the situation (i.e. low temperature at the walls, but maybe higher temperatures in the plasma). We assumed a gas temperature of 360 K. The electrical current corresponding to 75 Pa and 1000 V was then calculated to be 3.1 mA, which is reasonable, compared with experimental discharge conditions.

To investigate the influence of the discharge conditions (pressure, voltage and current) on the calculated results, the modeling calculations were carried out for a range of voltages and pressures, i.e. three different pressures (50, 75 and 100 Pa) and five discharge voltages for each pressure. Since the gas temperature increases in general with increasing current (and hence with increasing pressure when voltage is kept constant), we have assumed gas temperatures of 340 K at 50 Pa, 360 K at 75 Pa, and 380 K at 100 Pa.

It should be mentioned that the gas temperature is considered as a kind of fitting parameter in the calculations, i.e., it is chosen in order to obtain reasonable values for the electrical current. It was found that variations in the gas temperature had significant effect on the electrical current (e.g., 30 % variation in gas temperature yields already a change in electrical current of a factor of 2 (100 %)). Therefore, the quantitative results of the models have to be considered with caution. Nevertheless, the obtained values for the gas temperature seem reasonable, which indicates that the models present already a more or less realistic picture.

Figure 2.6 shows the calculated electrical current as a function of voltage for the three pressures investigated: it increases with pressure and voltage, as expected. Indeed, at higher pressures, there are more ionization collisions and hence creation of more ions and electrons. A larger number of ions and electrons means that more current will flow through the discharge cell. The effect of the voltage is explained as follows. At low voltages (below 600 V), the electrons have low energies (lower than the maximum in the electron impact ionization cross section (ca. 100 eV, see figure 2.2)). Increasing the voltage means that the electrons will reach more suitable energies for ionization, leading to more electrons and ions, and hence yielding a higher current. At voltages above 600 eV, the electrons have too high energies for efficient ionization, and increasing the voltage means that the amount of electron impact ionization will decrease again. However, at these high voltages, other processes come into play, i.e. argon ion and atom impact ionization. The cross sections of these processes reach their maxima at much higher energies (1000 eV and higher, see figure 2.4) allowing a further increase of current with rising voltage. Indeed, in the model described in ref. [80], argon ion and atom impact ionization were not yet incorporated, and the correct current-voltage behavior could therefore not be predicted.

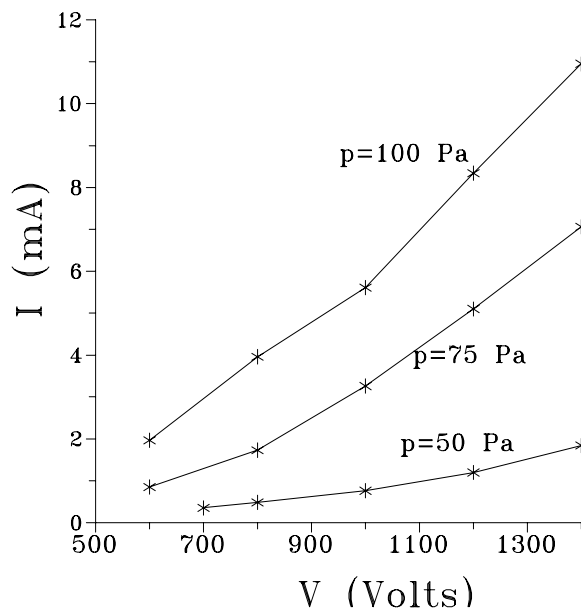


Figure 2.6: Calculated electrical current as a function of voltage at three pressures (copper cathode in argon).

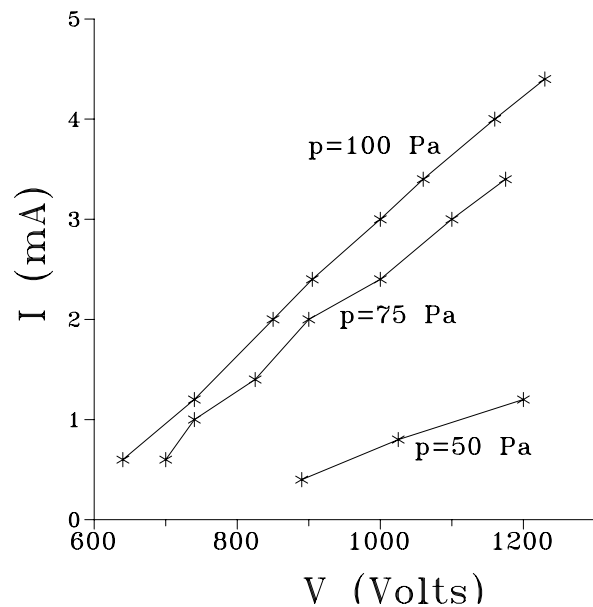


Figure 2.7: Measured electrical current as a function of voltage at three pressures for the VG9000 mass spectrometer (copper cathode in argon).

B. Comparison with experiment

Figure 2.7 presents the electrical current as a function of voltage at the same three pressures, measured for a VG9000 glow discharge cell with a copper cathode [105]. The VG9000 discharge cell used for the measurements was the so-called old flat cell and is not the same as the cell used for the calculations (which is the so-called new flat cell). Moreover, the measured pressures are subject to uncertainties, so that it is difficult to compare figures 2.6 and 2.7 quantitatively. However, it can be seen that the qualitative trends in both the theoretical and experimental current-voltage behavior are comparable.

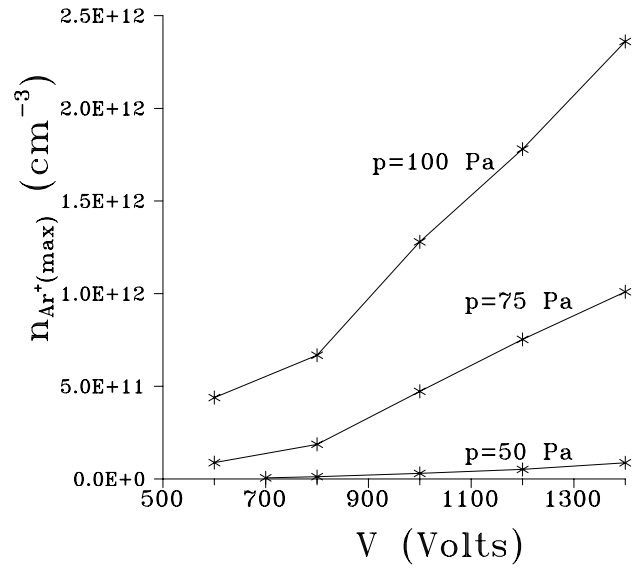
2.3.2. Densities of the plasma species

A. Calculated argon ion and slow electron density profiles

Figure 2.8 shows the density profile of the argon ions throughout the discharge, at 1000 V, 75 Pa and 3.1 mA. The density is nearly constant (slightly lower than 10^{10} cm^{-3}) close to the cathode (i.e. in the CDS), but increases rapidly further in the plasma (i.e. in the NG). Its maximum lies halfway the discharge (in the axial as well as in the radial direction), and takes a value of about $5.5 \times 10^{11} \text{ cm}^{-3}$. It decreases gradually towards the walls. Knowing that the argon gas atom density is about $1.5 \times 10^{16} \text{ cm}^{-3}$ (calculated for an ideal gas at 75 Pa and 360 K), the ionization degree of argon in the glow discharge is only about 10^{-5} . Hence, most of the argon occurs as neutrals in the discharge.

In figure 2.9 the slow electron density profile is illustrated, at 1000 V, 75 Pa and 3.1 mA. It is zero in the CDS and nearly equal to the argon ion density in the NG. This results in a net positive space charge in the CDS and nearly charge neutrality in the NG. Moreover, close to the anode sidewalls and backplate, the argon ion density is also a little higher than the slow electron density, resulting in a slight positive space charge there as well. Slow electron densities have been measured in the literature by Langmuir probe and by optical emission spectrometry measurements. Typical values have been reported at the order of 10^{11} cm^{-3} for a six-way cross glow discharge [106, 107] and about 10^{13} - 10^{14} cm^{-3} for a Grimm-type glow discharge [108-111]. The Grimm-type discharge operates at much higher pressures and currents and a higher electron density is therefore expected. Our calculated results are however in reasonable agreement with the values reported for the six-way cross glow discharge which operates at similar discharge conditions as used in the calculations.

Figure 2.10: Calculated argon ion (and slow electron) density at the maximum of its profile, as a function of voltage, at three pressures (copper cathode in argon).



B. Calculated fast electron density profile

The fast electron density, presented in figure 2.11, for 1000 V, 75 Pa and 3.1 mA, reaches a maximum slightly closer to the cathode and is about four orders of magnitude lower than the argon ion and slow electron densities. Hence, the fast electron group does not contribute to the space charge. The shape of the density profile of the fast electrons does not depend on voltage and pressure either, but the absolute value increases with voltage and pressure, as is illustrated in figure 2.12 (fast electron density taken at the maximum of its profile). The densities range from $2 \times 10^6 \text{ cm}^{-3}$ to $1.3 \times 10^8 \text{ cm}^{-3}$, which remains always negligible compared to the argon ion and slow electron densities.

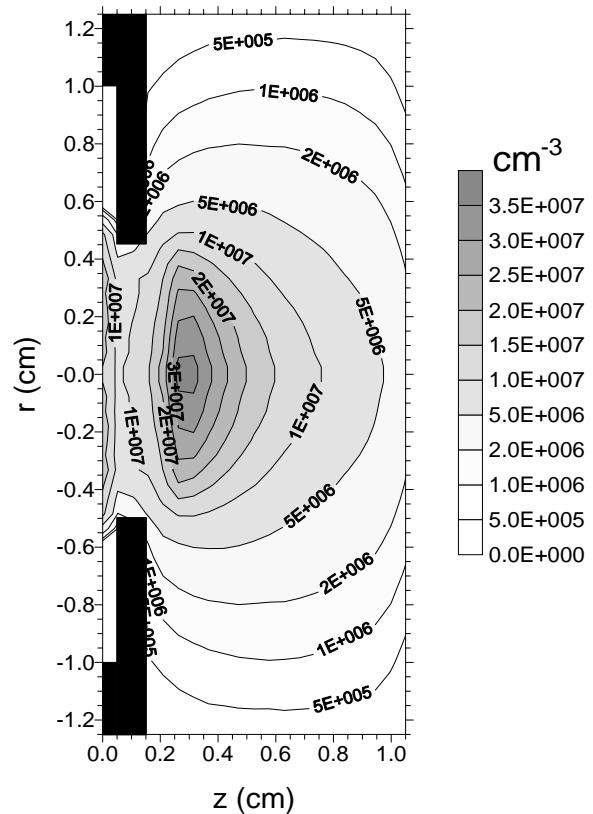


Figure 2.11: Calculated density profile of the fast electrons throughout the discharge (at 75 Pa, 1000 V, 3.1 mA, copper cathode in argon).

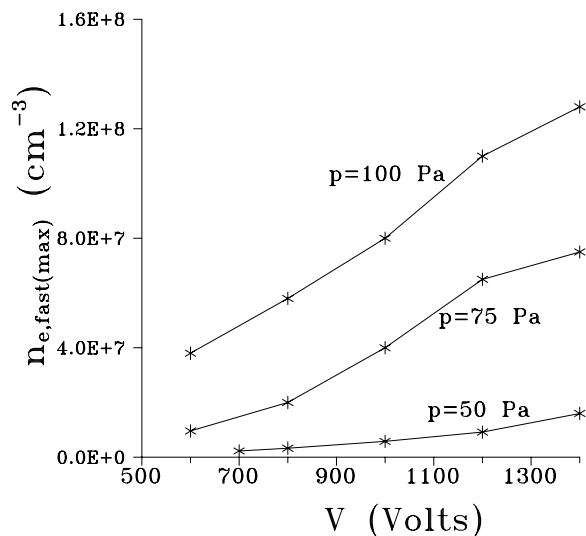


Figure 2.12: Fast electron density at the maximum of its profile, as a function of voltage, at three pressures (copper cathode in argon).

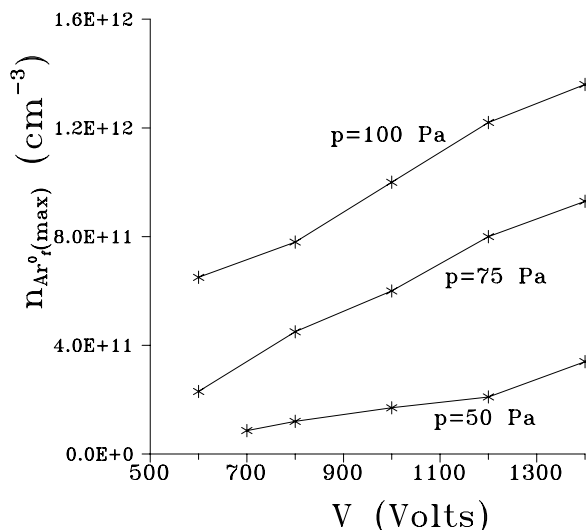
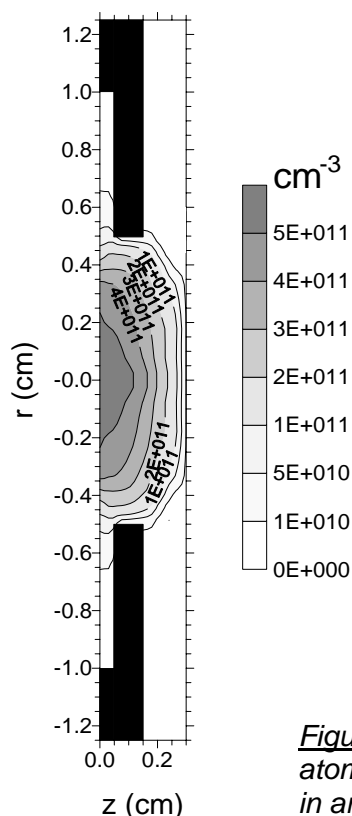


Figure 2.14: Fast argon atom density at the maximum of its profile, as a function of voltage, at three pressures (copper cathode in argon).



C. Calculated fast argon atom density profile

The fast argon atom density reaches a maximum of about $6 \times 10^{11} \text{ cm}^{-3}$ close to the cathode, at 1000 V, 75 Pa and 3.1 mA, as can be seen from figure 2.13. The figure shows only the CDS, since the fast argon atom density is zero in the NG. The density is negligible compared to the overall argon gas atom density (see above), so that it can indeed be stated that the argon gas is more or less at rest. Figure 2.14 presents the fast argon atom density at the maximum of its profile as a function of voltage and pressure. It increases also with voltage and pressure, but remains always negligible compared to the overall argon gas atom density.

Figure 2.13: Calculated density profile of the fast argon atoms in the CDS (at 75 Pa, 1000 V, 3.1 mA, copper cathode in argon).

D. Calculated metastable argon atom density profile

Figure 2.15 shows the argon metastable atom density profile, at 1000 V, 75 Pa and 3.1 mA. A pronounced maximum of about 10^{12} cm^{-3} is reached near the cathode. This is due to the high production of metastable atoms by argon ion and atom impact excitation close to the cathode, where the argon ions and atoms can reach high energies (see below). Further away from the cathode in the NG, the argon metastable atom density decreases gradually. Indeed, the production of argon metastable atoms, caused by electron impact excitation in this region, is efficiently compensated by loss processes (primarily by electron quenching to the nearby energy levels, see below). The density reaches however a second maximum at about 0.9 cm from the cathode, since the loss processes are not important enough anymore to compensate for the production of metastable atoms. Away from the cell axis, the argon metastable atom density spreads out by diffusion and decreases gradually towards zero at the walls.

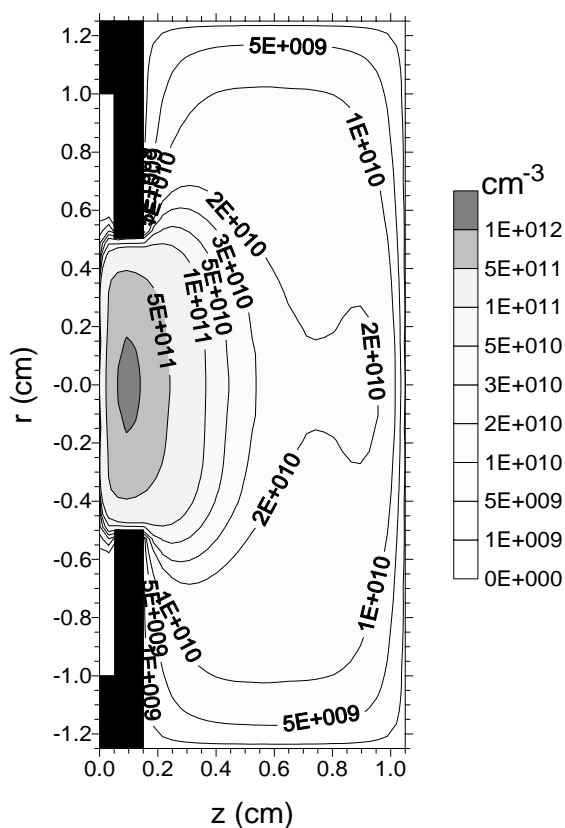


Figure 2.15: Calculated density profile of the argon metastable atoms throughout the discharge (at 75 Pa, 1000 V, 3.1 mA, copper cathode in argon).

It can be seen that the argon metastable atom density is of the same order of magnitude as the argon ion density at these discharge conditions (cfr. figure 2.8).

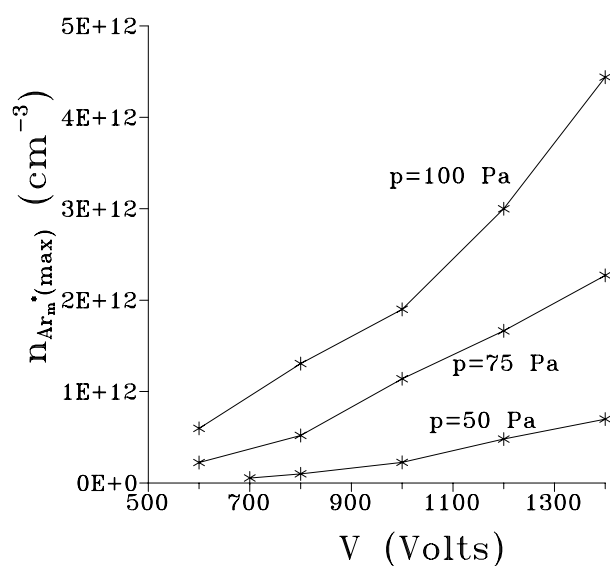


Figure 2.16: Calculated argon metastable atom density at the maximum of its profile, as a function of voltage, at three pressures (copper cathode in argon).

The metastable atom density profile changes slightly with pressure. Indeed, at higher pressures, the maximum is found closer to the cathode (i.e. at about 0.06 cm from the cathode), whereas at low pressures, the maximum extends somewhat further in the discharge (at about 0.15-0.2 cm from the cathode). Moreover, a few distinct small peaks can be found in the glow discharge plasma, depending on the discharge conditions. These peaks are however always considerably smaller than the pronounced peak in front of the cathode, so that the overall metastable density profile does not change noticeably with pressure and voltage. The absolute value of the argon metastable atom density, however, increases clearly with voltage and pressure, as is illustrated in figure 2.16. This is in complete agreement with our experimental observations [112] (see below) and with literature data. Some papers, however, report that the metastable density reaches a maximum at a certain pressure where after it decreases again, since the loss processes become more important than the production processes [50, 113, 114]. This pressure value is found to be 0.7 Torr in ref. [113] and about 2 Torr in ref. [50]. According to our calculations, such a pressure has not yet been attained, nor was it reached in our experiments (pressure range of 0.7-1.6 Torr) [112]. The metastable density increases to the same extent with voltage as the argon ion density, but it rises somewhat less rapidly with pressure. This means that at low pressures, the ratio of the argon metastable atom density to the argon ion density will be higher than at high pressures.

E. Calculated sputtered copper atom density profile

In glow discharges used for analytical purposes, special interest goes to the behavior of the sputtered atoms and corresponding ions. When the sputtered copper atoms leave the cathode, they are being thermalized due to collisions with the argon gas particles. Figure 2.17 shows the thermalization profile of the sputtered copper atoms, at 1000 V, 75 Pa and 3.1 mA, i.e. the number of atoms thermalized per cm^3 at a given position (normalized to one sputtered atom). It is seen that the majority of the sputtered atoms are already thermalized close to the cathode. Only a small part can reach the anode backplate before being thermalized.

The total copper atom density profile is composed of both the thermalized and non-thermalized copper atom densities. The non-thermalized atom density, illustrated in figure 2.18, for 1000 V, 75 Pa and 3.1 mA, decreases rapidly away from the cathode, since most of the sputtered atoms are, indeed, already thermalized at a few mm from the cathode (as could be seen from figure 2.17).

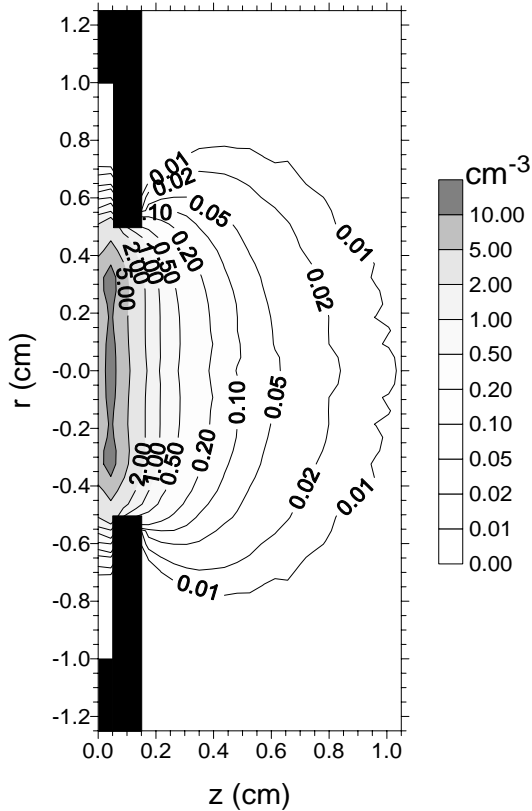


Figure 2.17: Calculated thermalization profile of the sputtered copper atoms throughout the discharge (at 75 Pa, 1000 V, 3.1 mA, copper cathode in argon).

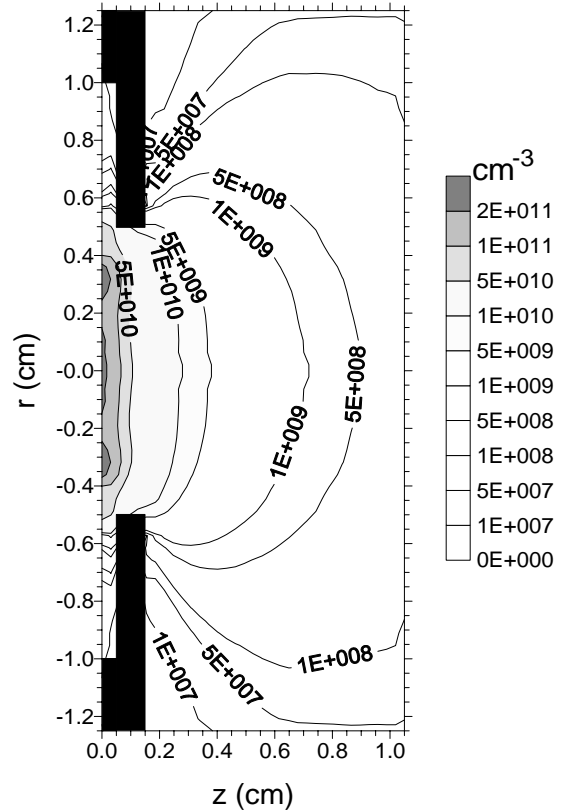


Figure 2.18: Calculated density profile of the non-thermalized sputtered copper atoms throughout the discharge (at 75 Pa, 1000 V, 3.1 mA, copper cathode in argon).

The density profile of the thermalized copper atoms is presented in figure 2.19, for 1000 V, 75 Pa and 3.1 mA. The density reaches a maximum of about $6.7 \times 10^{12} \text{ cm}^{-3}$ at a few mm from the cathode and decreases gradually further in the discharge towards low values at the cell walls. It can be seen that the non-thermalized copper atom density (figure 2.18) is negligible compared to the thermalized atom density (figure 2.19); hence, the thermalized and the total sputtered copper atom densities practically coincide.

The calculated density profile, with a maximum at a few mm from the cathode, is in good qualitative agreement with number density profiles obtained experimentally by atomic absorption and fluorescence [58, 101, 115-116]. The “dip” in front of the cathode was explained in refs. [58, 115, 116] by assuming that not all the cathode material is sputtered as neutral atoms, but that a certain amount is released as clusters or excited species, which are not detected by atomic absorption or fluorescence. This explanation sounds quite reasonable. However, this profile also results from the modeling calculations, without the need to assume that the sputtered species occur in the form of clusters. Indeed, the sputtered atoms leave the cathode

with energies of several eV, and they lose these initial energies very rapidly by collisions with argon gas atoms, until they are thermalized. This gives rise to a thermalization profile (figure 2.17), which shows a maximum at about 1 mm from the cathode. This explains why the sputtered atom population is at maximum at a few mm from the cathode. Indeed, a model where such an initial thermalization step is not included (e.g. ref. [58]) cannot predict the dip in front of the cathode. The present modeling result is also in excellent quantitative agreement with experimentally obtained profiles (see below).

Figure 2.20 shows the copper atom density at the maximum of its profile, as a function of voltage and pressure. At higher voltages and pressures, there will be more ions and atoms bombarding the cathode, giving rise to sputtering. Moreover, at higher voltages, the energy of the bombarding particles will be higher, so that sputtering becomes more efficient. Therefore, at higher voltages and pressures, the

sputtered copper atom density will be higher. The copper atom densities range from 10^{11} cm^{-3} to $3 \times 10^{13} \text{ cm}^{-3}$, which is about five to three orders of magnitude lower than the argon gas atom density, respectively.

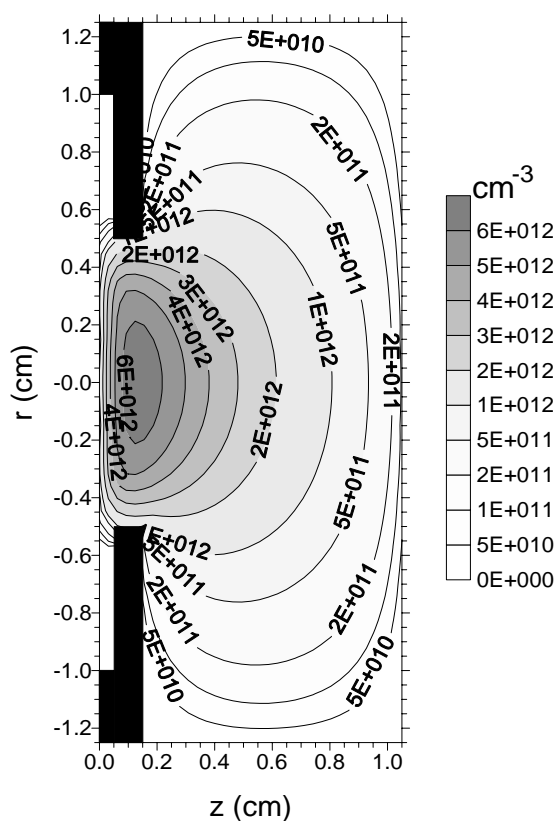


Figure 2.19: Calculated density profile of the thermalized sputtered copper atoms throughout the discharge (at 75 Pa, 1000 V, 3.1 mA, copper cathode in argon).

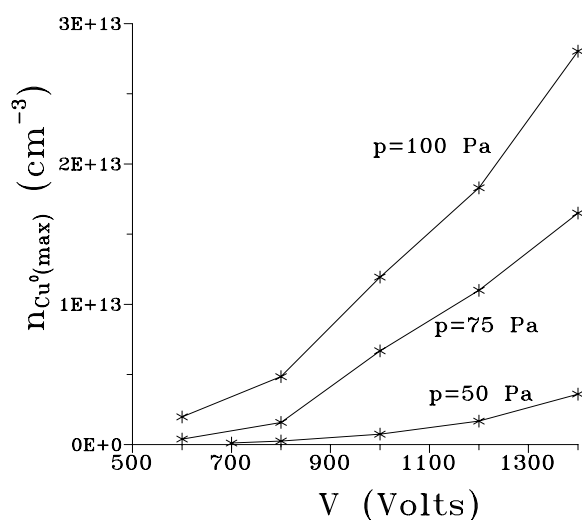


Figure 2.20: Calculated sputtered copper atom density at the maximum of its profile, as a function of voltage, at three pressures (copper cathode in argon).

F. Calculated copper ion density profile

In figure 2.21, the density profile of the copper ions formed by ionization of the copper atoms, at 1000 V, 75 Pa and 3.1 mA, is presented. The density is nearly constant in the CDS (ca. 10^8 cm^{-3} or slightly less), increases rapidly in the NG, and reaches a maximum of about $3.4 \times 10^9 \text{ cm}^{-3}$ at the center of the discharge. It decreases again to low values at the cell walls.

The influence of voltage and pressure on the copper ion density at the maximum is illustrated in figure 2.22. The copper ion density increases with voltage and pressure, as expected. The effect is clearly more pronounced than for the copper atoms. Indeed, the formation of copper ions depends on the copper atom density and on the degree of ionization (i.e. Penning ionization by argon metastable atoms, asymmetric charge transfer with argon ions, and electron impact ionization).

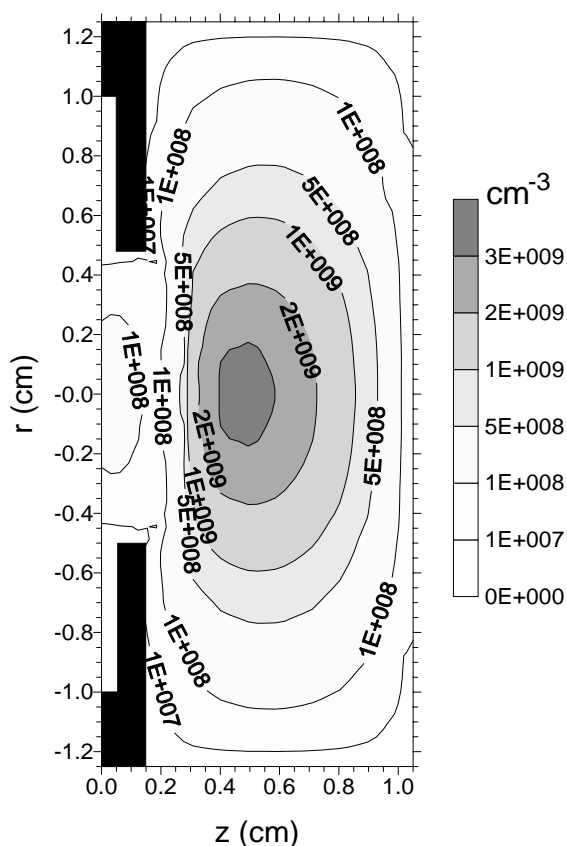


Figure 2.21: Calculated density profile of the copper ions throughout the discharge (at 75 Pa, 1000 V, 3.1 mA, copper cathode in argon).

Since both the copper atom density and the amount of ionization (densities of argon metastable atoms, argon ions and electrons) increase with pressure and voltage, the copper ion density will increase more rapidly. The copper ion density ranges from 10^6 cm^{-3} to 10^{11} cm^{-3} .

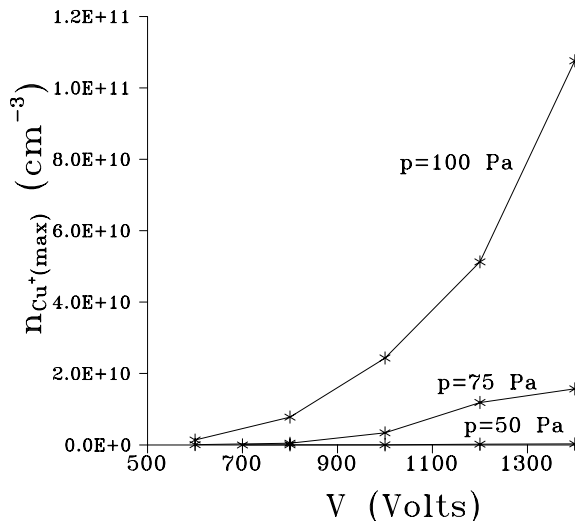


Figure 2.22: Calculated copper ion density at the maximum of its profile, as a function of voltage, at three pressures (copper cathode in argon).

The copper ion density profile has the same shape as the argon ion density profile (figure 2.8), but is about two orders of magnitude lower. In figure 2.23, the ratio of copper ion density to argon ion density is plotted as a function of pressure and voltage. The ratio is about 10^{-4} at low voltages and pressures and increases to about 0.04 (4 %) at high voltages and pressures. When we compare this with the ratio of copper atom density to argon gas atom density of about five to three orders of magnitude (see above), it can be concluded that the sputtered copper atoms are more efficiently ionized than the argon atoms, due to Penning ionization and asymmetric charge transfer, which are, of course, not working for the ionization of argon.

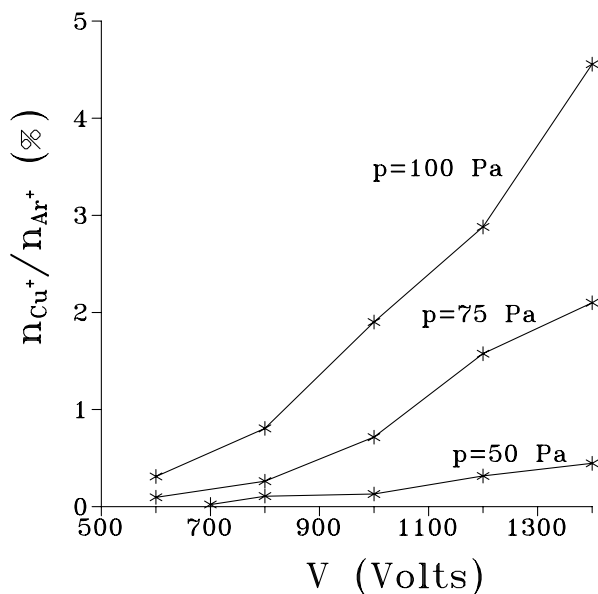


Figure 2.23: Calculated copper ion to argon ion density ratio, as a function of voltage, at three pressures (copper cathode in argon).

The ratio of the copper ion to argon ion flux throughout the plasma was also calculated to be in the percent order, rising with voltage and pressure. This is in reasonable agreement with experiment. Indeed, the ratio of the copper ion to argon ion flux at the anode backplate will be reflected in the ratio of the matrix (copper) ion peak to argon ion peak in the mass spectra of the VG9000 instrument. The latter is also in the percent order and rises with voltage and pressure. The experimentally obtained values are slightly higher (1-20 %), but in view of the fact that this ratio is calculated from the copper atom to argon atom density ratio of three to five orders of magnitude, the presently obtained value in the percent order is already in satisfactory agreement with experiment.

From the copper atom and copper ion densities, the ionization degree of copper can be deduced. At 75 Pa, 1000 V and 3.1 mA, it was calculated to be about 10^{-3} or 0.1 % (see figures 2.19 and 2.21). This is slightly lower than typical values reported in GDMS review articles [117,118] (i.e. 1 % or less). However, it is not very clear where these typical values come from and hence how reliable they are. The influence of voltage and pressure on the ionization degree of copper is illustrated in figure 2.24. Since the copper ion density increases more rapidly with voltage and pressure than the copper atom density, the ionization degree also rises with voltage and pressure. It is in the order of 0.001-0.01 % at low pressure and about 0.1-0.5 % at higher pressure. This is clearly higher than the ionization degree of argon in the glow discharge, as is illustrated in figure 2.25, which demonstrates again that the copper atoms are more efficiently ionized.

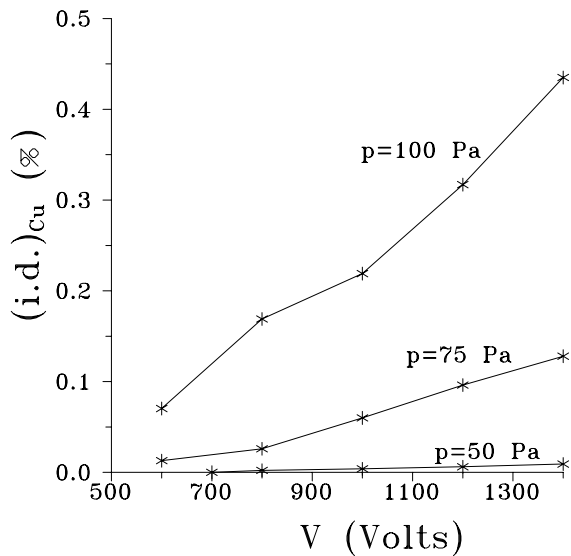


Figure 2.24: Calculated ionization degree (i.d.) of copper, as a function of voltage, at three pressures (copper cathode in argon).

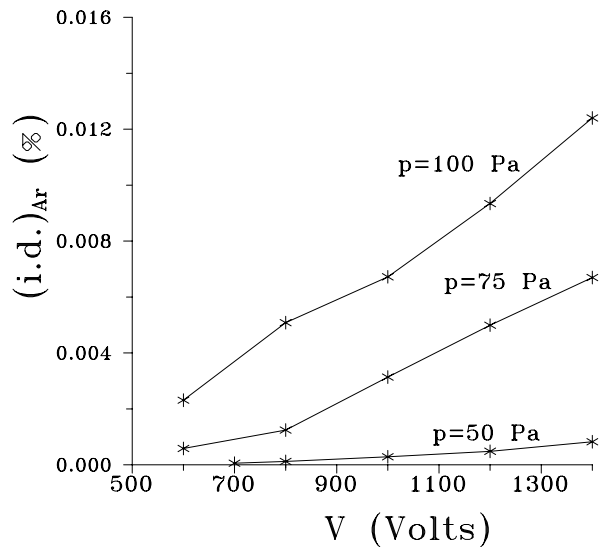


Figure 2.25: Calculated ionization degree (i.d.) of argon, as a function of voltage, at three pressures (copper cathode in argon).

It can be seen from the above density profiles that the calculated species densities are almost zero behind the front plate (see figure 2.1 for the position of the front plate). Indeed, this region does not really take part in the glow discharge plasma, since the distance between cathode and front plate is smaller than one CDS-length (see below), which is the necessary condition for a glow discharge to be created.

G. Experimental argon metastable atom density profile

To check the modeling results, we have measured three-dimensional density profiles of some plasma species (i.e. the argon metastable atoms, the sputtered atoms and corresponding ions), using laser induced fluorescence and atomic absorption. More details about these experiments can be found in refs. [101,112]. Since the measurements were performed on a six-way cross glow discharge with a tantalum cathode, the models were slightly modified to simulate the new discharge geometry, in order to make direct comparison with the experiment possible.

Figure 2.26 shows the argon metastable atom density profile, measured by laser induced fluorescence, at 1000 V, 1 Torr and 1.8 mA. The cathode of the cell is illustrated with the black line at $r=0$ and $z=0$ on the figure. The density reaches a maximum at a few mm from the cathode in the axial direction, it drops to a local minimum at about 7 mm and increases then again to a second maximum at about 12 mm from the cathode. The occurrence of two distinct maxima is also observed in the modeling result, as can be seen in figure 2.27 (calculated for the same cell geometry and discharge conditions as used in the experiment).

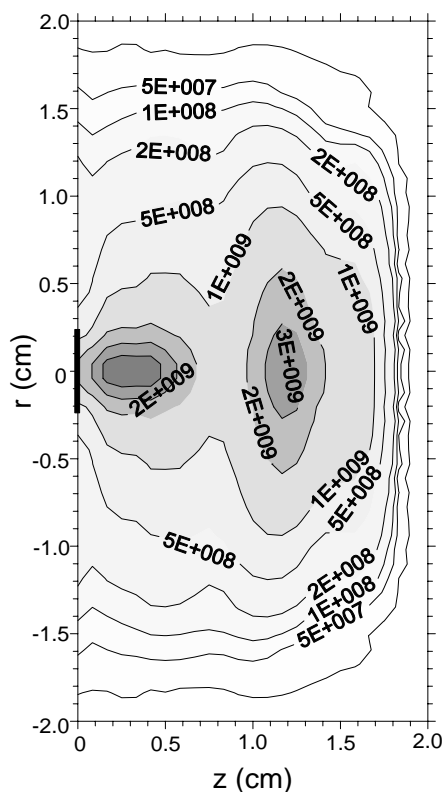


Figure 2.26: Experimental density profile of the argon metastable atoms throughout the discharge, measured with laser induced fluorescence (six-way cross glow discharge cell, 1 Torr, 1000 V, 1.8 mA, tantalum cathode in argon).

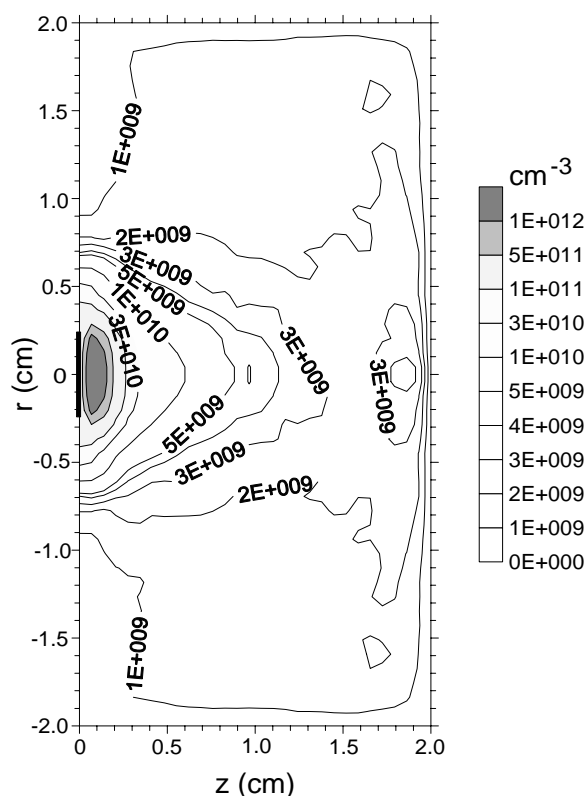


Figure 2.27: Calculated density profile of the argon metastable atoms throughout the discharge (six-way cross glow discharge cell, 1 Torr, 1000 V, 1.8 mA, tantalum cathode in argon).

However, the positions of the two maxima are somewhat different. This indicates that the production and loss processes incorporated in the model do not yet completely describe the real situation. It can be understood that it is indeed difficult to reach complete agreement, due to the complexity and diversity of the different production and loss processes and the rather large uncertainties in the rate constants of some of these processes. It is possible that the two peaks present in the experimental profile are caused by the same production and loss processes as

the two peaks in the calculated profile, but that the location of the various production and loss processes is not yet correctly described in the model. Due to uncertainties in the rate constants, the magnitude and hence the relative importance of the different production and loss processes are maybe also not yet correctly described in the model, leading to a local maximum at the wrong position.

On the other hand, it may also be that the present model is not yet complete and that other production and/or loss processes have to be included in order to reach agreement with experiment. Especially the high peak close to the cathode in the calculated result is in disagreement with the measured profile. Indeed, comparison of the numerical values in figures 2.26 and 2.27 shows that the experimental and theoretical results are in reasonable agreement with each other (densities in the same order of magnitude) except in the first few mm where the calculated density is two orders of magnitude higher than the experimentally obtained values. This would indicate that either the production process by ion and atom impact excitation is overestimated or that an additional loss process occurs in this region which is not incorporated in the model. It was indeed suggested that the cross sections of argon ion and atom impact excitation to the metastable levels have to be considered as upper limits [82]. However, even when lowering these cross sections by a factor of 100, which seems rather unrealistic, the peak in front of the cathode is still too high (see ref. [112]).

This suggests that there must be an additional loss process close to the cathode, to compensate for the high production of metastable argon atoms by ion and atom impact excitation. A possible candidate would be argon ion and atom impact ionization and excitation from the metastable level, in analogy to electron impact ionization and excitation from the metastable level. These processes may seem quite exotic, but it can be expected that they occur, since also ion and atom impact ionization and excitation from the ground state play a significant role close to the cathode. However, the cross sections of these processes are not available in the literature. A rapid calculation, based on similar cross section values as for electron impact ionization and excitation, shows that these processes are still a factor of 30 less important than argon ion and atom impact excitation from the ground state to the metastable level, since the metastable densities are still 4 orders of magnitude lower than the ground state density.

Another possibility is quenching of argon metastable atoms by collisions with molecular gas impurities. The rate constant of this reaction is typically 10^{-10} - 5×10^{-10} $\text{cm}^3 \text{s}^{-1}$ [119], which is in the same order of magnitude as the Penning ionization rate constant of sputtered atoms (see above). The sputtered copper atom density amounts to about $6 \times 10^{12} \text{ cm}^{-3}$ at the maximum in front of the cathode (see figure 2.19), which corresponds to an "impurity in the argon gas" of 400 ppm ($n_{\text{Ar}} = 1.5 \times 10^{16} \text{ cm}^{-3}$; see above). The loss of argon metastable atoms due to Penning ionization of copper atoms, which is incorporated in the model, is not able to

compensate for the high production of metastables in front of the cathode. Quenching by gas molecules can therefore only be important if the gas impurities are clearly higher than 400 ppm. The argon gas is typically characterized by only a few ppm impurities at maximum [120]. However, it may be that the impurities in the glow discharge cell are higher due to inherent vacuum leaks.

Another possible loss process is a sort of equivalent to electron collisional transfer to the nearby energy levels in the NG, since this process has a high rate constant. However, such a process has not been described in the literature to our knowledge, and this assumption can therefore not be checked.

The metastable atom density calculated for the VG9000 glow discharge cell is about one order of magnitude higher than the experimental and theoretical metastable densities obtained for the six-way cross glow discharge cell. In ref. [121, 122], argon metastable atom densities at the order of 10^{11} - 5×10^{11} cm^{-3} and 3×10^{12} - 10^{13} cm^{-3} , respectively, have been reported for a Grimm-type glow discharge, which operates at higher pressures and currents. In ref. [48, 123] metastable argon atom densities have been measured in a discharge tube operating at pressures and currents comparable to our conditions, and values in the order of 2×10^{10} - 2×10^{11} cm^{-3} are obtained. It seems that the metastable atom number densities can really vary over many orders of magnitude for different discharge conditions and geometries. When we take into account that such large variations can occur, the present agreement between experiment and theory is already satisfying. Moreover, the experimentally obtained metastable density profiles increased with pressure and voltage, which is also in agreement with our modeling results.

H. Experimental sputtered tantalum atom density profile

Figure 2.28 presents the sputtered tantalum atom density profile, measured by laser induced fluorescence in the six-way cross glow discharge cell at 1000 V, 1 Torr and 2 mA. It is in reasonable agreement with the calculated profile for the same discharge conditions, shown in figure 2.29. The modeling result is a factor of 2 higher at the maximum but falls off somewhat more rapidly so that it is of comparable magnitude, or slightly lower than the experimental profile further in the discharge cell. The tantalum atom density profile was also measured by atomic absorption, and was found to be a factor of 3 lower than the fluorescence result [101]. This illustrates that the calculated and experimental profiles are more or less equal to each other within the experimental error. The measured tantalum atom density profiles increased with voltage and pressure, which is in agreement with the results of the calculations.

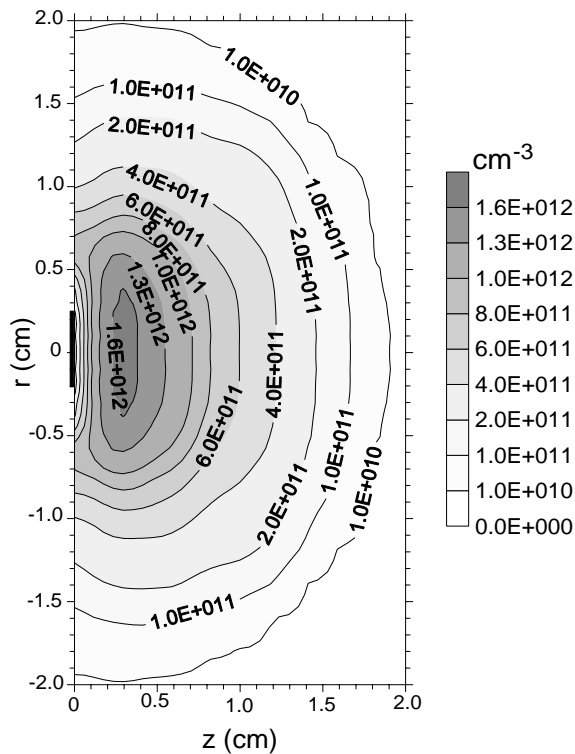


Figure 2.28: Experimental density profile of the sputtered tantalum atoms throughout the discharge, measured with laser induced fluorescence (six-way cross glow discharge cell, 1 Torr, 1000 V, 1.8 mA, tantalum cathode in argon).

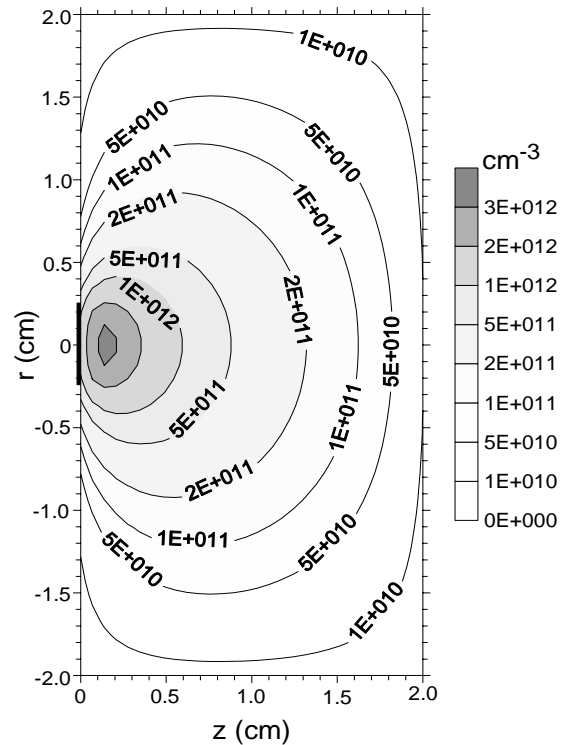


Figure 2.29: Calculated density profile of the sputtered tantalum atoms throughout the discharge (six-way cross glow discharge cell, 1 Torr, 1000 V, 1.8 mA, tantalum cathode in argon).

I. Experimental tantalum ion density profile

In figure 2.30 the density profile of the tantalum ions obtained by laser induced fluorescence at 1000 V, 1 Torr and 2 mA, is depicted. It shows excellent qualitative agreement with the result of the mathematical simulations for the same discharge conditions and cell, presented in figure 2.31. Indeed, the density is low in the CDS (the slight differences near the cathode are due to approximations in the geometry in the model) and it reaches a maximum at about 5-6 mm from the cathode. However, the absolute value at the maximum of the calculated number density is almost a factor of 10 lower than the experimental result. There can be two possible reasons, either the calculated values are too low or the experimental results are too high. In the mathematical model, the tantalum ion density is calculated from the tantalum atom density taking into account three ionization processes: electron impact ionization, Penning ionization and asymmetric charge transfer. Since the tantalum atom density is in good agreement with experiment, these observations suggest that the degree of ionization in the calculations is too low.

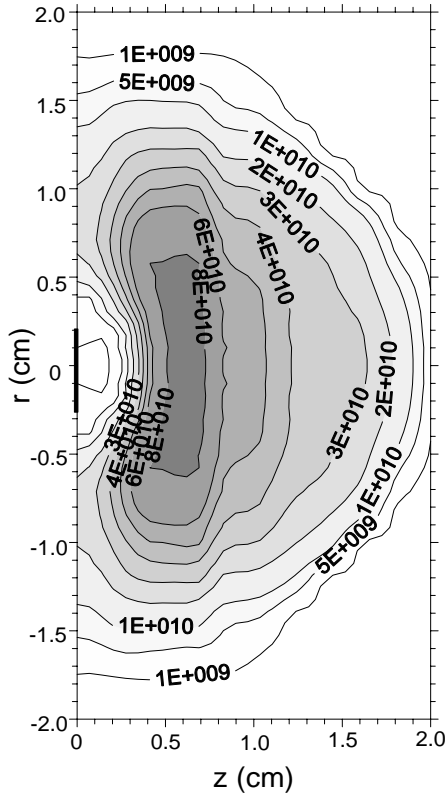


Figure 2.30: Experimental density profile of the tantalum ions throughout the discharge, measured with laser induced fluorescence (six-way cross glow discharge cell, 1 Torr, 1000 V, 1.8 mA, tantalum cathode in argon).

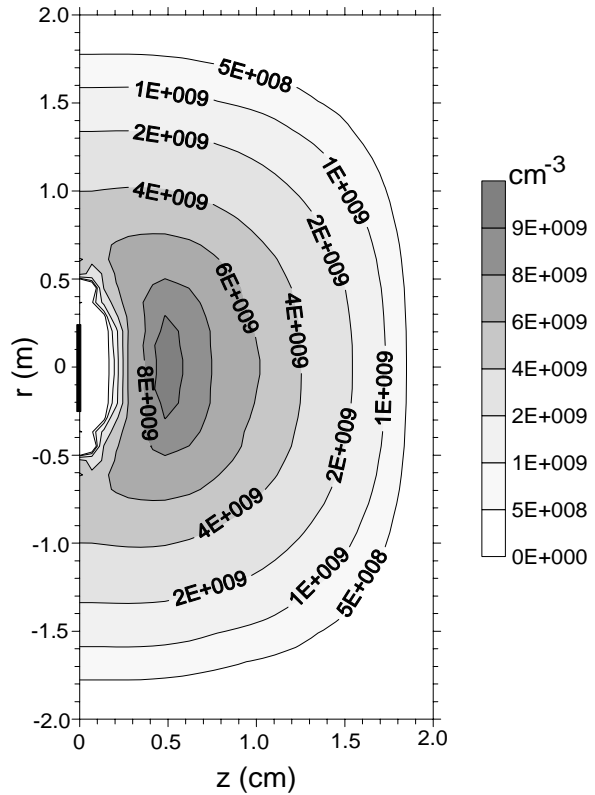


Figure 2.31: Calculated density profile of the tantalum ions throughout the discharge, (six-way cross glow discharge cell, 1 Torr, 1000 V, 1.8 mA, tantalum cathode in argon).

There are several possible reasons: either one of the above mentioned ionization mechanisms is underestimated or there are still other ionization pathways which are not incorporated in the model so far. The amount of electron impact ionization is determined by the electron flux and the cross section of electron impact ionization. The calculated electron flux is directly related to the calculated total electrical current, and since the latter is in excellent agreement with experiment (i.e. 2 mA), we think that the electron flux is more or less correct. The cross section values of electron impact ionization are rather well known in the literature for different elements. Therefore, the amount of electron impact ionization is assumed to be calculated correctly.

The amount of Penning ionization depends on the argon metastable atom density and the rate constant of Penning ionization. The calculated argon metastable atom density is in satisfactory agreement with the experimental results (see above). Close to the cathode, the modeling results were even too high compared with experiment, so that it is not very likely that the calculated argon

metastable atom density is underestimated. The rate constant of Penning ionization of tantalum was calculated from a formula in ref. [89], as explained before, and was found to be $2.76 \times 10^{-10} \text{ cm}^3 \text{ s}^{-1}$. Values at the order of $10^{-10} \text{ cm}^3 \text{ s}^{-1}$ are indeed generally cited in the literature for Penning ionization of different elements. Hence, the amount of Penning ionization is also expected to be calculated more or less correctly.

The extent of asymmetric charge transfer depends on the argon ion density and the rate constant of this process. The argon ion density is also directly related to the total electrical current and its value is therefore assumed to be more or less correct as well. The rate constant of asymmetric charge transfer between argon ions and tantalum atoms could not be found in the literature. It is stated in refs. [99, 100] that the rate constant for asymmetric charge transfer is at the same order of magnitude as the rate constant for Penning ionization if the element possesses ionic energy levels suitable for asymmetric charge transfer (i.e. lying close to the argon ion energy levels). We have carried out an extensive study about the availability of such levels for most elements in the periodic table (see Section 2.5). Tantalum was not included in this study, since the tantalum ion energy level scheme in the literature [124] is incomplete (i.e. the energy levels lying in the region of interest are not recorded for tantalum in ref. [124]). However, based on the periodic table, tantalum belongs to the group of elements which possess many levels for asymmetric charge transfer, therefore it is assumed that the rate constant of asymmetric charge transfer between argon ions and tantalum atoms is equal to the Penning ionization rate constant. Based on this assumption, it was calculated that asymmetric charge transfer is the dominant ionization mechanism for the present discharge conditions and geometry (i.e. the relative contributions of electron impact ionization, Penning ionization and asymmetric charge transfer amount to about 1 %, 8 % and 91 %, respectively). Although in earlier reviews of GDMS, it has often been stated that Penning ionization is the dominant process and that asymmetric charge transfer only plays a secondary role, some other papers demonstrate that this process is very important in a glow discharge for certain ion-atom combinations [125-133]. Due to the uncertainties in the rate constant, we have to be cautious about the role of asymmetric charge transfer. However, the fact that the calculated tantalum ion density is too low compared to experiment, could indicate that this process is indeed important and may still be underestimated. In fact, in ref. [61] a rate constant of $10^{-9} \text{ cm}^3 \text{ s}^{-1}$ was used between neon ions and copper atoms. Such a high rate constant would really give good agreement between the calculated and experimental tantalum ion density.

An alternative explanation for the discrepancy between experiment and theory would be that other ionization pathways are important which are now neglected in the model, like photoionization, ion and atom impact ionization, or dissociative ionization involving clusters of tantalum. The latter assumption is not too

unreasonable, since tantalum has a high affinity for oxygen. It may be possible that TaO molecules are dissociated and ionized into Ta⁺ upon impact by electrons or other plasma species. However, since the necessary data to prove this (i.e. the TaO number density in the plasma and cross sections of possible alternative ionization processes) are not available, this explanation remains only speculative.

On the other hand, it is also possible that the difference between experiment and theory is due to the fact that the experimental results are too high. It is difficult to estimate the experimental uncertainties. From the difference between fluorescence and absorption results for the tantalum atoms (see above), it was deduced that the experimental error can at least be a factor of 3 (and it may be more if the good agreement between the fluorescence and absorption data would only be coincidence). It is quite reasonable to believe that the discrepancy between figures 2.30 and 2.31 is a combination of some limitations in the model and some experimental errors. After all, a factor of 10 difference between experiment and theory is not too bad, when we consider that neither such experiments nor such modeling calculations have ever been performed and confronted before. The influence of pressure and voltage on the measured tantalum ion density distributions was found to be in excellent agreement with the calculations.

From the ratio of the tantalum ion to tantalum atom density, the ionization degree of tantalum can be deduced, in a similar way as was done for copper (see above). Experimentally (i.e. by comparing figures 2.28 and 2.30) a value of about 5 % is obtained, whereas the modeling calculations (i.e. figures 2.29 and 2.31) predict a value of 1.7 %. Hence, although the absolute values of the densities are not yet in complete agreement between experiment and theory, the ratio of atom and ion densities is in satisfactory agreement. The ionization degree obtained for tantalum (both experimentally and theoretically) in the six-way cross geometry and discharge conditions is clearly higher than the calculated value for copper in the VG9000 cell geometry. This indicates that it is dangerous to generalize the value of the ionization degree, since it depends on specific atom-ion combinations, on the discharge conditions and on the cell geometry.

2.3.3. Electric field and potential distributions

A. Calculated values

The densities of the charged plasma particles (electrons, ions) give rise to a certain electric field and potential distribution throughout the discharge, determined by Poisson's equation. Figure 2.32 shows the potential distribution, at 1000 V, 75 Pa and 3.1 mA. The potential is at -1000 V at the cathode. It increases rapidly in the CDS and reaches zero at about 0.24 cm from the cathode (thick line). This is defined as the interface between CDS and NG. Hence, the total voltage applied to the glow discharge cell, falls off in the CDS. Since the front plate of the cell is also at anode potential, and since the charged particle densities are almost zero behind the front plate (see above), the potential drops nearly linearly in this region. The potential reaches a small positive value in the NG (of the order of 9.5 V at maximum for the present discharge conditions), which is called the plasma potential. It returns to zero at the anode sidewalls and backplate. Hence, the plasma does not take a potential intermediate between cathode and anode, but it is the most positive region of the discharge.

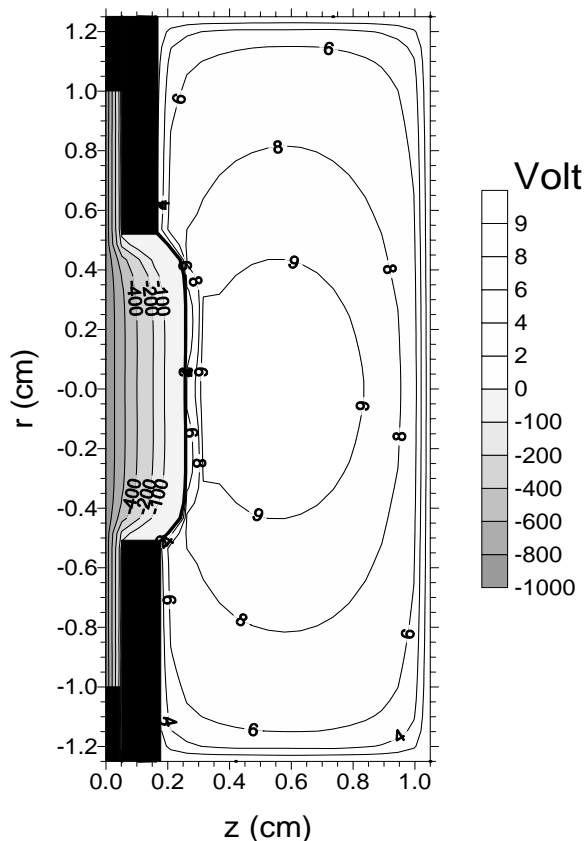


Figure 2.32: Calculated potential distribution throughout the discharge (at 75 Pa, 1000 V, 3.1 mA, copper cathode in argon).

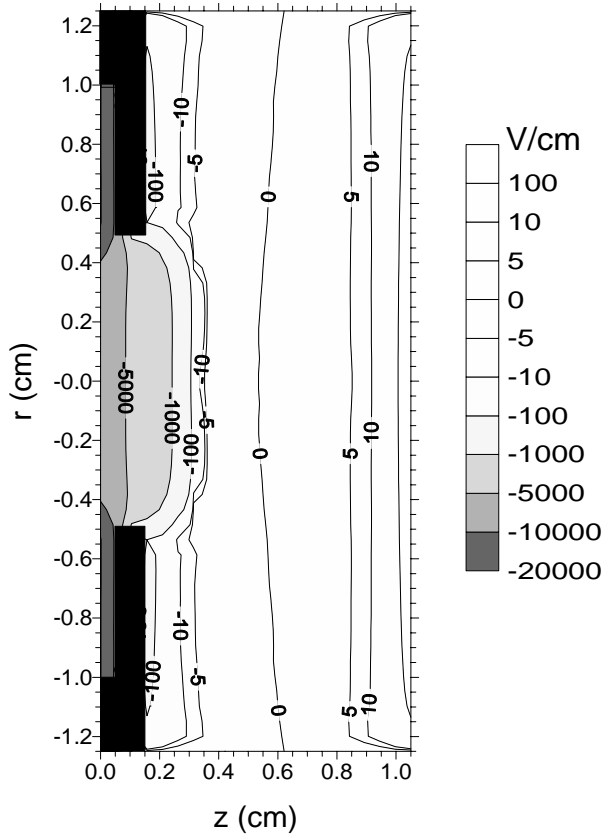


Figure 2.33: Calculated axial electric field distribution throughout the discharge (at 75 Pa, 1000 V, 3.1 mA, copper cathode in argon).

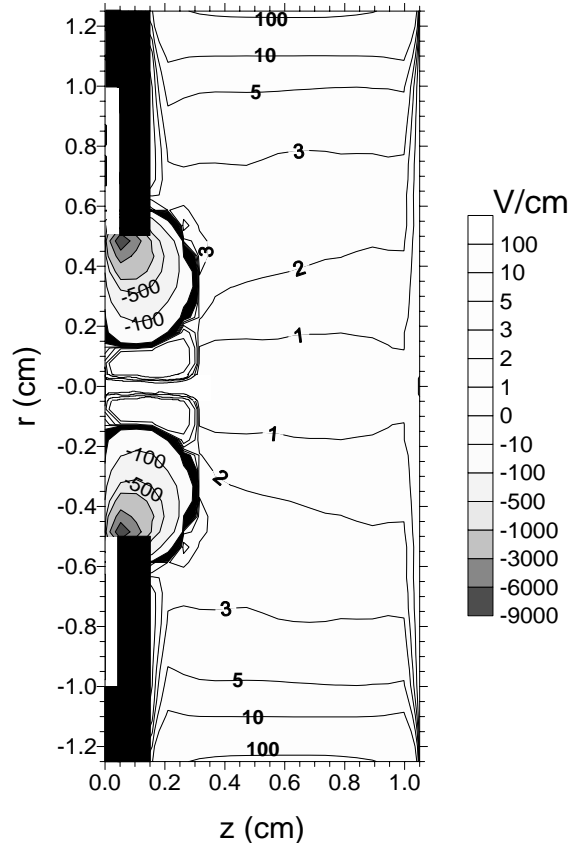


Figure 2.34: Calculated radial electric field distribution throughout the discharge (at 75 Pa, 1000 V, 3.1 mA, copper cathode in argon).

Figures 2.33 and 2.34 represent the axial and radial electric field distributions, at 1000 V, 75 Pa and 3.1 mA, respectively. Due to the large potential drop in the CDS, the axial field (figure 2.33) in this region is rather high. It reaches values of about -7.5 kV/cm at the cathode and decreases almost linearly towards the NG. It goes through zero halfway the discharge and increases again to slightly higher than 200 V/cm at the anode backplate. There is almost no radial gradient in the axial electric field in the NG, i.e. the axial electric field is only function of the axial position. Behind the frontplate, a very high axial electric field is observed, due to the large potential drop over a very short distance. The radial electric field (figure 2.34) is rather high near the frontplate due to the large potential drop between cathode and frontplate. It reaches values of about -10 kV/cm very close to the frontplate and decreases rapidly towards the cell axis. At about 0.1 cm from the cell axis, the radial electric field takes slightly positive values in the CDS (20 V/cm at maximum). It decreases again to zero at the cell axis. In the NG, the radial electric field is quite small, but it increases towards the sidewalls, reaching values of about 100 V/cm at the walls. Similarly, there is almost no axial gradient in the radial electric field in the

NG, except close to the anode backplate. Generally, the electric fields at the cell walls (i.e. about -7.5 kV/cm at the cathode and about 100 V/cm at the anode walls) are such as to repel the electrons trying to reach the walls.

The shapes of the electric field and potential distributions do not significantly change with voltage and pressure. The potential always drops off completely in the CDS, is slightly positive in the NG and returns to zero at the anode walls. The value of the potential in the NG (i.e. the plasma potential) increases barely with pressure and voltage. At the lowest pressure and voltage investigated, it was calculated to be about 7.5 V, and it rises to about 9.5 V at the highest pressure and voltage. Whereas the value varies only slightly with the discharge conditions, it seems to be more dependent on the cell geometry, since for a six-way cross configuration of 4 cm diameter, a plasma potential of just a few volts was calculated.

The position at which the potential crosses zero, defines the length of the CDS. It is influenced a bit more clearly by voltage and pressure, as is seen in figure 2.35. It increases with decreasing voltage and pressure, which is necessary to sustain the discharge. At extremely low pressures and voltages, the CDS would take up the entire discharge region. Indeed, the glow discharge can be maintained without NG, but the CDS is an essential zone. By further lowering the pressure and voltage, the discharge would stop. It can be seen that the pressure effect is definitely more pronounced than the voltage effect for the present discharge conditions.

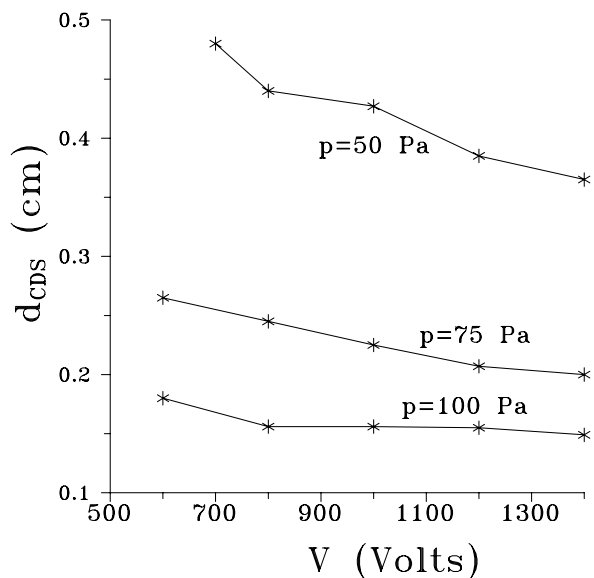


Figure 2.35: Calculated length of the cathode dark space (d_{CDS}) as a function of voltage, at three pressures (copper cathode in argon).

Since the CDS becomes shorter with increasing voltage, a larger potential drop has to fall off on a shorter distance. This results in a higher electric field in the CDS at higher voltages. Similarly, at higher pressures, the CDS length decreases when voltage is kept constant, so that the potential again has to drop off more rapidly, yielding also a higher electric field in the CDS. Figure 2.36 presents the absolute value of the axial electric field at the cathode as a function of voltage and pressure. The electric field is rather high (2-16 kV/cm) and it increases indeed with voltage and pressure. The electric field decreases rapidly in the CDS, changes sign somewhere at the center of the NG, and increases again towards the anode. The value at the anode walls is calculated to be of the order of 100-200 V/cm, increasing only slightly with pressure and voltage.

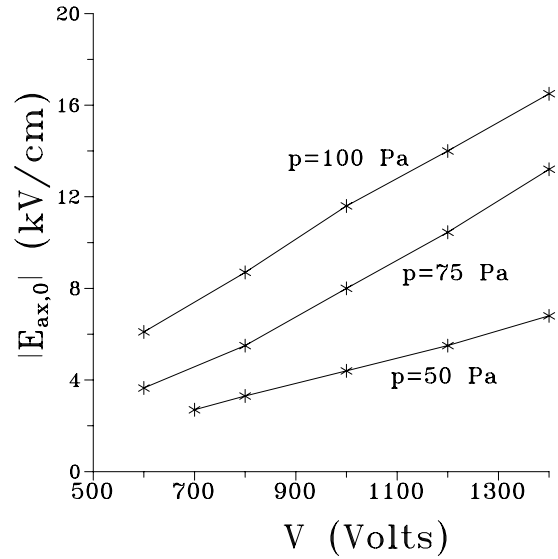


Figure 2.36: Calculated axial electric field at the cathode (absolute value), as a function of voltage, at three pressures (copper cathode in argon).

B. Comparison with literature data

We evaluated our calculated CDS lengths with an empirical relation proposed by Aston between the CDS length, d_{CDS} , and pressure and current in the discharge [134]:

$$d_{\text{CDS}} = \frac{A}{p} + \frac{B}{I^{1/2}}$$

where A and B are constants. In figure 2.37 it is indeed seen that there is a linear relationship between the calculated d_{CDS} and $I^{1/2}$ at constant pressure. The inverse proportionality between d_{CDS} and pressure at constant current is also more or less observed, although the CDS length seems to vary somewhat more than the pressure. In general, a satisfactory agreement between our calculated results and the empirical formula is found, which validates our present model.

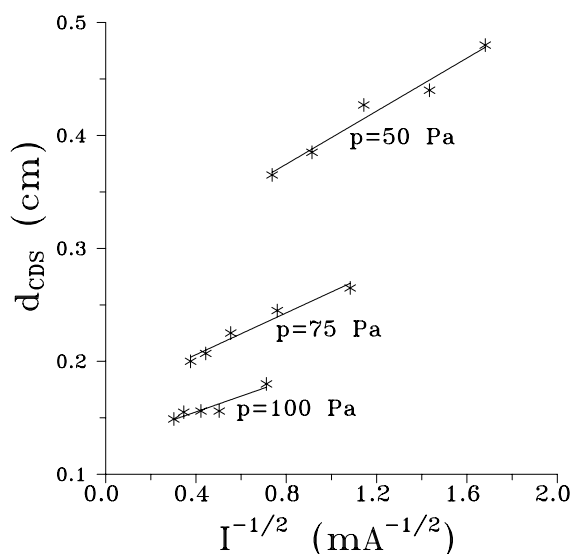


Figure 2.37: Relation between the calculated CDS length (d_{CDS}) and the discharge current, at three pressures (copper cathode in argon).

2.3.4. Energy distributions and mean energies of the species

A. Calculated energy of the electrons

Figure 2.38 shows the spatial variation of the flux energy distribution of the electrons throughout the discharge (i.e. at different positions from the cathode) at 1000 V, 75 Pa and 3.1 mA. The distribution is rather “noisy”. This is due to statistical reasons: a very high number of electrons has to be followed to obtain a completely smooth distribution. Moreover, the electrons created in the plasma by ionization collisions start in the model at discrete positions. This gives rise to a certain pattern in the distribution which is only artificial and is expected to be absent in reality.

Electrons are emitted from the cathode ($z=0$ cm, in front of the figure) with a mean energy of 4 eV. In the CDS, they gain energy by the electric field on their way to the CDS-NG interface. When they reach energies above the thresholds for excitation or ionization of the different plasma species, they can cause excitation or ionization, thereby losing energy and also (in the case of ionization) producing new electrons with lower energies. In this way, by moving towards the NG, the energy of the electrons increases due to the acceleration in the electric field, and at the same time, the energy is spread out over lower energies as a result of the collisions. At the end of the CDS (at 0.24 cm), a considerable fraction of the electrons has still not participated in any collision process in the CDS, as indicated by the peak at the maximum attainable energy (1000 eV) in figure 2.38. In the NG, the electrons do not gain much energy from the weak electric field anymore; on the contrary, they lose their energy more efficiently by collisions. Therefore, the energy distribution changes

shape: the low energy part grows whereas the high energy part diminishes slightly. The energy distribution is more or less the same in the entire NG, due to the back and forth scattering of the electrons in this region.

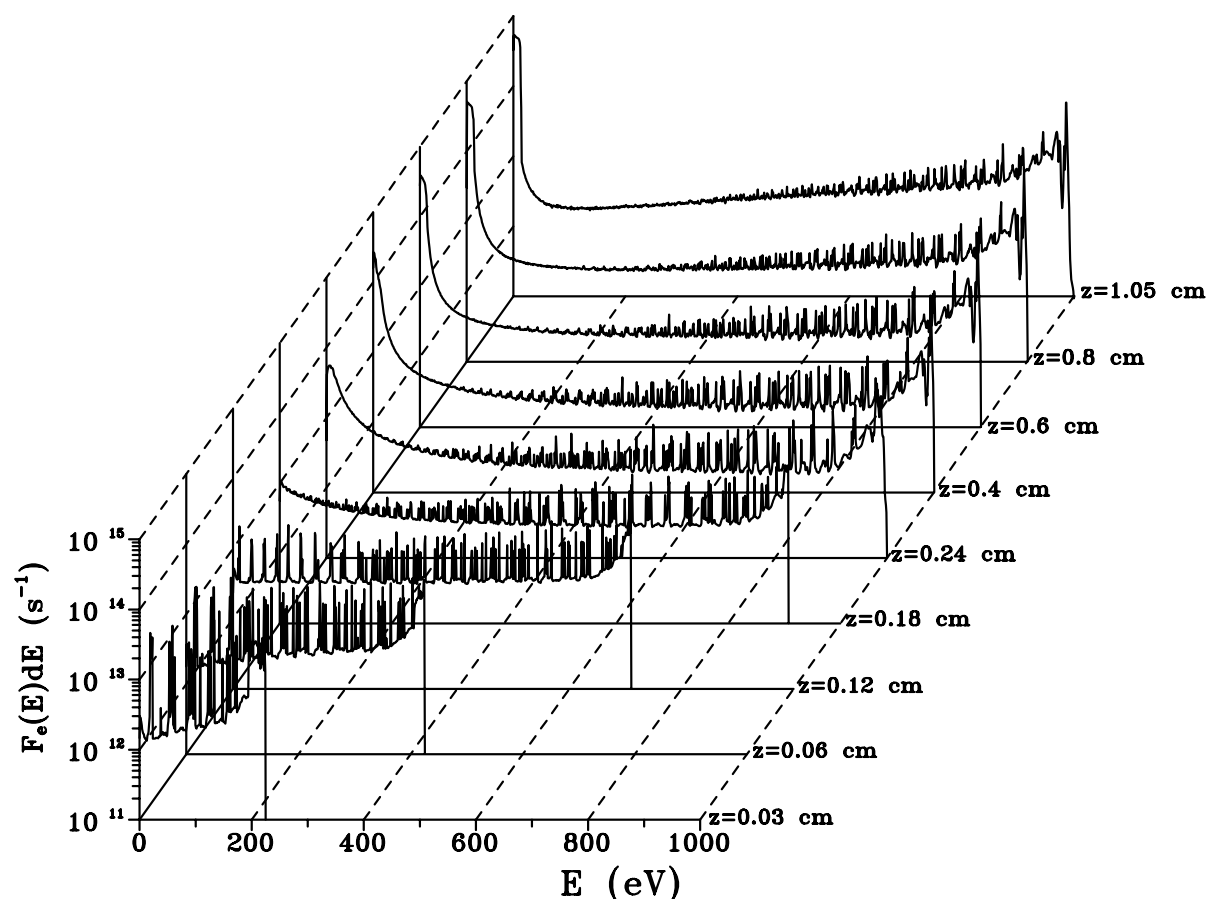


Figure 2.38: Calculated flux energy distribution of the electrons as a function of distance from the cathode (at 75 Pa, 1000 V, 3.1 mA, copper cathode in argon).

The electron energy distribution in the NG seems to consist of three distinct electron populations: (i) the slow electron group with energies too low for inelastic collisions (i.e. a few eV), (ii) the group of secondary electrons, which are emitted at the cathode but have lost energy by inelastic collisions or which have been created in the glow discharge plasma (they possess energies still high enough for inelastic collisions, i.e. ranging from several eV to slightly less than the full discharge voltage), and (iii) the primary electron group which are emitted from the cathode and have lost no energy by collisions (their energy is equal to the total voltage drop, i.e. 1000 V). At the present discharge conditions, about 50 % of the electrons belong to the slow group. The secondary electron group comprises about 48 % of the total electron

population, and about 2 % is found in the primary electron group, i.e. the ones which have traversed the discharge without any collisions.

Electron flux energy distributions have been measured with a retarding field analyzer in the NG of a helium glow discharge at a pressure of 10-15 Torr and a few hundred Volt discharge voltage [135]. It was found that most electrons have, indeed, low energies, but a small peak is observed at maximum energy. Hence, the results are in qualitative agreement with our modeling calculations.

In figure 2.39, the mean energy of the electrons throughout the discharge at 1000 V, 75 Pa and 3.1 mA is illustrated. The mean energy is low at the cathode but increases rapidly in the CDS due to the acceleration by the electric field. Since the electrons also lose energy by inelastic collisions, the mean energy is not equal to the total potential drop at the CDS-NG interface, but reaches a maximum of about 500 eV at the end of the CDS. In the NG, the mean energy decreases again to about 300-400 eV throughout the whole region, due to the energy losses from collisions.

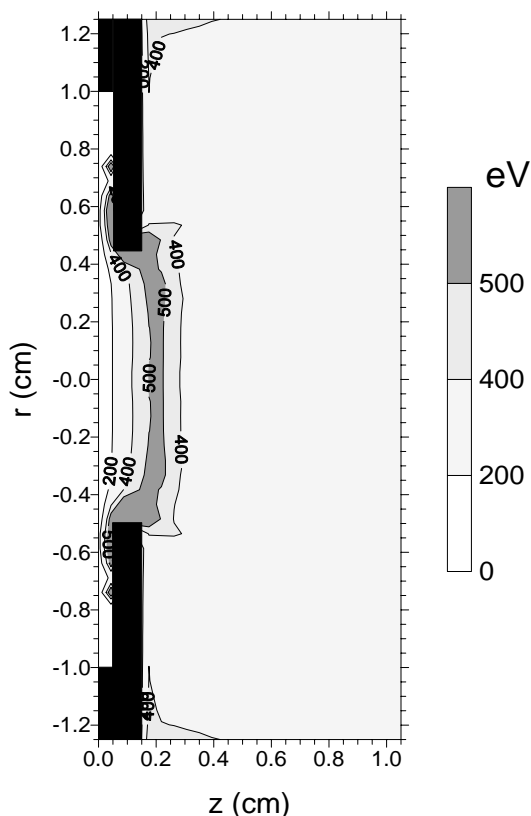


Figure 2.39: Calculated mean energy distribution of the electrons throughout the discharge (at 75 Pa, 1000 V, 3.1 mA, copper cathode in argon).

These values of 300-400 eV are only average values; indeed it is seen in figure 2.38 that electrons with energies ranging from 0 eV to 1000 eV are present in the plasma.

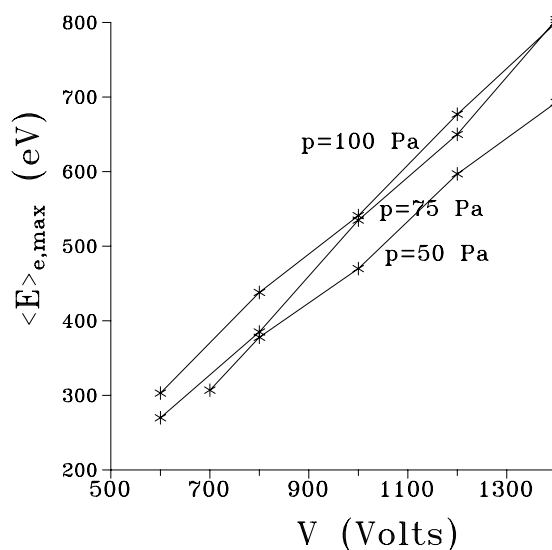


Figure 2.40: Calculated mean energy of the electrons at the maximum of its profile, as a function of voltage, at three pressures (copper cathode in argon).

Figure 2.40 shows the maximum mean energies of the electrons (i.e. at the end of the CDS) as a function of voltage and pressure. The energy rises with voltage, as is expected, since the electrons can take up more energy from the larger potential drop. It increases also slightly with pressure. This is at first sight unexpected. Indeed, at higher pressures, one expects more collisions and therefore more energy losses and hence lower energies. However, as was illustrated in figure 2.35, the CDS length decreases as pressure increases, and the electrons will undergo less collisions on the shorter distance. Both effects have to be taken into account: i.e. at higher pressure, the gas density increases, yielding more collisions per unit length, but on the other hand, the CDS length decreases, resulting in a shorter distance on which collisions are possible. Since the CDS length decreases more than linearly with pressure (see above), the net effect is that there will be less collisions at higher pressures, giving rise to slightly higher energies. By dividing the maximum mean energy by the discharge voltage, it is found that, on the average, the electrons can attain, at maximum, about 50 % of the total discharge voltage.

B. Calculated energy of the argon ions

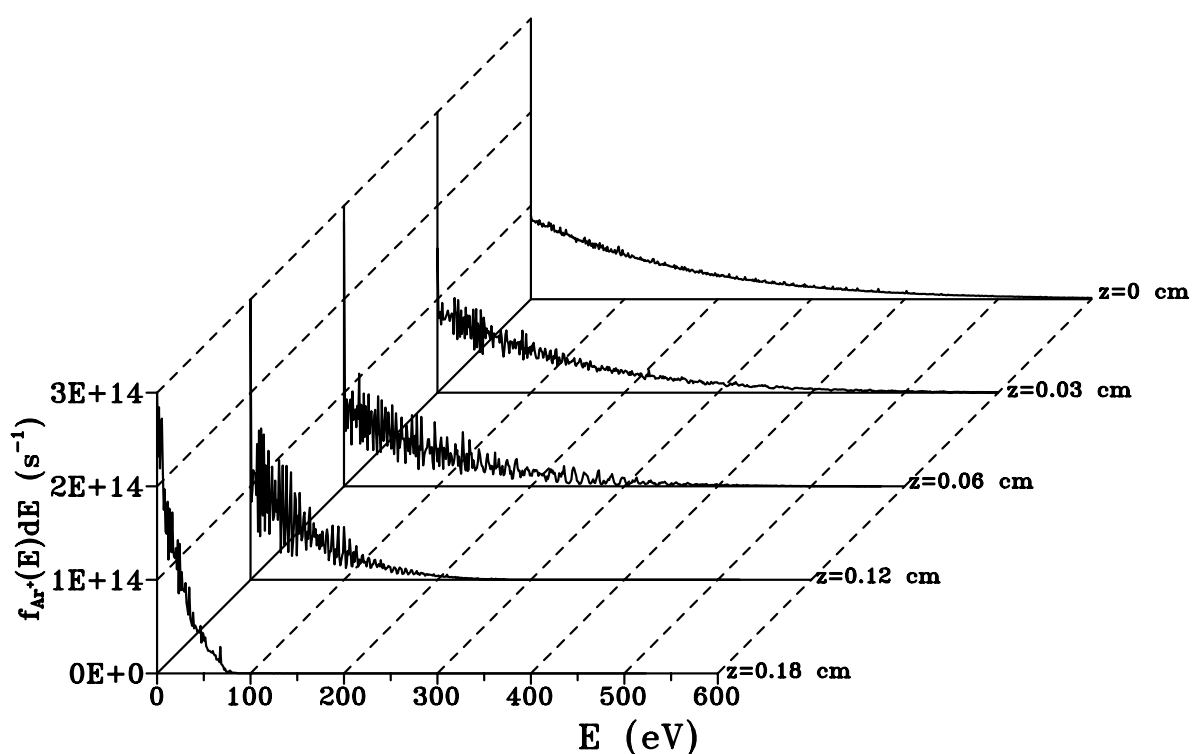
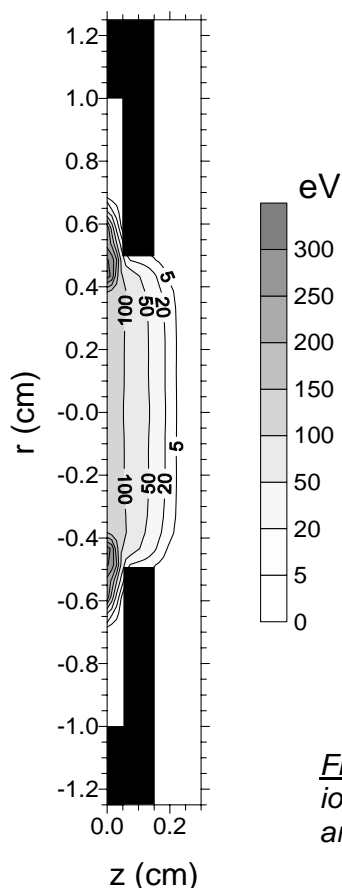


Figure 2.41: Calculated flux energy distribution of the argon ions in the CDS, as a function of distance from the cathode (at 75 Pa, 1000 V, 3.1 mA, copper cathode in argon).

The spatial variation of the flux energy distribution of the argon ions at 1000 V, 75 Pa and 3.1 mA is presented in figure 2.41. The argon ions are assumed to be more or less thermalized in the NG, so that only the CDS is shown. The argon ions start at the CDS-NG interface ($z=0.24$ cm, in front of the figure) with thermalized energies and move towards the cathode ($z=0$ cm, back of the figure), thereby gaining energy from the electric field and losing energy by collisions. Contrary to the electron energy distribution in the CDS, there is no peak at maximum energy, corresponding to ions which did not suffer any collision. Instead, the energy distribution peaks at low energy and decreases towards high energies. It can therefore be concluded that the argon ions lose their energy much more efficiently by collisions than the electrons. Indeed, the symmetric charge transfer and elastic collisions are more frequent than the electron impact ionization and excitation collisions (i.e. larger cross section, see figures 2.2 and 2.4) and lead to a stronger energy loss (i.e. the argon ions that have undergone a charge transfer collision, start again with zero energy, see Section 2.2.3). It should be noticed that the energy axis is truncated at 600 eV, i.e. lower than the total discharge voltage, because the energy axis beyond 600 eV gives no additional information.



The mean energy of the argon ions throughout the CDS, illustrated in figure 2.42, for 1000 V, 75 Pa and 3.1 mA, is also clearly lower than the electron mean energy. It is almost zero at the CDS-NG interface and increases gradually towards about 150 eV at the cathode. Near the frontplate, the ions can reach higher energies (300 eV at maximum), since they take up more energy from the strong electric field without losing much energy over such short distances. Similarly as for the electrons, the maximum mean energy of the argon ions (i.e. at the cathode), also increases clearly with voltage and slightly with pressure, as is illustrated in figure 2.43. On the average, the argon ions can reach only about 10-15 % of the total discharge voltage, since they lose their energies so efficiently by symmetric charge transfer and elastic collisions.

Figure 2.42: Calculated mean energy distribution of the argon ions in the CDS (at 75 Pa, 1000 V, 3.1 mA, copper cathode in argon).

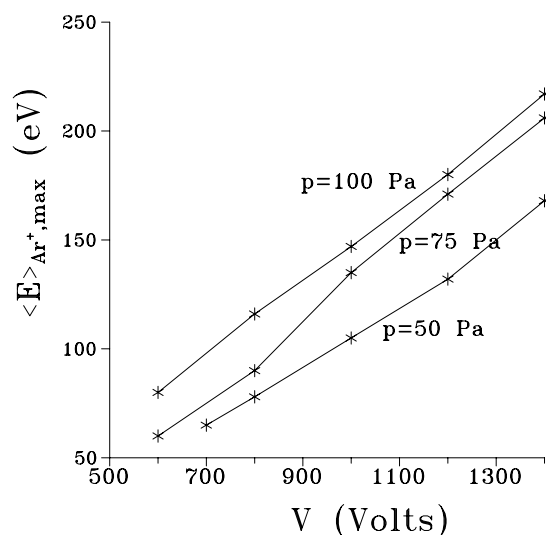


Figure 2.43: Calculated mean energy of the argon ions at the maximum of its profile, as a function of voltage, at three pressures (copper cathode in argon).

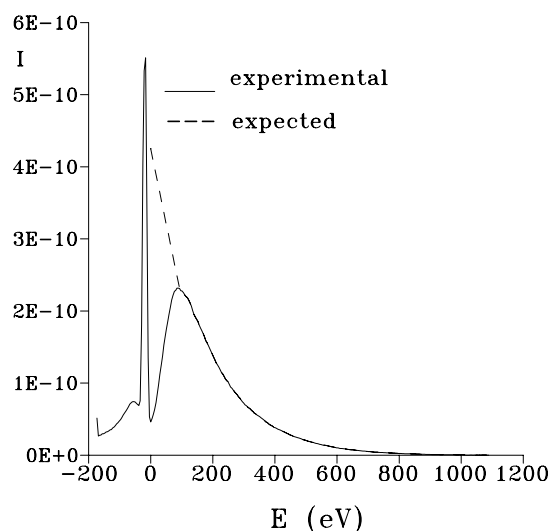


Figure 2.44: Experimental flux energy distribution of the argon ions bombarding the cathode, measured with the VG9000 glow discharge mass spectrometer (1000 V, 3 mA, copper cathode in argon).

C. Experimental flux energy distribution of the argon ions

Flux energy distributions of the argon ions bombarding the cathode in a glow discharge cell of the VG9000 mass spectrometer have been measured by van Straaten [103,136]. The energy scans were recorded with the double focussing mass spectrometer, by varying the acceleration voltage and keeping the magnetic field constant. The result at 1000 V and 3 mA is shown in figure 2.44. A dip in the distribution was observed at low energy. It was assumed that this was due to an experimental artefact. Indeed, a peak appeared at negative energy, and it was suggested that this peak corresponds to ions formed in the acceleration region outside the glow discharge cell, by symmetric charge transfer collisions of ions with low energy. The ions with low energy disappear therefore from the energy distribution, and this explains the dip at low energy. The dashed line in figure 2.44 represents the expected energy distribution, which is in good agreement with the modeling result of figure 2.41.

D. Calculated energy of the fast argon atoms

Figure 2.45 shows the spatial variation of the flux energy distribution of the fast argon atoms, at 1000 V, 75 Pa and 3.1 mA. Only the CDS is presented, since fast argon atoms exist only in this region. It should be borne in mind that the term “fast atoms” is used for those atoms with energies beyond 1 eV. Atoms with energies below 1 eV are assumed to belong to the thermalized group. This explains the dip in the distribution at 0 eV. Except from that, the energy distribution qualitatively resembles that of the argon ions (i.e. decreasing towards higher energies), which is obvious because the fast atoms are formed directly from the argon ions by symmetric charge transfer and elastic collisions. The energy distribution is however strongly shifted to lower energies compared to the argon ion distribution (energy axis truncated at 100 eV), because the atoms cannot gain energy from the electric field, they can only lose energy by collisions.

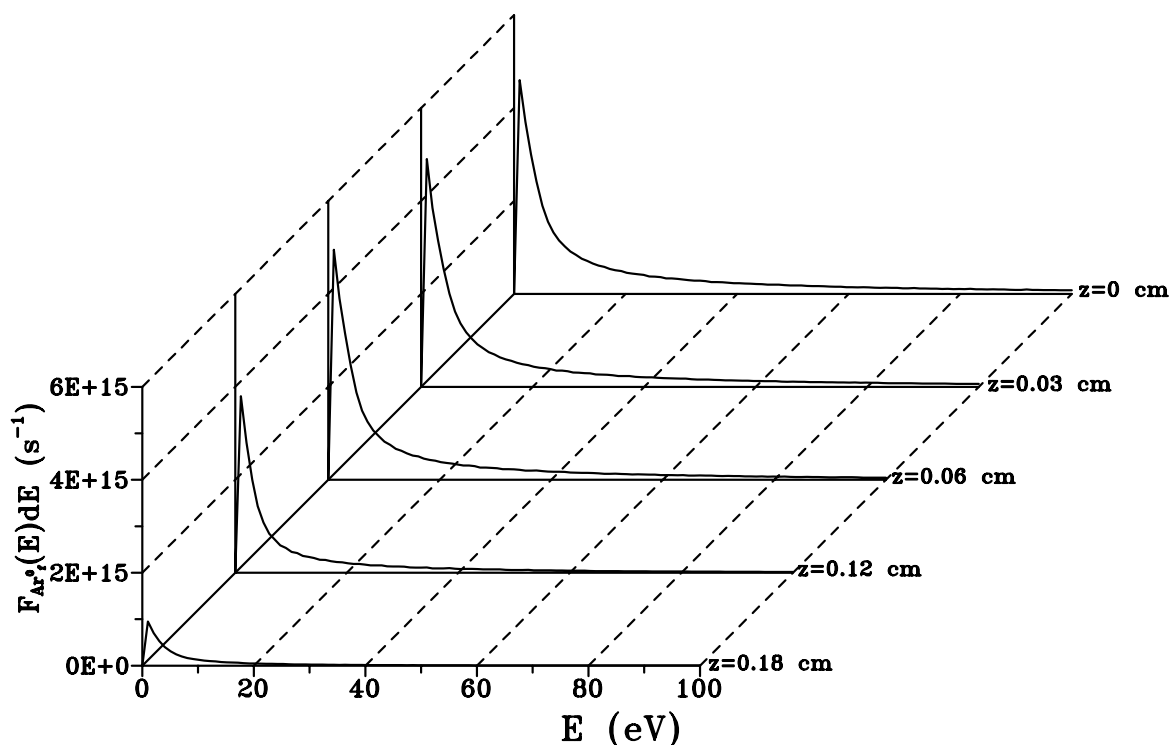


Figure 2.45: Calculated flux energy distribution of the fast argon atoms in the CDS, as a function of distance from the cathode (at 75 Pa, 1000 V, 3.1 mA, copper cathode in argon).

The mean energy of the fast argon atoms, represented in figure 2.46, for 1000 V, 75 Pa and 3.1 mA, reaches maximum values at the cathode of about 35 eV at the cell axis to about 50 eV near the front plate. The energy also increases slightly with pressure and more clearly with voltage, as appears from figure 2.47.

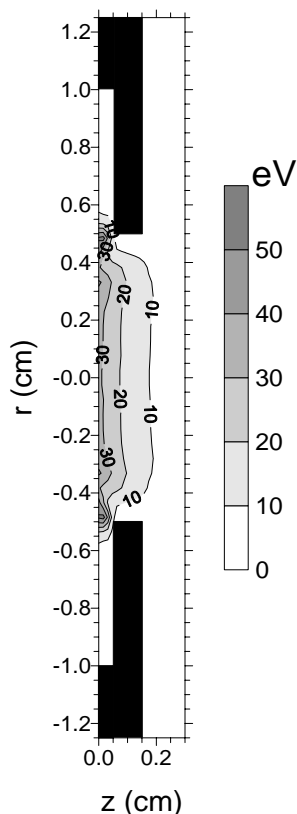


Figure 2.46: Calculated mean energy distribution of the fast argon atoms in the CDS (at 75 Pa, 1000 V, 3.1 mA, copper cathode in argon).

The argon atoms can attain however, on the average, only about 3 % of the total discharge voltage, since they cannot gain energy from the electric field.

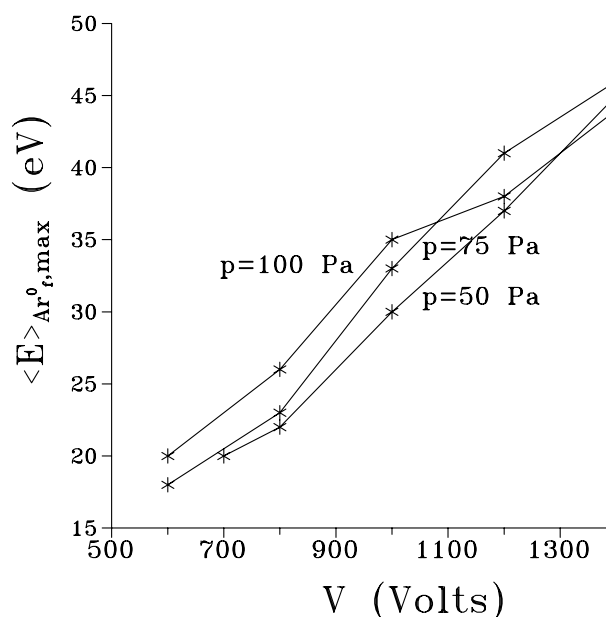


Figure 2.47: Calculated mean energy of the fast argon atoms at the maximum of its profile, as a function of voltage at three pressures (copper cathode in argon).

E. Calculated energy of the copper ions

The flux energy distribution of the copper ions as a function of distance from the cathode, at 1000 V, 75 Pa and 3.1 mA, is depicted in figure 2.48. Only the CDS is shown since the copper ions are thermalized in the NG. The copper ions start at the CDS-NG interface ($z=0.24$ cm, in front of the figure) with zero energy and they gain energy on their way to the cathode. In contrast to the energy distribution of the argon ions, the energy distribution of the copper ions is characterized by a pronounced peak at the maximum possible energy (note the logarithmic scale). This indicates that most of the copper ions originate from the NG and pass the CDS without collisions.

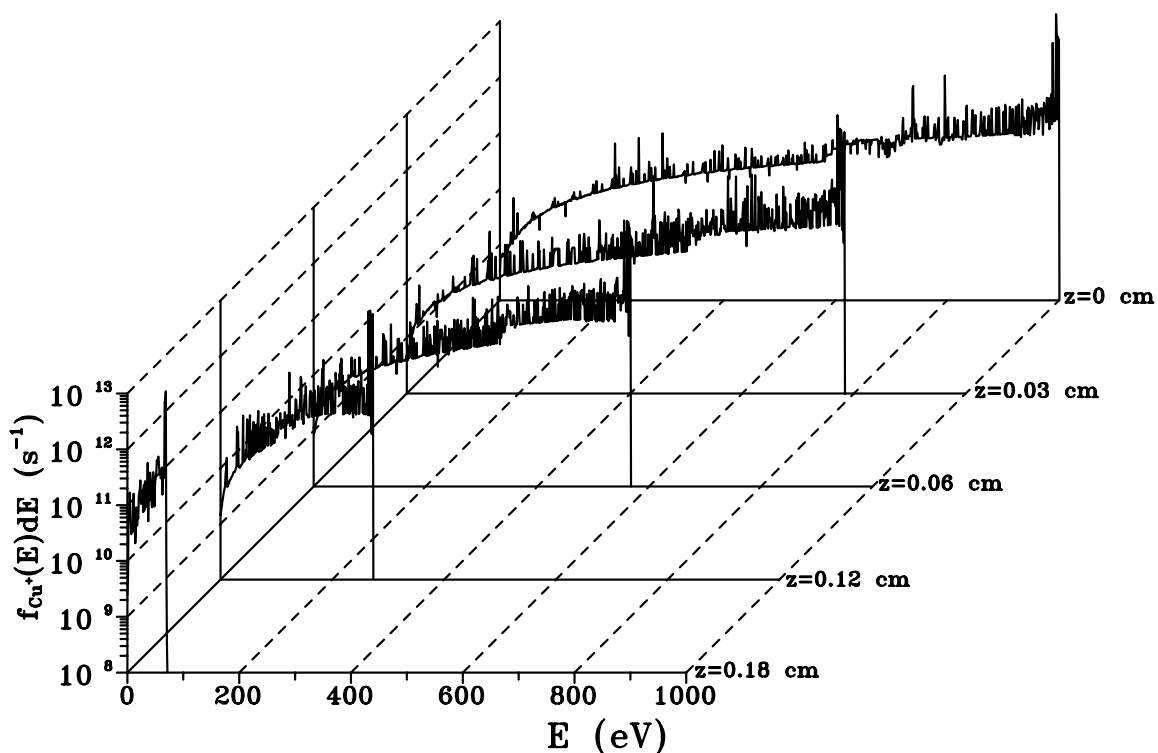
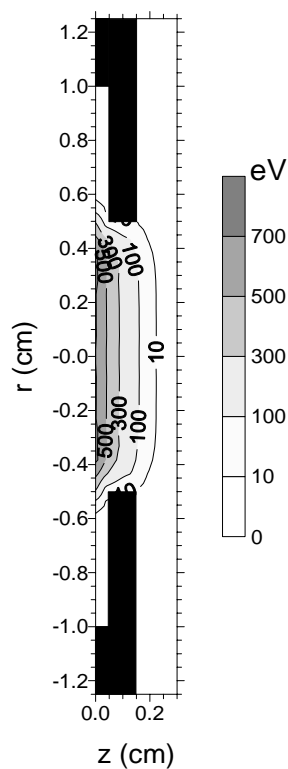


Figure 2.48: Calculated flux energy distribution of the copper ions in the CDS, as a function of distance from the cathode (at 75 Pa, 1000 V, 3.1 mA, copper cathode in argon).



The mean energy of the copper ions in the CDS is indeed significantly higher than the mean energy of the argon ions, as can be seen in figure 2.49. The mean energy of the copper ions at the maximum is presented in figure 2.50 as a function of voltage and pressure. It rises again with voltage and pressure. Moreover, from figure 2.50 is deduced that the copper ions can attain on the average about 60-80 % of the total discharge voltage, since they do not lose their energy so much in collisions.

Figure 2.49: Calculated mean energy distribution of the copper ions in the CDS (at 75 Pa, 1000 V, 3.1 mA, copper cathode in argon).

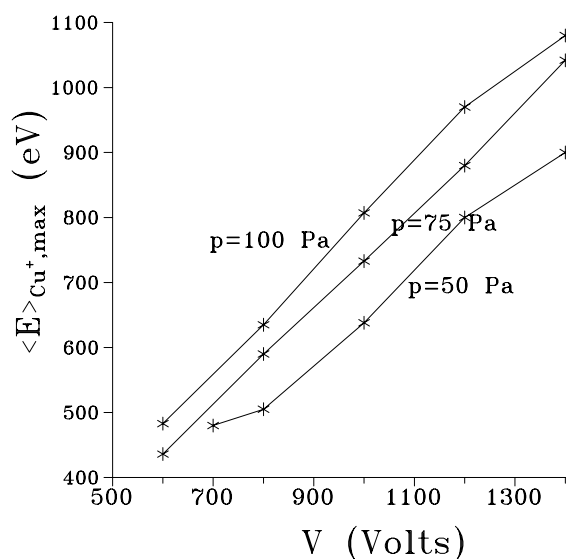


Figure 2.50: Calculated mean energy of the copper ions at the maximum of its profile, as a function of voltage, at three pressures (copper cathode in argon).

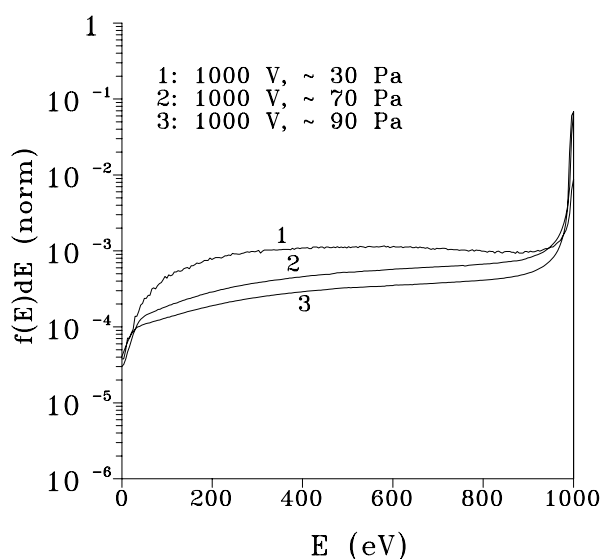


Figure 2.51: Experimental flux energy distributions of the copper ions bombarding the cathode, measured with the VG9000 glow discharge mass spectrometer (at 1000 V, three pressures, copper cathode in argon).

F. Experimental copper ion energy distribution

The copper ion energy distribution has also been measured at the cathode, with the double focussing mass spectrometer [103, 136]. The results are shown in figure 2.51. Since the pressure cannot be measured inside the glow discharge cell of the VG9000 instrument, three estimated pressure values are indicated for the three experimental energy distributions. Reasonable agreement is reached between the experimental energy distributions and the modeling result of figure 2.48.

G. Calculated sputter contributions at the cathode

From the calculated flux energy distributions of the species bombarding the cathode (i.e. argon ions, fast argon atoms and copper ions, figures 2.41, 2.45 and 2.48, resp.), the amount of sputtering is calculated. It appears that the flux of fast argon atoms bombarding the cathode is definitely higher than the fluxes of argon ions and copper ions (i.e. about $5 \times 10^{15} \text{ s}^{-1}$ compared to 10^{14} s^{-1} and 10^{13} s^{-1} , resp.). Therefore, the fast argon atoms play a dominant role in sputtering. However, the efficiency of sputtering increases with the energy of the bombarding particles (see Section 1.2.2.2), therefore it is expected that the contribution of copper ions to sputtering (self-sputtering) is non-negligible, in spite of their lower flux. It is

calculated that at 1000 V, 75 Pa and 3.1 mA, the fast argon atoms, argon ions and copper ions contribute for about 73 %, 26 % and 1 % to the sputtering, resp.

Figure 2.52 presents the relative contributions to sputtering of the fast argon atoms, argon ions and copper ions, as a function of voltage and pressure. The fast argon atoms are dominant at all voltages and pressures (i.e. about 70 %). Their contribution decreases only slightly with voltage and pressure. This dominant role was also demonstrated by Mason and coworkers [46]. From figure 2.52 follows that the argon ions always take the second place (i.e. about 25-30 %); their share increases slightly with pressure but is nearly independent of voltage. Nevertheless, the contribution of copper ions cannot be neglected. It amounts to about 0.1-5 % and increases clearly with voltage and pressure. Indeed, it was seen before that at higher voltages and pressures, the ratio of copper ion to argon ion density and flux increases, and hence the amount of self-sputtering will rise too.

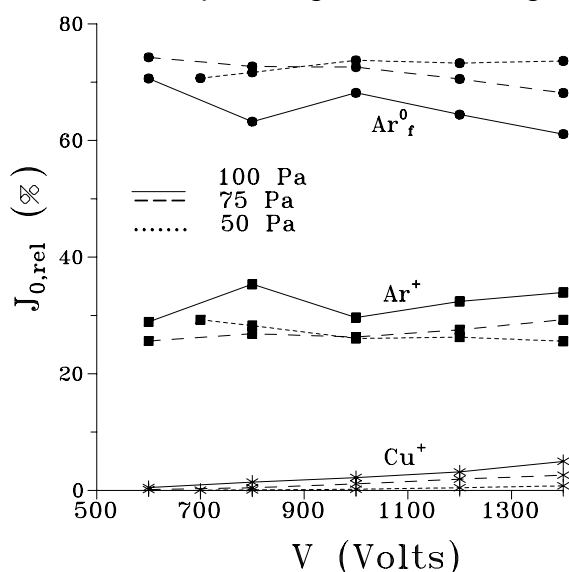


Figure 2.52: Calculated contributions to sputtering at the cathode, by fast argon atoms, argon ions and copper ions, as a function of voltage, at three pressures (copper cathode in argon).

The fact that self-sputtering could be important, was also suggested in other papers. In ref. [61,62] the sputtering contribution of copper ions was found to be larger than the one of neon ions, which was ascribed to the higher energy and of course also to the fact that neon ions are not very effective in sputtering due to their low masses. In ref. [103,136] the amount of self-sputtering was estimated by comparing the measured energy distributions of argon ions and copper ions, and a value of 42 % was found for copper in argon at 1000 V. This value does not take into account the contribution of fast argon atoms, and is therefore too high. Nevertheless, it indicates that self-sputtering can be quite significant.

H. Other plasma species

The other plasma species (bulk argon gas atoms, argon metastable atoms and sputtered copper atoms) are assumed to be thermalized throughout the plasma.

2.3.5. Collision processes of the plasma species

Since the Monte Carlo models describe the behavior of the plasma species explicitly, they can provide information about the individual collision processes incorporated in the model. Most of the collision processes in the models concern the argon gas atoms as target species, since these atoms have by far the largest density (see above). Also some collision processes with argon metastable atoms and with sputtered copper atoms as target species are incorporated. Collisions between two pairs of electrons, and between electrons and ions, are neglected, since they are less important due to the lower densities of these species.

A. Electron collision rates

Figures 2.53-2.59 show the collision rates (i.e. number of collisions per cm^3 and per sec.) of the electrons throughout the discharge, at 75 Pa, 1000 V, 3.1 mA.

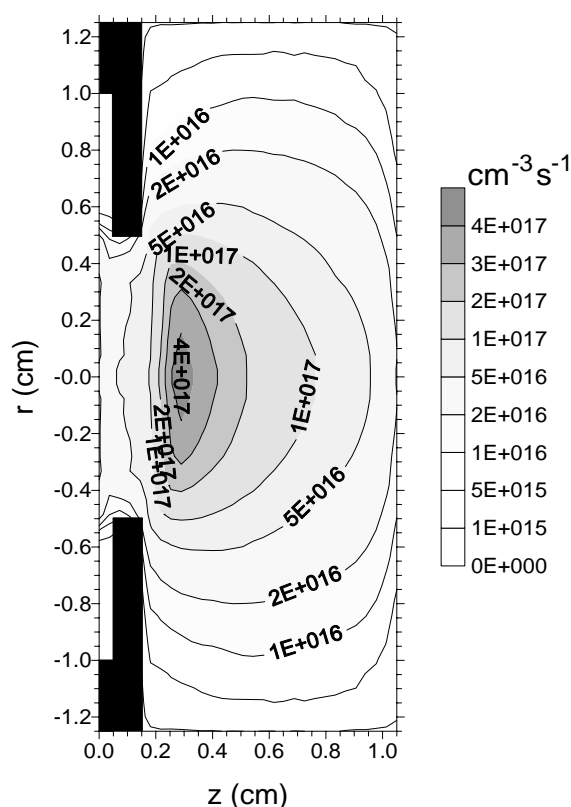


Figure 2.53: Calculated elastic collision rate of the electrons with argon atoms, throughout the discharge (at 75 Pa, 1000 V, 3.1 mA, copper cathode in argon).

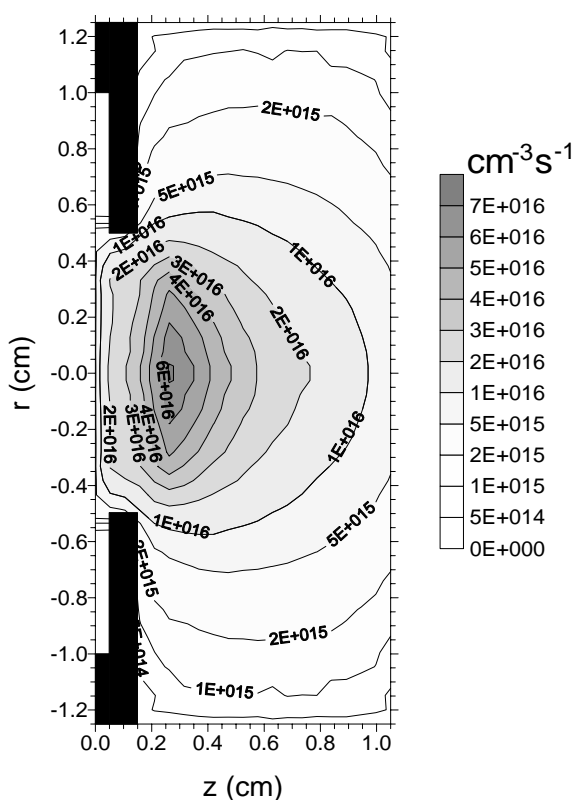


Figure 2.54: Calculated electron impact ionization rate of argon ground state atoms, throughout the discharge (at 75 Pa, 1000 V, 3.1 mA, copper cathode in argon).

The elastic collisions are the most frequent ones for the electrons. The collision rate (figure 2.53) reaches a maximum of about $4 \times 10^{17} \text{ cm}^{-3} \text{ s}^{-1}$ in the beginning of the NG and decreases gradually towards the cell walls. This is as expected since the electron density is highest at the beginning of the NG due to back and forth scattering in the plasma (see figure 2.11). The other collision rates of the electrons are all characterized by more or less the same shape. The electron impact ionization rate of argon ground state atoms (figure 2.54) has a maximum value of $7 \times 10^{16} \text{ cm}^{-3} \text{ s}^{-1}$, whereas the total electron impact excitation rate from the ground state atoms (figure 2.55) has a maximum of about $4 \times 10^{16} \text{ cm}^{-3} \text{ s}^{-1}$. The excitation processes, and the subsequent deexcitations, are responsible for the emission of light in the glow discharge. The calculated maximum of the excitation rate in the beginning of the NG is therefore in good agreement with experimental observations, since the beginning of the NG is indeed the brightest part of the discharge. The electron impact excitation rate to the argon metastable levels (figure 2.56) is about one tenth of the total excitation rate from the ground state. Hence about one tenth of the excitation leads to the metastable levels.

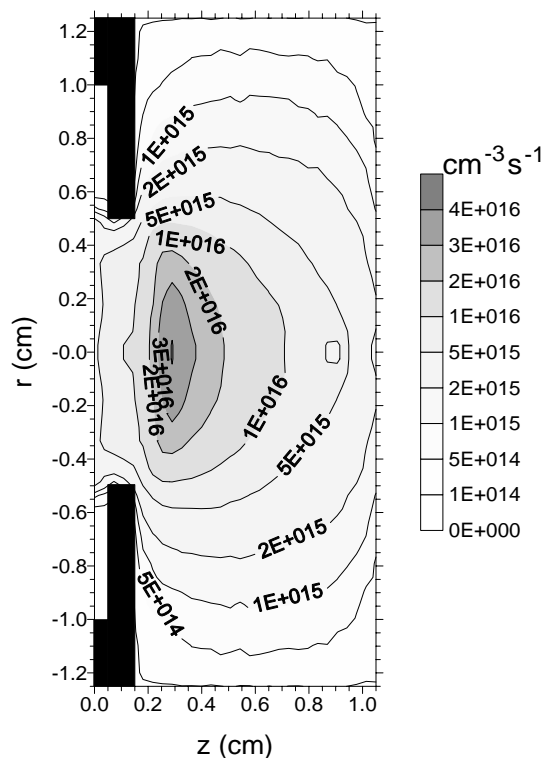


Figure 2.55: Calculated total electron impact excitation rate of argon ground state atoms, throughout the discharge (at 75 Pa, 1000 V, 3.1 mA, copper cathode in argon).

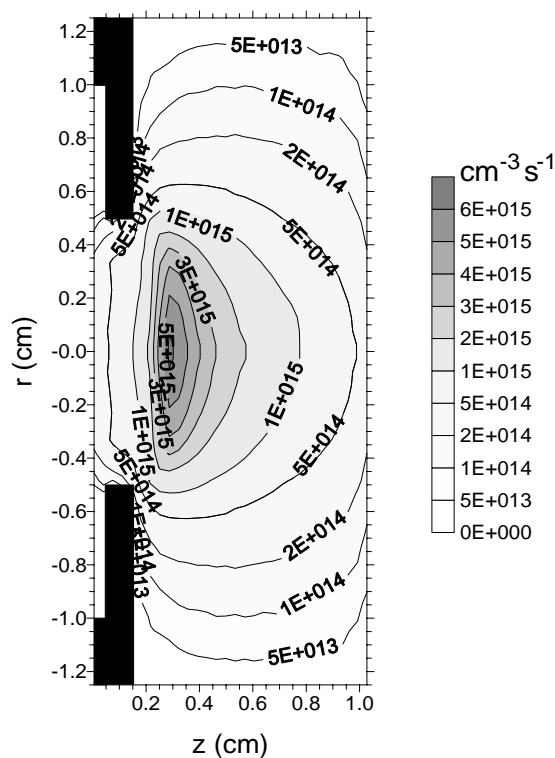


Figure 2.56: Calculated electron impact excitation rate of argon ground state atoms to the metastable level, throughout the discharge (at 75 Pa, 1000 V, 3.1 mA, copper cathode in argon).

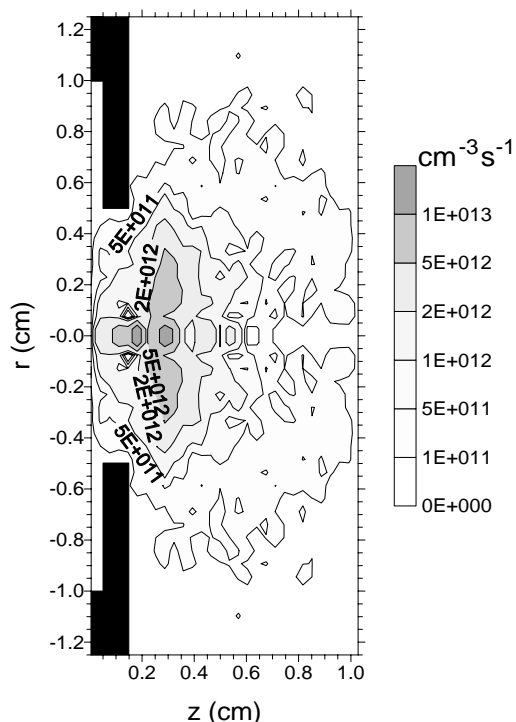


Figure 2.57: Calculated electron impact ionization rate of argon metastable atoms, throughout the discharge (at 75 Pa, 1000 V, 3.1 mA, copper cathode in argon).

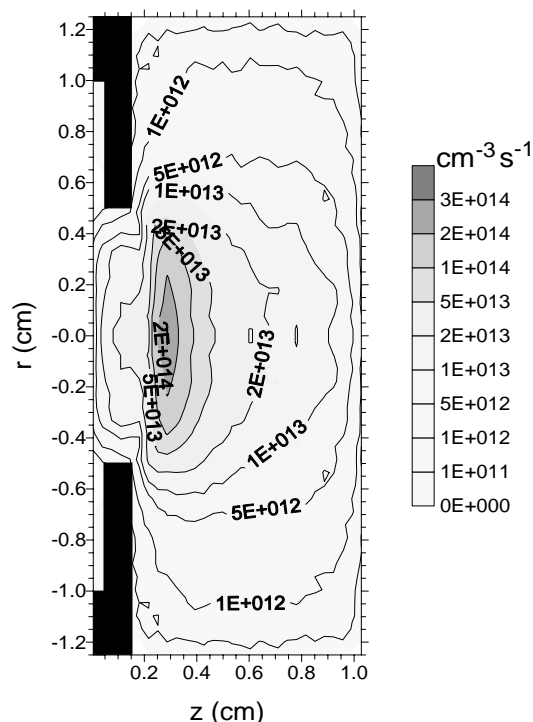
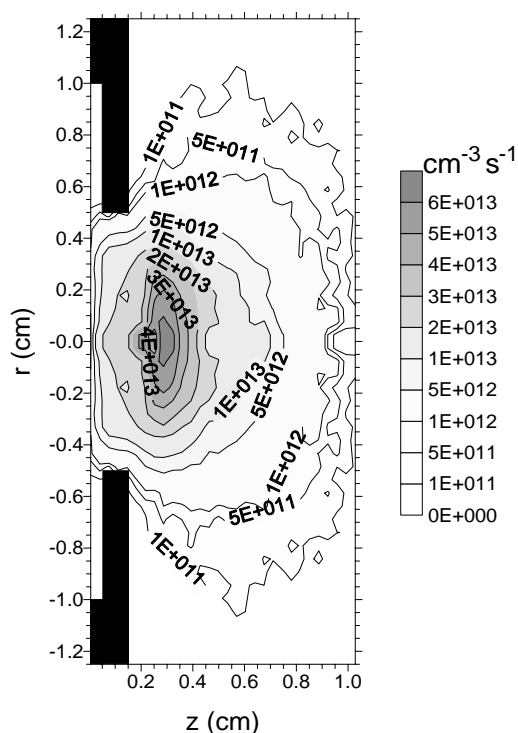


Figure 2.58: Calculated total electron impact excitation rate of argon metastable atoms, throughout the discharge (at 75 Pa, 1000 V, 3.1 mA, copper cathode in argon).

The electron impact ionization and excitation rates from the metastable levels are presented in figures 2.57 and 2.58. In spite of the higher cross sections of these processes (see figure 2.2), the collision rates are 4 and 2 orders of magnitude lower than the ionization and excitation rates from the ground state atoms, resp., due to the lower number density of the argon metastable atoms. The same is true for the electron impact ionization rate of the sputtered copper atoms (figure 2.59), which is about 3 orders of magnitude lower than the ionization rate of the argon atoms.

Figure 2.59: Calculated electron impact ionization rate of copper atoms, throughout the discharge (at 75 Pa, 1000 V, 3.1 mA, copper cathode in argon).



B. Argon ion collision rates and argon atom collision rates

In figures 2.60-2.63 the collision rates of the argon ions in the CDS are presented for 1000 V, 75 Pa and 3.1 mA. The two most important collision processes are symmetric charge transfer and elastic collisions. The rate of symmetric charge transfer (figure 2.60) is about $10^{17} \text{ cm}^{-3} \text{ s}^{-1}$ at the CDS-NG interface and increases gradually towards the cathode, reaching values of about $1.5 \times 10^{18} \text{ cm}^{-3} \text{ s}^{-1}$ close to the cathode. The rate of elastic collisions (figure 2.61) is at its maximum (ca. $4 \times 10^{17} \text{ cm}^{-3} \text{ s}^{-1}$) at the CDS-NG interface, where the argon ion energies are low, and it decreases to about $10^{17} \text{ cm}^{-3} \text{ s}^{-1}$ at the cathode.

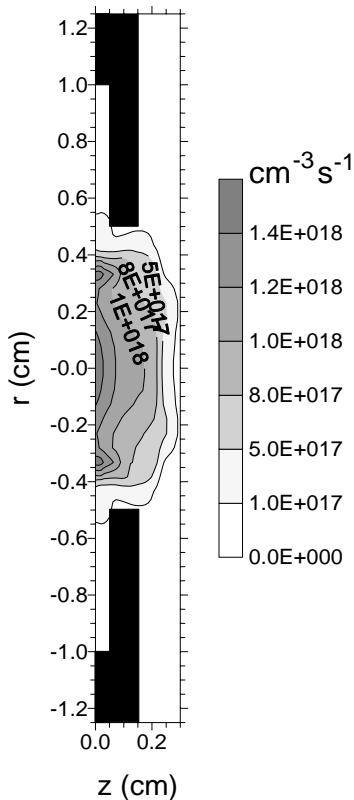


Figure 2.60

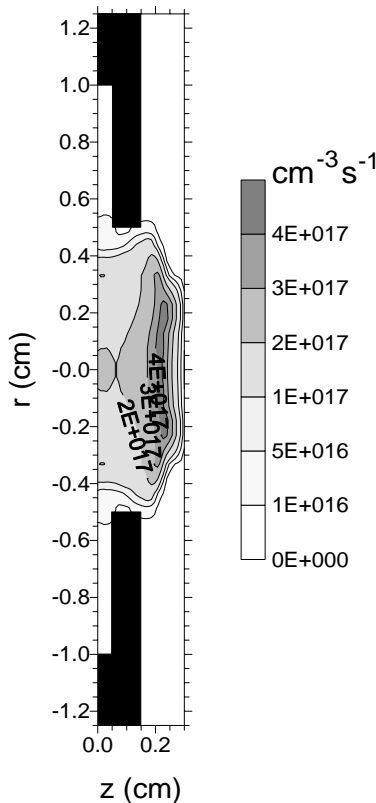


Figure 2.61

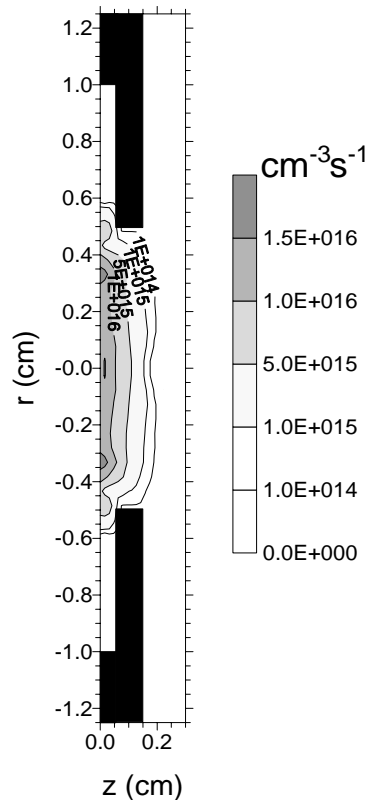
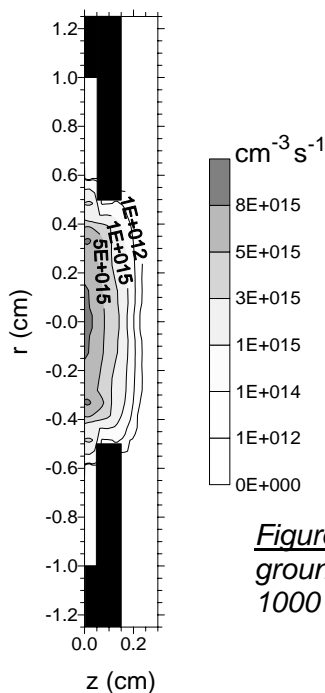


Figure 2.62

Calculated argon ion symmetric charge transfer rate (figure 2.60), argon ion elastic collision rate (figure 2.61) and argon ion impact ionization rate (figure 2.62) in the CDS (at 75 Pa, 1000 V, 3.1 mA, copper cathode in argon).

The argon ion impact ionization rate of argon ground state atoms (figure 2.62) is negligible at the CDS-NG interface but increases towards the cathode. Indeed, the cross section of this process increases with the ion energy (see figure 2.4), and the argon ions reach their highest energy close to the cathode (see figure 2.42). The argon ion impact excitation rate from the argon ground state to the metastable levels



has the same shape but is about a factor of 2 lower, as is seen from figure 2.63. Excitation processes to other levels have not been incorporated in the model, since the relevant cross sections are not available from the literature. However, it is expected that the total excitation rate by argon ion impact also reaches its maximum at the cathode. This is in agreement with experiment, since close to the cathode, a small bright layer is often observed, which can be ascribed to argon ion (and also fast atom, see below) impact excitation and subsequent deexcitation.

Figure 2.63: Calculated argon ion impact excitation rate of argon ground state atoms to the metastable levels, in the CDS (at 75 Pa, 1000 V, 3.1 mA, copper cathode in argon).

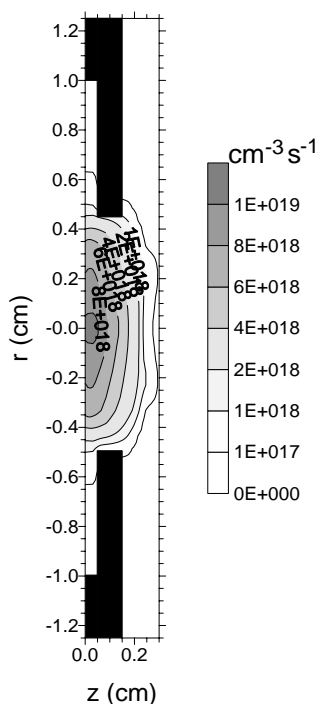


Figure 2.64

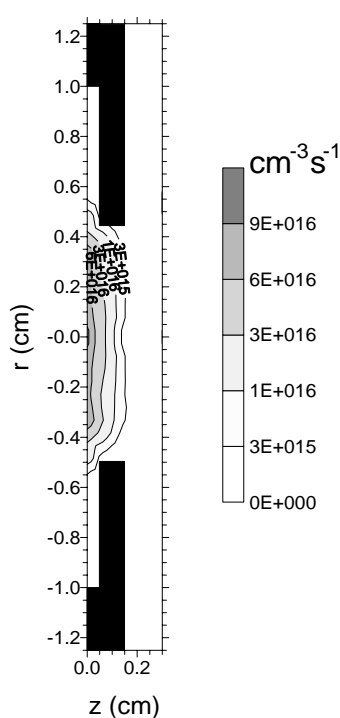


Figure 2.65

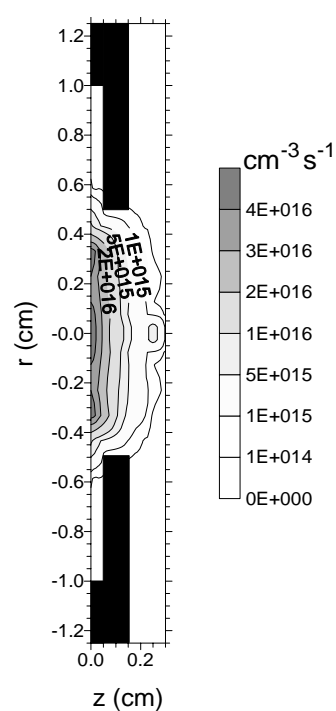


Figure 2.66

Elastic collision rate (figure 2.64), atom impact ionization rate (figure 2.65) and excitation rate to the metastable levels (figure 2.66) by the fast argon atoms in the CDS (at 75 Pa, 1000 V, 3.1 mA, copper cathode in argon).

The collision rates of the fast argon atoms in the CDS at 1000 V, 75 Pa and 3.1 mA, are illustrated in figures 2.64-2.66. The elastic collision rate (figure 2.64) is about 10^{18} - 10^{19} $\text{cm}^{-3} \text{s}^{-1}$ in the CDS, reaching a maximum close to the cathode where the fast argon atom density is at its maximum (see figure 2.13). The fast argon atom impact ionization rate and excitation rate to the metastable level (figures 2.65 and 2.66, respectively) reach their maximum values at the cathode, where the fast argon atoms have their highest energies.

C. Mechanisms for the ionization of argon atoms

Both for the argon ions and fast atoms, the ionization and excitation processes are only of minor importance, compared to charge transfer and elastic collisions. However, compared to electron impact ionization and electron impact excitation to the metastable levels (see figures 2.54 and 2.56, resp.), these processes are not negligible. Indeed, the maxima in the ionization rates by argon ion and argon atom impact are in the same order of magnitude as the maximum in the electron impact ionization rate, at the discharge conditions under consideration. Integrated over the total discharge region, the relative importances of these processes to the total ionization of argon are calculated to be about 89 % for electron impact (about 15 % in the CDS and about 74 % in the NG), about 2.5 % for argon ion impact and about 8.5 % for the fast argon atoms. In spite of the fact that electron impact ionization is clearly dominant, argon ion and atom impact ionization are not negligible at these discharge conditions. It was indeed demonstrated [137] that at discharge voltages above 600 V, the correct voltage-current characteristics of the glow discharge can only be obtained by the incorporation of these processes.

Beside the three above ionization processes, two other processes incorporated in the model, can be responsible for the formation of argon ions, i.e. electron impact ionization from the metastable levels, and metastable atom-metastable atom collisions leading to the ionization of one of the atoms (see below). However, both processes are only of minor importance at the present discharge conditions (i.e. contribution of 1 % or less).

Figure 2.67 shows the relative contributions of the different ionization mechanisms to the ionization of argon as a function of voltage, at 75 Pa. Electron impact ionization in the NG is the dominant process at all voltages. It is in the order of 70 % at 75 Pa. However, the contribution of electron impact ionization in the CDS is also quite important, especially when one takes into account that the CDS is only a small zone compared to the NG. It contributes for about 15-25 %, decreasing slightly with increasing voltage. The reason is that at high voltages the CDS becomes shorter and hence the total amount of ionization in this region decreases. This is also reflected in the pressure effect. Indeed, the relative contribution of electron impact ionization in the CDS clearly increases with decreasing pressure,

since the CDS occupies a larger part of the discharge. At 100 Pa, the contribution of electron impact ionization in the CDS and NG amount to about 8-15 % and 80 %, at 75 Pa, these values are 15-25 % and 70 %, whereas at 50 Pa, 30-45 % is due to electron impact ionization in the CDS and about 50 % is attributed to electron impact ionization in the NG. Argon ion and atom impact ionization are however not negligible for the ionization of argon. They take only place in the CDS where the argon ions and atoms can reach high energies (see above) and their contributions amount to about 1-4 % for the ions and about 3-14% for the atoms. The relative role of these processes is nearly independent of the pressure investigated, but the processes become clearly more important at high voltages, since the argon ions and atoms can reach higher energies.

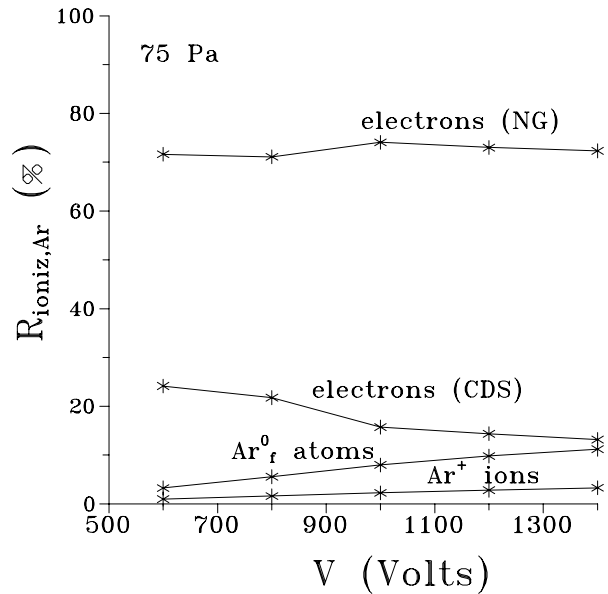


Figure 2.67: Calculated relative contributions of electron, argon ion and fast argon atom impact ionization to the ionization of argon atoms, as a function of voltage, at 75 Pa (copper cathode in argon).

D. Mechanisms for the ionization of sputtered copper atoms

For the ionization of the sputtered copper atoms, argon ion and atom impact ionization are not incorporated in the model, since the cross sections of these processes are not available in the literature, and since it is expected that these processes do not play a dominant role. However, besides electron impact ionization, two other ionization mechanisms are taken into account, i.e. Penning ionization by the argon metastable atoms, and asymmetric charge transfer with argon ions. The collision rates of both these processes, at 1000 V, 75 Pa and 3.1 mA, are represented in figures 2.68 and 2.69. Penning ionization (figure 2.68) is most significant close to the cathode, where the argon metastable atom density is at its maximum (see figure 2.15). Asymmetric charge transfer (figure 2.69) is especially important in the center of the NG, where the argon ion density is highest (see figure 2.8). By comparison of the numerical values of figures 2.59, 2.68 and 2.69, it can be concluded that Penning ionization is the dominant ionization mechanism at the present discharge conditions. Integrated over the total three-dimensional geometry, the relative contributions of Penning ionization, asymmetric charge transfer and electron impact ionization amount to about 59 %, 37 % and 4 %, respectively. Hence, Penning ionization and asymmetric charge transfer are clearly more

important than electron impact ionization for the copper atoms. Both these processes are excluded for the ionization of argon atoms; this explains why the ionization degree of copper is much higher than the one for argon.

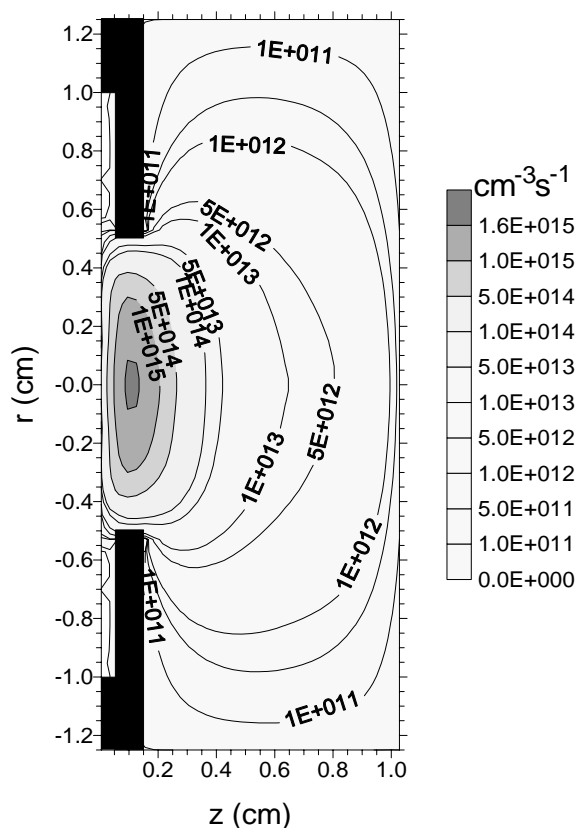


Figure 2.68: Calculated Penning ionization rate of sputtered copper atoms by argon metastable atoms, throughout the discharge (at 75 Pa, 1000 V, 3.1 mA, copper cathode in argon).

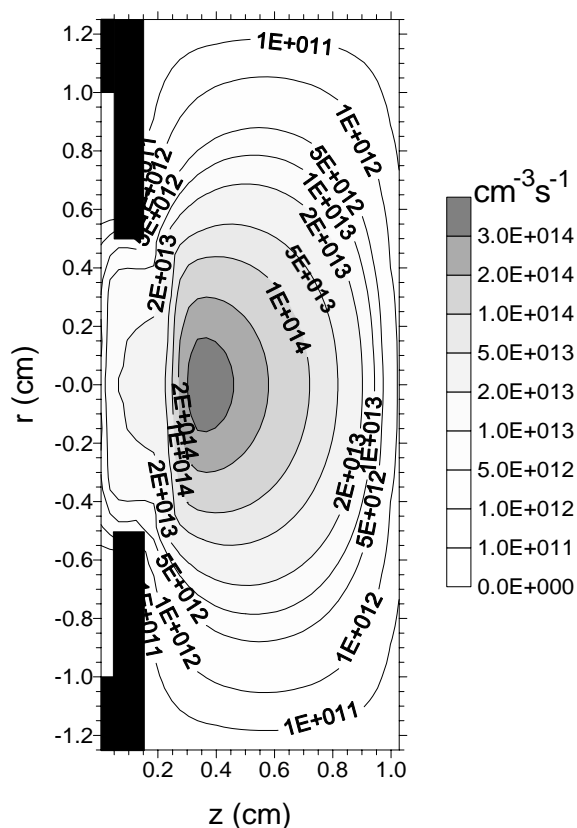


Figure 2.69: Calculated asymmetric charge transfer ionization rate of sputtered copper atoms by argon ions, throughout the discharge (at 75 Pa, 1000 V, 3.1 mA, copper cathode in argon).

In figure 2.70, the relative contributions of Penning ionization, asymmetric charge transfer and electron impact ionization to the ionization of the sputtered copper atoms are presented as a function of voltage at three pressures. The contribution of electron impact ionization was always found to be of minor importance (i.e. in the order of 2-5 %), increasing slightly with pressure, but nearly independent of voltage. The relative roles of Penning ionization and asymmetric charge transfer do not change considerably with voltage, but are strongly dependent on the pressure, as appears from figure 2.70. Indeed, Penning ionization is clearly more important at low pressures (i.e. about 90 % at 50 Pa, about 60 % at 75 Pa and about 35-40 % at 100 Pa), whereas the opposite was found for asymmetric charge

transfer (i.e. about 7-8 % at 50 Pa, about 30-40 % at 75 Pa and about 50-60 % at 100 Pa). These voltage and pressure effects are in qualitative agreement with literature data [138], where it is stated that Penning ionization is dominant in low pressure, low current discharges and that asymmetric charge transfer becomes increasingly important at high pressure, high current glow discharges.

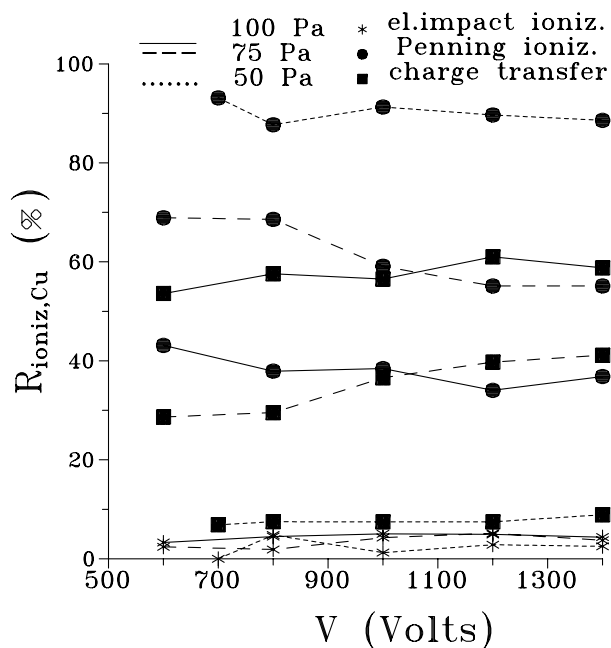


Figure 2.70: Calculated relative contributions of electron impact ionization, Penning ionization and asymmetric charge transfer to the ionization of sputtered copper atoms, as a function of voltage, at three pressures (copper cathode in argon).

E. Production processes of the metastable argon atoms

Some of the processes described above, are important in determining the density of the argon metastable atoms. The main production processes of the argon metastable atoms are argon ion and atom impact excitation close to the cathode (see figures 2.63 and 2.66, resp.), and electron impact excitation at the beginning of the NG (see figure 2.56). Integrated over the complete three-dimensional geometry, these processes account for about 17 %, 71 % and 12 %, respectively, at 1000 V, 75 Pa and 3.1 mA. The fact that argon ion and especially argon atom impact excitation are so significant was not realized up to now. The cross sections we adopted for these processes have to be considered as an upper limit. We have lowered them already by a factor of 2 (see Section 2.2.3), but it may still be that their contributions are somewhat overestimated and cannot be considered as quantitative data. However, even when lowering the cross sections by a factor of 10 or 100, the contributions of these processes remained dominant [112], so that it can at least qualitatively be concluded that they play an important role. Production of argon metastable atoms by electron-ion radiative recombination can be considered negligible (i.e. the contribution was calculated to be only 0.005 %). The relative order of importance of the three production processes is maintained at all discharge

conditions investigated; nevertheless, the relative contribution of electron impact excitation rises slightly with decreasing voltage, since the argon ions and atoms can then not reach such high energies and will not cause so much excitation. Electron recombination can be considered negligible as production process at all discharge conditions investigated (i.e. always less than 0.02 %).

F. Loss processes of the metastable argon atoms

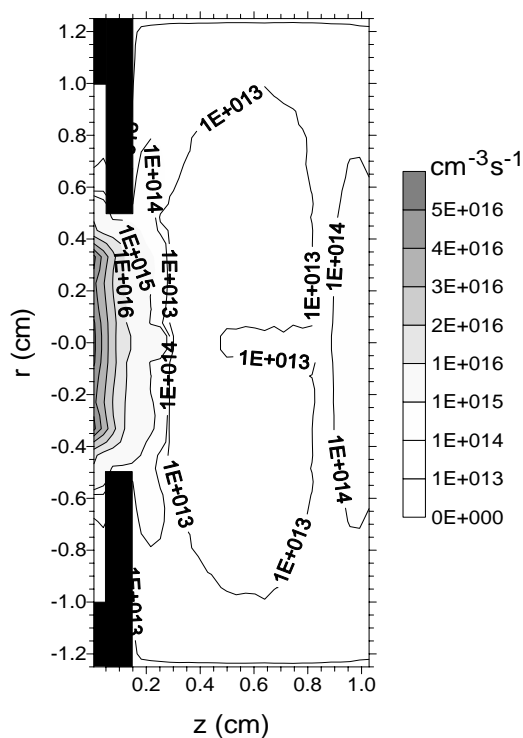


Figure 2.71: Calculated (local) loss rate of argon metastable atoms by diffusion throughout the discharge (at 75 Pa, 1000 V, 3.1 mA, copper cathode in argon).

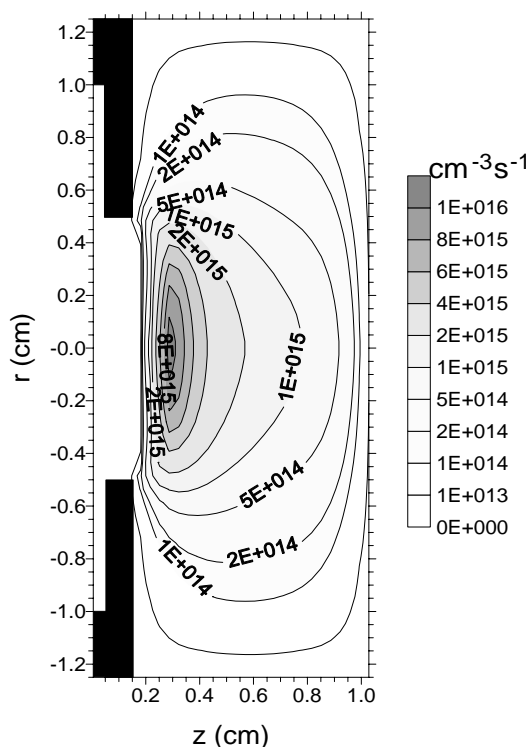


Figure 2.72: Calculated loss rate of argon metastable atoms by electron collisional transfer to the nearly energy levels, throughout the discharge (at 75 Pa, 1000 V, 3.1 mA, copper cathode in argon).

Concerning the loss processes of argon metastable atoms, diffusion towards regions of lower density together with deexcitation at the walls is mainly responsible for the loss of metastable atoms. The rate of this loss process at 1000 V, 75 Pa and 3.1 mA, is depicted in figure 2.71. Integrated over the total discharge volume, it amounts to about 82 % of the total loss. Besides diffusion, transfer to the nearby energy levels by collisions with slow electrons (electron quenching, see figure 2.72) is also a significant loss process, especially in the NG where the slow electron density is high (see above). It contributes for about 11 % over the total discharge region at the present discharge conditions. Penning ionization (see figure 2.68) and metastable atom - metastable atom collisions (figure 2.73) also account for a small part to the total loss (i.e. about 3.7 % and 3.0 %, resp., at 1000 V, 75 Pa and 3.1 mA) and are notable close to the cathode, where the sputtered copper atom density and the metastable atom density (see above) are at their maximum.

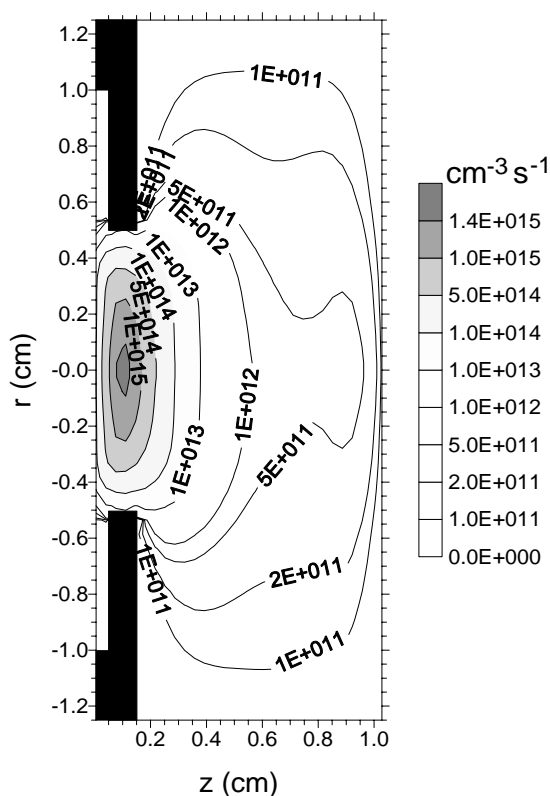


Figure 2.73: Calculated loss rate of argon metastable atoms by metastable atom - metastable atom collisions, throughout the discharge (at 75 Pa, 1000 V, 3.1 mA, copper cathode in argon).

The remaining processes can be considered negligible at the present discharge conditions. Indeed, electron impact excitation and ionization from the metastable levels (see figures 2.57 and 2.58 for the collision rates) contribute to about 0.3 % and 0.02 %, respectively, and two-body and three-body collisions with argon atoms (for the loss rates, see figures 2.74 and 2.75) amount to about 0.1 % and 0.01 %, respectively.

The relative importances of the loss processes remain the same at all discharge conditions investigated. Diffusion seems always to be the dominant loss mechanism, and it becomes still more important at lower pressures and lower voltages (i.e. 72-80 % at 100 Pa, 76-85 % at 75 Pa and 87-97 % at 50 Pa). Electron quenching becomes a little more significant at higher pressures (i.e. about 2-7 % at 50 Pa, 10-12 % at 75 Pa and about 12-18 % at 100 Pa). The losses due to Penning ionization and metastable atom - metastable atom collisions increase

slightly with pressure and voltage (ranging from 0.1 and 0.4 %, resp. at the lowest pressure and voltage values investigated, to about 9 and 6 %, resp. at the highest

pressure and voltage). The remaining four processes remain of minor significance at all discharge conditions investigated.

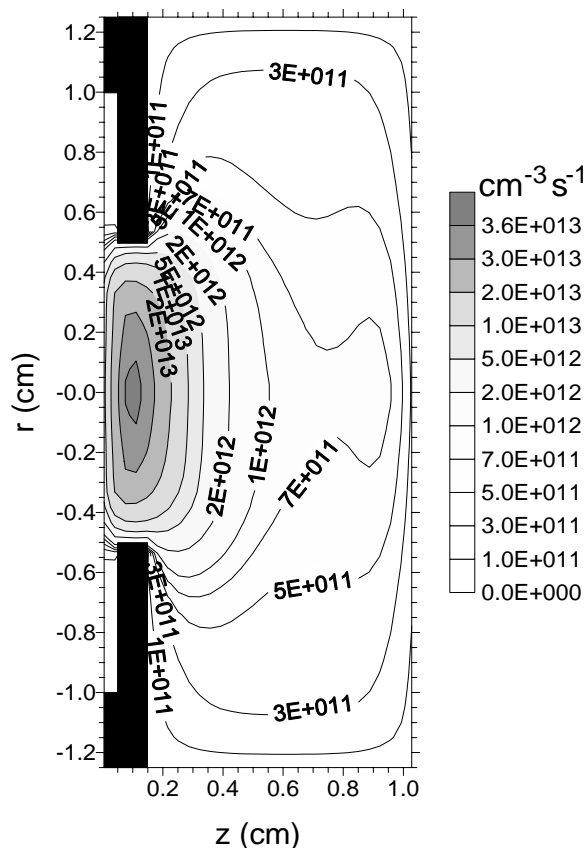


Figure 2.74: Calculated loss rate of argon metastable atoms by two-body collisions with argon ground state atoms, throughout the discharge (at 75 Pa, 1000 V, 3.1 mA, copper cathode in argon).

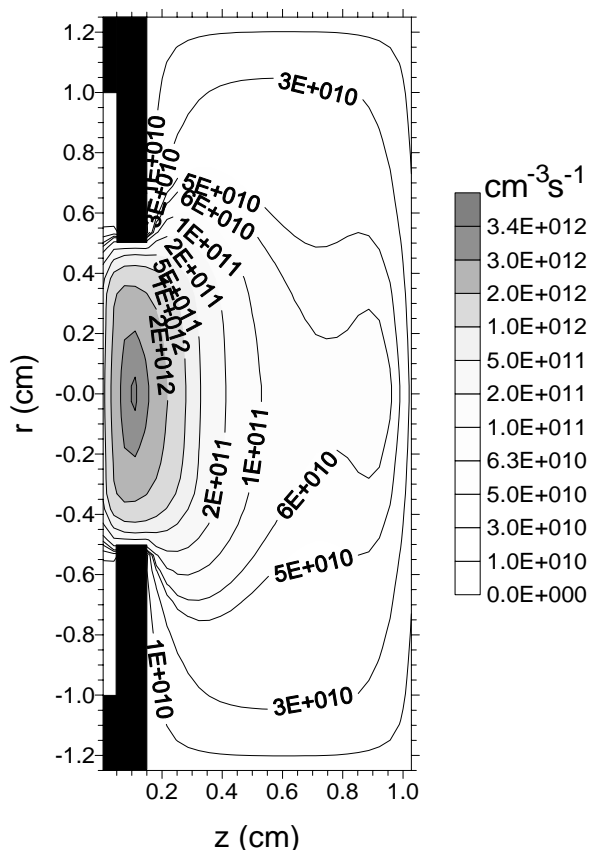


Figure 2.75: Calculated loss rate of argon metastable atoms by three-body collisions with argon ground state atoms, throughout the discharge (at 75 Pa, 1000 V, 3.1 mA, copper cathode in argon).

From these loss rates, the lifetime of the metastable argon atoms was estimated to be 10^{-4} - 10^{-5} sec. This is considerably longer than the lifetimes of the other energy levels, which can decay to the ground state by emission of radiation (i.e. the Einstein transition probabilities are typically at the order of 10^8 s^{-1} , hence the lifetimes of these energy levels are estimated to be about 10^{-8} sec).

2.3.6. Crater profiles and etching rates at the cathode

From the flux energy distributions of the plasma species bombarding the cathode as a function of the radial position, the crater profile at the cathode surface due to sputtering can be calculated. Since entire flux energy distributions at each different radial position require too much computer space, we used the fluxes and mean energies of the bombarding species as a function of radial position. From these fluxes and mean energies, the flux of sputtered copper atoms as a function of radial position was obtained. These “sputter fluxes” as a function of radial position were only used as relative values. The absolute values at each radial position are obtained by relating the relative numbers to the total sputter flux calculated from the total flux energy distribution at the cathode, which is more accurate.

A considerable fraction of the sputtered atoms is, however, again redeposited on the cathode due to backdiffusion. Indeed, at the present discharge conditions, the total flux of sputtered copper atoms was calculated to be $3.8 \times 10^{16} \text{ s}^{-1}$, whereas the total flux of redeposited copper atoms was $2.2 \times 10^{16} \text{ s}^{-1}$, leading to a net flux of sputtered atoms of $1.6 \times 10^{16} \text{ s}^{-1}$ (i.e. about 43 % of the total sputtered flux). It is the net flux of sputtered copper atoms as a function of radial position that gives rise to the crater profile. The conversion from flux to erosion rate is accomplished in the following way [136]:

$$ER = J_{\text{sput,net}} \frac{M}{N_A \rho}$$

where ER is the erosion rate (in cm/sec), $J_{\text{sput,net}}$ is the net sputtered flux (in $\text{cm}^{-2} \text{ s}^{-1}$), M and ρ are the atomic weight (g/mol) and density of the sample material ($\rho_{\text{Cu}} = 8.92 \text{ g/cm}^3$ [139]), and N_A is Avogadro’s number. The calculated crater profile after sputtering during one hour, at 1000 V, 75 Pa and 3.1 mA, is presented in figure 2.76. The shape of the crater profile as well as the absolute numbers of the crater depth (order of μm) are in reasonable agreement with experiment [140]. The modeled crater is much deeper at the sides than in the center. The reason for this is twofold. First, the equipotential surfaces in the CDS (see figure 2.32) are not completely parallel to the sample surface, but are bent in such a way that

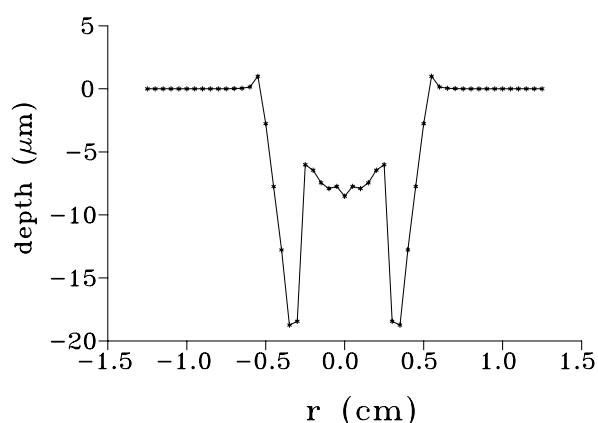


Figure 2.76: Calculated crater profile after one hour of sputtering at the cathode (at 75 Pa, 1000 V, 3.1 mA, copper cathode in argon).

the plasma species will bombard the cathode primarily at the edges of the crater. This explanation was given by Jakubowski [141] and was visualized by SIMION simulations [136,140,141] (see for example figure 2.77 [136]).

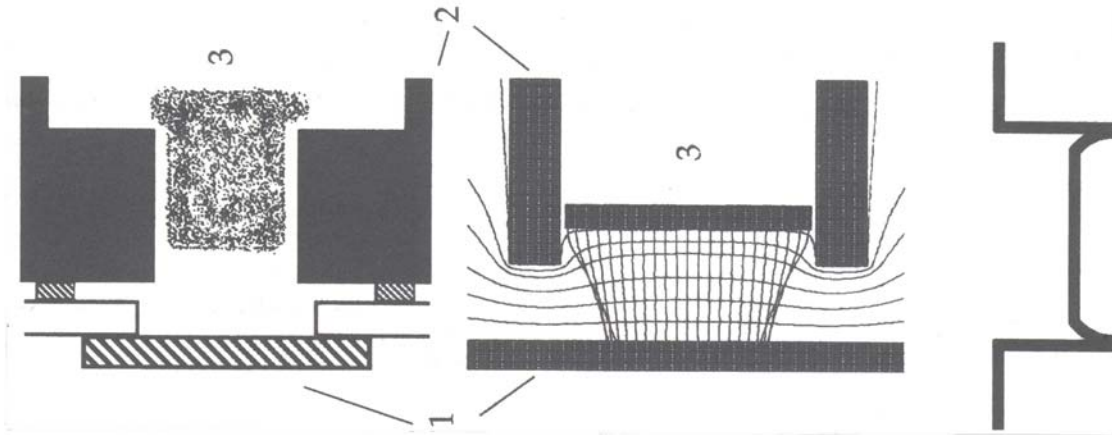


Figure 2.77: SIMION simulation of the trajectories of ions in the CDS, and schematic representation of the expected crater profile; (1) cathode; (2) anode; (3) negative glow [136].

Moreover, it was found in our calculations that also the energies of the bombarding plasma species are highest at the edges of the sample surface, due to the strong electric field in the vicinity of the front plate (see above, figures 2.42, 2.46 and 2.49). Since sputtering increases with the energy of the bombarding particles, the crater will, also for this region, be deepest at the edges. The crater edge effect [i.e. $(ER_{\text{edge}} - ER_{\text{center}})/ER_{\text{center}}$] was theoretically calculated to be about 130 %, which is still lower than the experiment, where typical values of about 200-400 % are encountered [140].

A second interesting feature of figure 2.76 is the fact that the crater bottom is not completely flat, but is more or less concave. Experimentally, concave, convex and flat crater bottoms can be obtained, depending on the discharge conditions. A convex or concave crater bottom is also the result of radially inhomogeneous sputtering. Indeed, in a model where radially homogeneous sputtering was assumed [136], only a convex crater bottom could be predicted, based on redeposition. Also the non-steep crater walls of the modeling result are backed up by the measured profiles [140], although the effect is not so pronounced in the experimental results. Finally, a small rise in the crater profile, further than 0.5 cm from the center, is observed in the calculated profile. This is due to the fact that more material is redeposited on the cathode than is sputtered away. In the experimental crater profiles, such a rise is also observed, but it is more pronounced than in the

calculated result. Nevertheless, the modeling calculations are already able to explain at least qualitatively the typical experimental crater profiles.

The influence of pressure and voltage on the calculated crater profiles is presented in figures 2.78 and 2.79.

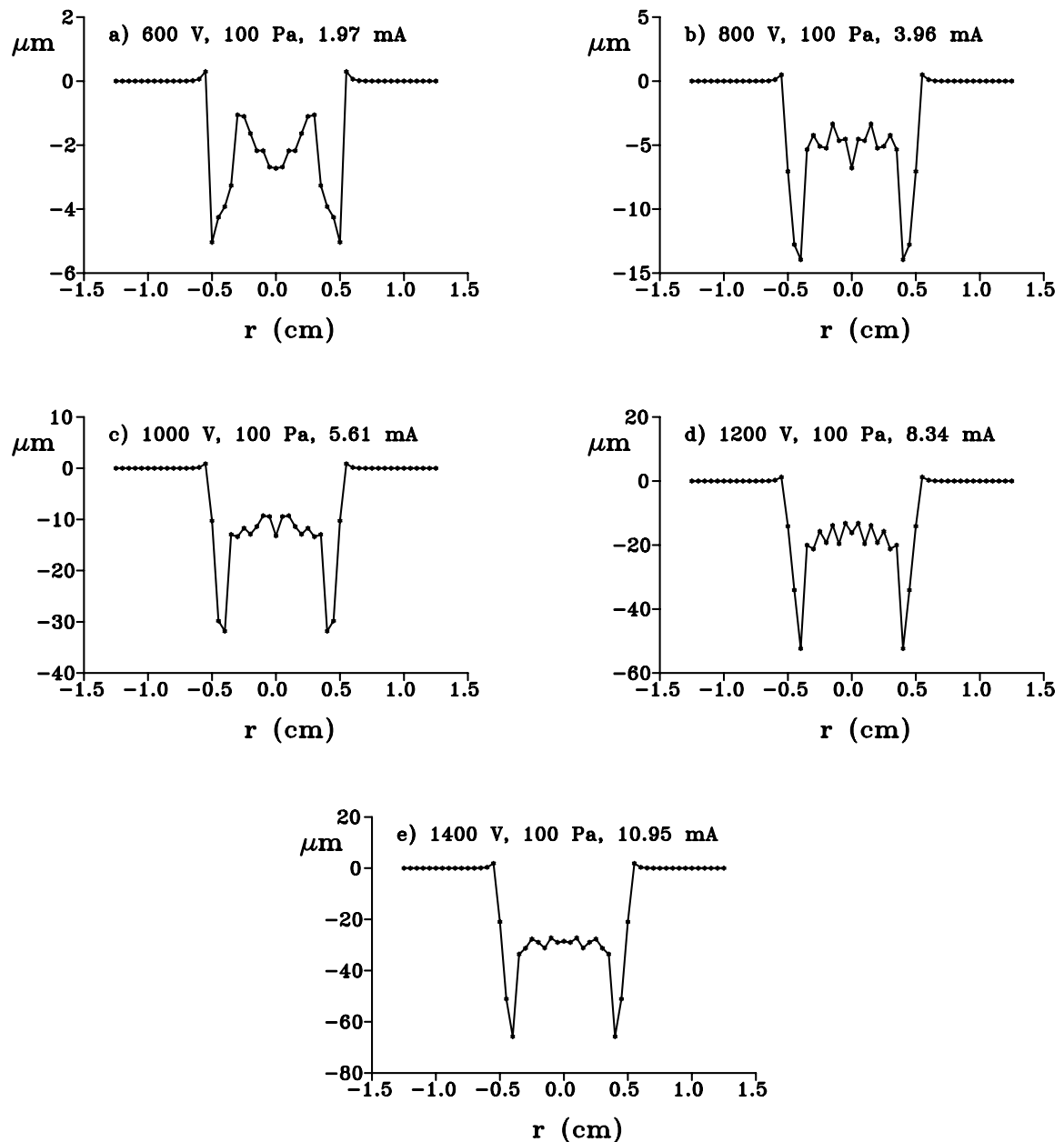


Figure 2.78: Calculated crater profiles after one hour of sputtering, at constant pressure (100 Pa) for five different voltages (and currents) (copper cathode in argon).

Figure 2.78 illustrates the effect of the voltage at constant pressure. It is seen that at increasing voltages, the depth of the crater profile increases. But also the shapes of the crater profiles change considerably. At low voltage and current, the crater profile has a pronounced concave shape. The crater profile calculated at 600 V, 100 Pa and 1.97 mA is unfavorable for depth profiling, since the depth is not constant as a function of radial position. However, when the voltage increases (and hence also the current when pressure is kept constant) the crater bottom becomes more and more flat, as can be observed in the crater profiles obtained for 1000 V, 1200 V and 1400 V.

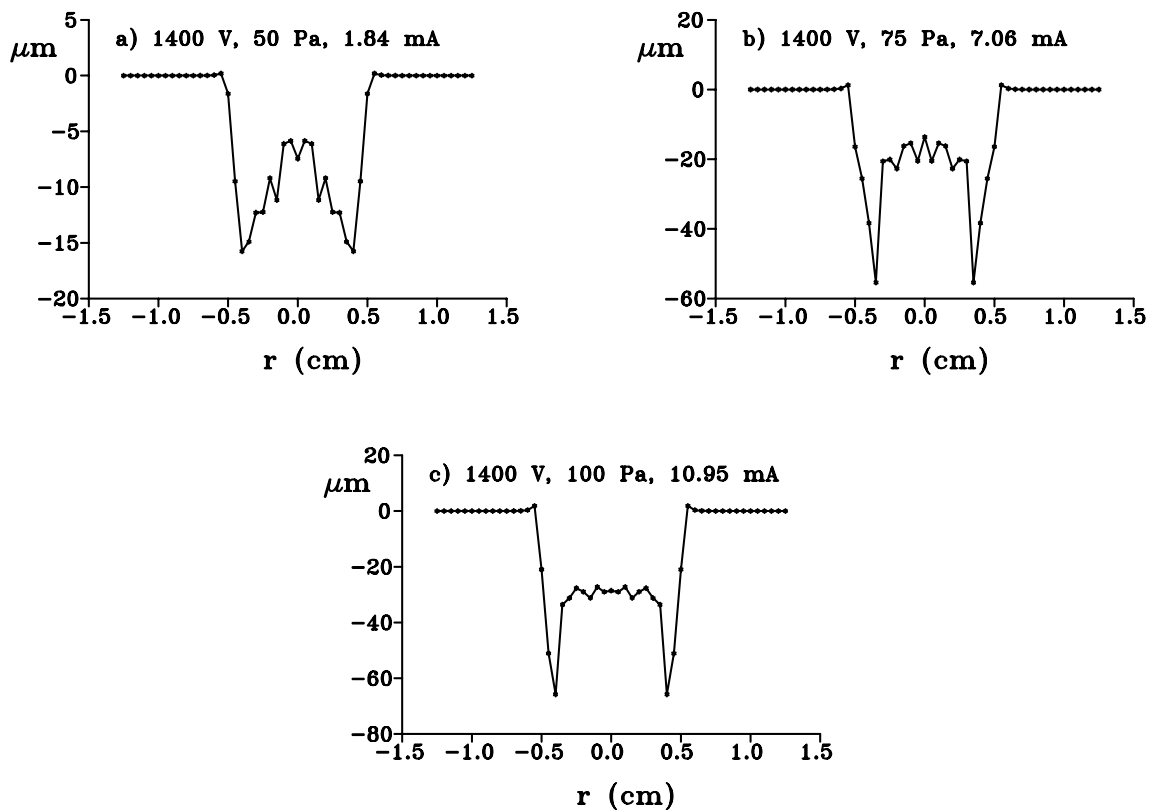


Figure 2.79: Calculated crater profiles after one hour of sputtering, at constant voltage (1000 V) for three different pressures (and currents) (copper cathode in argon).

The effect of pressure at constant voltage is presented in figure 2.79. Again, the depth of the crater profile increases considerably with pressure. Moreover, the shape of the profile is clearly influenced by the pressure. At 50 Pa, the crater profile is characterized by a pronounced convex shape. At rising pressure, the convexity decreases, and at 100 Pa, a flat crater bottom is attained.

Hence, the model predicts that it is advisable to work at high pressures, high currents and high voltages to reach an optimum (flat) crater profile. This is in very good agreement with experiment. Indeed, Jonkers [140] investigated the influence of voltage and current on the experimental crater profiles in the VG9000 glow discharge cell for analyzing flat samples (see figures 2.80 and 2.81).

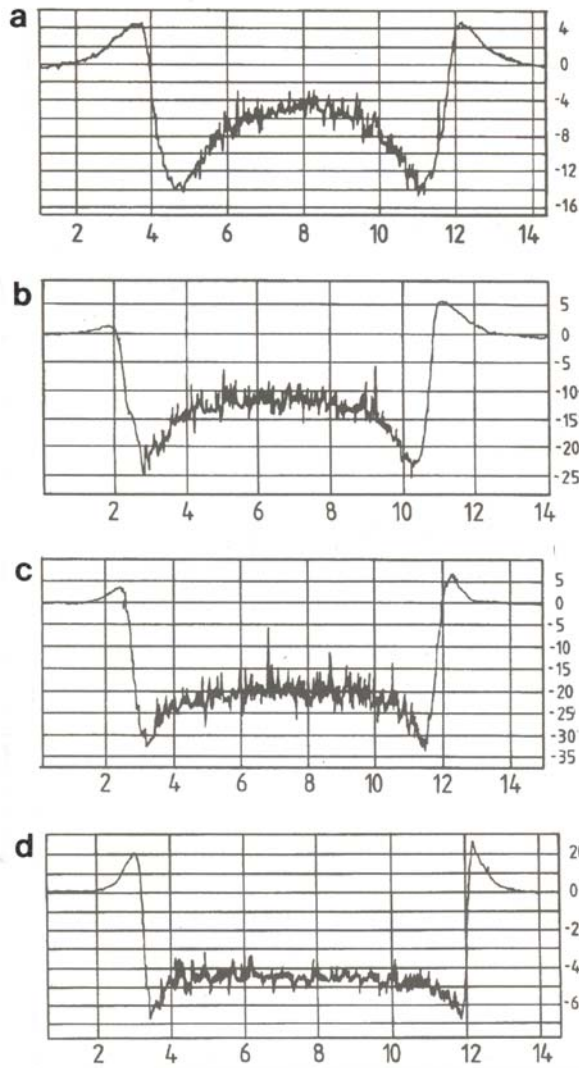


Figure 2.80: Experimental crater profiles after one hour of sputtering, at constant voltage (1000 V), for four different currents (and pressures), obtained with the VG9000 mass spectrometer (copper cathode in argon); (a) 1 mA, (b) 2 mA, (c) 3.5 mA, (d) 6 mA [140].

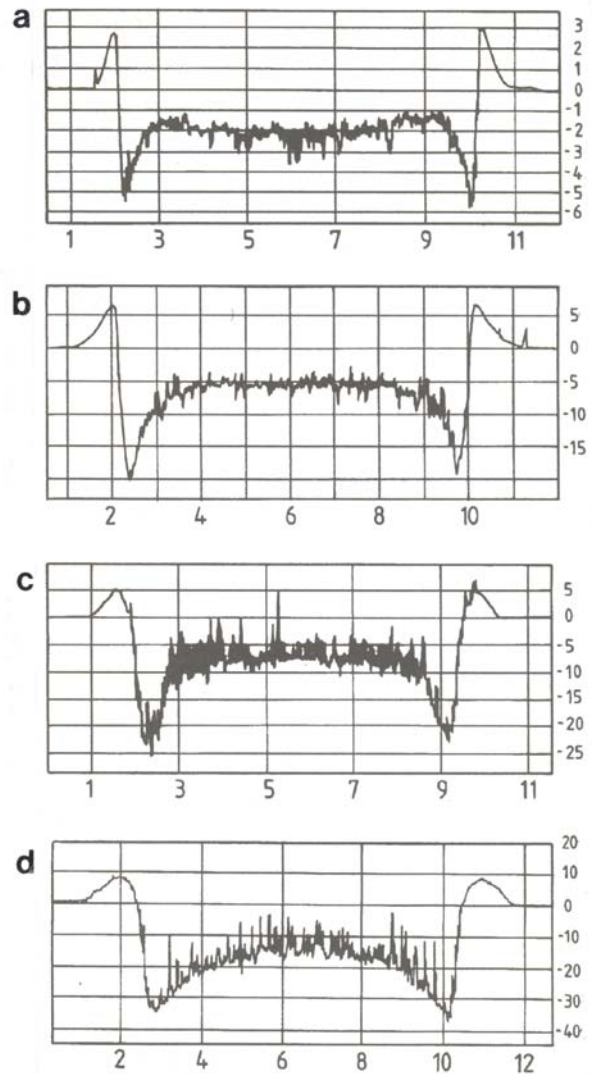


Figure 2.81: Experimental crater profiles after 45 minutes of sputtering, at constant current (3 mA), for four different voltages (and pressures), obtained with the VG9000 mass spectrometer (copper cathode in argon); (a) 500 V, (b) 750 V, (c) 1000 V, (d) 1250 V [140].

She found that by increasing the current at constant voltage (so that the pressure increases) the crater profiles change from a convex character to a more or less flat crater bottom (see figure 2.80 [140]), which is in good agreement with the effects illustrated in figure 2.79. Moreover, she found that by increasing the voltage at constant current, the crater profile changes from a concave to a convex shape (see figure 2.81 [140]). This is also in reasonable agreement with our modeling results. However, the influence of voltage cannot be completely compared, since in the modeling work the voltage was increased at constant pressure (so that current increased too), whereas in the experiments by Jonkers, the voltage was increased at constant current (so that the pressure had to decrease).

The influence of voltage and pressure on the erosion rate (or in other words on the crater depth at the center of the crater) is presented in figure 2.82. The erosion rate rises clearly with voltage and with pressure. Indeed, at higher pressures and voltages, the amount of sputtering increases, since there will be a higher flux of bombarding particles at the cathode and their energies will be higher too. The erosion rate increased from 0.1 $\mu\text{m}/\text{h}$ at the lowest pressure and voltage to about 30 $\mu\text{m}/\text{h}$ at the highest pressure and voltage investigated. This is in the same order of magnitude as experimental findings for the VG9000 mass spectrometer [140].

The erosion rate can also be expressed as weight loss per unit time. It can be calculated from the total net flux of sputtered copper atoms by:

$$ER = J_{\text{sput,net}} \frac{M}{N_A}$$

where ER is now the erosion rate in g s^{-1} and $J_{\text{sput,net}}$ is the total net sputtered flux (in s^{-1}), and M and N_A are defined above. Figure 2.83 presents the calculated erosion rate in weight loss as a function of pressure and voltage. It is seen that the erosion rate ranges from 0.1 to 5.6 $\mu\text{g}/\text{s}$, increasing with voltage and pressure. These values are in reasonable agreement with the typical numbers reported in the literature (e.g. 0.1-10 $\mu\text{g}/\text{s}$ [142], 25-100 $\mu\text{g}/\text{min}$ [143], 50-500 $\mu\text{g}/\text{min}$ [118]).

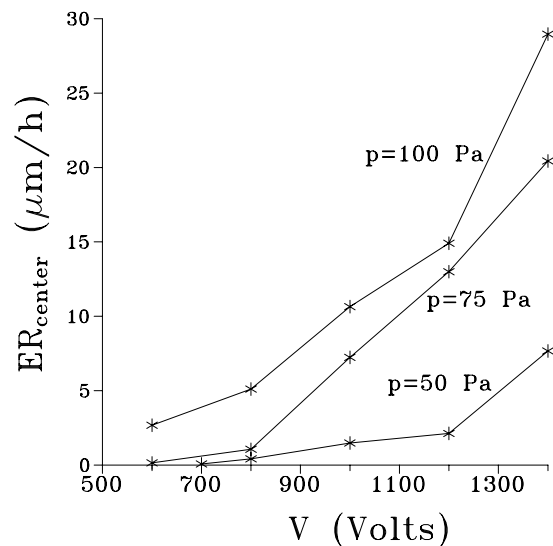


Figure 2.82: Calculated erosion rates (in depth per unit time), as a function of voltage, at three pressures (copper cathode in argon).

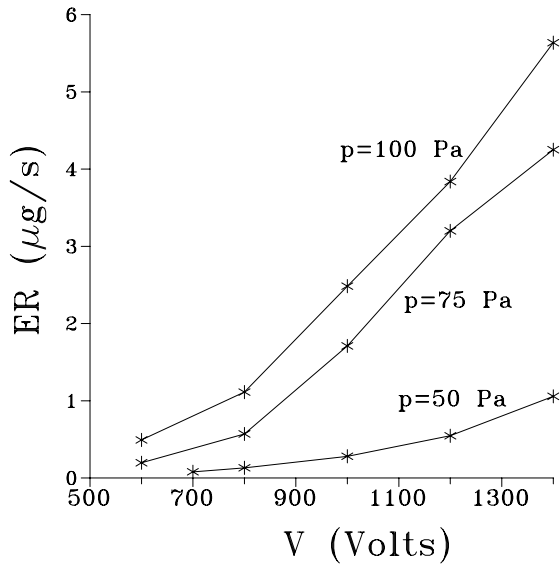


Figure 2.83: Calculated erosion rates (in weight loss per unit time), as a function of voltage, at three pressures (copper cathode in argon).

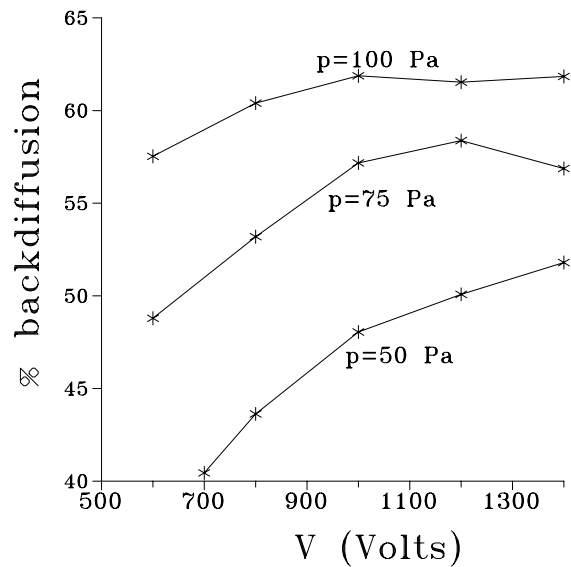


Figure 2.84: Calculated amount of backdiffusion to the cathode, as a function of voltage, at three pressures (copper cathode in argon).

Finally, the effect of voltage and pressure on the backdiffusion is presented in figure 2.84. We calculated that about 40-65 % of the sputtered atoms diffuses back and is redeposited on the cathode, the number increasing with voltage and pressure.

2.3.7. Remarks on the input parameters and conclusion

A set of three-dimensional models has been developed to describe a direct current glow discharge in argon. Typical results of the models include the total electrical current as a function of voltage and pressure, the densities of the different plasma species, the electrical field and potential distributions throughout the plasma, the energy distributions and mean energies of the species, information about the collision processes in the plasma, and the crater profiles and etching rates due to sputtering at the cathode. The calculated quantities are presented in the complete three-dimensional geometry of a glow discharge cell. Moreover, the influence of pressure and voltage on the results is investigated.

Input parameters in the models are the cell geometry, the pressure and voltage, the gas temperature, the cross sections of the collision processes as a function of the colliding particles' energies, the secondary electron emission coefficient at the cathode and anode walls, some data characteristic of the cathode

material to calculate the sputtering yield (i.e. mass, atomic number, sublimation energy, ...), and the sticking coefficients of the plasma species at the cell walls.

The three-dimensional cell geometry is the one corresponding to the new standard cell for analyzing flat samples in the VG9000 mass spectrometer. However, it is approximated here by a closed configuration. Some pressure and voltage values, typical for the VG9000 mass spectrometer are employed. However, the pressure inside the glow discharge cell cannot routinely be measured. Moreover, the gas temperature inside the cell, which is needed to calculate the argon gas atom number density, is unknown. It is therefore considered as a fitting parameter, in order to obtain reasonable values for the electrical current at given pressures and voltages. It was found that variations in the gas temperature had a significant effect on the calculations (e.g. 30 % variation in gas temperature yielded a factor of 2 variation in the electrical current). Therefore, the modeling results cannot yet be considered completely quantitative. Nevertheless, the obtained fitting values for the gas temperature are realistic numbers, which is a validation that the models present already a realistic picture of the glow discharge.

The cross section data used in the calculations are taken from the literature. These data are, however, subject to uncertainties. The cross sections of electron collisions have been studied by many authors and are rather well known. Nevertheless, for the electron impact ionization cross section, for example, relative differences of about 30 % can occur between various experimental values, as is shown in ref. [144]. The argon ion and atom symmetric charge transfer and elastic collisions have also been studied rather extensively. However, cross sections for argon ion and atom impact ionization and excitation, have been presented, to our knowledge, only by a few groups [82,145]. The authors of ref. [145] report systematic uncertainties of ~30 % for the ionization cross sections, and the excitation cross section values can only be considered as an upper limit, according to ref. [82]. Also, cross sections of Penning ionization and asymmetric charge transfer are very difficult to find in the literature, and when available, they are subject to large uncertainties. The effect of the uncertainties in the cross sections depends on the kind of collisions. Indeed, some collisions affect only a certain aspect of the glow discharge, like the excitation and elastic collisions. Other collisions, like ionization, determine the electron multiplication, and hence the overall discharge conditions. It was found that small variations in the electron, argon ion and atom impact ionization cross sections could have considerable effect on the total electrical current, due to the snowball effect (i.e. a high electron ionization cross section gives rise to high electron multiplication, and the large number of new electrons, combined with the high ionization cross section, yield again high electron multiplication, etc.).

Besides the cross sections, also the secondary electron emission coefficient, the data relevant for sputtering, and the sticking coefficients of the plasma species, have to be adopted from the literature. The secondary electron emission coefficient

and the data relevant for sputtering are rather easily available from the literature. The behavior of some plasma species at the walls is self-evident (e.g. the ions will be neutralized, and the metastable atoms will be deexcited at the walls, hence they disappear from the plasma). However, the treatment of other plasma species at the walls is less obvious. Indeed, the sticking coefficients, A_0 , of sputtered low-energy copper atoms at the walls are very difficult to find in the literature. Some models describing the behavior of the sputtered atoms use a sticking coefficient of 1 [55-57]. However, in ref. [61] it is stated that the sticking coefficient of copper atoms may vary between 0.5 and 0.01, depending on the structure of the surface. Since the actual value of the sticking coefficient is unknown, the authors of ref. [61] used this quantity as a fitting parameter, and they obtained values for copper between 0.02 and 0.05. In practice, however, a lot of material is found sticking at the walls, therefore, it is suggested that the sticking coefficients must be rather close to 1. We used a value of 0.5, since this yielded the best agreement with experiment [101].

Since the actual value of A_0 is unknown, we have performed calculations with different values for A_0 , ranging from 1 to 0, to investigate its influence on the results. We found that this parameter had considerable effect. Indeed, the copper atom density increased by more than two orders of magnitude, because the “sink” at the walls drops off gradually. Moreover, the pronounced maximum in the density profile at a few mm from the cathode disappears. The effect of A_0 is, however, not linear; i.e., changing A_0 from 1 to 0.5 had negligible influence on the shape and magnitude of the density profile, whereas the major effect is found for A_0 values close to 0 (when A_0 is lowered from 0.001 to 0, an increase in density of almost a factor of 10 was found). Changing A_0 from 1 to 0 also yielded an increase in the copper ion density of 2 orders of magnitude. The effect was, again, most significant at A_0 values close to 0 and almost negligible at A_0 values ranging from 1 to 0.1. It is expected that the sticking coefficient is closer to 1 than to 0 (i.e. the majority of atoms will stick at the walls). Therefore, using the value of 0.5 seems to be justified.

Due to the uncertainties connected with the input parameters, the modeling results have to be considered with some caution. Nevertheless, the results have been compared as much as possible with available literature data and with experimental observations, and although exact quantitative agreement cannot yet be expected, the qualitative trends and the order of magnitudes are already correctly predicted. This is a validation that, in spite of the uncertainties of the input data, the models present a realistic picture of the glow discharge.

2.4. COMPARISON WITH ONE-DIMENSIONAL MODELS

Modeling of a glow discharge in three dimensions (or two dimensions, if the cell is cylindrically symmetrical), is clearly more complicated than modeling in one dimension. Indeed, three-dimensional scattering of the particles has to be taken into account, and the solution algorithms and boundary conditions of the models become more intricate. Moreover, the three-dimensional models require considerably more calculation time, i.e. the particles in the Monte Carlo models have to be followed for a longer time in the plasma due to back and forth scattering, and the solution algorithms in the fluid models require an additional loop for the radial direction. On the other hand, three-dimensional models present, in principle, a more realistic picture of the glow discharge cell.

In order to investigate whether one-dimensional models also yield a satisfactory description of the reality or, in other words, whether it is worthwhile to incorporate three-dimensional effects in the models, the results of the present three-dimensional simulations have been compared with results of one-dimensional models. Two kinds of "one-dimensional" models have been examined. The first one is a combination of one-dimensional fluid models and three-dimensional Monte Carlo simulations. In the fluid models, cathode and anode are represented by two infinitely wide parallel plates without side-walls, so that the quantities in the plasma vary only with axial distance from the cathode. In the Monte Carlo models the exact three-dimensional cell geometry is already included and three-dimensional scattering of the particles is taken into account. However, the particles feel only the influence of an axial electric field, since this is what follows from the one-dimensional fluid approach. This kind of model can be expected to be more or less realistic if the length of the cell is smaller than its diameter, so that the side-walls have a minor effect anyhow. In the second kind of one-dimensional model, three-dimensional scattering of the particles in the Monte Carlo calculations is also neglected and it is assumed that the particles move only in one direction.

The results of the three-dimensional model described in this work, have been compared with results of both kinds of one-dimensional models considered above. For simplicity, the three-dimensional simulation is designated as 3D model, the combination of three-dimensional Monte Carlo and one-dimensional fluid models is specified as 3D1D model, whereas the complete one-dimensional approach is indicated as 1D model.

2.4.1. Discharge conditions

As discussed before, the total electrical current can be calculated when pressure and voltage are given. For a gas temperature of 360 K, the 3D model yielded a current of 3.1 mA at 1000 V and 75 Pa (see Section 2.3.1). When assuming the same gas temperature, the 3D1D model resulted in a current of 5.7 mA at the same voltage and pressure conditions. Indeed, in the one-dimensional argon ion-slow electron fluid model, the argon ions and slow electrons cannot get lost at the sidewalls. Hence there are more current carriers in the plasma, which manifests itself in a higher electrical current. A current of 3.1 mA could be obtained by increasing the gas temperature to 410 K. Indeed, at a higher gas temperature, the gas atom number density is lower, which results in less ionization collisions and hence in a lower current.

The 1D model calculated an electrical current of 1.8 mA at 360 K, 1000 V and 75 Pa, which is lower than in the 3D model. Indeed, in the one-dimensional Monte Carlo approximation, the electrons and ions move only in the forward direction, causing thereby less ionization collisions than in a three-dimensional Monte Carlo model where they can scatter back and forth and have a longer residence time in the plasma. Hence, in spite of the fact that the one-dimensional fluid model yields more current carriers (see above), the net effect is a lower electrical current than in the 3D model. When lowering the gas temperature to 330 K, the same electrical current of 3.1 mA could be obtained.

Since the exact gas temperature in the glow discharge is not known, it is used as a kind of fitting parameter (see Section 2.3.1). The values of 330 K, 360 K and 410 K all seem reasonable. Therefore, as long as the exact gas temperature is not known, it must be concluded that the three kinds of models yield realistic results for the electrical current. In order to make the best comparison between the three models, the 3D1D model and the 1D model were calculated at 410 K and at 330 K, respectively, so that the three kinds of models present results at the same voltage-pressure-current conditions.

2.4.2. Densities of the plasma species

Figure 2.85 shows the one-dimensional argon ion density profiles, calculated with the three different models. The results of the 3D model are taken at the cell axis ($r=0$). The slow electron density has almost the same profile, except that it is zero in the CDS and at the anode wall (see Section 2.3.2). The argon ion density calculated with the 3D model is a factor of about 2 lower than the results of the one-dimensional models. Indeed, as explained before, in the one-dimensional fluid model the argon ions and slow electrons do not get lost at the side walls, giving rise to a higher

density in the plasma. The argon ion density resulting from the 1D model is still a little higher than the one obtained with the 3D1D model, due to the slightly lower gas temperature which yields lower diffusion coefficients and hence somewhat higher densities.

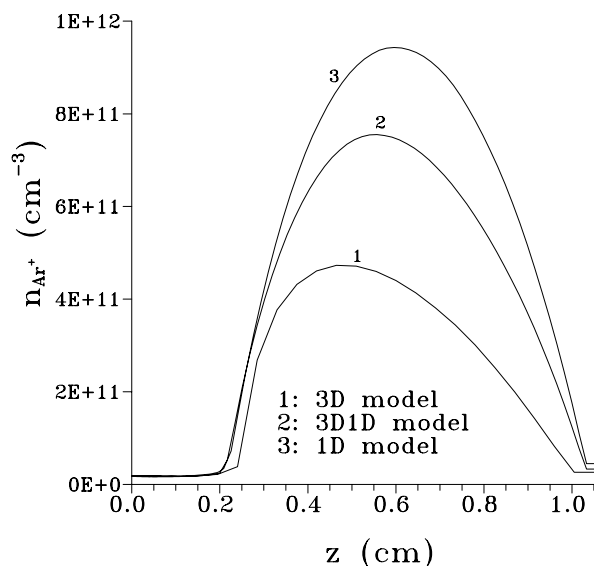


Figure 2.85: One-dimensional density profiles of the argon ions, calculated with the 3D model and two 1D models (at 75 Pa, 1000 V, 3.1 mA, copper cathode in argon).

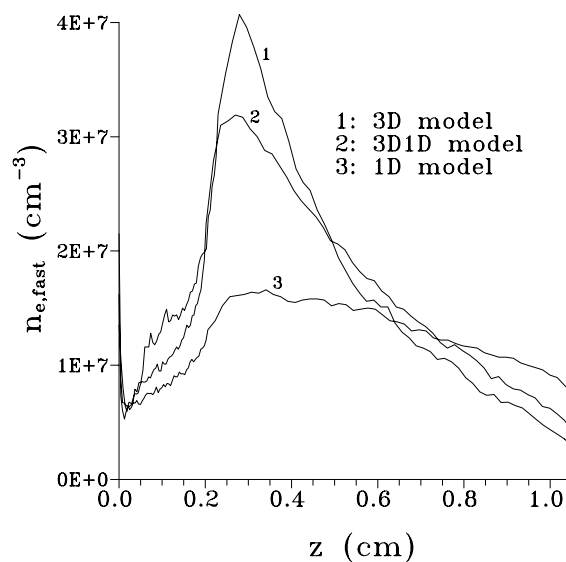


Figure 2.86: One-dimensional density profiles of the fast electrons, calculated with the 3D and two 1D models (at 75 Pa, 1000 V, 3.1 mA, copper cathode in argon).

The fast electron density feels the influence of the three dimensions in a different way, as appears from figure 2.86. Indeed, the densities calculated with the 3D and the 3D1D model (i.e. three-dimensional Monte Carlo models) are a factor of about 2 higher than the 1D results. This is attributed to the back and forth scattering of the electrons in the three-dimensional Monte Carlo models, giving rise to a higher residence time in the plasma and hence a higher density. The fact that the density obtained with the 3D model is somewhat higher than the 3D1D result is again ascribed to the slightly lower gas temperature, yielding a higher argon gas atom density and therefore more ionization collisions and more electron multiplication. The same trend as for the fast electron density was also observed for the fast argon atom density.

The argon metastable atom density does not show much variation among the different models, as can be seen from figure 2.87. The 3D result was found to be slightly higher than both one-dimensional densities. This is at first sight surprising, since one would expect a lower density due to deexcitation-losses at the sidewalls. However, another loss process (electron collisional transfer to the nearby energy levels) comes into play with the opposite effect. Indeed, this loss process is lower for the 3D model, due to a lower slow electron density (see above). The effect of the deexcitation-loss at the sidewalls seems to be of minor importance compared to the loss by electron collisional transfer, giving rise to a slightly higher density in the 3D model. The fact that the density computed from the 1D model is somewhat higher than the one obtained with the 3D1D model is again attributed to the difference in gas temperature (see above).

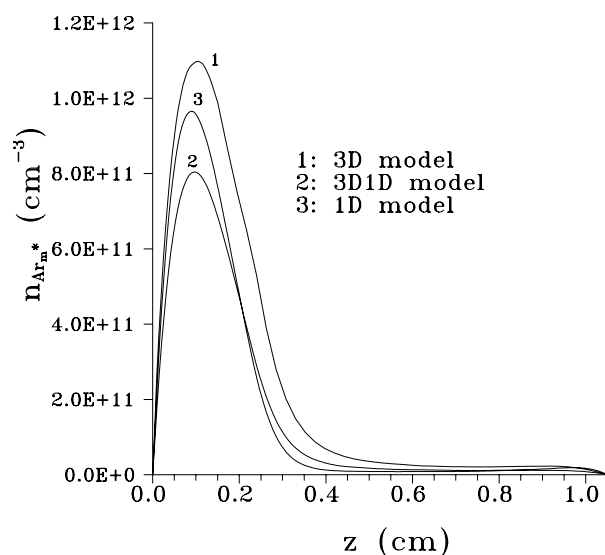


Figure 2.87: One-dimensional density profiles of the argon metastable atoms, calculated with the 3D model and two 1D models (at 75 Pa, 1000 V, 3.1 mA, copper cathode in argon).

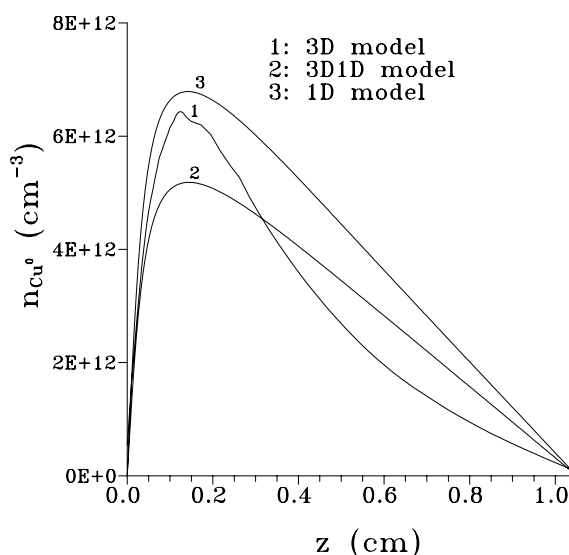


Figure 2.88: One-dimensional density profiles of the sputtered copper atoms, calculated with the 3D model and two 1D models (at 75 Pa, 1000 V, 3.1 mA, copper cathode in argon).

Also the sputtered copper atom density is only little affected by the three dimensions, as is presented in figure 2.88. The main effect of the 3D approach is the somewhat faster drop in the copper atom density after its maximum compared to the one-dimensional fluid models. Indeed, in the one-dimensional models the density spreads out by diffusion along the cell axis only, whereas in the 3D model it can spread also in the radial direction, yielding a lower density at the cell axis. The small difference in the absolute values of the copper atom density calculated in the three models, is owing to the variations in the gas temperature: a higher gas temperature yields a higher diffusion coefficient and hence a lower density.

Figure 2.89 illustrates the effect of the three dimensions on the copper ion density. The density calculated with the 3D model is a factor of 3 lower than the 3D1D model and a factor of 5 lower compared to the 1D model. The copper ion density is calculated from the copper atom density and the amount of ionization. The latter is given by electron impact ionization, Penning ionization and asymmetric charge transfer. The copper atom density varies only slightly among the different models (see above). Electron impact ionization is of minor importance (see Section 2.3.5) and the amount of Penning ionization (determined by the argon metastable atom density) is also barely influenced by the three-dimensional effects (see above). The amount of asymmetric charge transfer ionization (determined by the argon ion density), however, varies more clearly among the different models. The latter effect is responsible for the increase in copper ion number density in the order of 3D, 3D1D, 1D model.

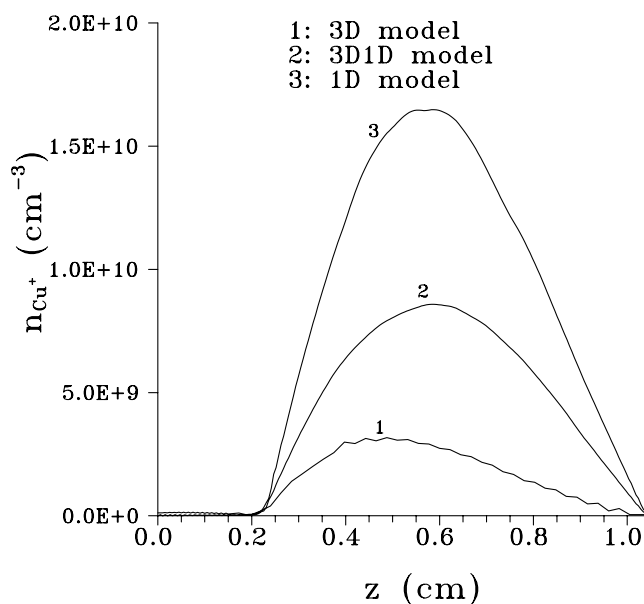


Figure 2.89: One-dimensional density profiles of the copper ions, calculated with the 3D model and two 1D models (at 75 Pa, 1000 V, 3.1 mA, copper cathode in argon).

From figures 2.88 and 2.89 follows that the calculated degree of ionization of copper is also slightly different among the three approaches: the 3D model yielded a value of 0.1%, the 3D1D model 0.14 %, and the 1D model 0.2 %. In general, it can be concluded that the number densities resulting from the three kinds of models vary only slightly. The shapes of the profiles are barely influenced and the absolute values of the densities stay in the same order of magnitude.

2.4.3. Electric field and potential distributions

Both the axial electric field and the potential distributions are quite similar for the three kinds of models, and are therefore not presented here. The computed CDS length was only slightly smaller in the 1D and 3D1D models than in the 3D models (i.e. 0.2 cm compared to 0.24 cm). The most significant difference is the absence of a radial electric field in the 1D and 3D1D models, but the latter does not seem to have a large effect on the behavior of the species in the plasma.

2.4.4. Energies of the plasma species

Since the electric field distributions of the three models are barely different, the energies of the plasma species are quite similar to each other too. The largest difference was found for the electron energies, which are shown in figure 2.90. The average energy calculated with the 1D model is somewhat higher, since the electrons move only in the forward direction and they do not lose so much energy as when they would scatter back and forth. The 3D and 1D3D results are almost identical. The energies of the argon ions, fast argon atoms and copper ions calculated with the three kinds of models, nearly coincide, and are therefore not shown here.

The relative contributions of argon ions, fast argon atoms and copper ions to the sputtering at the cathode are comparable for the three models: the contributions amount to about 72-73 % for the fast argon atoms and about 25-26 % for the argon ions. The contribution of the copper ions (i.e. the amount of self-sputtering) rises slightly from the 3D model (ca. 1 %) over the 3D1D model (ca. 1.7 %) to the 1D model (ca. 2.4 %), as could be expected from the increased copper ion density (see figure 2.89).

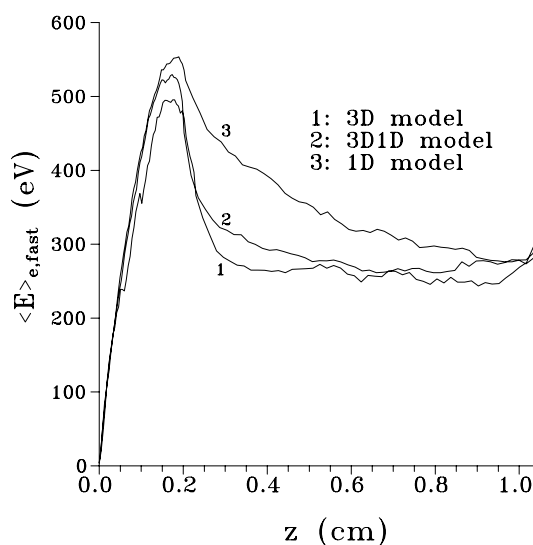


Figure 2.90: One-dimensional profiles of the electron mean energies, calculated with the 3D model and two 1D models (at 75 Pa, 1000 V, 3.1 mA, copper cathode in argon).

2.4.5. Collision processes of the plasma species

Figure 2.91 presents the one-dimensional profiles of the electron impact excitation rates, calculated with the three models. This figure can be seen as a representative example for the other electron collision rates, which behave in the same manner. The excitation rate obtained with the 3D model is somewhat higher than the 3D1D result. This is attributed to the slightly lower gas temperature adopted as input parameter, yielding a higher argon gas atom density and hence more collisions. The 1D model computed the lowest excitation rate, in spite of the lower gas temperature used. The reason for this is the fact that the electrons cannot scatter back and forth in the one-dimensional Monte Carlo model, giving rise to less excitation in the beginning of the NG. However, in the one-dimensional Monte Carlo

model, a larger number of electrons can reach the backplate of the cell since they cannot get lost at the sidewalls. This results in a slightly higher excitation rate at the end of the cell. Since it is known from optical emission profiles [27] that the excitation rate is characterized by a peak in the beginning of the NG, it can be concluded that the three-dimensional Monte Carlo models yield more realistic results.

The collision rates of the argon ions are not significantly influenced by the three-dimensional effects. Indeed, the most frequent collision processes for the argon ions are symmetric charge transfer collisions. Each time an argon ion undergoes a charge transfer collision, it starts again from rest in a direction parallel to the electric field. Hence, even in the three-dimensional Monte Carlo models, the argon ions move mainly in the forward direction. Therefore, the difference between the three-dimensional and one-dimensional models is only small. The same is true for the fast argon atoms, since they are created by charge transfer collisions from the argon ions. It was found that they undergo slightly more collisions in the 3D model, compared to the 3D1D model, due to the lower gas temperature which was selected, giving rise to more collisions; and the latter model calculates in turn slightly more collisions than the 1D model, due to the possibilities of back and forth scattering. However, the effects are almost negligible.

The relative contributions of electron impact, fast argon ion impact and fast argon atom impact ionization to the ionization of argon atoms, are nearly the same for the three kinds of models. Concerning the ionization of the sputtered copper atoms, it was mentioned before that asymmetric charge transfer becomes more important in the 3D1D model and especially in the 1D model, due to the higher argon ion density (see above). The importance of Penning ionization and electron impact ionization remains more or less the same. Hence, the relative contribution of asymmetric charge transfer becomes more important in both one-dimensional models, as can be seen from table 2.2.

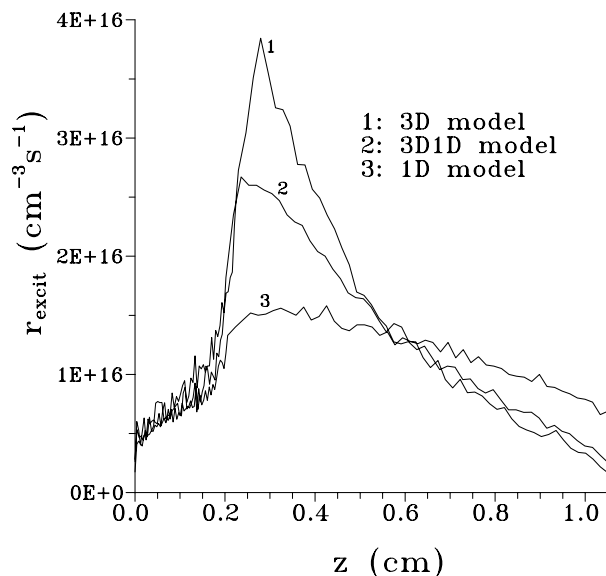


Figure 2.91: One-dimensional electron impact excitation rates of argon, calculated with the 3D model and two 1D models (at 75 Pa, 1000 V, 3.1 mA, copper cathode in argon).

Table 2.2: Relative contributions of the three ionization mechanisms for copper, calculated with the three models.

	3D	3D1D	1D
Penning ionization	59 %	41 %	40 %
Asymmetric charge transfer	37 %	55 %	58 %
Electron impact ionization	4 %	4 %	2 %

Also the relative roles of the different production and loss processes for the argon metastable atoms change slightly in the three models, as is illustrated in table 2.3.

Table 2.3: Relative contributions of the different production and loss processes for the argon metastable atoms, calculated with the three models.

	3D	3D1D	1D
Prod: electron impact excitation	12 %	32 %	23 %
Prod: argon ion impact excitation	17 %	15 %	16 %
Prod: argon atom impact excitation	71 %	53 %	61 %
Prod: radiative recombination	~ 0.005 %	~ 0.05 %	~ 0.09 %
Loss: diffusion	82 %	53 %	58 %
Loss: electron collisional transfer	11 %	40 %	33 %
Loss: Penning ionization of copper atoms	3.7 %	3.7 %	5.4 %
Loss: metastable-metastable collisions	3.0 %	2.4 %	3.3 %
Loss: electron impact excitation	~ 0.3 %	~ 0.8 %	~ 0.1 %
Loss: electron impact ionization	~ 0.02 %	~ 0.02 %	~ 0.002 %
Loss: two-body collision with argon	~ 0.1 %	~ 0.1 %	~ 0.2 %
Loss: three-body collision with argon	~ 0.01 %	~ 0.01 %	~ 0.02 %

The main difference is that electron collisional transfer to the nearby energy levels gains importance in both one-dimensional models, at the expense of diffusion and deexcitation at the walls. Indeed, electron collisional transfer is more significant due to the higher slow electron densities in the one-dimensional models (see above), and diffusion followed by deexcitation at the walls is of minor importance due to the absence of sidewalls. Moreover, electron impact excitation is a little more important in both one-dimensional models, at the expense of argon ion and atom impact excitation. However, the qualitative trends in the roles of the different production and loss processes remain more or less the same in the three kinds of models.

2.4.6. Crater profiles and etching rates at the cathode

One of the main trumps of the three-dimensional model compared to both one-dimensional models is the possibility to calculate crater profiles. Indeed, the one-dimensional models yield no information about variations in the radial direction, hence, they are not able to calculate crater profiles. From the total flux of sputtered copper atoms and the flux of copper atoms redepositing on the cathode, the net flux of sputtered atoms (i.e. the erosion rate) can however still be calculated. In both one-dimensional models, a value of 1.4 $\mu\text{m/h}$ was obtained. This is significantly lower than the three-dimensional result at the same discharge conditions (i.e. about 8 $\mu\text{m/h}$ at the center of the crater, see figure 2.76). The reason for this can be attributed to the much higher redeposition flux of copper atoms on the cathode in the one-dimensional models. Indeed, the latter was calculated to be about 94 % of the total sputtered flux in both one-dimensional models, whereas the three-dimensional model computed a value of 57 % (see Section 2.3.6). It was found that the erosion rate calculated with the three-dimensional model is in better agreement with experiment [140] than the values obtained with the one-dimensional model. This was also observed by van Straaten et al. [57]. The erosion rates calculated with their one-dimensional model were too low compared to experiment, due to the high redeposition flux to the cathode. The authors introduced a fitting parameter (i.e. an effective sink distance from the cathode at which the same amount of sputtered material is removed from the plasma, as the combined effects of the side walls), in order to reach agreement with experiment. In their two-dimensional description of the diffusion process, the fitting parameter was not necessary anymore. Hence, it can indeed be concluded that the three-dimensional model calculates more realistic values for the erosion rate than the one-dimensional models.

2.4.7. Conclusion

In general, the differences among the three approaches are rather small for the discharge geometry investigated. The qualitative trends are similar in the three models; only some minor quantitative variations are observed. The electrical current calculated for a given pressure, voltage and gas temperature stayed within a factor of three. A value of 3.1 mA could be obtained in the three models at 1000 V and 75 Pa, when selecting the gas temperature between 330 K and 410 K. Since the actual value of the gas temperature is unknown, it must be concluded that the three models calculate realistic discharge characteristics.

The number densities of the plasma species are computed to be in the same order of magnitude in the three models. The main difference is found for the copper ion density, which is somewhat higher in the one-dimensional models compared to

the three-dimensional model. This also results in a slightly higher ionization degree of copper, and a somewhat higher contribution of self-sputtering in the one-dimensional models. The electrical field and potential distributions are similar in the three models. Also the particles' energies and the collision rates deviate only slightly from each other. The differences in the calculated etching rates are, however, somewhat larger, and it was found that the results of the three-dimensional model are in better agreement with experiment than the one-dimensional results. Moreover, the three-dimensional model is able to calculate the crater profiles at the cathode. The latter can easily be compared with experiment, to test the validity of the model.

Summarized, the one-dimensional models present already a realistic picture of the glow discharge, for the discharge geometry investigated. In a first approximation, they are sufficient to obtain better insight in the discharge processes. However, the three-dimensional models can give additional information, like the behavior of the calculated quantities throughout the whole three-dimensional discharge volume, and can therefore be seen as a progress in order to obtain a more complete description of the glow discharge.

Moreover, it should be borne in mind that the results of this comparison are characteristic for the VG9000 glow discharge cell, and may not necessarily be generalized to other cell geometries.

2.5. EXPLANATION OF RELATIVE SENSITIVITY FACTORS IN GDMS BY MEANS OF THE MODELING WORK

2.5.1. Introduction

One of the benefits of GDMS is the fairly uniform sensitivity for multielement analysis. The relative sensitivity factors (RSFs) lie generally within one order of magnitude. The RSF in GDMS is defined as the multiplication factor that has to be applied to the measured ion current ratio in order to obtain the relative concentration of the elements in the sample (and has therefore actually the meaning of unsensitivity factor):

$$\frac{C_x}{C_s} = \text{RSF} \left[\frac{x}{s} \right] * \frac{I_x}{I_s}$$

where I and C are the ion current and the concentration in mass units, respectively, and x and s represent the element x and the internal standard s, respectively. Usually, but not necessarily, the internal standard is the matrix element, with a concentration assumed to be 100 %. The RSF value is related to the relative ion yield (RIY) in the following way:

$$\text{RSF} \left[\frac{x}{s} \right] = \frac{1}{\text{RIY} \left[\frac{x}{s} \right]} * \frac{M_x}{M_s} \quad (2.1)$$

where M_x and M_s are the atomic masses.

For quantitative analytical results, the RSF values have to be known as accurately as possible. This information can be obtained by analyzing certified reference materials. Such measurements have been reported for different kinds of matrices (for references, see Chapter 1, Section 1.4.3.1). Furthermore, empirical models have been developed to predict RSF values; they are based on fitting parameters in order to reach the best agreement between calculated and experimental values [146-150]. These models generally reach a more or less satisfactory agreement between calculated and experimental RSF values - one model being better than the other - but all of them are based on the assumption of some kind of equilibrium in the plasma, which certainly does not exist. Moreover, by using fitting parameters, one can actually always achieve some agreement with experimental values, but because of their weak theoretical basis, the fitting parameters do not always have a real physical meaning.

The empirical model that describes the physical processes occurring in GDMS in the most realistic way is that of Vieth and Huneke [146]. However, it is also based on fitting parameters which can take arbitrary, physically unrealistic values when comparing experimental and calculated RSFs. Moreover, the observed discrepancy between experimental and calculated RSF values for some elements cannot be explained. The model we have developed to understand experimental RSF values is partly based on their model. However, using the physical background we have acquired by our explicit modeling work on the dc glow discharge, we are able to offer a rationalization of the experimental RSF values without the need of fitting parameters. This section starts with a short description of the empirical model by Vieth and Huneke, since our approach is based on it. Next, our model is described and used to explain the variations in RSF values between elements. It will be argued that, apart from transport of sputtered atoms and from Penning ionization (electron impact ionization is of minor importance), asymmetric charge transfer between the sputtered atoms and argon ions is mainly responsible for the variations in RSF values among different elements.

2.5.2. The empirical model by Vieth and Huneke

The model by Vieth and Huneke states that the RIY in GDMS is, in principle, determined by (i) processes taking place in the glow discharge source, (ii) the ion transmission efficiency through the mass spectrometer, and (iii) the detector sensitivity. The second and third factors are assumed to be element independent, and are set equal to 1. The first factor comprises the sputtering, the transport of sputtered atoms, the ionization and recombination, and the ion extraction into the mass spectrometer. The sputtering (in steady state conditions) and the ion extraction are also assumed to be element independent, so that only the transport and the ionization/recombination effects remain:

$$\text{RIY}\left[\frac{x}{s}\right] = S_T\left[\frac{x}{s}\right] * S_I\left[\frac{x}{s}\right]$$

where S_T and S_I describe the transport and ionization/recombination, respectively.

Transport occurs by diffusion and it is stated that elements with a higher diffusion coefficient will diffuse more quickly towards the walls, where they will be lost, so that their concentration in the plasma will be less:

$$S_T \left[\frac{x}{s} \right] = \frac{D_s}{D_x} = \frac{(r_{Ar} + r_x)^2 \sqrt{\mu_x}}{(r_{Ar} + r_s)^2 \sqrt{\mu_s}} \quad (2.2)$$

since $D_x \propto \frac{1}{(r_{Ar} + r_x)^2 \sqrt{\mu_x}}$; μ_x is the reduced mass of atoms x and argon, and r is the atomic radius.

Ionization is assumed to occur by Penning ionization and electron impact ionization due to secondary and thermalized electrons, whereas the recombination is determined by three-body recombination with two electrons. A detailed description of these processes can be found in ref. [146].

Since Vieth and Huneke did not know any values for the densities of electrons and argon metastable atoms, two fitting parameters, b and cq were used: b is the ratio of the thermalized electron density to secondary electron density, c is the ratio of the metastable argon density to the secondary electron density, and q is the proportionality factor for Penning ionization ($\sigma_{PI} = q^* \alpha$ [151], where σ_{PI} is the cross section for Penning ionization and α is the atomic polarizability). Best results were obtained for b=1600 and cq=1300. When using Fe as the internal standard, the agreement between calculated and experimental RSF values was found to be satisfactory for some elements (especially for those used in the fitting procedure), but for other elements (for example Li, Be, B, Mg, Al, Zn, Cd, etc.) a discrepancy appeared which could not be explained. Moreover, the fitting parameters have actually no real physical meaning. The parameter b was calculated to be 1600. However, our calculations have shown that this ratio of thermalized to secondary electron density is about 10^4 - 10^5 (i.e. ca. $5 \times 10^{11} \text{ cm}^{-3}$ for the thermalized electrons and ca. $2\text{-}3 \times 10^7 \text{ cm}^{-3}$ for the secondary electrons, at 75 Pa, 1000 V and 3.1 mA; see figures 2.9 and 2.11). Moreover, the thermalized electrons have too low energies to cause electron impact ionization and their incorporation in the model as being responsible for ionization, is therefore unrealistic. The parameter cq was computed to be 1300. Model calculations however predict a value of 10^3 - 10^5 for c (i.e. ca. 10^{10} - 10^{12} cm^{-3} for the argon metastables and ca. $2\text{-}3 \times 10^7 \text{ cm}^{-3}$ for the secondary electrons), whereas the proportionality factor q ranges from about 10 to 40 \AA^{-1} , according to ref. [151]. Since nothing is mentioned in ref. [146] about the units of q, any fitting value can be obtained for this, but it has not necessarily a real physical meaning. In spite of the fact that the model of Vieth and Huneke was a real progress in the work about RSF values in GDMS, its weak point remains the use of fitting parameters to achieve agreement between experimental and calculated values, but which can easily take physically unrealistic values.

2.5.3. The explicit approach based on the modeling results

To some extent, the same reasoning is followed as in the model by Vieth and Huneke. It is also assumed that the RIY is only determined by the transport and ionization factors. The transport factor, S_T , is adapted from their model, and is given by equation (2.2). However, the ionization factor is treated more explicitly, based on the cross section data of the different processes and on the densities of the plasma species, which are calculated by our explicit mathematical modeling work, instead of using fitting parameters.

The three ionization processes considered are Penning ionization, electron impact ionization and asymmetric charge transfer. Electron-ion recombination is neglected since it is generally accepted that this process is of minor importance in the glow discharge, due to the relatively low electron density in the plasma (see Chapter 1). This yields the following equation for the RIY:

$$\begin{aligned} \text{RIY} \left[\frac{x}{s} \right] &= S_I \left[\frac{x}{s} \right] * S_T \left[\frac{x}{s} \right] \\ &= \frac{n_x n_{Ar_m^*} k_{PI,x} + n_x \sum_E j_e(E) \sigma_{EI,x}(E) + n_x n_{Ar^+} k_{CT,x}}{n_s n_{Ar_m^*} k_{PI,s} + n_s \sum_E j_e(E) \sigma_{EI,s}(E) + n_s n_{Ar^+} k_{CT,s}} * \frac{(r_{Ar} + r_x)^2 \sqrt{\mu_x}}{(r_{Ar} + r_s)^2 \sqrt{\mu_s}} \\ &= \frac{n_{Ar_m^*} k_{PI,x} + \sum_E j_e(E) \sigma_{EI,x}(E) + n_{Ar^+} k_{CT,x}}{n_{Ar_m^*} k_{PI,s} + \sum_E j_e(E) \sigma_{EI,s}(E) + n_{Ar^+} k_{CT,s}} * \frac{(r_{Ar} + r_x)^2 \sqrt{\mu_x}}{(r_{Ar} + r_s)^2 \sqrt{\mu_s}} \end{aligned}$$

where $n_{Ar_m^*}$, n_{Ar^+} and $j_e(E)$ are the argon metastable number density, the argon ion number density and the electron flux energy distribution, respectively; k_{PI} , k_{CT} and $\sigma_{EI}(E)$ are the Penning ionization and asymmetric charge transfer rate constants and the electron impact ionization cross section as a function of the electron energy, respectively; r and μ are defined above, and n_x and n_s are the densities of element x and internal standard s , respectively. To calculate the RIY's of the elements, the densities of the elements x and s do not play a role. It can be assumed in the equation that $n_x = n_s$, so that they can be cancelled against each other.

The argon metastable atom density, the argon ion density and the electron flux energy distribution are calculated with the models described in Section 2.2. k_{PI} and $\sigma_{EI}(E)$ for different elements are obtained with the formulae used in Section 2.2. The numerical value of k_{CT} for a given element is however more difficult to find in the literature (see Chapter 1, Section 1.2.1.2, for an overview of the relevant literature). The process occurs only if the energy difference between the argon ion ground state (or metastable level) and the energy levels of the resulting analyte ion is sufficiently small; the efficiency of the process generally decreases with

growing energy difference between the levels. Charge transfer is therefore a more or less selective process. This is unlike Penning ionization which occurs unselectively for all elements having an ionization potential below the argon metastable energy level, independently of the relative position of the energy levels. The process of asymmetric charge transfer appears to be fairly complicated, for example, it is not always true that the smallest energy difference between energy levels yields the highest cross section [152,153]. It is therefore impossible to deduce the cross sections from data for other elements. The process can only be treated adequately by quantum mechanics to calculate cross section values.

Since the cross sections or rate constants of asymmetric charge transfer are not generally known for all elements, the work was carried out in reverse order. The process of asymmetric charge transfer is neglected in first instance. Since electron impact ionization is clearly of minor importance compared to Penning ionization (i.e. the contributions of electron impact ionization and Penning ionization to the ionization of sputtered atoms are about 2-5 % and 35-90 %, respectively; see Section 2.3.5), electron impact ionization can also be neglected. Therefore, the RIY of the elements is calculated, taking only the transport and Penning ionization contributions into account. The calculated RIYs are then compared with the experimental RIYs and the relative differences are calculated.

Moreover, by systematic investigation, the individual energy levels of all the element ions that lie close to the argon ion ground or metastable level, and which could therefore be important for asymmetric charge transfer were sought. The relative difference between experimental and calculated RIYs is related to these energy levels, in order to identify the actual role of asymmetric charge transfer in determining the RIY.

2.5.4. Results

Table 2.4: Summary of the experimental relative sensitivity factors (RSFs) and relative ion yields (RIYs), the calculated Penning ionization ($S_{PI}(x/Fe)$) and transport ($S_T(x/Fe)$) factors and calculated RIYs, the relative differences between calculated and experimental RIYs and the number of levels suitable for asymmetric charge transfer (CT), for the different elements investigated.

Element	$(RSF)_{exp}$	$(RIY)_{exp}$	$S_{PI}(x/Fe)$	$S_T(x/Fe)$	$(RIY)_{calc}$	$\Delta(RIY)_{rel}$	Number of levels suitable for CT
Li	1.8	0.069	0.64	0.61	0.39	+ 1.40	none
Be	2.3	0.07	0.50	0.52	0.26	+ 1.15	none
B	1.22	0.16	0.42	0.45	0.19	+ 0.17	none
C	4.51	0.048	0.41	0.45	0.18	+ 0.74	none
N	35	0.0073	no P.I.	-	-	-	-
O	65	0.0044	no P.I.	-	-	-	-
Na	2.5	0.17	1.3	1.15	1.50	+ 1.60	none
Mg	1.29	0.34	1.05	0.99	1.04	+ 1.02	none
Al	1.39	0.35	0.94	0.91	0.86	+ 0.84	none
Si	1.96	0.26	0.78	0.79	0.62	+ 0.83	1 (far)
P	3.51	0.16	0.74	0.77	0.57	+ 1.13	none
S	3.34	0.17	0.74	0.77	0.57	+ 1.07	none
Cl	5	0.13	no P.I.	-	-	-	-
Ca	0.57	1.26	1.58	1.39	2.18	+ 0.54	many
Ti	0.42	2.04	1.14	1.10	1.25	- 0.48	many
V	0.55	1.66	1.06	1.04	1.10	- 0.40	many
Cr	2.23	0.42	1.01	1.00	1.01	+ 0.83	many
Mn	1.48	0.67	0.99	0.99	0.98	+ 0.38	many
Fe	$\equiv 1$	$\equiv 1$	$\equiv 1$	$\equiv 1$	$\equiv 1$	0	many
Co	1.14	0.93	1.00	1.01	1.01	+ 0.085	many
Ni	1.54	0.68	1.00	1.00	1.00	+ 0.38	many
Cu	4.96	0.23	1.04	1.04	1.08	+ 1.30	(1)
Zn	5.46	0.21	1.13	1.11	1.25	+ 1.42	1

2.5. Explanation of relative sensitivity factors in GDMS by means of the modeling work

Ga	4.45	0.28	1.12	1.10	1.24	+ 1.26	1 (far)
Ge	5.1	0.26	1.17	1.14	1.34	+ 1.36	1(+1)
As	3.1	0.43	1.05	1.05	1.10	+ 0.87	none
Se	3.1	0.46	0.98	1.00	0.98	+ 0.73	none
Zr	0.64	2.55	1.42	1.34	1.90	- 0.29	many
Mo	1.3	1.32	1.23	1.20	1.48	+ 0.11	many
Ru	0.93	1.95	1.18	1.16	1.37	- 0.35	many
Rh	1.39	1.33	1.20	1.18	1.41	+ 0.059	many
Pd	1.87	1.02	1.22	1.20	1.46	+ 0.36	none
Ag	3.5	0.55	1.30	1.25	1.62	+ 0.98	none
Cd	9.3	0.22	1.39	1.32	1.83	+ 1.58	none
In	4.8	0.43	1.44	1.36	1.96	+ 1.28	none
Sn	2.38	0.89	1.46	1.38	2.01	+ 0.77	none
Sb	3.9	0.56	1.50	1.40	2.11	+ 1.16	none
Te	3.42	0.67	1.33	1.28	1.71	+ 0.88	none
W	1.46	2.25	1.34	1.30	1.75	- 0.25	many
Re	1.3	2.57	1.31	1.28	1.67	- 0.43	many
Pt	2.48	1.41	1.32	1.29	1.70	+ 0.19	2
Au	2.6	1.36	1.38	1.33	1.84	+ 0.30	1
Tl	4.9	0.75	1.70	1.56	2.65	+ 1.12	1
Pb	2.19	1.69	1.75	1.59	2.78	+ 0.49	1
Bi	4.29	0.87	1.84	1.66	3.06	+ 1.11	(2)

The results of this work are presented in table 2.4. The first column shows all elements incorporated in the present study. In the second column, the experimental RSF values for all elements, taken from ref. [146] are presented. They were obtained with the VG9000 glow discharge mass spectrometer at 1000 V and 3 mA, which are similar discharge conditions to the ones used in the present calculations. Iron is taken as internal standard, and therefore has an RSF value equal to 1. The experimental RIYs computed from the RSFs with equation (2.2) are given in the third column. Columns 4 and 5 represent the Penning ionization and transport factor of each element, respectively. The calculated RIY is obtained by multiplication of the Penning ionization and transport factor, and is given in the sixth column. In column 7, the relative difference between calculated and experimental RIYs is shown:

$$\Delta(\text{RIY})_{\text{rel}} = \frac{2 \cdot [(\text{RIY})_{\text{calc}} - (\text{RIY})_{\text{exp}}]}{[(\text{RIY})_{\text{calc}} + (\text{RIY})_{\text{exp}}]}$$

Column 8 indicates the number of energy levels of the element ions that can possibly play a role in charge transfer with argon ions. These were obtained by systematic investigation of the energy levels of all elemental ions under study [124]. It is not known exactly how close the energy levels must lie to each other in order to allow efficient charge transfer. According to ref. [152] charge transfer can occur as long as the energy difference is less than 2 eV (the energy level of the element ion lying below the energy level of the argon ion). Ref. [153] states that asymmetric charge transfer is most effective for energy differences of 0.1-0.4 eV but that it can still take place at energy differences of 1 eV. Hence, it is not straightforward to give an exact number of the energy levels suitable for charge transfer. Therefore, in the table “none” is written if there are certainly no levels which can play a role (i.e. there are no levels lying within about 2 eV of the argon ion levels); “many” means that a large number of energy levels are available which can account for charge transfer (i.e. many levels lying within about 1 eV below and about 0.02 eV above the argon ion levels). If there are only a few levels suitable for charge transfer, this number is mentioned in the table. When this number is in parentheses, the level can only give charge transfer with the argon ion metastable state, which could be less important in low pressure discharges.

As an example, the energy levels of argon ions and of ions for three elements (Fe, Cu and Ag) are shown schematically in figure 2.92. It is seen that FeII possesses many levels suitable for asymmetric charge transfer (i.e. a variety of 3d⁶4p levels and also some 3d⁶4s and 3d⁵4s² levels). CuII has no levels lying close to the ArII ground state and only one level showing close overlap with the ArII metastable state (i.e. the 4p ³P₀ level). AgII has no levels at all that could account for charge transfer.

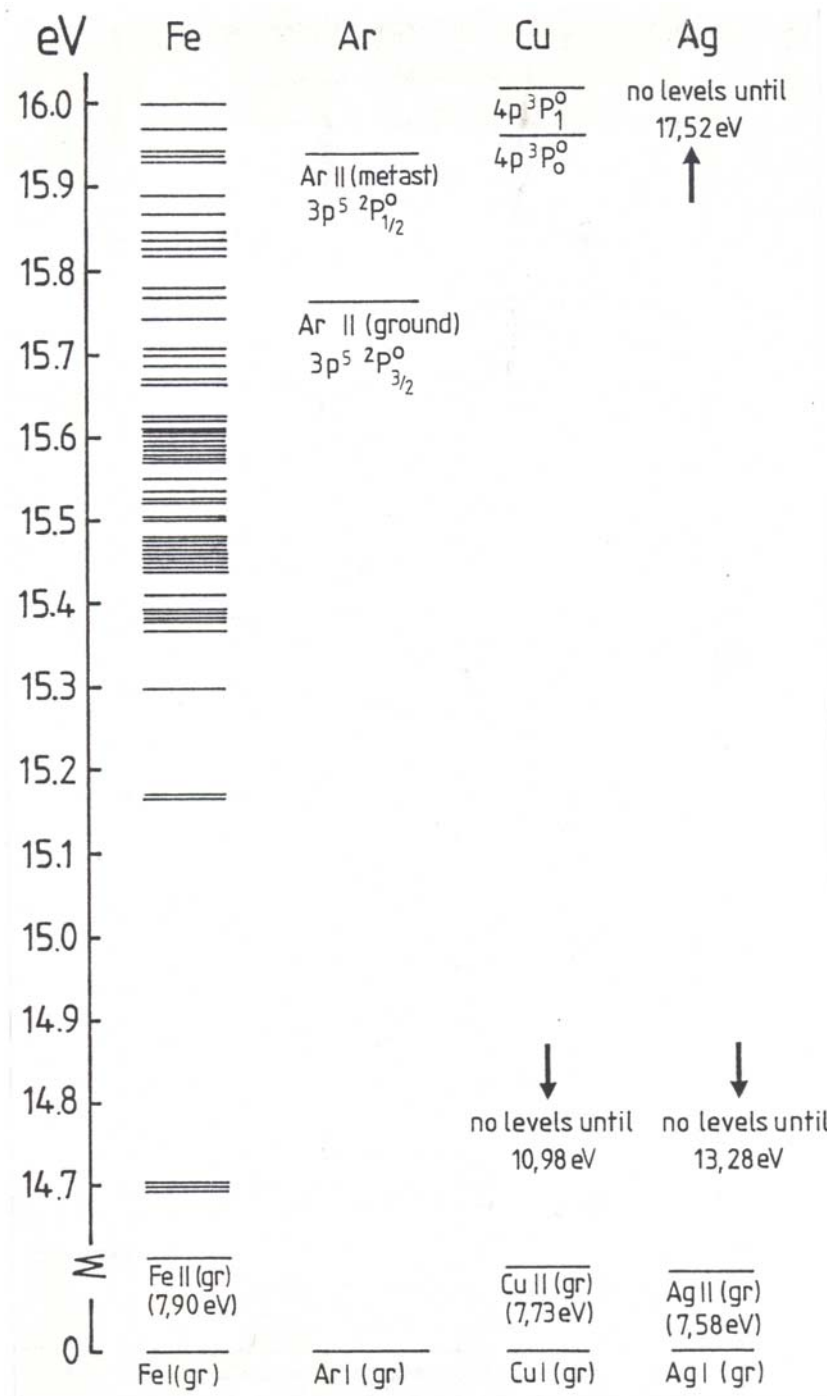


Figure 2.92: Schematic representation of the energy levels of the element ions that could account for charge transfer with argon ions, for three elements (Fe, Cu and Ag). The zero level is taken at the ground state of the atoms. Only the region of interest for charge transfer is shown (i.e., 14.7-16.0 eV; the Ar II ground state and metastable levels are situated at 15.76 and 15.937 eV, respectively, and it is assumed that levels lying from 1 eV below to 0.02 eV above these Ar II levels are suitable for charge transfer.

Columns 7 and 8 show that the elements can roughly be subdivided into several groups (corresponding to two categories), according to the relative difference between calculated and experimental RIYs, and to the availability of energy levels suitable for charge transfer. It is important at this point to realize that the internal standard, Fe, is an element with many levels which allow charge transfer.

(i) For the elements Li to S, the calculated RIY is clearly higher than the experimental one [average $\Delta(\text{RIY})_{\text{rel}} \approx +1.0$]. Only B forms a minor exception. For N, O and Cl, the RIY is not calculated since these elements have an ionization potential higher than the argon metastable energy and can therefore not be ionized by Penning ionization. This is clearly reflected in the low RIY and high RSF that were found experimentally. Moreover, the elements of this group will not undergo asymmetric charge transfer with argon, in accordance with the absence of suitable energy levels.

(ii) For the elements Ca to Ni, the experimental and calculated RIYs are more or less comparable with each other, i.e. the relative difference (average value is $\approx +0.17$) is clearly smaller than for group (i), except for Cr. The calculated RIY is somewhat higher for the elements Ca, Cr, Mn, Co and Ni, whereas for Ti and V, the calculated RIY is slightly lower. For Fe, both experimental and calculated RIYs are by definition equal to one, and the relative difference is therefore zero. The elements of this group hence show a behavior similar to the internal standard Fe, i.e. possibility of charge transfer, as could have been expected from the energy scheme of their ions.

(iii) The elements Cu to Se again belong to the first category, since the calculated RIYs are clearly higher than the experimental ones, the relative difference being rather large ($\approx +1.2$ on average), i.e. no charge transfer, in accordance with the energy levels of their ions.

(iv) The elements Zr to Rh fit into the second category (occurrence of asymmetric charge transfer), with the experimental and calculated RIYs being of comparable magnitude [average $\Delta(\text{RIY})_{\text{rel}} \approx -0.12$]. For Mo and Rh, slightly higher calculated RIYs are obtained, while the reverse is true for Zr and Ru.

(v) The group from Pd to Te is again characterized by systematically higher calculated RIYs compared with the experimental values; $\Delta(\text{RIY})_{\text{rel}} \approx +1.0$ on average, i.e., no asymmetric charge transfer, as confirmed by the unfavourable energy levels of their ions.

(vi) For W, Re and Pt again comparable experimental and calculated RIYs are obtained [$\Delta(\text{RIY})_{\text{rel}} \approx -0.2$ on average]; for W and Re, the calculated RIY is lower, while for Pt the calculated value is slightly higher. These elements allow charge transfer with argon ions, and their behavior is similar to that of the internal standard Fe.

(vii) The last group is formed by Au to Bi, and for these elements, the calculated RIYs are again higher than the experimental values, the relative difference is $\approx +0.8$ on average, being rather small for Au and Pb, but clearly large for Tl and Bi. The ions of these elements are not likely to be formed by asymmetric charge transfer with argon ions.

2.5.5. Conclusion

It appears that the systematic subdivision into different groups according to the relative difference between calculated and experimental RIY values is directly correlated with the presence or absence of ionic energy levels suitable for asymmetric charge transfer with argon ions, illustrated in column 8 of table 2.4. Indeed, the elements of the groups (i), (iii), (v) and (vii) for which the calculated RIYs are too high compared with the experimental values (category 1), possess no or almost no energy levels that are suitable for asymmetric charge transfer, whereas the elements of the groups (ii), (iv) and (vi) for which the calculated RIYs are more comparable (category 2), are characterized by a fairly large number of energy levels that can account for asymmetric charge transfer.

This excellent correlation, based on 42 elements of the periodic table, strongly suggests that the occurrence or absence of asymmetric charge transfer can explain the variations in RIYs of the elements. Fe, which belongs to category 2, is taken as internal standard. Hence for the elements of category 2, the agreement between experimental and calculated RIYs is satisfactory, since asymmetric charge transfer is comparable to Fe, and a so-called charge transfer factor would be of the order of 1. However, the calculated RIYs of the elements of category 1, for which asymmetric charge transfer is clearly less important than for Fe, must be corrected by a charge transfer factor of less than 1, in order to reach agreement with the experimental RIYs.

The fact that a few elements (i.e. B, Cr and the elements in the last group) show some discrepancy in their behavior could be due to uncertainties in the experimental RSFs or to the fact that for these elements still other effects are important. Moreover, asymmetric charge transfer is a complicated process and the most suitable energy difference for charge transfer is not known. Further, it appears that the cross section also depends on the quantum states involved. Hence it is impossible to explain exactly the variations in the relative differences among the elements within category 2. The behavior of Cr might indicate that, in spite of the large number of levels that, on energy considerations, could account for charge transfer, no such excitation occurs, owing to selection rules (i.e., Wigner spin rule) [131].

In spite of the discrepancy for a few individual elements, which cannot be explained in detail yet, the important role of asymmetric charge transfer in defining the RIY values seems highly probable.

2.6. REFERENCES

1. J. D. P. Passchier and W. J. Goedheer, *J. Appl. Phys.* **73**, 1073 (1993).
2. J. D. P. Passchier and W. J. Goedheer, *J. Appl. Phys.* **74**, 3744 (1993).
3. J. P. Boeuf, *Phys. Rev. A* **36**, 2782 (1987).
4. J. P. Boeuf, *J. Appl. Phys.* **63**, 1342 (1988).
5. F. F. Young and C. John Wu, *J. Appl. Phys.* **74**, 839 (1993).
6. W. Schmitt, W. E. Kohler and H. Ruder, *J. Appl. Phys.* **71**, 5783 (1992).
7. D. B. Graves and K. F. Jensen, *IEEE Trans. Plasma Science*, **14**, 78 (1986).
8. M. Meyyappan and J. P. Kreskovsky, *J. Appl. Phys.* **68**, 1506 (1990).
9. M. Meyyappan and T. R. Govindan, *J. Appl. Phys.* **74**, 2250 (1993).
10. P. Belenguer and J. P. Boeuf, *Phys. Rev. A* **41**, 4447 (1990).
11. J. W. Bradley, *J. Phys. D* **29**, 706 (1996).
12. R. J. Carman and A. Maitland, *J. Phys. D* **20**, 1021 (1987).
13. I. Abril, *Computer Physics Comm.* **51**, 413 (1988).
14. R. J. Carman, *J. Phys. D* **22**, 55 (1989).
15. Tran Ngoc An, E. Marode and P. C. Johnson, *J. Phys. D* **10**, 2317 (1977).
16. J. P. Boeuf and E. Marode, *J. Phys. D* **15**, 2169 (1982).
17. S. Hashiguchi, *IEEE Trans. Plasma Sci.* **19**, 297 (1991).
18. Z. Wronski, *Vacuum* **42**, 635 (1991).
19. J. Sun, Ye Gong and D. Wang, *J. Phys. D* **26**, 436 (1993).
20. Y. Weng and M. Kushner, *Phys. Rev. A* **42**, 6192 (1990).
21. Z. Liu and H. Wei, *Physica A* **215**, 283 (1995).
22. M. J. Kushner, *IEEE Trans. Plasma Sci.* **14**, 188 (1986).
23. S. Hashiguchi and M. Hasikuni, *Jpn. J. Appl. Phys.* **27**, 1010 (1988).
24. J. Li, Q.-M. Chen and Z.-G. Li, *J. Phys. D* **28**, 681 (1995).
25. Z. Donko, K. Rozsa and R. C. Tobin, *J. Phys. D* **29**, 105 (1996).
26. W. Helin, L. Zuli, L. Daming and Y. Boming, *Vacuum* **47**, 167 (1996).
27. M. Surendra, D. B. Graves and G. M. Jellum, *Phys. Rev. A* **41**, 1112 (1990).
28. J-H. Tsai and C-H Wu, *J. Phys. D* **26**, 496 (1993).
29. A. C. Dexter, T. Farrell and M. I. Lees, *J. Phys. D* **22**, 413 (1989).
30. T. J. Sommerer and M. J. Kushner, *J. Appl. Phys.* **71**, 1654 (1992).
31. K. H. Schoenbach, H. Chen and G. Schaefer, *J. Appl. Phys.* **67**, 154 (1989).
32. N. Sato and H. Tagashira, *IEEE Trans. Plasma Sci.* **19**, 102 (1991).
33. J. P. Boeuf and L. C. Pitchford, *IEEE Trans. Plasma Sci.* **19**, 286 (1991).
34. A. Fiala, L. C. Pitchford and J. P. Boeuf, *Phys. Rev. E* **49**, 5607 (1994).
35. F. Y. Huang and M. J. Kushner, *J. Appl. Phys.* **78**, 5909 (1995).

36. D. Vender and R. W. Boswell, *IEEE Trans. Plasma Sci.* **18**, 725 (1990).
37. M. Surendra and D. B. Graves, *IEEE Trans. Plasma Sci.* **19**, 144 (1991).
38. P. Meyer, G. Wunner, W. Schmitt and H. Ruder, *J. Appl. Phys.* **77**, 992 (1995).
39. V. V. Ivanov, A. M. Popov and T. V. Rakhimova, *Plasma Phys. Reports* **21**, 692 (1995).
40. G. Lapenta, F. Iino and J. V. Brackbill, *IEEE Trans. Plasma Sci.* **23**, 769 (1995).
41. T. H. Chung, H. J. Yoon, T. S. Kim and J. K. Lee, *J. Phys. D* **29**, 1014 (1996).
42. I. Abril, A. Gras-Marti and J. A. Valles-Abarca, *J. Phys. D* **17**, 1841 (1984).
43. A. Gras-Marti, I. Abril and J. A. Valles-Abarca, *Thin Solid Films* **124**, 59 (1985).
44. Z. Wronski, J. L. Sullivan and S. O. Saied, *J. Phys. D* **25**, 1607 (1992).
45. P. W. May, D. Field and D. F. Klemperer, *J. Appl. Phys.* **71**, 3721 (1992).
46. R. S. Mason and R. M. Allott, *J. Phys. D* **27**, 2372 (1994).
47. K. Nanbu and Y. Kitatani, *J. Phys. D* **28**, 324 (1995).
48. C. M. Ferreira, J. Loureiro and A. Ricard, *J. Appl. Phys.* **57**, 82 (1985).
49. T. Kubota, Y. Morisaki, A. Ohsawa and M. Ohuchi, *J. Phys. D* **25**, 613 (1992).
50. K. A. Hardy and J. W. Sheldon, *J. Appl. Phys.* **53**, 8532 (1982).
51. E. A. Den Hartog, D. A. Doughty and J. E. Lawler, *Phys. Rev. A* **38**, 2471 (1988).
52. E. A. Den Hartog, T. R. O'Brian and J. E. Lawler, *Phys. Rev. Lett.* **62**, 1500 (1989).
53. D. P. Lymberopoulos and D. J. Economou, *J. Appl. Phys.* **73**, 3668 (1993).
54. A. Gras-Marti and J. A. Valles-Abarca, *J. Appl. Phys.* **54**, 1071 (1983).
55. J. A. Valles-Abarca and A. Gras-Marti, *J. Appl. Phys.* **55**, 1370 (1984).
56. M. van Straaten, R. Gijbels and A. Vertes, *Anal. Chem.* **64**, 1855 (1992).
57. M. van Straaten, A. Vertes and R. Gijbels, *Spectrochim. Acta* **46B**, 283 (1991).
58. N. P. Ferreira and H. G. C. Human, *Spectrochim. Acta* **36B**, 215 (1981).
59. R. M. Allott, P. D. Miller, J. J. Jones and R. S. Mason, in *Recent Advances in Plasma Source Mass Spectrometry*, edited by G. Holland (K. D. M. International Scientific, Exeter, 1995), pp. 102-115.
60. R. S. Mason and M. Pichilingi, *J. Phys. D* **27**, 2363 (1994).
61. E. M. van Veldhuizen and F. J. de Hoog, *J. Phys. D* **17**, 953 (1984).
62. B. E. Warner, K. B. Persson and G. J. Collins, *J. Appl. Phys.* **50**, 5694 (1979).
63. S. C. Rae and R. C. Tobin, *J. Appl. Phys.* **64**, 1418 (1988).
64. J. Clark, U. Greb, G. Ronan and D. Wheeler: Lecture presented at the 2nd International Conference on Plasma Source Mass Spectrometry, Durham, UK (1990).
65. B. Chapman, *Glow Discharge Processes*, Wiley, New York (1988).

-
66. G. Marsaglia and A. Zaman, *Computers in Physics* **8**, 117 (1994).
 67. W. C. Fon, K. A. Berrington, P. G. Burke and A. Hibbert, *J. Phys. B* **16**, 307 (1983).
 68. F. J. de Heer, R. H. J. Jansen and W. van der Kaay, *J. Phys. B* **12**, 979 (1979).
 69. E. Eggarter, *J. Chem. Phys.* **62**, 833 (1975).
 70. N. J. Mason and W. R. Newell, *J. Phys. B* **20**, 1357 (1987).
 71. H. A. Hyman, *Phys. Rev. A* **18**, 441 (1978).
 72. H. A. Hyman, *Phys. Rev. A* **20**, 855 (1979).
 73. L. Vriens, *Phys. Lett.* **8**, 260 (1964).
 74. J. B. Hasted, *Physics of Atomic Collisions*, Butterworth, London (1972).
 75. N. R. Whetten, R. C. Weast and M. J. Astle, *CRC Handbook of Chemistry and Physics*, 63rd ed., CRC, Boca Raton (1982), p E-372.
 76. L. Reimer, *Scanning Electron Microscopy*, Springer, Berlin (1985).
 77. L. S. Frost, *Phys. Rev.* **105**, 354 (1957).
 78. H. K. Gummel, *IEEE Trans. Electron. Devices* **11**, 455 (1964).
 79. D. L. Scharfetter and H. K. Gummel, *IEEE Trans. Electron. Devices* **16**, 64 (1969).
 80. A. Bogaerts, R. Gijbels and W. J. Goedheer, *J. Appl. Phys.* **78**, 2233 (1995).
 81. A. V. Phelps, *J. Appl. Phys.* **76**, 747 (1994).
 82. A. V. Phelps, *J. Phys. Chem. Ref. Data* **20**, 557 (1991).
 83. A. V. Phelps, private communication.
 84. K. Tachibana, *Phys. Rev. A* **34**, 1007 (1986).
 85. J. H. Kolts and D. W. Setser, *J. Chem. Phys.* **68**, 4848 (1978).
 86. A. V. Phelps and J. P. Molnar, *Phys. Rev.* **89**, 1202 (1953).
 87. M. A. Biondi, *Phys. Rev.* **129**, 1181 (1963).
 88. C. M. Ferreira and A. Ricard, *J. Appl. Phys.* **54**, 2261 (1983).
 89. L. A. Riseberg, W. F. Parks and L. D. Schearer, *Phys. Rev. A* **8**, 1962 (1973).
 90. S. Inaba, T. Goto and S. Hattori, *J. Phys. Soc. Jpn* **52**, 1164 (1983).
 91. D. U. von Rosenberg, *Methods for the Numerical Solution of Partial Differential Equations*, Elsevier, New York (1969).
 92. N. Matsunami, Y. Yamamura, Y. Itikawa, N. Itoh, Y. Kazumata, S. Miyagawa, K. Morita, R. Shimizu and H. Tawara, *Atom. Data and Nucl. Data Tables* **31**, 1 (1984).
 93. I. M. Torrens, *Interatomic Potentials*, Academic, New York (1972).
 94. J. Lindhard, V. Nielsen and M. Scharff, *Mat. Fys. Medd. Dan. Vid. Selsk.* **36**, No. 10 (1968).
 95. K. B. Winterborn, P. Sigmund and J. B. Sanders, *Mat. Fys. Medd. Dan. Vid. Selsk.* **37**, No. 14 (1970).
-

-
96. J. Sielanko, *Radiation Effects Letters* **86**, 185 (1984).
 97. J. O. Hirschfelder, C. F. Curtiss and R. B. Bird, *Molecular Theory of Gases and Liquids*, Wiley, New York (1964).
 98. E. W. McDaniel, *Collision Phenomena in Ionized Gases*, Wiley, New York (1964).
 99. P. Baltayan, J. C. Pebay-Peyroula and N. Sadeghi, *J. Phys. B* **18**, 3618 (1985).
 100. P. Baltayan, J. C. Pebay-Peyroula and N. Sadeghi, *J. Phys. B* **19**, 2695 (1986).
 101. A. Bogaerts, E. Wagner, B. W. Smith, J. D. Winefordner, D. Pollmann, W. W. Harrison and R. Gijbels, *Spectrochim. Acta, Part B* (submitted).
 102. R. S. Robinson, *J. Vac. Sci. Technol.* **16**, 185 (1979).
 103. M. van Straaten, A. Bogaerts and R. Gijbels, *Spectrochim. Acta* **50B**, 583 (1995).
 104. H. Oechsner, *Phys. Rev. B* **17**, 1052 (1978).
 105. M. van Straaten, unpublished results.
 106. D. Fang and R. K. Marcus, *Spectrochim. Acta*, **45B**, 1053 (1990).
 107. D. Fang and R. K. Marcus, *Spectrochim. Acta*, **46B**, 983 (1991).
 108. P. A. Büger, *Z. Naturforsch. A*, **30**, 216 (1975).
 109. N. P. Ferreira, H. G. Human and L. R. P. Butler, *Spectrochim. Acta*, **35B**, 287 (1980).
 110. M. Kuraica, N. Konjevic, M. Platisa and D. Pantelic, *Spectrochim. Acta*, **50B**, 1337 (1995).
 111. A. Bogaerts, A. Quentmeier, N. Jakubowski and R. Gijbels, *Spectrochim. Acta*, **50B**, 1337 (1995).
 112. A. Bogaerts, R. D. Guenard, B. W. Smith, J. D. Winefordner, W. W. Harrison and R. Gijbels, *Spectrochim. Acta, Part B* (submitted).
 113. R. L. Smith, D. Serxner and K. R. Hess, *Anal. Chem.* **61**, 1103 (1989).
 114. P. G. Browne and M. H. Dunn, *J. Phys. B* **6**, 1103 (1973).
 115. A. J. Stirling and W. D. Westwood, *J. Phys. D* **4**, 246 (1971).
 116. K. Hoppstock and W. W. Harrison, *Anal. Chem.* **67**, 3167 (1995).
 117. W. W. Harrison, *Glow Discharge Mass Spectrometry*, in *Inorganic Mass Spectrometry*, F. Adams, R. Gijbels and R. Van Grieken (eds.), Wiley, New York (1988), Chapter 3.
 118. K. R. Hess and R. K. Marcus, *Spectroscopy*, **2**, (1987).
 119. L. G. Piper, J. E. Velazco and D. W. Setser, *J. Chem. Phys.* **59**, 3323 (1973).
 120. Catalogue Alpagaz, l'Air Liquide.
 121. N. I. Uzelac and F. Leis, *Spectrochim. Acta*, **47B**, 877 (1992).
 122. N. P. Ferreira, J. A. Strauss and H. G. C. Human, *Spectrochim. Acta*, **37B**, 273 (1982).
-

123. C. M. Ferreira and A. Ricard, *J. Appl. Phys.* **54**, 2261 (1983).
124. C. E. Moore, *Atomic Energy Levels, Volume I-III*, Nat. Stand. Ref. Data Ser., Nat. Bur. Stand. (U.S.), 1971.
125. S. Johansson and U. Litzen, *J. Phys. B* **11**, L703 (1978).
126. K. Danzmann and M. Koch, *J. Phys. B* **14**, 2989 (1981).
127. P. B. Farnsworth and J. P. Walters, *Spectrochim. Acta*, **37B**, 773 (1982).
128. R. S. Hudson, L. L. Skrumeda and W. Whaling, *J. Quant. Spectrosc. Radiat. Transfer*, **38**, 1 (1987).
129. E. B. M. Steers and R. J. Fielding, *J. Anal. Atom. Spectrom.* **2**, 239 (1987).
130. E. B. M. Steers and F. Leis, *Spectrochim. Acta*, **46B**, 527 (1991).
131. E. B. M. Steers and A. P. Thorne, *J. Anal. Atom. Spectrom.* **8**, 309 (1993).
132. E. B. M. Steers, A. P. Thorne and Z. Weiss, 12th European Sectional Conference on the Atomic and Molecular Physics of Ionized Gases, Europhysics Conference Abstracts, **18E**, 65 (1994).
133. K. Wagatsuma and K. Hirokawa, *Spectrochim. Acta*, **51B**, 349 (1996).
134. F. W. Aston, *Proc. Roy. Soc. London, Ser. A*, **79**, 80 (1907).
135. P. Gill and C. E. Webb, *J. Phys. D: Appl. Phys.* **10**, 299 (1977).
136. M. van Straaten, *Analytical Glow Discharge Mass Spectrometry: Physical aspects and Applications*, Ph. D. Dissertation, University of Antwerp (1993).
137. A. Bogaerts and R. Gijbels, *J. Appl. Phys.* **78**, 6427 (1995).
138. M. K. Levy, D. Serxner, A. D. Angstadt, R. L. Smith and K. R. Hess, *Spectrochim. Acta*, **46B**, 253 (1991).
139. R. C. Weast and M. J. Astle, *CRC Handbook of Chemistry and Physics, 63rd Edition*, CRC Press, Boca Raton (1982-1983).
140. C. Jonkers, *Analyse van Metalen en Metaaloppervlakken met Glimontladingsmassaspectrometrie*, Ph. D. Dissertation, University of Antwerp (1995).
141. N. Jakubowski, *Analyse von Oberflächen und Oberflächennaher Metallischer Schichten mittels Niederauflösender Glimmentladungsmassenspektrometrie*, Ph. D. Dissertation, University of Hohenheim (1991).
142. W. W. Harrison, K. R. Hess, R. K. Marcus and F. L. King, *Anal. Chem.* **58**, 341A (1986).
143. W. W. Harrison, *J. Anal. Atom. Spectrom.* **3**, 867 (1988).
144. L. R. Peterson and J. E. Allen, Jr., *J. Chem. Phys.* **56**, 6068 (1972).
145. P. O. Haugsjaa and R. C. Amme, *J. Chem. Phys.* **52**, 4874 (1970).
146. W. Vieth and J. C. Huneke, *Spectrochim. Acta*, **46B**, 137 (1991).
147. R. W. Smithwick, III, *J. Am. Soc. Mass Spectrom.* **3**, 79 (1992).
148. R. W. Smithwick, III, D. W. Lynch and J. C. Franklin, *J. Am. Soc. Mass Spectrom.* **4**, 278 (1993).

149. G. I. Ramendik, B. M. Manzon, D. A. Tyurin, N. E. Benyaev and A. A. Komleva, *Talanta*, **34**, 61 (1987).
150. G. I. Ramendik, D. A. Tyurin and Yu. I. Babikov, *Anal. Chem.* **62**, 2501 (1990).
151. M. Bourène and J. Le Calvé, *J. Chem. Phys.* **58**, 1452 (1973).
152. J. M. Green and C. E. Webb, *J. Phys. B* **7**, 1698 (1974).
153. A. R. Turner-Smith, J. M. Green and C. E. Webb, *J. Phys. B* **6**, 114 (1973).

Summary and conclusion
Samenvatting en besluit

MATHEMATICAL MODELING OF A DIRECT CURRENT GLOW DISCHARGE IN ARGON

A glow discharge is a plasma, a partially ionized gas, consisting of positive and negative charges and a large number of neutral species. It can be obtained by simply inserting two electrodes in a low pressure gas environment (~ 100 Pa). A voltage of about 1 kV is applied between the two electrodes and causes electrical breakdown of the gas, thereby producing positive ions and electrons. The positive ions are accelerated towards the cathode, where they can release electrons. These electrons enter the glow discharge plasma and are subject to collisions (primarily excitation and ionization). The excitation collisions, followed by deexcitations with emission of light, are responsible for the characteristic name of the “glow” discharge. The ionization collisions create new ions and electrons, which is necessary for the glow discharge to be self-sustaining.

The use of a glow discharge as an analytical spectroscopic source for elemental analysis is attributed to the phenomenon of sputtering. In analytical glow discharges, the cathode is constructed of the material to be analyzed. In addition to electron emission, the ion (and fast atom) bombardment of the cathode also causes the sputtering of cathode material (mainly free atoms). The sputtered cathode atoms enter the plasma and are also subject to ionization and excitation collisions. Therefore, the glow discharge plasma can be considered as an atom and ion reservoir with a composition characteristic for the material to be analyzed. Glow discharges in analytical chemistry have been primarily coupled to mass spectrometers and optical emission spectrometers, although they are also used as sources in atomic absorption and fluorescence spectrometry, and in hybrid constructions (in combination with lasers, magnetic fields, etc.). Moreover, besides the analytical applications, glow discharges are extensively used for etching, deposition and surface modification purposes, e.g. in the microelectronics industry, and as metal vapor ion lasers.

To acquire better results in these application fields, a good insight in the glow discharge is desirable. In this work, we try to achieve this by mathematical modeling. A set of three-dimensional models has been developed to obtain an overall picture of the argon direct current glow discharge, used in analytical chemistry. The species assumed to be present in the plasma, are argon gas atoms at rest, uniformly distributed over the discharge, singly charged positive argon ions, fast argon atoms created by charge transfer collisions from the argon ions, argon metastable atoms, fast and slow electrons, and sputtered cathode atoms and the corresponding ions (copper is taken as example).

Basically, three kinds of models can be applied to describe glow discharges. A fluid model considers the plasma species more or less in equilibrium with the electric field. The relevant equations are the continuity and transport equations (based on diffusion and migration). This model is fairly simple but it is only approximate. Indeed, it is not able to describe accurately the behavior of fast plasma species which are not in equilibrium with the electric field. A Boltzmann model copes with the non-equilibrium behavior of the plasma species and treats them as a beam of particles in a Boltzmann transport equation. The most accurate way of modeling is by Monte Carlo simulations, which describe the behavior of the particles explicitly. The particles' trajectories are computed by Newton's laws and their collisions are treated with random numbers. By following a large number of particles in this statistical way, the glow discharge can be simulated. This approach requires, however, long calculation times for slow-moving particles. Hence, each model has its advantages and disadvantages. Therefore, a combination of these models has been utilized in this work for the different plasma species.

The fast electrons are treated with a Monte Carlo model; collision processes incorporated are elastic collisions with argon atoms, electron impact excitation and ionization from the argon ground state and from the metastable level, and ionization of sputtered copper atoms. The behavior of the slow electrons and the argon ions is calculated in a fluid model; the continuity and transport equations are coupled with the Poisson equation to obtain a self-consistent electric field distribution. Moreover, the argon ions are described with a Monte Carlo model in the cathode dark space (CDS), as well as the fast argon atoms which are created by charge transfer and elastic collisions from the argon ions. The collision processes taken into account are symmetric charge transfer for the argon ions, elastic collisions with argon atoms for both argon ions and fast atoms, and fast argon ion and atom impact ionization and excitation of argon atoms. The argon metastable atoms are handled with a fluid model, consisting of a balance equation with different production and loss processes. The thermalization process of the sputtered copper atoms is described with a Monte Carlo model. The subsequent diffusion, the creation of copper ions and the transport of these copper ions, are handled in a fluid model. Finally, the behavior of the copper ions in the CDS is also treated with a Monte Carlo model. All these models are combined into a comprehensive modeling network, and solved iteratively until final convergence is reached, to obtain an overall picture of the glow discharge. The models are developed in three dimensions (or in two dimensions for the fluid models, due to the cylindrical symmetry of the cell), and applied to the geometry of the standard cell for analyzing flat samples in the VG9000 glow discharge mass spectrometer.

The results of the models are shown at typical discharge conditions for the VG9000 mass spectrometer. The influence of pressure and voltage on the results is investigated. Moreover, the results are compared with available literature data and experimental observations, to test the validity of the models.

The electrical current as a function of pressure and voltage is computed and compared with experimental values of the VG9000 mass spectrometer. Rather good qualitative agreement is reached. Quantitative agreement cannot yet be expected, since the exact pressure and gas temperature in the discharge cell are unknown.

The density profiles of the different plasma species are also calculated. The argon ion density is low and constant in the CDS and reaches a maximum in the middle of the discharge. The slow electron density profile is quite similar, except that it is zero in the CDS and at the cell walls. This results in a net positive space charge in the CDS and nearly charge neutrality in the negative glow (NG). The slow electron density is in reasonable agreement with Langmuir probe and optical emission spectrometry results (cooperation with the Institute of Spectrochemistry and Applied Spectroscopy, Dortmund, D). The calculated fast electron density has its maximum in the beginning of the NG. It is about four orders of magnitude lower than the argon ion and slow electron density, hence it has no influence on the space charge. The fast argon atom density is also negligible compared to the overall argon gas atom density. The calculated argon metastable atom density has a pronounced maximum close to the cathode. It was compared with results of laser induced fluorescence (LIF) measurements, and reasonable agreement was reached (cooperation with the Department of Chemistry, University of Florida, Gainesville, FL, USA). The sputtered (copper) atoms become already thermalized close to the cathode. The non-thermalized atom density was found to be negligible compared to the thermalized atom density. The latter reaches a maximum at a few mm from the cathode, which is in excellent agreement with our LIF results. The copper ion density has a similar profile as the argon ion density but is about two orders of magnitude lower. This is in agreement with mass spectrometric observations in the VG9000 instrument, where the copper ion to argon ion peak ratio is in the percent order. The ionization degree of copper was calculated to be about 0.1 %. Both the copper ion density profile and the ionization degree are in reasonable agreement with the results of our LIF experiments.

The calculated potential distribution is negative at the cathode, it increases steeply in the CDS, and is slightly positive in the NG. The position where the potential goes through zero is defined as the interface between CDS and NG. This calculated value as a function of discharge conditions is in good agreement with results of an empirical formula found in the literature. The axial and radial electric field distributions have also been calculated. The electric field is slightly positive at the anode walls and extremely negative at the cathode.

The models also give information about the energies of the plasma species. The electrons gain energy in the CDS by the electric field but also lose energy by collisions. In the NG, they mainly lose energy, so that their energy distribution at the end of the NG is highest at low energy. However, a small peak at maximum energy is observed, indicating that some electrons have traversed the entire discharge without collisions. The argon ions lose their energy more efficiently by (charge transfer) collisions. Therefore, their energy distribution is a decreasing curve towards high energies. This is in rather good agreement with the argon ion energy distribution at the cathode, measured by van Straaten with the VG9000 mass spectrometer. The fast argon atom energy distribution is similar to the argon ion energy distribution but drops even faster towards high energies, since the atoms cannot gain energy from the electric field. The copper ion energy distribution, however, is characterized by a pronounced peak at maximum energy, which is in excellent agreement with experimental results of the VG9000 mass spectrometer. From the energy distributions of the species bombarding the cathode, the sputtering flux and the contributions of different species to sputtering can be calculated. The fast argon atoms play a dominant role, followed by the argon ions. The contribution of copper ions (self-sputtering) is however not negligible.

From the Monte Carlo models, information can be obtained about the collision processes of the plasma species. The rates of the electron, argon ion and fast argon atom collisions throughout the discharge are presented. Moreover, the relative contributions of the different ionization mechanisms for argon and copper are computed. Electron impact ionization is dominant for argon, but fast argon ion and atom impact ionization are not negligible, especially at high voltages. For copper, electron impact ionization is of minor importance compared to Penning ionization and asymmetric charge transfer. Also the relative roles of different production and loss processes for the argon metastable atoms are calculated. Electron, fast argon ion and atom impact excitation are found to be the dominant production processes, whereas diffusion and electron collisional transfer to the nearby energy levels are the most important loss processes.

Finally, the crater profiles and etching rates due to sputtering at the cathode have been calculated. The characteristic crater profile found experimentally can at least qualitatively be reproduced by our model. The calculated etching rates are typically 1-20 $\mu\text{m/h}$ or 0.1-5 $\mu\text{g/s}$, which is in agreement with literature data.

In general, the good accordance with experimental data illustrates that the models give a realistic picture of the glow discharge.

The three-dimensional models presented in this work are clearly more complex and consume more computer time than one-dimensional models. To test whether it is really necessary to develop three-dimensional models or whether the one-dimensional approach yields already a satisfactory description of the glow

discharge, the results of three-dimensional modeling have been compared with those in one dimension. It was found that for the investigated cell geometry, the results are more or less comparable. Hence, one-dimensional models are in a first approximation sufficient to obtain a better insight in the glow discharge. However, three-dimensional models can give additional information (e.g. crater profiles at the cathode) and are therefore a progress when a more complete description of the discharge is intended.

Finally, as a spin-off, the models are used to explain experimentally observed differences in relative sensitivity factors (RSF's) in glow discharge mass spectrometry. Since the cross sections of asymmetric charge transfer ionization of different elements are not available from the literature, a model was developed for calculating RSF's based on transport and Penning ionization only (electron impact ionization is of minor importance), to test the influence of asymmetric charge transfer. A systematic investigation for 42 elements showed that a correlation exists between the discrepancy between calculated and experimental RSF's on the one hand and the availability of suitable energy levels for asymmetric charge transfer on the other. Therefore, it is strongly suggested that asymmetric charge transfer can explain the differences in RSF's for different elements.

Generally, it can be concluded that mathematical modeling is a useful tool to obtain better insight in the fundamental aspects of the glow discharge. Although experimental validation will always be necessary, modeling can be complementary, in the sense that it can often provide information which is experimentally hard to acquire.

WISKUNDIGE SIMULATIES VAN EEN GELIJKSTROOM-GLIMONTLADING IN ARGON

Een glimontlading is een soort plasma, d.w.z. een partieel geïoniseerd gas bestaande uit positieve en negatieve ladingen en een groot aantal neutrale deeltjes. De ontleding kan verkregen worden door twee elektroden in een gas bij lage druk (~ 100 Pa) te plaatsen. Een spanning van ongeveer 1 kV wordt tussen de elektroden aangelegd en veroorzaakt elektrische doorslag van het gas, waarbij positieve ionen en elektronen gevormd worden. De positieve ionen worden versneld naar de kathode, waar ze elektronen lossen. De elektronen komen in het plasma terecht en geven o.m. aanleiding tot botsingen (hoofdzakelijk excitatie en ionisatie). De excitatie-botsingen, gevolgd door deëxcitatie met uitzenden van licht, zijn verantwoordelijk voor de karakteristieke naam van de "glim"ontlading. De ionisatie-botsingen geven ontstaan aan nieuwe ionen en elektronen, wat noodzakelijk is om de glimontlading in stand te houden.

Het gebruik van de glimontlading als analytische spectroscopische bron voor elementanalyse is mede gebaseerd op het fenomeen "sputteren". De kathode in een analytische glimontlading is gemaakt uit het te analyseren materiaal. Naast het lossen van elektronen maakt het bombardement van ionen (en snelle atomen) op de kathode ook kathodemateriaal (voornamelijk atomen) vrij. Dit proces noemt men "sputteren". De gesputterde atomen komen in het plasma en zijn ook onderhevig aan ionisatie- en excitatie-botsingen. Het glimontladingsplasma kan dan ook als een atoom- en ionreservoir beschouwd worden, met een samenstelling die karakteristiek is voor het te analyseren materiaal. Glimontladingsplasma wordt gebruikt voor analytische toepassingen worden voornamelijk gekoppeld aan massaspectrometers en optische emissie spectrometers. Daarnaast worden ze ook gebruikt als atoomreservoir in atoom absorptie en fluorescentie spectrometrie en in gecombineerde opstellingen (gekoppeld met lasers, magnetische velden, e.d.). Naast de analytische toepassingen worden ze uitvoerig gebruikt voor het etsen en behandelen van oppervlakken en het afzetten van lagen, o.m. in de microëlectronica, en als metaaldamp ionlasers.

Om de resultaten in deze diverse toepassingsdomeinen te verbeteren, is een goed inzicht in de glimontlading wenselijk. In dit werk proberen wij dit te verwerven door wiskundige simulaties. Een set van drie-dimensionele modellen werd ontwikkeld om een algemeen beeld te krijgen van een gelijkstroom-glimontlading in argon, gebruikt in analytische scheikunde. De deeltjes die verondersteld worden aanwezig te zijn in het plasma, omvatten argon gas atomen in rust en gelijkmatig verdeeld over de ontleding, enkelvoudig geladen positieve argon ionen, snelle argon atomen gevormd door ladingsuitwisselings-botsingen van de argon ionen, argon

metastabiele atomen, snelle en trage elektronen, gesputterde kathode-atomen en hun overeenkomstige ionen (koper werd als voorbeeld genomen).

Drie soorten modellen kunnen worden aangewend om glimontladingen te beschrijven. Een continuüm model beschouwt de plasmadeeltjes min of meer in evenwicht met het elektrisch veld. De relevante vergelijkingen zijn de continuïteits- en transportvergelijkingen (gebaseerd op diffusie en migratie). Dit model is vrij eenvoudig, maar het is enkel een benadering. Inderdaad, het is niet in staat het gedrag van snelle plasmadeeltjes, die niet in evenwicht zijn met het elektrisch veld, nauwkeurig te beschrijven. Een Boltzmann model houdt rekening met het niet-evenwichtsgedrag van de plasmadeeltjes en behandelt ze als een bundel van deeltjes in een Boltzmann transportvergelijking. De meest nauwkeurige benadering wordt verkregen via Monte Carlo simulaties, die het gedrag van de deeltjes expliciet beschrijven. Het traject van de deeltjes wordt berekend met de wetten van Newton en hun botsingen worden met random getallen behandeld. Door een groot aantal deeltjes op deze statistische wijze te volgen, kan de glimontlading beschreven worden. Dit model vergt echter een lange rekentijd voor trage deeltjes. Elk model heeft dus zijn voor- en nadelen. Daarom gebruiken we een combinatie van deze modellen voor de verschillende plasmadeeltjes.

De snelle elektronen worden met een Monte Carlo model behandeld; de botsingsprocessen die in rekening gebracht worden, omvatten elastische botsingen met argon atomen, elektron impact excitatie en ionisatie vanuit de argon grondtoestand en het metastabiele niveau, en ionisatie van de gesputterde koperatomen. Het gedrag van de trage elektronen en de argon ionen wordt in een continuümmodel berekend; de continuïteits- en transportvergelijkingen worden aan de Poisson vergelijking gekoppeld om een zelf-consistent elektrisch veld te bekomen. Bovendien worden de argon ionen in de kathode donkere ruimte (CDS) met een Monte Carlo model beschreven, samen met de snelle argon atomen die gevormd zijn door ladingsuitwisseling en elastische botsingen van de argon ionen. De botsingsprocessen in rekening gebracht in dit model zijn symmetrische ladingsoverdracht voor de argon ionen, elastische botsingen met argon atomen, voor zowel argon ionen en snelle atomen, en snelle argon ion en atoom impact ionisatie en excitatie van argon atomen. De argon metastabiele atomen worden in een continuümmodel behandeld, dat is opgebouwd uit een balansvergelijking met verschillende vormings- en verliesprocessen. Het thermalisatieproces van de gesputterde koperatomen wordt beschreven via Monte Carlo simulaties. De verdere diffusie, de vorming van koperionen en het transport van deze koperionen, worden behandeld in een continuümmodel. Het gedrag van de koperionen in de CDS, tenslotte, wordt beschreven met een Monte Carlo model. Al deze modellen worden gecombineerd tot een uitgebreid netwerk, en iteratief opgelost tot convergentie bereikt wordt, om een algemeen beeld van de glimontlading te verkrijgen. De modellen werden in drie dimensies ontwikkeld (of in twee dimensies voor de

continuümmodellen, wegens de cilindrische symmetrie van de cel), en werden toegepast op de geometrie van de standaard cel voor de analyse van vlakke monsters in de VG9000 glimontladingsmassaspectrometer.

De resultaten van deze modellen worden getoond voor de typische ontladingsvoorwaarden van de VG9000 massaspectrometer, en de invloed van druk en spanning op de resultaten wordt bestudeerd. Bovendien worden de resultaten vergeleken met beschikbare literatuurgegevens en experimentele waarden, om de geldigheid van de modellen te testen.

De elektrische stroom in functie van druk en spanning werd berekend en vergeleken met experimentele waarden, waargenomen met de VG9000 massaspectrometer. Kwalitatief is er een vrij goede overeenkomst. Kwantitatieve overeenstemming kan echter nog niet verwacht worden, vermits de exacte druk en gastemperatuur in de ontladingscel niet gekend zijn.

Tevens werden de dichtheidsprofielen van de verschillende plasmadeeltjes berekend. De argon ionendichtheid is laag en constant in de CDS en bereikt een maximum in het midden van de ontlading. De dichtheid van de trage elektronen is zeer gelijkaardig, maar ze is nul in de CDS en aan de celwanden. Dit leidt tot een netto positieve ruimtelading in de CDS en nagenoeg ladingsneutraliteit in het negatieve glimlicht (NG). De dichtheid van de trage elektronen is in redelijke overeenstemming met resultaten van Langmuir probe metingen en optische emissie spectrometrie (samenwerking met het Institut für Spektrochemie und Angewandte Spektroskopie, Dortmund, D). De berekende dichtheid van de snelle elektronen bereikt een maximum in het begin van de NG. Ze is ongeveer vier grootteorden lager dan de dichtheid van de argon ionen en trage elektronen, en heeft bijgevolg geen invloed op de ruimtelading. De dichtheid van de snelle argon atomen is ook verwaarloosbaar vergeleken met de totale argon gas atoombichtheid. De berekende dichtheid van de argon metastabiele atomen heeft een uitgesproken maximum dichtbij de kathode. Deze werd vergeleken met laser geïnduceerde fluorescentie (LIF) metingen en de overeenkomst is bevredigend (samenwerking met het Department of Chemistry, University of Florida, Gainesville, FL, USA). De gesputterde koperatomen worden reeds vlakbij de kathode gethermaliseerd. De dichtheid van de niet-gethermaliseerde koper atomen blijkt verwaarloosbaar vergeleken met deze berekend voor de gethermaliseerde atomen. Deze laatste bereikt een maximum op enkele mm van de kathode, wat in uitstekende overeenstemming is met onze LIF resultaten. De dichtheid van de koper ionen heeft een gelijkaardig profiel als deze van de argon ionen, maar is ongeveer twee grootteorden lager. Dit is in overeenstemming met massaspectrometrische waarnemingen, waar de signaalverhouding van koper ionen tot argon ionen in het percentgebied ligt. De berekende ionisatiegraad van koper is ongeveer 0.1 %. Zowel het dichtheidsprofiel van de koper ionen als de ionisatiegraad zijn in vrij goede overeenstemming met de resultaten van onze LIF experimenten.

De berekende potentiaalverdeling is negatief aan de kathode, stijgt snel in de CDS, en is licht positief in de NG. De plaats waar de potentiaal door nul gaat, wordt gedefinieerd als de overgang tussen CDS en NG. Deze berekende waarde in functie van de ontladingsvoorwaarden is in goede overeenstemming met resultaten van de empirische formule uit de literatuur. De axiale en radiale elektrische veldverdelingen werden ook berekend. Het elektrisch veld is licht positief aan de anode wanden en uitgesproken negatief aan de kathode.

De modellen geven ook informatie over de energieën van de plasmadeeltjes. De elektronen winnen energie in de CDS door het elektrisch veld, maar ze verliezen tevens energie door botsingen. In de NG verliezen ze voornamelijk energie, zodat op het einde van de NG vooral elektronen met lage energie voorkomen. Een klein maximum wordt echter ook waargenomen bij de maximale energie van de energieverdeling, hetgeen betekent dat sommige elektronen de hele ontlading doorlopen hebben zonder botsingen. De argon ionen verliezen hun energie meer efficiënt door (ladingsuitwisselings)botsingen: de berekende energieverdeling is derhalve een dalende curve naar hogere energieën toe. Dit is in vrij goed overeenstemming met de energieverdeling van de argon ionen aan de kathode, gemeten door van Straaten met de VG9000 massaspectrometer. De energieverdeling van de snelle argon atomen is gelijkaardig aan die van de argon ionen, maar daalt sneller naar hoge energieën toe, omdat de atomen geen energie kunnen winnen van het elektrisch veld. De berekende energieverdeling van de koper ionen is echter gekarakteriseerd door een uitgesproken piek bij maximale energie, wat in uitstekende overeenstemming is met de resultaten van de VG9000 massaspectrometer. De energieverdelingen van de deeltjes die op de kathode botsen, worden gebruikt om de flux van gesputterde atomen en de bijdragen van de verschillende deeltjes tot sputtering te berekenen. De snelle argon atomen spelen een dominante rol, gevolgd door de argon ionen. De bijdrage van de koper ionen (zelfsputtering) is echter niet verwaarloosbaar.

Uit de Monte Carlo modellen kan ook informatie verkregen worden over de botsingsprocessen van de plasmadeeltjes. De berekende botsingssnelheden van de elektronen, argon ionen en snelle atomen doorheen de ontlading worden in dit werk weergegeven. Ook de relatieve bijdragen van verschillende ionizatiemechanismen voor argon en koper werden berekend. Elektron impact ionisatie is dominant voor argon, maar snelle argon ion and atoom impact ionisatie zijn toch niet verwaarloosbaar, vooral bij hoge aangelegde spanningen. Voor koper is elektron impact ionisatie echter van ondergeschikt belang, vergeleken met Penning ionisatie en asymmetrische ladingsoverdracht. Bovendien werden de relatieve bijdragen van verschillende vormings- en verliesprocessen voor de metastabiele argon atomen berekend. Elektron, snelle argon ion en atoom impact ionisatie blijken de dominante vormingsprocessen te zijn, terwijl diffusie en overdracht naar de nabijgelegen energieniveaus door elektronenbotsing de belangrijkste verliesprocessen zijn.

Tenslotte werden de kraterprofielen en etssnelheden door kathode-sputtering berekend. Het karakteristieke kraterprofiel dat experimenteel waargenomen wordt, kan ten minste kwalitatief door het model voorspeld worden. De berekende etssnelheden zijn typisch 1-20 $\mu\text{m/u}$ of 0.1-5 $\mu\text{g/s}$, wat in overeenstemming is met literatuurgegevens.

Algemeen toont de goede overeenstemming met het experiment aan dat de modellen een realistisch beeld geven van de glimontlading.

De in dit werk voorgestelde drie-dimensionale modellen zijn duidelijk complexer en tijdrovender dan één-dimensionele modellen. Om te testen of drie-dimensionele modellen werkelijk nodig zijn of dat één-dimensionele modellen ook al een bevredigende beschrijving van de glimontlading kunnen geven, werden de resultaten van beide beschrijvingen met elkaar vergeleken. Voor de bestudeerde celgeometrie bleken de resultaten min of meer vergelijkbaar. Eén-dimensionele modellen zijn dus in eerste benadering voldoende om een beter inzicht in de glimontlading te verwerven. Drie-dimensionele modellen geven echter bijkomende informatie (o.m. kraterprofielen aan de kathode) en zijn daarom toch een vooruitgang als we een meer volledige beschrijving van de ontlading wensen te maken.

Tenslotte werden, als spin-off, de modellen gebruikt om verschillen in relatieve gevoeligheidsfactoren (RSF) in glimontladingsmassaspectrometrie te verklaren. Vermits de botsingswerkzame doorsneden van asymmetrische ladingsoverdracht ionisatie voor verschillende elementen in de literatuur niet beschikbaar zijn, werd een model ontwikkeld om RSF waarden te berekenen, enkel gebaseerd op transport en Penning ionisatie (elektron impact ionisatie is van ondergeschikt belang), om de invloed van asymmetrische ladingsoverdracht te onderzoeken. Een systematische studie voor 42 elementen toonde aan dat er een verband bestaat tussen het verschil in berekende en experimentele RSF waarden enerzijds, en de beschikbaarheid van gepaste energieniveaus voor asymmetrische ladingsoverdracht anderzijds. Dit geeft ons sterke aanwijzingen dat asymmetrische ladingsoverdracht de verschillen in RSF waarden voor verschillende elementen kan verklaren.

Algemeen kunnen we besluiten dat wiskundige simulaties nuttig zijn om beter inzicht in de fundamentele aspecten van de glimontlading te verwerven. Hoewel experimentele verificatie steeds nodig zal zijn, kunnen de simulaties complementair beschouwd worden, vermits ze vaak informatie kunnen verschaffen die experimenteel moeilijk te verkrijgen is.

Appendix

PUBLICATIONS

- 1) Monte Carlo simulation of an analytical glow discharge: motion of electrons, ions and fast neutrals in the cathode dark space.
A. Bogaerts, M. van Straaten and R. Gijbels, *Spectrochim. Acta, Part B*, **50**, 179-196 (1995).
- 2) Experimental determination of energy distributions of ions bombarding the cathode surface in a glow discharge.
M. van Straaten, A. Bogaerts and R. Gijbels, *Spectrochim. Acta, Part B*, **50**, 583-605 (1995).
- 3) Description of the thermalization process of the sputtered atoms in a glow discharge, using a three-dimensional Monte Carlo method.
A. Bogaerts, M. van Straaten and R. Gijbels, *J. Appl. Phys.* **77**, 1868-1874 (1995).
- 4) Plasma diagnostics of analytical glow discharges in argon and in neon: Langmuir probe and optical emission spectrometry measurements.
A. Bogaerts, A. Quentmeier, N. Jakubowski and R. Gijbels, *Spectrochim. Acta, Part B*, **50**, 1337-1349 (1995).
- 5) Hybrid Monte Carlo-fluid model of a direct current glow discharge.
A. Bogaerts, R. Gijbels and W.J. Goedheer, *J. Appl. Phys.*, **78**, 2233-2241 (1995).
- 6) Mathematical modelling of an analytical dc glow discharge.
A. Bogaerts, M. van Straaten and R. Gijbels, in "Recent advances in Plasma Source Mass Spectrometry", G. Holland (Ed.), BPC Wheatons Ltd, Exeter, UK (1995), p. 82-90.
- 7) Mass spectrometric analysis of inorganic solids: GDMS and other methods.
R. Gijbels, M. van Straaten and A. Bogaerts, in "Advances in Mass Spectrometry, volume 13", I.Cornides, G.Horvath and K.Vekey (Eds.), Wiley, New York (1995), p. 241-256.
- 8) Modeling of the role of metastable argon atoms in a direct current glow discharge in argon.
A. Bogaerts and R. Gijbels, *Phys. Rev. A*, **52**, 3743-3751 (1995).

- 9) The role of fast argon ions and atoms in the ionization of argon in a direct current glow discharge: a mathematical simulation.
A. Bogaerts and R. Gijbels, *J. Appl. Phys.*, **78**, 6427-6431 (1995).
- 10) Role of sputtered Cu atoms and ions in a direct current glow discharge: combined fluid and Monte Carlo model.
A. Bogaerts and R. Gijbels, *J. Appl. Phys.*, **79**, 1279-1286 (1996).
- 11) Mathematical description of a direct current glow discharge in argon.
A. Bogaerts and R. Gijbels, *Fres. J. Anal. Chem.* (in press: July-August 1996).
- 12) Plasma Models.
A. Bogaerts and R. Gijbels, Chapter in "Glow Discharge Optical Emission Spectrometry", R. Payling, D. G. Jones and A. Bengtson (eds.), Wiley (in press).
- 13) Two-dimensional model of a direct current glow discharge: description of the electrons, argon ions and fast argon atoms.
A. Bogaerts, R. Gijbels and W. J. Goedheer, *Anal. Chem.* (in press: July 1996).
- 14) Two-dimensional model of a direct current glow discharge: description of the argon metastable atoms, sputtered atoms and ions.
A. Bogaerts and R. Gijbels, *Anal. Chem.* (in press: August 1996).
- 15) Relative sensitivity factors in glow discharge mass spectrometry: the role of charge transfer ionization.
A. Bogaerts and R. Gijbels, *J. Anal. Atom. Spectrom.* (in press: September 1996).
- 16) Three-dimensional density profiles of sputtered atoms and ions in a direct current glow discharge: experimental study and comparison with calculations.
A. Bogaerts, E. Wagner, B. W. Smith, J. D. Winefordner, D. Pollmann, W. W. Harrison and R. Gijbels, *Spectrochim. Acta, Part B* (accepted).
- 17) Three-dimensional density profiles of the argon metastable atoms in a direct current glow discharge: experimental study and comparison with calculations.
A. Bogaerts, R. D. Guenard, B. W. Smith, J. D. Winefordner, W. W. Harrison and R. Gijbels, *Spectrochim. Acta, Part B* (accepted).

CONTRIBUTIONS AT CONFERENCES

- 1) The cathode dark space; modelling of ion and electron transport processes.
A. Bogaerts, M. van Straaten and R. Gijbels.
Poster at "XXVIII Colloquium Spectroscopicum Internationale, Postsymposium on Glow Discharges", July 4-7, 1993, York, UK.
- 2) Ion energy distributions at the cathode surface of a glow discharge: the relative importance of sputtering by gas and cathode ions.
M. van Straaten, A. Bogaerts and R. Gijbels.
Poster at "1994 Winter Conference on Plasma Spectrochemistry", January, 1994, San Diego.
- 3) The cathode dark space; modelling of ion and electron transport processes.
A. Bogaerts, M. van Straaten and R. Gijbels.
Poster at "1994 Winter Conference on Plasma Spectrochemistry", January, 1994, San Diego.
- 4) Fundamentele aspecten van glimontladingsmassaspectrometrie.
A. Bogaerts, M. van Straaten and R. Gijbels.
Oral presentation at "2e KVCV Jongerencongres", March 9, 1994, Antwerpen.
- 5) Fundamentele Aspekte der Glimmentladung.
A. Bogaerts, M. van Straaten and R. Gijbels.
Oral presentation at "17. Arbeitstreffen Festkörper-Massenspektrometrie", May 2-4, 1994, Jülich, Germany.
- 6) The cathode dark space; modelling of ion and electron transport processes.
A. Bogaerts, M. van Straaten and R. Gijbels.
Poster at "17. Arbeitstreffen Festkörper-Massenspektrometrie", May 2-4, 1994, Jülich, Germany.
- 7) Monte Carlo simulation of electron, ion and fast neutral transport in the cathode dark space of a dc glow discharge, and comparison with other models.
A. Bogaerts, M. van Straaten and R. Gijbels.
Poster at "XIIth Europhysics Sectional Conference on Atomic and Molecular Physics of Ionized Gases", August 23-26, 1994, Noordwijkerhout, The Netherlands.

- 8) Mathematical modelling of an analytical dc glow discharge.
A. Bogaerts, M. van Straaten and R. Gijbels.
Oral presentation at "4th International Conference on Plasma Source Mass Spectrometry", September 11-16, 1994, Durham, UK.

- 9) Plasma diagnostics of analytical glow discharges in argon and in neon: Langmuir probe and optical emission spectrometry measurements.
A. Bogaerts, A. Quentmeier, N. Jakubowski and R. Gijbels.
Poster at "1995 European Winter Conference on Plasma Spectrochemistry", January 8-13, 1995, Cambridge, UK.

- 10) Mathematical modelling of a dc glow discharge.
A. Bogaerts, M. van Straaten and R. Gijbels.
Oral presentation at "1995 European Winter Conference on Plasma Spectrochemistry", January 8-13, 1995, Cambridge, UK.

- 11) Hybride Monte Carlo-fluidum model voor een dc glimontlading.
A. Bogaerts, R. Gijbels en W. J. Goedheer.
Oral presentation at "Symposium Plasma- en gasontladingsphysica", 12-13 april 1995, Lunteren, The Netherlands.

- 12) Modelling of a direct current glow discharge: combined models for the electrons, argon ions and metastables.
A. Bogaerts and R. Gijbels.
Poster at "10th International Colloquium on Plasma Processes (CIP'95)", June 11-15, 1995, Antibes, France.

- 13) Modelling of a direct current glow discharge: combined models for the electrons, argon ions and metastables.
A. Bogaerts and R. Gijbels.
Poster at "18. Arbeitstreffen Festkörpermassenspektrometrie", June 12-14, 1995, Freiburg, Germany.

- 14) Mathematical modeling of direct current glow discharges.
A. Bogaerts and R. Gijbels.
Oral presentation at "18. Arbeitstreffen Festkörpermassenspektrometrie", June 12-14, 1995, Freiburg, Germany.

- 15) Modelling of a direct current glow discharge in argon.
A. Bogaerts and R. Gijbels.
Seminar at the University of Mons-Hainaut, Departement des Materiaux, Mons, June 21, 1995.
- 16) Mathematical modelling of the electrons, argon ions and argon metastables in a direct current glow discharge.
A. Bogaerts and R. Gijbels.
Poster at "XXIX Colloquium Spectroscopicum Internationale (CSI)", August 27 - September 1, 1995, Leipzig, Germany.
- 17) Modelling of a direct current glow discharge in argon.
A. Bogaerts and R. Gijbels.
Oral presentation at "CSI Post-symposium on Glow Discharge Spectroscopy", September 1-4, 1995, Dresden, Germany.
- 18) Theoretical study of the role of metastable argon atoms in a dc glow discharge.
A. Bogaerts and R. Gijbels.
Poster at "CSI Post-symposium on Glow Discharge Spectroscopy", September 1-4, 1995, Dresden, Germany.
- 19) Mathematical modeling of the behavior of the sputtered atoms and corresponding ions in a direct current glow discharge.
A. Bogaerts and R. Gijbels.
Oral presentation at "1996 Winter Conference on Plasma Spectrochemistry", January 8-13, 1996, Fort Lauderdale, FL, USA.
- 20) Relative ion yields in glow discharge mass spectrometry: the role of charge transfer ionization.
A. Bogaerts and R. Gijbels.
Oral presentation at "1996 Winter Conference on Plasma Spectrochemistry", January 8-13, 1996, Fort Lauderdale, FL, USA.
- 21) Mathematical modelling of a direct current glow discharge.
A. Bogaerts and R. Gijbels.
Poster at "Belgian Physical Society: General Scientific Meeting", June 6-7, 1996, Université Libre de Bruxelles, Brussels.

- 22) Mathematical modeling of a direct current glow discharge.
A. Bogaerts and R. Gijbels.
Poster at “XIIIth European Sectional Conference on Atomic and Molecular Physics of Ionized Gases”, August 26-30, 1996, Poprad, Slovakia.
- 23) Mathematical modeling of a direct current glow discharge in argon.
A. Bogaerts and R. Gijbels.
Seminar at the Institute of Physics, Academy of Sciences of the Czech Republic, Prague, Czech Republic, September 2, 1996.
- 24) Mathematische Modellberechnungen einer Gleichstrom Glimmentladung.
A. Bogaerts and R. Gijbels.
Oral Presentation at “3. Symposium Massenspektrometrische Verfahren der Elementspurenanalyse”, September 24-26, 1996, Jülich, Germany.
- 25) Three-dimensional modeling of a dc glow discharge in argon, and comparison with experiment.
A. Bogaerts and R. Gijbels.
Poster or oral presentation at “49th Annual Gaseous Electronics Conference, October 20-24, 1996, Argonne, IL, USA.

SCIENTIFIC VISITS

- 1) Institut für Spectrochemie und angewandte Spektroskopie, Dortmund, Germany.
“Plasma diagnostics of an analytical glow discharge: Langmuir probe and optical emission spectrometry measurements”.
February 1 - April 30, 1994.
- 2) University of Florida, Department of Chemistry, Gainesville, FL, USA.
“Plasma diagnostics of an analytical glow discharge: Laser atomic absorption and fluorescence spectrometry”.
January 15 - February 23, 1996.

SCIENTIFIC PRIZES

- 1) June 1993: Jongerenprijs van de Koninklijke Vlaamse Chemische Vereniging.
- 2) June 1996: DSM-prijs voor Chemie en Technologie: 1e prijs.
- 3) 1996: Travel grant award for the “49th Annual Gaseous Electronics Conference”, Argonne, IL, USA.